



Durham E-Theses

Galaxy Evolution in Groups and Clusters

Wilman, David John

How to cite:

Wilman, David John (2004) *Galaxy Evolution in Groups and Clusters*, Durham theses, Durham University. Available at Durham E-Theses Online: <http://etheses.dur.ac.uk/2816/>

Use policy

The full-text may be used and/or reproduced, and given to third parties in any format or medium, without prior permission or charge, for personal research or study, educational, or not-for-profit purposes provided that:

- a full bibliographic reference is made to the original source
- a [link](#) is made to the metadata record in Durham E-Theses
- the full-text is not changed in any way

The full-text must not be sold in any format or medium without the formal permission of the copyright holders.

Please consult the [full Durham E-Theses policy](#) for further details.

Galaxy Evolution

in Groups and Clusters

by David John Wilman

PhD Thesis, September 2004

Abstract

In this thesis, we investigate the extent to which galaxy evolution is driven by processes common to the group and cluster environments. A bimodality of galaxy properties such as star formation, strongly dependent upon the local overdensity of galaxies, suggests that the passive, early type galaxies common to groups and clusters originate in transformation processes, which are nurtured by the environment. This can only be important to global galaxy evolution if transformations are common in groups, which contain $\gtrsim 50\%$ of the local galaxy population.

We present deep Magellan spectroscopy and HST ACS imaging of our group and field samples at $0.3 \leq z \leq 0.55$, selected from the CNOC2 survey by Carlberg et al. (2001b). We find that these groups contain significantly more passive galaxies than the field, with excesses of S0, elliptical and passive spiral galaxy types. The morphological composition is closely matched to that of irregular and X-ray-faint clusters at a similar epoch. In contrast with a low-redshift group sample selected from 2dFGRS (Eke et al., 2004), we find that the fraction of passive galaxies, f_p , is strongly evolving in the group environment, with parallel evolution in the field population. Simple models confirm that galaxy transformations are required to match the evolution of both group and field populations. Qualitatively similar evolution and dependence on environment is found in physically-motivated simulations. However, these do not quantitatively match the environmental nor luminosity dependence in the evolution of f_p . We also present a complementary method using photometric redshifts to identify infalling groups in the outskirts of clusters with Wide Field Imaging (WFI) technology.

Finally, we identify the key developments which will help to unravel the history of galaxy evolution in coming years.

Galaxy Evolution in Groups and Clusters

by David John Wilman

A thesis submitted to the University of Durham
in accordance with the regulations for
admittance to the Degree of Doctor of Philosophy.

Department of Physics
University of Durham
September 2004

**A copyright of this thesis rests
with the author. No quotation
from it should be published
without his prior written consent
and information derived from it
should be acknowledged.**



2 8 FEB 2005

Contents

1	Introduction	1
1.1	The fundamental properties of galaxies	3
1.1.1	Stellar Populations along the Hubble sequence	3
1.1.2	Measurement of Star Formation	4
1.2	Groups and Clusters of galaxies	6
1.2.1	Detection and abundance of Groups and Clusters	6
1.2.2	Properties of galaxies in Groups and Clusters	7
1.3	Galaxy Evolution	8
1.4	Structure of this thesis	10
2	Star Formation in Low Redshift Galaxy Groups	13
2.1	Introduction	13
2.2	The Sample	14
2.3	Star Formation in 2PIGG Groups	16
3	Star Formation in Galaxy Groups at $0.3 \leq z \leq 0.55$	19
3.1	Introduction	19
3.2	Groups in the CNOC2 Survey	20
3.2.1	The CNOC2 survey	20
3.2.2	The CNOC2 groups	21
3.2.3	Deeper LDSS2 data	21
3.3	Measurement of star formation using EW[OII]	22
3.4	Data Processing	24
3.4.1	Data Reduction	24
3.4.2	Redshift Measurement	24
3.4.2.1	Emission Line Equivalent Width Measurements	26

3.4.2.2	Comparison with CNOC2 data	27
3.4.3	K-corrected rest frame magnitudes	27
3.4.4	Group Membership	28
3.5	Individual Group Analysis	35
3.5.1	Basic Parameters	35
3.5.2	Star Formation in the CNOC2 groups	37
3.5.2.1	Trends with group concentration	38
3.5.2.2	Trends with group velocity dispersion	42
3.6	The Stacked Group	44
3.6.1	Completeness in the stacked group	45
3.6.2	Selection Functions	45
3.6.3	Magellan Redshift Completeness	49
3.6.4	The properties of stacked group galaxies	51
3.6.4.1	The fraction of passive galaxies in the stacked group	53
3.6.4.2	Environmental dependencies in the luminosity function of galaxies	54
3.6.4.3	Discussion	59
3.7	Conclusions	61
4	The Morphological Composition of Galaxy Groups at $0.3 \leq z \leq 0.55$	63
4.1	Introduction	63
4.2	Data	66
4.2.1	The Observations:	66
4.2.2	HST-ACS Data Processing	66
4.2.3	Galaxy Identification	67
4.3	Morphological Classification	84
4.3.1	Galaxy Classifications	86
4.3.2	Comparison of morphological classifications	107
4.4	Results	107
4.4.1	Are early-type galaxies more prevalent in groups than in the field?	111
4.4.2	Star Formation across the Hubble Sequence	111
4.4.3	Are S0 type galaxies significantly more common in groups?	113
4.4.4	Are spiral galaxies more passive in groups?	115
4.4.5	How can we characterise the excess of elliptical galaxies in groups?	118

4.4.6	Other Morphological trends	120
4.4.7	Peculiar and Interacting galaxies	124
4.4.7.1	Are peculiar or interacting galaxies more common in groups?	124
4.4.7.2	Do galaxies with peculiar morphologies form more stars than an average galaxy?	127
4.5	Discussion	128
4.6	Summary	131
5	Evolution in Galaxy Groups	133
5.1	Introduction	133
5.2	Data	134
5.2.1	The galaxy luminosity function in groups and the field	134
5.2.1.1	Luminosity limits	134
5.2.2	EW[OII] in 2dF and CNOC2	136
5.2.2.1	Diagnostics of Star Formation for a Galaxy Population	137
5.2.2.2	Aperture bias	137
5.3	Results	138
5.3.1	The dependence of f_p on redshift, environment and luminosity	138
5.3.2	The properties of the star-forming population	139
5.3.3	Dependence of f_p in groups upon group-centric radius and velocity dispersion	140
5.4	Discussion	142
5.4.1	Implications	142
5.5	Conclusions	143
6	Aperture Effects and the Origin of Colour Gradients in Galaxies	145
7	Modelling Galaxy Evolution and Environmental Effects	149
7.1	Simple Models of Galaxy Evolution	149
7.1.1	The Quiescent Evolution Scenario	150
7.1.1.1	The Modelling Procedure	150
7.1.1.2	The Influence of Quiescent Evolution on f_p	152
7.1.2	The Truncation Scenario	153
7.1.2.1	The Modelling Procedure	153
7.1.2.2	The Influence of Truncation on the Evolution of f_p	157

7.2	Semi-Analytic Models of Galaxy Formation	160
7.2.1	Introduction	160
7.2.2	H α and [OII] Equivalent Width Distributions	161
7.2.3	The Behaviour of the fraction of passive galaxies, f_p	164
7.2.4	Summary	169
7.3	Conclusions	171
8	Mapping the Infall Regions of Galaxy Clusters with a Wide Field Imaging Camera	173
8.1	Introduction	173
8.2	Calibrating Wide Field Imaging Data	176
8.3	Our Wide Field Imaging Data	180
8.3.1	Data Reduction	181
8.3.2	Preliminary Results	185
8.3.3	Optimal Calibration Method	186
8.4	How we will proceed	191
9	Conclusions and Future Prospects	193
9.1	Summary	194
9.1.1	Stellar Populations in Group and Field Galaxies	194
9.1.2	Morphological Properties of Group and Field Galaxies	195
9.1.3	Modelling the Evolution of Group and Field Galaxies	196
9.2	Discussion	197
9.3	Future Prospects	201
9.3.1	Understanding Individual Groups	201
9.3.2	Multi-Wavelength Studies of Star Formation	202
9.3.3	Direct Observations of a Transforming Galaxy	202
9.3.4	The Millennium Run	202
9.3.5	Higher Redshift Groups and Clusters	203
9.3.6	Isolated Galaxies	204

List of Figures

- 2.1 The percentage of local 2dFGRS galaxies (brighter than $M_{b_j} = -19$) in haloes of mass $\geq M$ (M_\odot) as inferred using the 2PIGG catalogue and equation 4.7 of Eke et al. (2004). In reality the percentages will be lower, especially in the larger systems in which interlopers might contaminate the clusters by as much as 40%. Only galaxies and groups at $z \leq 0.1$ are considered. 16
- 2.2 The fraction of galaxies with $\text{EW}[\text{H}\alpha] > 4\text{\AA}$ as a function of local density Σ_5 for the 2dFGRS (bottom panels) and SDSS (top panels) samples. The solid lines represent the full galaxy sample, in bins each containing 250 galaxies. The dashed lines are restricted to galaxies which lie in groups or clusters with the indicated velocity dispersion, in bins of 50 galaxies each. Poisson distribution uncertainties are typically ~ 0.1 on the dashed lines and ~ 0.05 on the solid lines. This figure is reproduced from Balogh et al. (2004a) with permission of Michael Balogh. We note that their terminology is slightly different with $\text{EW}[\text{H}\alpha]$ instead labelled $W_0(\text{H}\alpha)$ 17
- 2.3 The distribution of $\text{EW}[\text{H}\alpha]$ for galaxies in 2dFGRS (left panel) and SDSS (right panel) with $\text{EW}[\text{H}\alpha] > 4\text{\AA}$, in low density environments ($\Sigma_5 < 0.2 \text{Mpc}^{-2}$, dotted line) and high density environments ($\Sigma_5 > 2 \text{Mpc}^{-2}$, solid line). We show Poisson-distributed error bars on the high density subsample which is the smaller of the two. This figure is reproduced from Balogh et al. (2004a) with permission of Michael Balogh. We note that their terminology is slightly different with $\text{EW}[\text{H}\alpha]$ instead labelled $W_0(\text{H}\alpha)$ 18

3.1	A comparison of velocity and EW[OII] measurements in CNOC2 and LDSS2 measurements using the 32 galaxies with matched redshifts in the comparison sample. Left: Rest-frame velocity offset, $(cz_{CNOC2} - cz_{LDSS2})/(1+z)$ and Right: Comparison between rest-frame EW[OII] measurements, for the galaxies in which redshifts and EW[OII] have been obtained from LDSS2 spectra <i>and</i> in the original CNOC2 catalogue.	26
3.2	Bottom: Redshift Distributions in the regions of 2 groups; Top: Velocity Distribution of the group members; The smooth line represents a gaussian with $\sigma = \sigma(v)_{obs}$	32
3.3	The distribution of our CNOC2 groups in $\sigma(v)_{intr}$ -z space. There is no strong correlation, indicating that our highest redshift groups are not necessarily our most massive (highest velocity dispersion) groups.	32
3.4	Top: Kinematic (dv) and projected spatial (dr) offsets from the group centre, as determined by the group membership allocation algorithm (section 3.4.4). The solid line shows the running median of kinematic offset (dv), computed over 50 neighbour-galaxies along the spatial axis. Bottom: The same as in the top panel but with the kinematic and spatial offsets each normalised by the rms values of the parent group. This removes any false dv-dr trend originating from the variable physical sizes of the groups.	33
3.5	Intrinsic Velocity Dispersion of galaxy groups, $\sigma(v)_{intr}$ plotted against the number of galaxy members within 1Mpc and brighter than $M_{b_j} = -20$, corrected for incompleteness (N_{mem}). Errors on N_{mem} represent the Poisson error on the number of candidate members estimated to lie in the group (see Section 3.4.4 for definition).	34
3.6	The luminosity of the brightest group galaxy (within $1h_{75}^{-1}$ Mpc of the luminosity-weighted group centre) as a function of group velocity dispersion, $\sigma(v)_{intr}$. Some of these groups are keyed on the morphology of the brightest galaxy, where this is known from recent HST imaging (the open symbols). The open circles represent early-type galaxies and the stars represent later galaxy types.	35

3.7	The 13 groups with lowest $\sigma(v)_{intr}$. <i>Passive galaxies, star-forming galaxies</i> and <i>highly star-forming galaxies</i> (defined in the text) are represented by circles, triangles and stars respectively. <i>Luminous members</i> are represented by larger symbols than <i>faint members</i> . Crosses represent <i>candidate luminous members</i> . These are bright galaxies without measured redshifts and whilst in some groups these will be mostly or all foreground / background galaxies, in other groups (preferentially the most massive ones) a significant number may also be group members. The $1h_{75}^{-1}Mpc$ radius of each group is also shown centred on the luminosity-weighted centre computed using all known members. We also show a $0.5h_{75}^{-1}Mpc$ radius circle, centred on an iteratively defined centre (see Section 3.5.2). With each group, we also display the group redshift, velocity dispersion $\sigma(v)_{intr}$ and completeness within $1h_{75}^{-1}Mpc$ and brighter than the R_c -band magnitude required for the galaxy to have a luminosity $M_{b_j} \leq -20$ should the galaxy be at the group redshift. Completeness is a function of redshift and the fraction of targeted objects in the group vicinity. Note that groups are ordered by velocity dispersion, $\sigma(v)_{intr}$	39
3.8	As Figure 3.7 for the 13 groups with highest $\sigma(v)_{intr}$	40
3.9	Top: The distribution of EW[OII] for the C-group galaxies (solid histogram), L-group galaxies (dotted histogram, renormalised to match the number of C-group galaxies) and the L-group galaxies, resampled to match the luminosity distribution of galaxies in the concentrated groups (dashed histogram - method described in text). The sample is limited to galaxies brighter than $M_{b_j} \leq -20.0$ and to within $0.5h_{75}^{-1}Mpc$ of the iteratively determined group centre (smaller circles in Figures 3.7 and 3.8). Bottom: The same as above, but incorporating all galaxies down to the fainter limit of $M_{b_j} \leq -18.5$	43

- 3.10 The fraction of passive galaxies f_p (brighter than $M_{b_j} \leq -20.0$ and within $0.5h_{75}^{-1}$ Mpc of the iteratively determined group centre), in each group as a function of the group velocity dispersion, $\sigma(v)_{intr}$. The galaxies in each group without redshift measurement (candidate members) are resampled from the measured- z galaxies in the same region of sky, on the basis of their luminosity and $(B - R_c)$ colour. Groups are also keyed on the allocated group-class with open circles to represent concentrated groups, squares to represent loose groups, large filled circles to represent massive groups and small filled circles to represent unclassified groups. The arrow indicates an upper limit on the velocity dispersion of group 28. We also show the value of f_p in combined groups for 3 bins of $\sigma(v)_{intr}$ (solid line) and for the field (dashed line). The shaded area represents the error on these values computed using the Jackknife technique. There is no clear trend of f_p with $\sigma(v)_{intr}$ in groups for galaxies brighter than $M_{b_j} \leq -20.0$ 44
- 3.11 Radial selection function of the stacked data as a function of angular distance from the target group centre. Filled circles represent the fraction of galaxies with Magellan redshifts ($S_{rad}(L_z)$); triangles represent the fraction of galaxies targeted by Magellan ($S_{rad}(L_{obs})$) and diamonds represent galaxies with CNOC2 or Magellan redshifts ($S_{rad}(L_z) + S_{rad}(C_z)$). Only galaxies within $240''$ and with $R_C \leq 22.0$ are considered in our analysis. 47
- 3.12 Selection functions of the stacked group sample as a function of R_c -band magnitude. Filled circles represent the fraction of galaxies with Magellan redshifts, weighted by W_{rad} ($S_{mag}(L_z)$) and diamonds represent galaxies with CNOC2 or Magellan redshifts ($S_{mag}(L_z) + S_{mag}(C_z)$). Only galaxies brighter than $R_c = 22$ are considered in our analysis. 48
- 3.13 $B - R_c$ colour vs R_c magnitude for $R_C \leq 22$ objects targeted with Magellan. The top panel (stars) and middle panel (circles) show the positions of the 187 emission redshift objects and 196 absorption redshift objects in this plane respectively. Filled symbols represent objects which make the redshift and luminosity cuts for our analysis ($\sim 50\%$ of all objects in the range $0.3 \leq z \leq 0.55$; $M_{b_j} \geq -18.5$). The bottom panel locates in the colour-magnitude plane the 124 objects targeted with Magellan which failed to yield redshifts. The magnitude limit ($R_c = 22$) and a rough division in colour at $B - R_c = 2.0$ are also shown (dotted lines). 50

- 3.14 The fraction of passive galaxies, f_p , as a function of apparent magnitude for all galaxies in the range $0.3 \leq z \leq 0.55$. Galaxies are weighted by W_C to account for selection bias. The solid line does not make any correction to account for bias in Magellan redshift incompleteness. Jackknife errors are computed in this case. The dashed line represents the case where galaxies with Magellan redshifts have also been weighted by an additional weight W_{NoZ} , effectively resampling Magellan *lost* galaxies (no redshifts) in colour-magnitude space. The dotted line case applies this additional weight only to red ($B - R_c \geq 2$) galaxies. 52
- 3.15 **Top:** The fraction of passive galaxies, f_p , in the stacked group within $0.5h_{75}^{-1} Mpc$ of the iteratively determined group centre (solid line) and the field (dashed line) as a function of galaxy luminosity, M_{b_j} . The field symbols are offset slightly in luminosity for clarity. Statistical errors on f_p are computed using a Jackknife method. **Bottom:** The same as above, except including all galaxies within $1h_{75}^{-1} Mpc$ of the original centroid computed in Section 3.4.4 (the luminosity-weighted centre of all confirmed group members). 54
- 3.16 f_p ($M_{b_j} \leq -18.5$) in the stacked group as a function of physical distance from the group centre where the group centre is defined to be the luminosity-weighted centre of all confirmed group members. The horizontal solid line and dashed lines represent the field f_p and $\pm 1\sigma$ uncertainties respectively (The luminosity limit is deeper than in Figure 3.10 and so f_p is reduced). All errors on f_p are computed using the Jackknife method. 55
- 3.17 f_p ($M_{b_j} \leq -18.5$) in the stacked group as a function of the projected distance to the nearest neighbour ($\Delta h_{75}^{-1} Mpc$). The horizontal solid line and dashed lines represent the field f_p and $\pm 1\sigma$ uncertainties respectively. All errors on f_p are computed using the Jackknife method. We find a correlation between f_p and Δ where group galaxies located in more overdense regions ($\Delta \lesssim 0.4h_{75}^{-1} Mpc$) have an enhanced likelihood of being passive. 55
- 3.18 The luminosity functions for group (solid line), field (dotted line) and redshift-weighted field (dashed line) galaxies weighted by selection, W_C and within our redshift range ($0.3 \leq z \leq 0.55$). The vertical line represents the approximate luminosity limit of the sample at the redshift limit $z = 0.55$. 56

3.19	As Figure 3.18 but with group galaxies split into 3 bins of velocity dispersion, $\sigma(v)_{intr}$ going from low $\sigma(v)_{intr}$ (top 2 panels) to high $\sigma(v)_{intr}$ (bottom 2 panels); and with star-forming and passive galaxies shown separately in the upper and lower panels of each plot.	58
4.1	The “tuning fork” diagram depicting the Hubble Sequence of galaxy morphological types. This figure derives from the diagram found at: <i>http://www.iitk.ac.in/ac/right/mag/galaxy.htm</i> . We note that we consider the galaxy here denoted ‘Sa’ to be closer to an edge-on ‘S0’ type, due to the large bulge.	64
4.2	HST field 23 and members of group g23 at $z = 0.351$ (445 ± 75 km s ⁻¹). Circles represent passive galaxies ($EW[OII] < 5\text{\AA}$); Triangles represent star-forming galaxies ($5\text{\AA} \leq EW[OII] \leq 30\text{\AA}$) and stars represent highly star-forming galaxies ($EW[OII] \geq 30\text{\AA}$)	68
4.3	HST field 24 and members of group g24 at $z = 0.359$ (< 119.6 km s ⁻¹). Symbols are the same as for figure 4.2	69
4.4	HST field 25 and members of group g25 at $z = 0.361$ (470 ± 75 km s ⁻¹). Symbols are the same as for figure 4.2	70
4.5	HST field 28 and members of group g28 at $z = 0.372$ (160 ± 80 km s ⁻¹). Symbols are the same as for figure 4.2	71
4.6	HST field 31 and members of group g31 at $z = 0.392$ (565 ± 352 km s ⁻¹). Symbols are the same as for figure 4.2	72
4.7	HST field 32 and members of group g32 at $z = 0.394$ (519 ± 98 km s ⁻¹). Symbols are the same as for figure 4.2	73
4.8	HST field 34 and members of group g34 at $z = 0.465$ (408 ± 106 km s ⁻¹). Symbols are the same as for figure 4.2	74
4.9	HST field 37 and members of group g37 at $z = 0.471$ (419 ± 97 km s ⁻¹). Symbols are the same as for figure 4.2	75
4.10	HST field 38 and members of group g38 at $z = 0.51$ (808 ± 68 km s ⁻¹). Symbols are the same as for figure 4.2	76
4.11	HST field 39 and members of group g39 at $z = 0.536$ (454 ± 88 km s ⁻¹). Symbols are the same as for figure 4.2	77
4.12	HST field 129 and members of group g129 at $z = 0.317$ (225 ± 76 km s ⁻¹). Symbols are the same as for figure 4.2	78

4.13 HST field 134 and members of group g134 at $z = 0.392$ ($284 \pm 78 \text{ km s}^{-1}$). Symbols are the same as for figure 4.2	79
4.14 HST field 137 and members of group g137 at $z = 0.425$ ($314 \pm 84 \text{ km s}^{-1}$). Symbols are the same as for figure 4.2	80
4.15 HST field 138 and members of group g138 at $z = 0.437$ ($711 \pm 81 \text{ km s}^{-1}$). Symbols are the same as for figure 4.2	81
4.16 HST field 139 and members of group g139 at $z = 0.439$ ($314 \pm 84 \text{ km s}^{-1}$). Symbols are the same as for figure 4.2	82
4.17 HST field 244 and members of group g244 at $z = 0.47$ ($270 \pm 54 \text{ km s}^{-1}$). Symbols are the same as for figure 4.2	83
4.18 Members of group g23 at $z = 0.351$ ($445 \pm 75 \text{ km s}^{-1}$). Galaxies are labelled as described in the text.	87
4.19 Members of group g24 at $z = 0.359$ ($<119.6 \text{ km s}^{-1}$). Galaxies are labelled as described in the text.	88
4.20 Members of group g25 at $z = 0.361$ ($470 \pm 75 \text{ km s}^{-1}$). Galaxies are labelled as described in the text.	89
4.21 Members of group g28 at $z = 0.372$ ($160 \pm 80 \text{ km s}^{-1}$). Galaxies are labelled as described in the text.	90
4.22 Members of group g31 at $z = 0.392$ ($565 \pm 352 \text{ km s}^{-1}$). Galaxies are labelled as described in the text.	91
4.23 Members of group g32 at $z = 0.394$ ($519 \pm 98 \text{ km s}^{-1}$). Galaxies are labelled as described in the text.	92
4.24 Members of group g33 at $z = 0.406$ ($194 \pm 100 \text{ km s}^{-1}$). Galaxies are labelled as described in the text.	93
4.25 Members of group g34 at $z = 0.465$ ($408 \pm 106 \text{ km s}^{-1}$). Galaxies are labelled as described in the text.	94
4.26 Members of group g37 at $z = 0.471$ ($419 \pm 97 \text{ km s}^{-1}$). Galaxies are labelled as described in the text.	95
4.27 Members of group g38 at $z = 0.51$ ($808 \pm 68 \text{ km s}^{-1}$). Galaxies are labelled as described in the text.	96
4.28 Members of group g39 at $z = 0.536$ ($454 \pm 88 \text{ km s}^{-1}$). Galaxies are labelled as described in the text.	97
4.29 Members of group g129 at $z = 0.317$ ($225 \pm 76 \text{ km s}^{-1}$). Galaxies are labelled as described in the text.	98

4.30	Members of group g132 at $z = 0.359$ (375 ± 34 km s ⁻¹). Galaxies are labelled as described in the text.	99
4.31	Members of group g133 at $z = 0.373$ (204 ± 38 km s ⁻¹). Galaxies are labelled as described in the text.	100
4.32	Members of group g134 at $z = 0.392$ (284 ± 78 km s ⁻¹). Galaxies are labelled as described in the text.	101
4.33	Members of group g137 at $z = 0.425$ (314 ± 84 km s ⁻¹). Galaxies are labelled as described in the text.	102
4.34	Members of group g138 at $z = 0.437$ (711 ± 81 km s ⁻¹). Galaxies are labelled as described in the text.	103
4.35	Members of group g139 at $z = 0.439$ (314 ± 84 km s ⁻¹). Galaxies are labelled as described in the text.	104
4.36	Members of group g140 at $z = 0.465$ (98 ± 129 km s ⁻¹). Galaxies are labelled as described in the text.	105
4.37	Members of group g244 at $z = 0.47$ (270 ± 54 km s ⁻¹). Galaxies are labelled as described in the text.	106
4.38	The fraction of each morphological type of galaxy, f_{type} , in 3 bins of luminosity: Bright ($M_{b_j} < -21.0$), Control ($-21.0 \leq M_{b_j} < -20.0$) and Faint ($-20.0 \leq M_{b_j} \leq -18.5$). The solid line with the filled circles represents the group galaxy population and the dashed line with the open circles represents the field population. Errors are estimated using the Jackknife technique and field points are offset slightly in M_{b_j} for clarity. This figure clearly shows that the CNOC2 groups possess a larger fraction of early galaxy types (elliptical and S0) than the field, in place of spiral galaxies, more common in the field.	110
4.39	The distribution of EW[OII](Å) of field (dashed line) and group (solid line) galaxies, for classified galaxies of each morphological class. Galaxies of later morphological type are more frequently star-forming, as expected.	112
4.40	The luminosity (M_{b_j}) distribution of field (dashed line) and group (solid line) galaxies, for classified galaxies of each morphological class. Early-type galaxies (ellipticals and S0s) are often more luminous in groups than in the field.	113

- 4.41 As figure 4.39 except with the field sample resampled to match the luminosity distribution of the group galaxies for each morphological class. The resampled field galaxies do not include a passive population of early-type spirals to match that found in groups. 114
- 4.42 Luminosity Functions of S0 galaxies. The solid and dashed lines represent the group and field galaxy populations respectively. Galaxies are weighted by the selection weight W_C . We show the unweighted number of group and field galaxies in each sample in the top left hand corner of the plot. This figure shows that there is a significant (3.5σ) excess of bright ($M_{b_j} \leq -20.5$) S0 galaxies in groups. 116
- 4.43 Luminosity Functions of S0 galaxies for group (solid line) and field (dashed line) samples divided into 3 bins of group velocity dispersion $\sigma(v)_{intr}$. **Top:** The least massive group sample ($\sigma(v)_{intr} \leq 400 \text{ km s}^{-1}$); **Middle:** The intermediate mass group sample ($400 \text{ km s}^{-1} < \sigma(v)_{intr} \leq 600 \text{ km s}^{-1}$) and **Bottom:** The most massive group sample ($\sigma(v)_{intr} > 600 \text{ km s}^{-1}$). The bright S0 population is clearly concentrated in the intermediate mass groups. 117
- 4.44 Luminosity Functions of spiral galaxies. The solid and dashed lines represent the group and field galaxy populations respectively. Galaxies are weighted by the selection weight W_C . We show the unweighted number of group and field galaxies in each sample in the top left hand corner of the plot. We see an excess of bright spiral galaxies in the group population. 118
- 4.45 The fraction of spiral galaxies which are passive, f_p , in groups (solid line, filled circles) and in the field (dashed line, open circles) in 3 bins of luminosity: Bright ($M_{b_j} < -21.0$), Control ($-21.0 \leq M_{b_j} < -20.0$) and Faint ($-20.0 \leq M_{b_j} \leq -18.5$). Errors are estimated using the Jackknife technique. The passive fraction in group spirals is only significantly greater than in the field brighter than $M_{b_j} = -20.0$ 119
- 4.46 The fraction of spiral galaxies brighter than $M_{b_j} = -20.0$ which are passive, f_p , in the field (solid horizontal line) and in 3 bins of group velocity dispersion, $\sigma(v)_{intr}$ ($\sigma(v)_{intr} < 400 \text{ km s}^{-1}$, $400 \text{ km s}^{-1} \leq \sigma(v)_{intr} < 600 \text{ km s}^{-1}$, $\sigma(v)_{intr} > 600 \text{ km s}^{-1}$) with errors estimated using the Jackknife technique (or Poisson errors in the case of the massive groups). The passive galaxies are found mostly in smaller groups ($\sigma(v)_{intr} \leq 600 \text{ km s}^{-1}$). 120

- 4.47 The fraction of spiral galaxies brighter than $M_{b_j} = -20.0$ which are passive, f_p , in the field (solid horizontal line) and in groups as a function of (**Top:**) group-centric radius, dr , and (**Bottom:**) group-centric radius, normalised by the rms value of the parent group. Errors are computed using the Jackknife technique. The likelihood that a spiral galaxy is no longer forming significant numbers of stars is a clear function of its position in the group. 121
- 4.48 The fraction of elliptical galaxies, f_E , in the field (solid horizontal line) and in 3 bins of group velocity dispersion, $\sigma(v)_{intr}$ ($\sigma(v)_{intr} < 400 \text{ km s}^{-1}, 400 \text{ km s}^{-1} \leq \sigma(v)_{intr} < 600 \text{ km s}^{-1}, \sigma(v)_{intr} > 600 \text{ km s}^{-1}$) with errors estimated using the Jackknife technique. The excess of elliptical galaxies in groups is most evident in the most massive groups ($\sigma(v)_{intr} > 600 \text{ km s}^{-1}$). 122
- 4.49 As Figure 4.48 but only for faint galaxies ($-20.0 < M_{b_j} \leq -18.5$). 122
- 4.50 The fraction of spiral galaxies, f_{sp} in the field (solid horizontal line) and in 3 bins of group velocity dispersion, $\sigma(v)_{intr}$ ($\sigma(v)_{intr} < 400 \text{ km s}^{-1}, 400 \text{ km s}^{-1} \leq \sigma(v)_{intr} < 600 \text{ km s}^{-1}, \sigma(v)_{intr} > 600 \text{ km s}^{-1}$) with errors estimated using the Jackknife technique. There is a deficit of spiral galaxies in groups, most prominent in the most massive groups ($\sigma(v)_{intr} > 600 \text{ km s}^{-1}$). 123
- 4.51 Luminosity Functions of star-forming spiral galaxies in small groups ($\sigma(v)_{intr} < 400 \text{ km s}^{-1}$ - solid line) and the field (dashed line). Galaxies are weighted by the selection weight W_C and the field luminosity function is renormalised to match the area of the group luminosity function. We show the unweighted number of group and field galaxies in each sample in the top-left-hand corner of the plot. There appears to be a brighter population of spiral galaxies in the small groups than is seen anywhere in the field. However this is not a significant result. 124
- 4.52 The fraction of galaxies with disturbance index D which possess each value of D . $D = 0$ infers a galaxy contains no peculiar features and progressively larger values of D infer more peculiar features. The solid circles represent the group galaxy population and the open circles represent the field galaxy population. Errors are estimated using the Jackknife technique and points are horizontally offset slightly for clarity. The likelihood that group galaxies have a peculiar morphology is significantly lower than for field galaxies. . 125

4.53	The fraction of all classified galaxies which possess each value of anomaly index, I . $I = 1$ galaxies have tidal arms but no obvious counterpart; $I = 2$ galaxies have visible interaction with another object and $I = 3$ galaxies have visible signs of undergoing a recent merger. The solid circles represent the group galaxy population and the open circles represent the field galaxy population. Errors are estimated using the Jackknife technique and points are horizontally offset slightly for clarity. Whilst galaxies undergoing visible interaction with another object are more common in the group population, the fraction with visible signs of undergoing a recent merger is consistent with the field value.	126
4.54	The fraction of passive galaxies in the combined sample for each disturbance index D (left) and anomaly index I (right). $D = 0$ implies a galaxy contains no peculiar features and progressively larger values of D imply more peculiar features. $I = 1$ galaxies have tidal arms but no obvious counterpart; $I = 2$ galaxies have visible interaction with another object and $I = 3$ galaxies have visible signs of undergoing a recent merger. Errors are estimated using the Jackknife technique.	127
4.55	As Figure 4.54 but showing the fraction of highly star-forming galaxies, f_{hsf} as a function of disturbance index D (left) and anomaly index I (right).	128
5.1	Luminosity functions of the group galaxies (top) and field galaxies (below) for 2dF and CNOC2. Field and Group CNOC2 data are each normalised to match total number in CNOC2 sample for $M_{b_j} < -20.25$	135
5.2	Normalised distributions of $\text{EW}[\text{OII}]$ of the group and field galaxies in 2dF ($0.05 \leq z \leq 0.1$) and CNOC2 ($0.3 \leq z \leq 0.55$) samples where $M_{b_j} \leq -18.5$. The data is normalised to match the total number of galaxies in the CNOC2 analysis.	137
5.3	Fraction of galaxies with $\text{EW}[\text{OII}] < 5\text{\AA}$ (the passive population), f_p , in 2dF and CNOC2 groups (within 1 projected Mpc of group centre) and field, as a function of M_{b_j} . The 2dF points are slightly offset in M_{b_j} for clarity. . .	138
5.4	Cumulative distributions of $\text{EW}[\text{OII}]$ in star-forming galaxies in the field and group galaxies of 2dF ($0.05 \leq z \leq 0.1$) and CNOC2 ($0.3 \leq z \leq 0.55$) samples. The arrows indicate the mean values of $\text{EW}[\text{OII}]$ for star-forming galaxies in each sample.	139

5.5	The median EW[OII] (\AA) of star-forming galaxies, $\langle \text{EW}[\text{OII}] \text{SF} \rangle$, in the 2dF and CNOC2 galaxies in the groups (within 1 projected Mpc of group centre) and field, as a function of M_{b_j} . The 2dF points are slightly offset in M_{b_j} for clarity.	140
5.6	The fraction of galaxies with $\text{EW}[\text{OII}] < 5 \text{\AA}$ (the passive population) (f_p) in 2dF and CNOC2 groups, as a function of physical radius. The field level is overplotted and only galaxies where $M_{b_j} \leq -18.5$ are considered.	141
5.7	Fraction of galaxies with $\text{EW}[\text{OII}] < 5 \text{\AA}$ (passive galaxies) (f_p) in 2dF and CNOC2 groups, as a function of group line of sight velocity dispersion. The points represent 2dF groups and the triangles represent CNOC2 groups.	142
6.1	(u-g) colour distribution of SDSS galaxies <i>inside</i> (left) and <i>outside</i> (right) the fibre for <i>bright</i> ($-22 \leq M_{b_j} \leq -21.5$) galaxies (top), intermediate brightness ($-21 \leq M_{b_j} \leq -20.5$) and <i>faint</i> ($-19 \leq M_{b_j} \leq -18.5$) galaxies (below). Each colour distribution is fitted by a double gaussian representing the bimodal populations of galaxies (thick line).	146
6.2	The fraction of galaxies located in the red peak of the bimodal distribution (f_{red}) as a function of luminosity, both inside and outside the fibre. The crosses represent the fibre colour distribution and the diamonds the colour distribution outside the fibre.	147
6.3	The central position (mean) of the red peak (Top , μ_{red}) and the blue peak (Bottom , μ_{blue}) of the bimodal distribution as a function of luminosity, both inside and outside the fibre. The crosses represents the fibre colour distribution and the diamonds the colour distribution outside the fibre.	148
7.1	The fraction of passive galaxies, f_p , in the 2dF (solid line) and CNOC2 group (within 1 projected h_{75}^{-1} Mpc of group centre) and field galaxy populations, as a function of M_{b_j} . The CNOC2 galaxies are shown as observed (dotted-line), and evolved to z_{2dF} using a quiescent model with a Kennicutt IMF, $z_{\text{form}} = 10$, solar metallicity and dust extinction (dashed-line). The 2dF points are slightly negatively offset, and the CNOC2 data points slightly positively offset in M_{b_j} for clarity.	153

7.2	Similar to Figure 7.1, but assuming an extreme quiescent evolution model for the CNOC2 population, with a Salpeter IMF, $z_{form} = 3$, solar metallicity and no dust extinction (dashed-line). This represents the maximum evolution expected from any realistic quiescent model. The 2dF points are slightly negatively offset, and the CNOC2 data points slightly positively offset in M_{b_j} for clarity.	154
7.3	The probability (per Gyr) that star formation has been truncated (P_{trunc}) as a function of M_{b_j} as determined by modelling the evolution of f_p between the CNOC2 ($0.3 \leq z_{CNOC2} \leq 0.55$) and 2dF ($0.05 \leq z_{2dF} \leq 0.1$) samples. The crosses represent the group galaxies and the diamonds represent the field population which has been artificially offset by 0.05mag for clarity. Here, there is assumed to be no density evolution, i.e. all group galaxies were already in groups by z_{CNOC2} ($\xi_{gr} = 100\%$). The vertical line represents the location of a M_* galaxy in 2dF as determined from the luminosity function of Norberg et al. (2002).	158
7.4	As Figure 7.3, but assuming local 2dF groups comprise 50% CNOC2 group galaxies and 50% CNOC2 field galaxies ($\xi_{gr} = 50\%$).	158
7.5	A comparison of the distribution of EW[H α] in 2dF galaxies (solid black line) with the model galaxy population at $z = 0$ in bright galaxies ($M_{b_j} \leq -20.0$, Top 2 panels) and fainter galaxies ($-20.0 \leq M_{b_j} \leq -18.5$, Bottom 2 panels). The red line represents the emission line model with extinction due to diffuse dust only ($A_{V0} = 0$). The green and blue lines represent emission line models with an additional metallicity-dependent dust extinction in HII regions, with $A_{V0} = 1.0$ and $A_{V0} = 2.0$ respectively. As the galaxy population is bimodal (Chapter 2) we show both the complete distribution and the distribution of star forming galaxies only. Left: Distributions are normalised to the fraction of the total population per \AA . Right: Distributions are normalised to the fraction of the Star Forming population only (selected to have EW[H α] $\geq 4\text{\AA}$).	162
7.6	As Figure 7.5 but showing a comparison of the EW[OII] distribution in 2dF galaxies with the model galaxy population at $z = 0$. The Star Forming population is defined to have EW[OII] $\geq 5\text{\AA}$	163
7.7	As Figure 7.6 but showing a comparison of the EW[OII] distribution in CNOC2 galaxies with the model galaxy population at $z = 0.4$	164

7.8	The fraction of passive galaxies f_p as a function of luminosity (M_{b_j}) in 4 bins of halo mass, M_{halo} (4 labelled panels). The 3 lines on each panel represent the model galaxy population at $z = 0$ (solid black), $z = 0.4$ (dashed red) and $z = 1$ (dot-dashed green) in each bin of halo mass. . . .	165
7.9	The fraction of passive galaxies f_p as a function of luminosity (M_{b_j}) in the field population of 2dF (solid black line). This is compared with the model population at $z = 0$, considering [OII] emission with extinction due to diffuse dust only ($A_{V0} = 0$, dashed red line) and with an additional metallicity-dependent dust extinction in HII regions (dot-dashed green and dotted blue lines). We apply $A_{V0} = 1.0$ (green line) and $A_{V0} = 2.0$ (blue line). The 3 panels show the behaviour of f_p for all model galaxies (Top), central galaxies only (Middle) and satellite galaxies only (Bottom). In all cases we compare with the full 2dF population. Whilst the model succeeds in reproducing the shallow luminosity dependence of f_p faintwards of $M_{b_j} \sim M_* (-20.28)$, we find f_p to be overestimated in the model at fainter luminosities.	166
7.10	As Figure 7.9 but for the CNOC2 field population compared with the model galaxy population at $z = 0.4$	167
7.11	As Figure 7.9 but for the 2dFGRS group population compared with the model galaxy population in haloes of $M_{halo} \geq 10^{13} M_\odot$ at $z = 0$	168
7.12	As Figure 7.9 but for the CNOC2 group population compared with the model galaxy population in haloes of $M_{halo} \geq 10^{13} M_\odot$ at $z = 0.4$	169
8.1	The array of CCDs at the focal plane of the WFI instrument on the AAT.	175
8.2	Example of the small-scale residual patterns visible in some CCDs even after dome-flattening (This is CCD4 in a B-band frame).	182

- 8.3 Comparison of measured aperture magnitudes for each star located in two different observations, with the second observation offset from the first. Each panel represents the difference in magnitude ($d(mag)$) as a function of the y-axis CCD position of the star in the second observation. In the top 2 panels we compare the magnitudes of stars which lie on the same CCD in both observations. The lower 6 panels compare the magnitude of stars which appear on one CCD in the first pointing and on a different CCD at the second pointing. These images were flattened using dome-flats and we only include data from standard fields imaged during conditions which are logged as “photometric”. Preliminary calibration has already been performed using the L92 standard stars to obtain ZP for each CCD separately (and a global R-band colour term). However, significant large scale variations, CCD to CCD offsets and scatter remain. 184
- 8.4 An example colour-magnitude plot in the region of RXJ1347. The points represent objects located on CCD2 at position E in the field of RXJ1347 which contains the cluster centre. V-R colour (y-axis) is measured using aperture magnitudes and R magnitude (x-axis) is measured using the estimated total magnitude (SExtractor’s MAGBEST parameter). Simulations indicate that at the redshift of the cluster, $z = 0.451$, the red sequence should be found at $V-R \sim 1.24$ for M_* galaxies ($R \sim 20.6$). The solid line indicates this isochrone and dashed lines indicate the boundary for galaxies within 0.1 magnitude of this colour. A concentration of objects can be seen at $V-R \sim 1.2$ which might represent this red sequence. 187
- 8.5 A contour plot of objects in the central mosaic position of RXJ1347 (position E). Objects located within the colour range $V-R = 1.24 \pm 0.1$ and brighter than $R = 22.5 \sim M_* + 2$ are represented by filled circles. The contour levels show the relative local density levels of these objects. We see a filamentary structure in the NE to SW direction with possible subclumps of galaxies located at a greater distance ($\sim 3h_{75}^{-1} Mpc$ from the cluster centre) along this axis. 188

- 9.1 The fraction of passive galaxies, f_p , plotted as a function of redshift in different environments. The group and field data are selected from our 2dF and CNOC2 samples. We overplot the equivalent fractions in cluster cores, selected from the samples of Nakata et al. (2004). These data originate in the 2dFGRS, CNOC1 and high redshift cluster samples of van Dokkum et al. (2000) and Postman et al. (2001). Cluster data are selected only within the inner $0.75h_{75}^{-1}$ Mpc of the cluster centre and we match the luminosity limit of Nakata et al. (2004) ($M_{b_j} = -19.65$). This figure shows the strong decline of f_p in the Universe since $z \sim 0.4$ in groups and clusters whilst the passive population in the dense core regions of clusters is consistent with having been mostly in place since $z \sim 1$ 199
- 9.2 The predicted fraction of passive galaxies f_p computed in the GALFORM semi-analytic model (Cole et al., 2000; Baugh et al., 2004), plotted as a function of redshift in a range of environments (halo mass). The galaxy sample is limited to $M_{b_j} = -19.65$ to match Figure 9.1. The model displays a remarkably similar rate of evolution in each environment with perhaps slightly stronger evolution in the global population (the field) as more galaxies are accreted onto more massive halos. Whilst the direction of evolution and the environmental dependence of f_p is in agreement with observations, the rate of evolution is too weak since $z = 0.4$ in groups and the field, and potentially too strong in massive clusters. 200

List of Tables

3.1	The number of galaxies targeted in each targeted group and the $0.3 \leq z \leq 0.55$ Carlberg et al. (2001b) groups serendipitous in these fields.	23
3.2	<i>Individual Group Properties:</i> Including : Luminosity-weighted group centroid positions in spatial coordinates; Mean redshift, z ; Velocity dispersion, $\sigma(v)_{intr}$; Total number of galaxies in each group with redshift, N_{tot} ; The number of members brighter than $M_{b_j} = -20$ and within $1h_{75}^{-1}$ Mpc, weighted to account for incompleteness, N_{mem} ; The manually classified group <i>class</i> ; The luminosity of the brightest group galaxy (within $1h_{75}^{-1}$ Mpc of the centre), M_{b_j} (Br); The fraction of passive galaxies in the group, f_p (brighter than $M_{b_j} = -20.0$ and within $0.5h_{75}^{-1}$ Mpc of the iteratively determined group centre) Note: Computation of f_p includes resampling to account for galaxies without redshifts in the region of each group (See Section 3.5.2.2).	36
3.3	The fractions of passive (f_p , $EW[OII] < 5\text{\AA}$) and highly star forming (f_{hsf} , $EW[OII] \geq 30\text{\AA}$) galaxies in C-group galaxies (concentrated into dense clumps), L-group galaxies (looser structure) and resampled L-group galaxies (to match the luminosity distribution of C-group galaxies). Galaxy populations are defined within $0.5h_{75}^{-1}$ Mpc of the iteratively determined group centre and down to $M_{b_j} = -20.0$ (1) and $M_{b_j} = -18.5$ (2). Statistical errors are computed using the Jackknife technique.	42
3.4	Field Luminosity Function Properties: The Bright to Control ($R_{(B/C)}$) and Bright to Faint ($R_{(B/F)}$) ratios of the galaxy populations in the CNOc2 field:	59

3.5	Group Luminosity Function properties: The Bright to Control ($R_{(B/C)}$) and Bright to Faint ($R_{(B/F)}$) ratios of the passive and star-forming galaxy populations in the CNOC2 groups and the redshift-weighted field ($R_{(B/F)_{wf}}$) and the enhancement of $R_{(B/C)}$ or $R_{(B/F)}$ in the groups relative to the field with associated error ($\Delta R_{B/C} \pm \sigma(R_{(B/C)})$, $\Delta R_{B/F} \pm \sigma(R_{(B/F)})$) and significance of each enhancement ($S_{B/C}$, $S_{B/F}$).	59
4.1	The number of galaxies with each combination of my classification and AO classification.	108
7.1	Values assigned to truncation model parameters, whether kept constant or allowed to vary. We note that the parameters IMF, z_{form} , metallicity Z, dust and the choice of τ for each galaxy have little effect on the results. This is because the evolution of f_p to $z_{2dF} = 0.08$ mostly depends upon P_{trunc}	157
8.1	LDSS2 Observations made in the region of the massive cluster of galaxies RXJ1347 in April 2002.	192
8.2	LDSS2 Observations made in the region of the massive cluster of galaxies RXJ1347 in March 2003.	192

Declaration

The work described in this thesis was undertaken between 2001 and 2004 while the author was a research student under the supervision of Dr. Richard Bower in the Department of Physics at the University of Durham. This work has not been submitted for any other degree at the University of Durham or any other University.

Portions of this work have appeared in the following papers:

- Wilman, D. J., Balogh, M. L., Bower, R. G., Mulchaey, J. S., Oemler Jr, A., Carlberg, R. G., Morris, S. L. and Whitaker, R. J., “Galaxy Groups at $0.3 \lesssim z \lesssim 0.55$. I. Group Properties”, MNRAS, 2004, submitted
- Wilman, D. J., Balogh, M. L., Bower, R. G., Mulchaey, J. S., Oemler Jr, A., Carlberg, R. G., Eke, V. R., Lewis, I. J., Morris, S. L. and Whitaker, R. J., “Galaxy Groups at $0.3 \lesssim z \lesssim 0.55$. II. Evolution”, MNRAS, 2004, submitted

The copyright of this thesis rests with the author. No quotation from it should be published without his prior written consent and information derived from it should be acknowledged.

Acknowledgements

This thesis would not have been possible without the financial support of the Particle Physics and Astronomy Research Council (PPARC). I would like to thank in particular the tireless patience of my supervisor Richard Bower and Michael Balogh who must have often felt that they were facing the inquisition. Without their dedication and experience, I would still have no direction in my work. John Mulchaey also deserves special thanks for his enthusiastic support of the CNOC2 groups project, in particular the HST imaging, and for showing me the fine restaurants of Los Angeles. Also thanks to Gus Oemler for painstakingly morphologically classifying hundreds of galaxies and to Ray Carlberg for the CNOC2 group catalogue, without which this thesis could not be.

In Durham I would also like to extend my thanks to Alan Lotts and Lydia Heck for keeping the computer system up and running smoothly; Dorothy Jenkins, the group secretary; Roger Davies, my first year supervisor, and to my local collaborators Simon Morris, Richard Whitaker, Fumiaki Nakata and Vince Eke for some helpful conversations and useful data! Dave Gilbank deserves a special mention for his enthusiastic help with data reduction and the software packages he has introduced to Durham.

I would like to thank the Magellan staff for their tremendous support and the full CNOC2, 2dFGRS and SDSS teams for outstanding datasets. Thanks in particular to Ian Lewis for his emission line measurements in 2dFGRS and to Bob Nichol and Chris Miller for their help in producing the SDSS catalogues. The data was collected from Magellan with the help of Phil Outram, Tom Shanks, Nigel Metcalfe and Marc Vallbe who are also thanked. Thanks also to Dan Kelson for the use of his spectral reduction software and to Lori Lubin for the IRAF script used in the morphological classification of galaxies. I also thank my examiners, Trevor Ponman and Ray Sharples, for some very interesting discussions regarding the analysis and interpretation of our results. I also acknowledge *noao* for the wealth of IRAF tools used during data reduction.

I also thank Gustavo Bruzual and Stéphane Charlot for their publicly available spectrophotometric evolutionary modelling software GALAXEV and Carlton Baugh and Cedric Lacey for helping with the full modelling process and providing galaxy catalogues produced using GALFORM. In this Dmitry Klochkov has been particularly important, collaborating with me in the comparisons between observed and model galaxy populations during his International Summer School project.

Thanks to Richard Wilman for his spell checking abilities and to Graham Smith,

Richard McDermid, Dajana Dzanovic, Mark Swinbank, Ian Smail, Tadayuki Kodama and Nathan Courtney for help at various points throughout my PhD. Also in Durham, I thank Tom Theuns, Alistair Edge and my fellow students, in particular Geraint Harker, Rowena Malbon, Chris Power, John Helly and Kevin Pimblett for helpful hints along the way. And thanks to Magnus Bower for his insightful drawings!

Finally, I would like to say that as I have discovered, a PhD is not just a piece of work but it also requires a certain piece of mind and self-confidence that only comes when feeling happy and comfortable in ones life. With this in mind my most special thanks of all go to my family and to my girlfriend, Niki Frankenberg, without whom life just would not seem quite the same.

Chapter 1

Introduction

Galaxies represent the fundamental building blocks of our Universe. We know that a large fraction of mass in the Universe must exist as “dark matter” (invisible to telescopes sensitive only to electromagnetic radiation), providing the additional gravitational pull required to explain the high velocity dispersions of gravitationally-bound clusters of galaxies (Zwicky, 1937) and non-Keplerian flat rotation curves in spiral galaxies (Babcock, 1939). The precise nature of this dark matter is still a mystery as the direct detection of these particles has remained elusive. However, indirect evidence such as the extent of galaxy clustering and the inhomogeneity of the cosmic microwave background (mapping the inhomogeneities of the very early Universe) has led to a growing consensus amongst the astronomical community that a specific category of particles labelled “cold dark matter” (CDM) is responsible (e.g. Davis et al., 1985). More recently, observations of distant type Ia supernovae (which have well-constrained luminosity) has led to the startling conclusion that the Universe is not only expanding (as discovered by Hubble, 1929), but that it is actually accelerating in its expansion (Perlmutter et al., 1999). This is attributed to the mysterious “dark energy” which is encapsulated in Einstein’s cosmological constant, Λ . Thus, in the current paradigm of a Λ CDM Universe, galaxy formation and evolution are governed by the hierarchical clustering of cold dark matter “haloes” to form structure in an expanding Universe. As gas radiates its energy, it cools onto the centre of gravitational potential wells, located in the cores of these dark matter haloes, to form galaxies. The observable components of galaxies in the form of gas and stars (baryonic matter) trace the dark matter structures and are subjected to intense gravitational clustering and merging activity themselves as the massive dark matter haloes in which they are embedded do likewise. By the present epoch galaxies have accumulated a long and complex history of accretion, mergers, interactions and internal activity.

To disentangle this complex web of galaxy evolution we must employ a number of completely different yet complementary techniques in parallel. In the nearby Universe we have large statistical redshift surveys and high resolution IFU (Integral Field Unit) observations of galaxy dynamics and stellar populations. In the past decade there has



been unprecedented allocation of telescope time to the acquisition of large numbers of galaxy spectra, resulting in highly complete redshift surveys over significant volumes of the Universe. Since the CfA survey of 1100 galaxies (de Lapparent et al., 1986), survey coverage has improved by many orders of magnitude, resulting in the 232,000 galaxies in the 2 degree Field Galaxy Redshift Survey (2dFGRS, Colless et al., 2003) and a projected 1 million galaxies in the Sloan Digital Sky Survey (SDSS, Kent, 1994). These data provide an unprecedented resource to investigate the statistical interdependencies of galaxy properties in the local Universe (discussed later in this introduction). Complementary to this are detailed observations of individual galaxies such as those using high resolution IFU technology. By providing optical and infra-red spectroscopy for each element of a 2D grid, we can resolve spatially distinct stellar populations and the internal dynamics of a galaxy (e.g. Emsellem et al., 2004). Together, detailed studies of individual galaxies and large statistical surveys provide a zeropoint for the properties of galaxies in the local Universe ($z = 0$).

This is complemented by extending observations back along the redshift axis to witness first-hand the evolution of galaxy properties. With modern $\gtrsim 8\text{m}$ telescopes it is possible to detect individual galaxies as distant as $z \sim 7$ (e.g. Kneib et al., 2004, when the Universe was $\sim \frac{1}{20}$ its current age) and to obtain highly complete spectroscopic galaxy redshift surveys at $z \gtrsim 1$ (e.g. Madgwick et al., 2003; Cowie et al., 2004; Vanzella et al., 2004, from when the Universe was $\lesssim \frac{2}{5}$ its current age).

Finally, today's large super-computer simulations can track the evolution of up to $\sim 10^{10}$ dark matter particles (in the Millennium run). Semi-analytic techniques are used to mimic the physics involved in the formation and evolution of galaxies, implanting them into the dark matter haloes generated in the simulation (e.g. Cole et al., 2000). Alternatively high resolution simulations can examine the evolution of a single galaxy in more detail (e.g. Abadi et al., 2003). By matching the observed evolution and detailed properties of galaxies to that achieved in the simulations, we are unravelling the history of galaxy evolution.

In this thesis we¹ will investigate the influence of clustering on galaxy evolution by focusing on the dependence of fundamental galaxy properties on redshift, environment and luminosity. To introduce this work we begin in Section 1.1 by asking: "What are the fundamental properties of galaxies?". This is divided into how stellar populations vary with galaxy morphology along the Hubble Sequence (Section 1.1.1) and how we

¹Throughout this thesis I use the conventional form 'we' to refer to the first person.

can measure the recent star formation in galaxies (Section 1.1.2). Section 1.2 deals with the gravitationally bound clumps of galaxies known as groups and clusters. We split this section into two parts. First we outline how these associations of galaxies are detected and the relative abundance of galaxies in such systems (Section 1.2.1). Then we move into one of the fundamental topics covered by this thesis: How are galaxy properties influenced by the group and cluster environment? (Section 1.2.2). This leads into Section 1.3 in which the evolving galaxy population is discussed with particular focus on how that evolution might depend upon the local environment of each galaxy. Finally we outline this thesis in Section 1.4 with a brief introduction to the subsequent chapters.

1.1 The fundamental properties of galaxies

1.1.1 Stellar Populations along the Hubble sequence

Despite their complex histories, galaxies in the local Universe fall into rather predictable categories. Early-type galaxies are dominated by an elliptical bulge which is pressure supported with little or no disk component (de Vaucouleurs, 1959; Sandage, 1961; Young et al., 1978). They are almost all red in colour with old stellar populations and no current star formation (Baum, 1955). Indeed early-type galaxies form a tight red sequence in colour-magnitude space characterised by the colour of a population of old main sequence stars (as more massive, bluer stars have evolved off the main sequence) of metallicity dependent upon galaxy luminosity (e.g. Bower et al., 1992). Late-type galaxies on the other hand are usually dominated by rotationally-supported disks with a spiral or irregular structure. They are characteristically blue in colour with blue light originating in the considerable population of young stars with a high level of ongoing star formation (Humason, 1936; Bell et al., 2003). The rate at which late-type galaxies form stars is a strong function of Hubble type. Later-type spirals and irregular galaxies form stars at a rate consistent with a ratio of current to past-averaged SFR (Star Formation Rate) of ~ 1 whilst the SFR in early-type spirals (Sa-Sb) is much reduced from their past-averaged value (Kennicutt, 1983; Kennicutt et al., 1994; Brinchmann et al., 2004). Star formation in late-type galaxies occurs mostly as quiescent star formation in the HII regions of disks.

Galaxies can also reach a very high level of star formation in a dramatic and short-lived event known as a starburst. Starbursts occur over a period of $\sim 10^8 - 10^9$ yrs when gas is driven into the compact circumnuclear regions of a galaxy, triggering a burst of intense star formation, sometimes over ~ 1000 times the normal level (e.g. Weedman et al., 1981;

Sekiguchi, 1987). These events are apparently associated with external influences such as galaxy mergers and tidal interactions (Joseph & Wright, 1985; Sofue & Habe, 1992). As these events were more common in the past, it is thought that starbursts may have dominated global star formation beyond $z \sim 2$ (van den Bergh, 2002). In any case they were certainly more important at early times and it seems likely that starbursts played a significant part in the origin of today's early-type galaxies (Shier & Fischer, 1998; Conselice et al., 2004).

The large galaxy surveys of modern astronomy allow us to investigate the statistical properties of large ($\sim 10^6$) galaxy samples at low redshift. In the Sloan Digital Sky Survey (SDSS) and the 2 degree Field Galaxy Redshift Survey (2dFGRS) there now exists strong evidence that galaxy properties are strongly bimodal in the local Universe. Bimodality of galaxies is observed in the galaxy colour distribution (Strateva et al., 2001; Blanton et al., 2003; Baldry et al., 2004) and in the distribution of SFR normalised to integrated galaxy mass or continuum luminosity (Balogh et al., 2004a; Kauffmann et al., 2004). Therefore it is important to understand the origin of these two distinct populations if we hope to understand galaxy evolution. In particular we ask the question: "When, where and how are blue star-forming galaxies transformed into red passive galaxies?"

1.1.2 Measurement of Star Formation

The spectral features of stellar light are highly dependent upon the internal properties of a star. Massive hot stars are short-lived ($\lesssim 1$ Gyr) but extremely luminous at UV wavelengths. Once massive stars have evolved to the giant stage they are extremely luminous at blue optical wavelengths. Conversely, intermediate type main sequence stars are much redder but also much longer lived ($\lesssim t_H$, the Hubble time) and thus more numerous. As the integrated light from a galaxy is dominated by these star types, the spectral colour of a galaxy can be used to infer the relative contributions from each type. The population of short-lived stars inferred from the blue and UV light represents a population of young stars. Therefore recent star formation must have occurred in a blue galaxy with strong UV emission (Kennicutt, 1998). In fact the UV flux is so intimately linked to the recent star formation that a conversion formula can be used to compute a galaxy's SFR from its UV emission (e.g. Madau et al., 1998). This method suffers only from the high opacity of the Earth's atmosphere to UV light and the sensitivity to metallicity and extinction by dust which can be highly variable between galaxies and star-forming HII regions.

More useful calibration of SFR in ground-based studies can be made using measurements of optical emission line flux. Nebular emission lines effectively re-emit the integrated UV flux from galaxies shortward of the Lyman limit. The H α emission line is stronger than other lines and suffers less from stellar absorption. Therefore it provides an ideal diagnostic for the calibration of SFR at optical wavelengths (e.g. Kennicutt, 1998; Hopkins et al., 2003). Calibration using H α suffers only in that it is assumed that all ionizing UV radiation is reprocessed by the ionized gas and that it is also sensitive to extinction. However it becomes problematic to detect H α at high redshift as it first becomes contaminated by the increasing frequency of night sky lines at red wavelengths and finally gets redshifted completely out of the optical window at $z \sim 0.4$. The strongest emission feature visible in the optical spectrum at $z \gtrsim 0.4$ is the [OII] emission doublet. Whilst [OII] is a forbidden line, its excitation is related to the ionization state and abundance of the gas and thus it can be used to calibrate SFR, and exhibits strong correlations with H α strength (Jansen et al., 2001; Hopkins et al., 2003; Kewley et al., 2004). As this thesis is concerned with star formation at high redshift, we will make extensive use of [OII] emission lines to infer the presence of star formation. This will be justified in more detail in Chapter 3.

A galaxy's SFR can also be inferred by measuring a wide variety of spectral properties right across the electromagnetic spectrum, from X-rays to infra-red and radio wavelengths. Synchrotron radiation produced by relativistic electrons accelerated by supernovae (during the death of massive stars) drives a strong correlation between 1.4GHz radio continuum emission and SFR. Far infra-red (FIR) emission measures the thermal re-radiation of dust grains in star-forming regions, as they absorb the UV and blue light from massive stars. Thus there is a tight correlation between FIR and 1.4GHz radio emission in galaxies (e.g. Hopkins et al., 2003). X-ray luminosity may also be an important SFR estimator (e.g. Georgakakis et al., 2003). However, very deep X-ray observations are required to detect X-ray emission related to star formation. As this thesis is only concerned with measurements at optical wavelengths we will not go into any more detail here. The interested reader can find more useful information on these topics in Kennicutt (1998, overall review), Hopkins et al. (2003, multi wavelength comparison in SDSS), Flores et al. (2004, infra-red), Pierini & Möller (2003, infra-red) and Reddy & Steidel (2004, multi-wavelength).

1.2 Groups and Clusters of galaxies

1.2.1 Detection and abundance of Groups and Clusters

In a Λ CDM Universe, the growth of large scale structure is a consequence of the hierarchical clustering process. Clusters of galaxies represent the extreme tail of the resulting density distribution with total halo masses of $\gtrsim 10^{14} M_{\odot}$. It is not surprising that early extragalactic observers found clusters immediately appealing (e.g. Abell, 1958): the richness and high surface density of galaxies in clusters makes them easy to detect and a focal point for galaxy interactions. Even today clusters are still the focus of much attention and many mysteries remain concerning galaxy evolution in this unique environment (see Section 1.2.2 for more information). However, the fraction of galaxies located in galaxy clusters is only $\sim 10\%$ even at the present epoch and so to examine how clustering influences the history of galaxy evolution on a global scale it is essential that more emphasis is directed at understanding galaxy evolution in lower density regimes. Galaxy groups ($10^{13} M_{\odot} \lesssim M_{halo} \lesssim 10^{14} M_{\odot}$) for example contain perhaps over 50% of galaxies in the local Universe (Eke et al., 2004) and thus these environments may play a more significant role.

Cluster detection is easy: you can even do it by simply looking for regions of high surface density on photographic plates (Abell, 1958). Alternatively you can look for extended X-ray sources which map the hot intracluster gas trapped by the cluster potential (e.g. Gioia & Luppino, 1994; Vikhlinin et al., 1998). More recently, photometric techniques have been developed which can be used to detect large numbers of clusters in shallow imaging surveys (e.g. Dalcanton, 1996; Kodama et al., 1999; Gladders & Yee, 2000).

To isolate regimes of lower density is not so straightforward. One possibility involves surveying the outskirts of a known cluster using multicolour wide field imaging (Kodama et al., 2001). We discuss this method in more detail in Chapter 8. However, galaxies in this regime may still be influenced by the cluster: Some may even have already passed through the cluster core (Balogh et al., 2000; Mamon et al., 2004). Isolated galaxy groups are inevitably much more difficult to detect than clusters, with a relative paucity of members and significantly lower density hot gas. Therefore, in most cases the group selection criteria are either not well understood, or biased in some way. In particular, one successful method has been to search for the most overdense, compact groups (Hickson, 1982; Severgnini & Saracco, 2001; Coziol et al., 2004); however, such systems may be atypical of the average group environment. X-ray detection of extended emission from some groups

is possible but becomes more difficult at non-local redshifts and is likely to bias selection towards more massive and evolved groups (Mulchaey & Zabludoff, 1998; Mulchaey et al., 2003; Osmond & Ponman, 2004). By preselecting groups as overdensities associated with a luminous elliptical, which can for example be identified by strong radio power (Allington-Smith et al., 1993), the resulting sample is also unlikely to be representative of groups in general.

It is perhaps inevitable that the best and least biased method of group selection is also the most difficult. Groups can be selected kinematically in redshift space where large and complete spectroscopic surveys exist. Today new opportunities are afforded by large, complete catalogues of nearby groups compiled from redshift surveys such as SDSS and the 2dFGRS (e.g. Eke et al., 2004). Higher redshift catalogues of groups also now exist (Cohen et al., 2000; Carlberg et al., 2001b). These and future spectroscopically selected group catalogues will provide the tools required to understand the important role of groups in driving galaxy evolution.

1.2.2 Properties of galaxies in Groups and Clusters

There is a long standing recognition that galaxy properties in clusters are very different from in the field (e.g. Abell, 1965; Bahcall, 1977). The cluster population exhibits a galaxy population dominated by passive red galaxies falling onto a tight colour-magnitude relation (e.g. Bower et al., 1992). In particular, Dressler (1980) discovered a strong correlation between the fraction of early-type galaxies and the local galaxy density. Large spectroscopic surveys such as SDSS and 2dFGRS have shown that both the galaxy colour distribution (e.g. Pimbblet et al., 2002; Blanton et al., 2003; Balogh et al., 2004b) and star formation rate distribution (Lewis et al., 2002a; Martínez et al., 2002; Gómez et al., 2003; Balogh et al., 2004a; Kauffmann et al., 2004) depend on local galaxy density over a wide dynamic range. Similar trends have also been determined at redshifts up to $z \sim 0.5$ (Dressler et al., 1997; Balogh et al., 1999; Kodama et al., 2001; Treu et al., 2003). Recently, Pimbblet et al. (2002) and Balogh et al. (2004b) have shown that, while the fraction of red galaxies in the nearby Universe increases with local density, the colour distribution of the blue, star-forming galaxies is nearly independent of environment. A similar trend was observed in the $H\alpha$ equivalent width ($EW[H\alpha]$) distribution (Balogh et al., 2004a; Kodama et al., 2004a). A possible interpretation of these trends is that dense environments transform galaxies from blue to red on a relatively short timescale, $\lesssim 0.5$ Gyr.

Relationships between local density and star formation extend to densities equivalent to that found in the smallest groups ($\lesssim 1 \text{ Mpc}^{-2}$) and are independent of proximity to a massive cluster (Lewis et al., 2002a; Gómez et al., 2003; Balogh et al., 2004a). Coupling this with their high abundance, galaxy groups must represent an important regime for the evolution of galaxy properties. Studies of nearby groups (e.g. Postman & Geller, 1984; Zabludoff & Mulchaey, 1998) show that their galaxy populations vary from cluster-like (mostly early-types) to field-like (mostly late-types), suggesting that a nurturing process of galaxy evolution may well be taking place (e.g. Zabludoff & Mulchaey, 2000; Hashimoto & Oemler, 2000; Tran et al., 2001). Another important indication that galaxy evolution is active in the group environment is the apparent dependence on group mass of the luminosity function of galaxies (Christlein, 2000). Group galaxies have a less complex history than cluster galaxies and yet they may play a more important role in galaxy evolution, and in contributing to the global population. With this in mind, we concentrate firmly on galaxy evolution in the group environment for the majority of this thesis.

1.3 Galaxy Evolution

Star formation rates derived from high-redshift UV surveys and low-redshift spectral analysis indicate that the global star formation rate has declined since $z \sim 1.5$ by an uncertain factor of between 4.0 and 40.0 (e.g. Lilly et al., 1996; Madau et al., 1998; Wilson et al., 2002; Hopkins, 2004). This evolution is apparently associated with “downsizing” (Cowie et al., 1999; Kauffmann et al., 2003), such that the characteristic mass of star-forming galaxies decreases with time. Thus, whilst cosmic star formation is dominated by massive galaxies in the high redshift Universe, smaller galaxies play a much more important role today. The precise cause of this decline, however, is unknown. It may be driven by internal (local) processes, leading to the exhaustion of the gas reservoir, or by interactions with the local environment. This is often referred to as the nature versus nurture dichotomy of galaxy evolution.

Our goal is to understand to what extent the global evolution of galaxy properties can be driven by galaxy clustering. As the abundance of galaxies in groups and clusters grows hierarchically, more galaxies are subject to interactions with the local environment. In rich clusters, a strong evolution in the fraction of blue galaxies, f_{blue} , was detected by Butcher & Oemler (1984) and later by others (e.g. Margoniner et al., 2001; De Propris et al., 2003b), although even this result is still a matter of some debate (e.g. Andreon

& Ettori, 1999; Andreon et al., 2004). The most significant evolution may be in the outskirts of clusters, characterised by infalling groups (Ellingson et al., 2001; Fairley et al., 2002) with little evolution in the dense cluster cores since $z \sim 1$ (Nakata et al., 2004). A strong evolution since $z \sim 0.5$ in clusters of the fraction of lenticular S0-type galaxies was detected by Dressler et al. (1997) suggesting an evolution in the morphology-density relation. Evidence is just coming to light that in high density regimes at $z \sim 1$, the red sequence of galaxies disappears in galaxies fainter than $\sim M_* + 2$, indicating that a transition in galaxy activity exists in rich clusters, even at high redshift (e.g. De Lucia et al., 2004; Kodama et al., 2004b). This is analogous to the downsizing of star-forming galaxies in the field (e.g. Cowie et al., 1999) with lower luminosity galaxies migrating onto the red sequence at more recent times. Along the same lines, Poggianti et al. (2004) observe a much lower characteristic luminosity for post-starburst galaxies in the Coma cluster (with strong $H\delta$ line strength, indicating a strong burst of recent star formation), when compared with clusters at higher redshift (Dressler et al., 1999; Poggianti et al., 1999).

The level of evolution in galaxy clusters has yet to be reconciled with galaxy evolution in groups and in the field. In Allington-Smith et al. (1993), a sample of groups was photometrically selected in the vicinity of bright radio galaxies at low ($z \leq 0.25$) and intermediate ($0.25 \leq z \leq 0.50$) redshift. They tentatively confirm an analogous evolution in the fraction of blue galaxies (f_{blue}), in larger groups. However, the statistical limitations of photometric data are significant, particularly through field contamination. In addition, the radio selection might bias the choice of groups. It is therefore important to repeat this study using a redshift-space selected sample of spectroscopically confirmed groups. Without a full understanding of how galaxy evolution compares in different environments it will be nearly impossible to disentangle the effects of internal galaxy evolution from evolution driven by the local environment.

We return to the question: “When, where and how are blue star-forming galaxies transformed into red passive galaxies?”. “When” is likely to be at all times since the first galaxies were formed and at a rate which depends strongly on “where” and on the mass of galaxy. “Where” must account for the strong correlation between red, passive fraction and local density (Balogh et al., 2004a,b) and depends critically upon “how”. “How” must depend upon galaxy mass and brings us back to the nature versus nurture dichotomy of galaxy evolution. If the transformation is primarily driven by internal processes (nature) then the environmental dependence of galaxy properties must be already imprinted

on proto-groups and clusters at high redshift. However there are numerous proposed mechanisms for transforming galaxies in dense environments (nurture) and observational evidence suggests that some of these at least are still active (e.g. Shier & Fischer, 1998; Kenney et al., 2004). Although some mechanisms such as ram-pressure stripping (Gunn & Gott, 1972; Quilis et al., 2000) are considered unlikely to be effective in small groups, many other effects, such as strangulation (Larson et al., 1980; Balogh et al., 2000; Cole et al., 2000; Diaferio et al., 2001), tidal interactions (Byrd & Valtonen, 1990; Gnedin, 2003), or galaxy mergers and interactions (e.g. Joseph & Wright, 1985; Moore et al., 1996) may be more widespread. In particular, galaxy interactions are likely to be most common in groups, where the velocity dispersion of the groups is not much larger than that of the constituent galaxies (Barnes, 1985; Zabludoff & Mulchaey, 1998; Hashimoto & Oemler, 2000; Carlberg et al., 2001a).

1.4 Structure of this thesis

From the above discussion it is clear that the properties of galaxies at intermediate densities typical of groups are influenced by their environment. However historical difficulties in isolating groups, particularly at high redshift, means that galaxy evolution in this important regime is not well understood. Catalogues of kinematically selected groups now exist both at low redshift (e.g. Eke et al., 2004) and at higher redshift (Cohen et al., 2000; Carlberg et al., 2001b). In this thesis we utilise these catalogues and our own supplementary data to address the subject of galaxy evolution in groups. In Chapter 2 we introduce our local group sample selected from 2dFGRS (Eke et al., 2004) and relevant analysis of this sample. Chapter 3 introduces our spectroscopy of intermediate redshift groups, selected at redshifts $0.3 \leq z \leq 0.55$ from the CNOC2 (Canadian Network for Observational Cosmology 2) field survey. These data allow us to contrast the spectroscopic and photometric properties of intermediate redshift group galaxies with serendipitously observed field galaxies, selected from the same redshift slice. We also contrast the morphological properties of group and field galaxies using the deep HST ACS (Hubble Space Telescope - Advanced Camera for Surveys) observations of our CNOC2 groups, presented in Chapter 4.

With kinematically selected group catalogues at both low and intermediate redshift, we can deduce evolution in the galaxy population of groups and the field since $z \sim 0.45$. This we do in Chapter 5 using the presence of significant [OII] emission to infer that a galaxy

belongs to the actively star-forming population. To ensure a fair comparison we must ensure that the differences in aperture size between the two surveys have little effect on our results. In Chapter 6 we examine the importance of aperture effects by adopting colour as an indicator of recent star formation, using resolved multicolour imaging of a large sample of galaxies from SDSS. By modelling the population as a bimodal combination of red (passive) galaxies and blue (star-forming) galaxies we show that the fraction of red passive galaxies is insensitive to the aperture size. This also provides important clues regarding the origin of colour gradients in galaxies. Having established the level of galaxy evolution in groups and the field, we make comparisons with the evolution predicted using simple physical models in Chapter 7. Ultimately it will be the combination of observations with detailed modelling which will disentangle the complex history of galaxy evolution and reveal the physical processes responsible.

In Chapter 8 we describe a complementary project designed to use a WFI (Wide Field Imaging) camera to map the infall regions of galaxy clusters at $z \sim 0.45$, the regime of infalling galaxy groups. The author worked on this project during the first year of this PhD, 2001-2002, but progress was marred by difficulties in establishing accurate calibration of the data. Work was ultimately ended by the precedence of the CNOC2 groups project. In this chapter we describe the difficulties in calibrating our data and how recent wisdom in the calibration of WFI data may or may not allow us to improve upon our calibration.

Finally in Chapter 9 we summarize what we have learned from this thesis and how it impacts our understanding of the influence of clustering on galaxy evolution. In particular we highlight areas which would benefit most from further investigation and how this might be tackled observationally.

Throughout this thesis we assume a Λ CDM cosmology of $\Omega_M = 0.3$, $\Omega_\Lambda = 0.7$ and $H_0 = 75 \text{ km s}^{-1} \text{ Mpc}^{-1}$.

Chapter 2

Star Formation in Low Redshift Galaxy Groups

2.1 Introduction

Clusters of galaxies have received intensive observational study over the last decades. Extensive observational effort has led to clear results on the way galaxy properties, such as morphology and star formation rate, vary within clusters and how these properties evolve between clusters at different redshifts (Dressler, 1980; Butcher & Oemler, 1984; Dressler et al., 1997; Poggianti et al., 1999, see Bower & Balogh 2004 for a recent review). In contrast, the study of galaxy groups and their evolution has only recently attracted such extensive observational interest. Groups have much lower density contrast against the background galaxy population so that extensive observational catalogues have been difficult to produce. Most work has concentrated on groups which are either unusually compact or unsuitable for statistical analysis (Hickson et al., 1989; Zabludoff & Mulchaey, 1998) or are X-ray luminous (Mulchaey et al., 2003). The advent of large field galaxy redshift surveys has, however, made it possible to study galaxy groups selected purely on the basis of their three dimensional galaxy density (Huchra & Geller, 1982; Ramella et al., 1989; Hashimoto et al., 1998; Tucker et al., 2000; Martínez et al., 2002; Eke et al., 2004).

Recently there has been a surge of interest in the properties of galaxies in groups. The group environment is likely to have a significant impact on star formation rates in the member galaxies (Zabludoff & Mulchaey, 1998; Hashimoto et al., 1998; Tran et al., 2001) and recent work has emphasised that even for galaxies now in rich clusters, much of the transformation of the galaxies' properties may have taken place in groups embedded in the filamentary structure (Kodama et al., 2001; Balogh et al., 2004a)

In addition, while few galaxies in the local universe are located in clusters, up to 50% (Huchra & Geller, 1982; Eke et al., 2004) may be located in galaxy groups. Thus the

properties of galaxies in groups and the impact of the group environment on the evolution of galaxies can have an important bearing on the decline in the cosmic star formation rate from $z = 1$ to the present-day (Lilly et al., 1996; Madau et al., 1998; Hopkins, 2004). As the large-scale structure of the universe develops, a larger and larger fraction of galaxies become members of groups. Thus the environment-driven evolution of group galaxies may make a significant contribution to the decline in the average star formation rate (see Bower & Balogh, 2004).

However, despite the extensive recent work on the properties of galaxies in low redshift groups, the properties of higher redshift groups have been relatively little explored. This is largely because of the difficulty in finding suitable systems, and the low success rate of spectroscopic follow-up of group members. In Chapter 3 we will introduce our group sample, selected from the intermediate redshift Canadian Network for Observational Cosmology 2 (CNOC2) survey by Carlberg et al. (2001b). This thesis also seeks to address the evolution of galaxy properties in the group environment. Therefore, to study galaxy evolution in groups we also require a large and consistently selected sample of local groups. In this chapter we introduce our choice of local group catalogue and review how the galaxy populations depend upon the group environment in these nearby groups. This will give us the tools with which to isolate the important properties of the group galaxy population at higher redshift and to study its evolution to $z = 0$.

2.2 The Sample

A convenient local redshift galaxy sample originates in the large 2 degree Field Galaxy Redshift Survey (2dFGRS) with over 220 000 galaxy spectra selected in the b_J -band. Rest-frame absolute magnitudes in the b_J -band are computed using k-corrections taken from Norberg et al. (2002), which are generally small. The galaxy sample is effectively volume limited (with low incompleteness, the sample is representative of the whole population) in the redshift range $0.05 \leq z \leq 0.1$ for galaxies with $M_{b_J} \leq -18.85$. Although there were problems with the atmospheric dispersion corrector prior to August 1999 which affect the instrument throughput (Lewis et al., 2002b), we find our results are unchanged if we exclude data obtained in this period.

Although defining the contents of a group is a subjective problem, there exist some tools which make the task easier. The 2dFGRS Percolation-Inferred Galaxy Group catalogue (2PIGG Eke et al., 2004) is based on a *friends-of-friends* percolation algorithm. The

task of locating galaxy groups in redshift space is often assigned to a friends-of-friends (FOF) algorithm (e.g. Huchra & Geller, 1982; Ramella et al., 1989). The algorithm links together all galaxies within a particular linking volume centred on each galaxy. By specifying the size and shape of this linking volume depending upon the depth of the survey, a group catalogue can be generated by associating groups of linked galaxies. Peculiar motion of galaxies moving in a gravitational potential artificially lengthens the group along the line-of-sight direction in redshift space (the *Finger of God effect*). From the virial theorem, one can make the assumption that the projected spatial and line-of-sight dimensions of a group in redshift space are approximately in constant proportion. An axial ratio (defined as the line-of-sight length relative to the projected spatial length) of ~ 11 is used to link 2dFGRS galaxies together in a friends-of-friends algorithm, forming a large catalogue of local groups. Group velocity dispersions are computed using the Gapper algorithm which is insensitive to outliers, providing an accurate estimate of the velocity dispersion for small groups (Beers et al., 1990). Full details of the 2PIGG group-finding algorithm and description of the catalogue can be found in Eke et al. (2004).

The 2PIGG catalogue is optimised to be highly complete in the detection of physical groups. This can sometimes lead to the contamination by unphysical systems. However, assuming zero contamination we can examine the fraction of galaxies in 2PIGG groups as a function of halo mass, estimated using Equation 4.7 from Eke et al. (2004). In Figure 2.1 we show the percentage of 2dFGRS galaxies brighter than $M_{b_j} = -19$ and at $z \leq 0.1$ in haloes of mass $\geq M$ (M_\odot). Neglecting contamination, Figure 2.1 shows that $\sim 55\%$ of galaxies are located in groups and $\sim 18\%$ are located in cluster-sized systems ($\gtrsim 10^{14} M_\odot$). In reality the percentages will be lower, especially in the larger systems in which interlopers, mostly members of infalling groups, might contaminate the clusters by as much as $\sim 40\%$. Unphysical systems are more likely to be a problem in groups with few members. To eliminate these spurious systems from our analysis we only investigate groups with number of known members $N_m \geq 10$ where this contamination is known to be small. Even with the $N_m \geq 10$ requirement for 2PIGG groups, the majority of groups still have low measurements of velocity dispersion ($\sigma(v)_{intr} \lesssim 400 \text{ km s}^{-1}$). We only consider galaxies more distant than $z = 0.05$ to limit our sensitivity to aperture effects. The upper limit of $z = 0.1$ is selected to create an approximately volume-limited sample down to $M_{b_j} \sim -18.85$ and to restrict evolution within this low redshift sample.

From now on we will refer to the 2dFGRS sample simply as the *2dF sample*. The 2dF field is defined as *everything* in the 2dF galaxy catalogue and represents the global

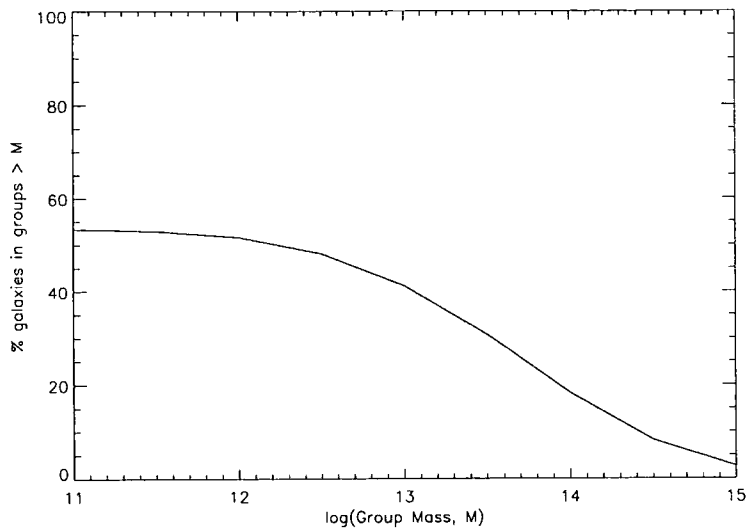


Figure 2.1: The percentage of local 2dFGRS galaxies (brighter than $M_{b_j} = -19$) in haloes of mass $\geq M$ (M_\odot) as inferred using the 2PIGG catalogue and equation 4.7 of Eke et al. (2004). In reality the percentages will be lower, especially in the larger systems in which interlopers might contaminate the clusters by as much as 40%. Only galaxies and groups at $z \leq 0.1$ are considered.

galaxy population in the $0.05 \leq z \leq 0.1$ redshift range. Within chosen magnitude limits ($M_{b_j} \lesssim -18.5^1$) the field sample contains 50981 galaxies. The 2dF group sample contains 5490 galaxies. Selection is made to include galaxies in the $0.05 \leq z \leq 0.1$ redshift range brighter than $M_{b_j} \lesssim -18.5$ and within $1h_{75}^{-1} Mpc$ of the centre of 2PIGG groups with number of members $N_m \geq 10$.

2.3 Star Formation in 2PIGG Groups

The 2PIGG catalogue is ideal for investigating how star formation is influenced by the group environment at low redshift. Using $EW[H\alpha]$ to measure the SFR of a galaxy relative to its continuum luminosity, Balogh et al. (2004a) find that the full galaxy population in 2dFGRS or SDSS is clearly bimodal, with a division at $EW[H\alpha] \sim 4\text{\AA}$. Figure 2.2 shows how the fraction of galaxies with $EW[H\alpha] > 4\text{\AA}$ (star-forming galaxies) depends critically on the local surface density of galaxies, Σ_5 , in both surveys. The solid line represents the full galaxy sample and shows that the fraction of star-forming galaxies correlates with local density even down to densities lower than typically found in groups ($\Sigma_5 \lesssim 0.3 \text{ Mpc}^{-2}$).

¹see Chapter 3 for motivation

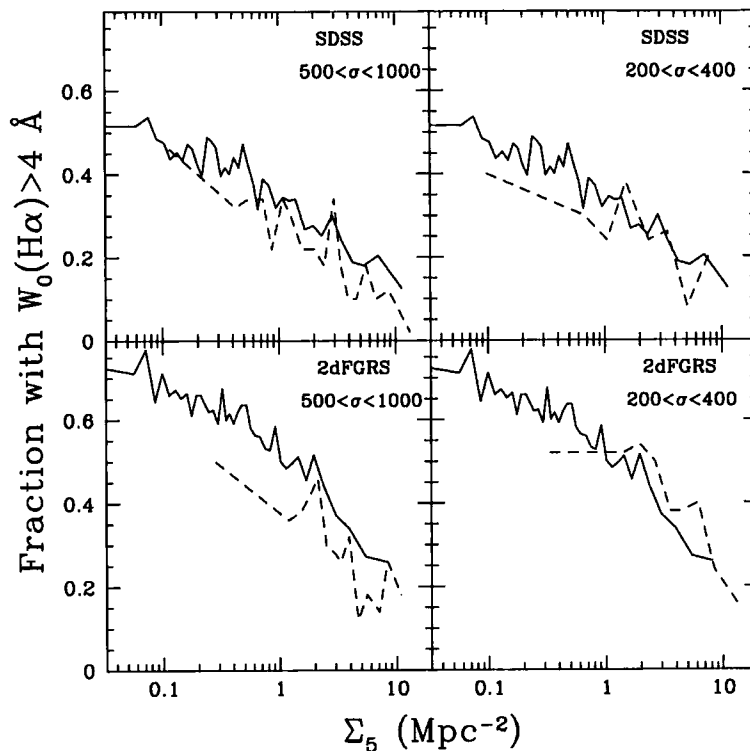


Figure 2.2: The fraction of galaxies with $EW[H\alpha] > 4\text{\AA}$ as a function of local density Σ_5 for the 2dFGRS (bottom panels) and SDSS (top panels) samples. The solid lines represent the full galaxy sample, in bins each containing 250 galaxies. The dashed lines are restricted to galaxies which lie in groups or clusters with the indicated velocity dispersion, in bins of 50 galaxies each. Poisson distribution uncertainties are typically ~ 0.1 on the dashed lines and ~ 0.05 on the solid lines. This figure is reproduced from Balogh et al. (2004a) with permission of Michael Balogh. We note that their terminology is slightly different with $EW[H\alpha]$ instead labelled $W_0(H\alpha)$.

The dashed lines represent the group galaxies (from 2PIGG in the case of 2dFGRS) in 2 bins of velocity dispersion. It is clear that the group galaxies follow the same correlation with local density that was found for the whole population. Groups cover a range of local densities for which there is a strong change in the fraction of star-forming galaxies, indicating that this is an important regime for galaxy transformation. There is a hint that the fraction of star-forming galaxies in more massive groups or clusters is lower in 2PIGG groups than in regions of similar local density in the whole population. However this is not seen in SDSS.

Figure 2.3 shows the distribution of $EW[H\alpha]$ for 2dFGRS (left panel) and SDSS (right panel) galaxies with $EW[H\alpha] > 4\text{\AA}$, in low density environments ($\Sigma_5 < 0.2 \text{ Mpc}^{-2}$, dotted

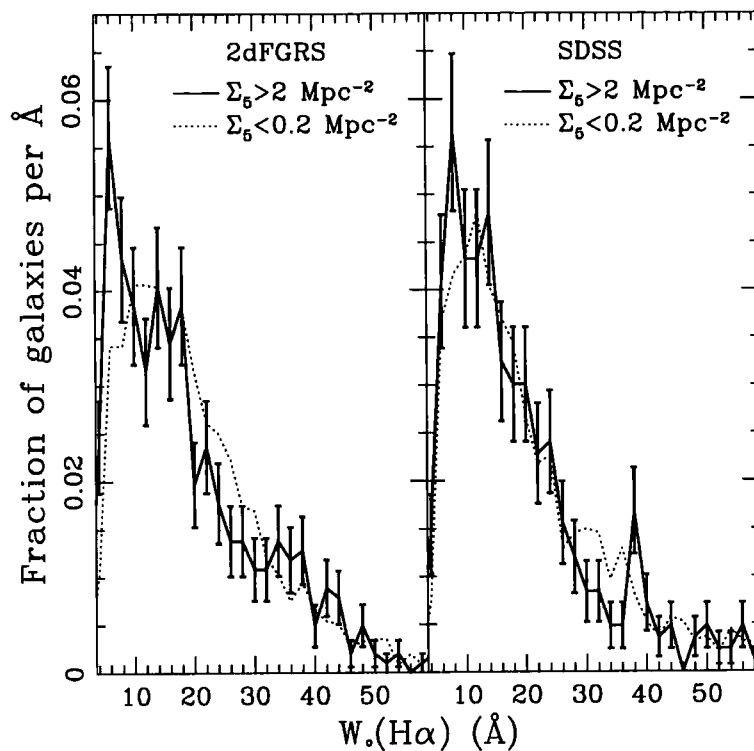


Figure 2.3: The distribution of $EW[H\alpha]$ for galaxies in 2dFGRS (left panel) and SDSS (right panel) with $EW[H\alpha] > 4\text{\AA}$, in low density environments ($\Sigma_5 < 0.2 \text{ Mpc}^{-2}$, dotted line) and high density environments ($\Sigma_5 > 2 \text{ Mpc}^{-2}$, solid line). We show Poisson-distributed error bars on the high density subsample which is the smaller of the two. This figure is reproduced from Balogh et al. (2004a) with permission of Michael Balogh. We note that their terminology is slightly different with $EW[H\alpha]$ instead labelled $W_0(H\alpha)$.

line) and high density environments ($\Sigma_5 > 2 \text{ Mpc}^{-2}$, solid line). The distributions in low and high density environments are startlingly similar; a Kolmogorov-Smirnov test (K-S test) does not reject the hypothesis that both are drawn from the same parent population with more than 1σ confidence. Therefore whilst the fraction of galaxies with effectively no star formation leaves a strong imprint on how star formation depends upon environment (Figure 2.2), the process which truncates the star formation must act on short timescales ($\lesssim 1 \text{ Gyr}$) such that the distribution of $EW[H\alpha]$ amongst star-forming galaxies is not significantly altered in dense environments (Figure 2.3). For a more detailed analysis of these figures see Balogh et al. (2004a).

Chapter 3

Star Formation in Galaxy Groups at $0.3 \leq z \leq 0.55$

3.1 Introduction

Studies of nearby groups show that their galaxy populations exhibit properties which vary from cluster-like (mostly early-type) to field-like (mostly late-type) (Zabludoff & Mulchaey, 1998). However we know that groups span a wide range in local density, upon which the morphological composition (Postman & Geller, 1984; Zabludoff & Mulchaey, 1998; Tran et al., 2001) and the mean star-forming properties (Hashimoto et al., 1998; Balogh et al., 2004a) strongly depend (e.g. Dressler, 1980; Postman & Geller, 1984; Hashimoto et al., 1998; Gómez et al., 2003; Balogh et al., 2004a; Kauffmann et al., 2004). The wide range of galaxy populations found in nearby groups is likely to be a natural consequence of these correlations. Conversely, the powerful dependence of galaxy properties on local densities typical of groups (seen in Figure 2.2) suggests that groups provide the ideal environment for galaxy transformations. This may result in the strong dependence of early-type fraction and passive dwarf galaxy abundance on group velocity dispersion and X-ray luminosity, observed in nearby groups (Zabludoff & Mulchaey, 1998, 2000; Christlein, 2000). In particular, galaxy interactions are expected to be common in groups, in which the velocity dispersion is typically not much larger than that of the constituent galaxies (Hashimoto et al., 1998; Severgnini & Saracco, 2001).

To witness the role of groups in actively transforming the galaxy population, these nearby data must be complemented with group catalogues at higher redshift. Clusters of galaxies have been extensively surveyed up to $z \gtrsim 1$ in recent decades (e.g. Butcher & Oemler, 1984; Couch & Sharples, 1987; Dressler et al., 1997; Ellingson et al., 2001; Postman et al., 2001; Nakata et al., 2004). This effort has been invaluable in our un-

derstanding of the way galaxy properties, such as morphology and star formation rate evolve between clusters at different redshifts. However, to date there are few examples of high redshift group catalogues, largely because they are difficult to detect. Only in the last few years has it been possible to compile catalogues of kinematically selected groups at $z > 0.3$ (Cohen et al., 2000; Carlberg et al., 2001b; Gerke & DEEP2 Team, 2003). Carlberg et al. (2001a) studied the properties of group galaxies in the CNOC2 group sample at intermediate redshift. Amongst other things, they discovered a trend in the mean galaxy colours, which on average become redder than the field toward the group centres.

In this chapter, we present new spectroscopic data obtained in the region of 26 CNOC2 groups at $0.3 \leq z \leq 0.55$ with LDSS2 on Magellan. In Sections 3.2 and 3.3 we introduce the data and explain why we have chosen to use the [OII] emission line to study statistical trends in star formation. In Section 3.4 we begin by describing the data reduction procedure and our method for determination of redshifts and emission line equivalent widths for each galaxy. Section 3.4.4 then goes on to explain our procedure for group membership allocation. In Section 3.5 we present the properties of the 26 individual groups in order to examine any trends of structural group properties with star formation. Finally, in Section 3.6 groups are stacked to enable detailed statistical analysis, and we investigate the link between the group environment and star formation by contrasting the stacked group with our sample of field galaxies selected from the same redshift range.

3.2 Groups in the CNOC2 Survey

3.2.1 The CNOC2 survey

The second Canadian Network for Observational Cosmology Redshift Survey (CNOC2) was recently completed with the aim of studying galaxy clustering in the redshift range $0.1 < z < 0.6$ (Yee et al., 2000; Shepherd et al., 2001). The CNOC2 survey is split into 4 patches, approximately equally spaced in RA and totalling 1.5 square degrees in area. The survey consists of 5 colour $UBVR_CI_C$ photometry with $\sim 4 \times 10^4$ galaxies down to the photometric limit $R_C = 23.0$. The MOS spectrograph on the CFHT 3.6m telescope was used to obtain spectra for over ~ 6000 galaxies in total, 48% complete down to $R_C = 21.5$. Combination of the imaging and spectroscopy lead to a very well determined selection function for the spectroscopic sample (Yee et al., 2000) and comparisons with

our deeper spectroscopy suggest that brighter than this limit the CNOC2 survey is not biased towards emission line objects. The transmission efficiency of the band-limiting filter and grism combination was above half power in the wavelength range $4387 - 6285 \text{ \AA}$, effectively limiting the redshift range of the survey. The most prominent absorption features (Ca II H and K) lie in this wavelength range for galaxies in the redshift range $0.12 < z < 0.58$, whereas either the [OII] or [OIII] emission lines fall in this wavelength range for all galaxies in the range $0 < z < 0.68$.

3.2.2 The CNOC2 groups

Distant groups have always been difficult to recognise because of their sparse galaxy populations. The presence of high-redshift groups has typically been inferred indirectly via the presence of a radio galaxy or X-ray emitting intragroup medium (IGM) (Allington-Smith et al., 1993; Jones et al., 2002). Whilst these surveys provide a useful insight into the evolution of galaxy properties in rich galaxy groups, the selection criteria strongly bias the selection towards these richer elliptical dominated groups, whereas low-redshift samples point to a more numerous population of low density, X-ray faint, spiral-dominated groups (Mulchaey et al., 2003).

The CNOC2 survey provided a powerful opportunity to generate a kinematically-selected sample of galaxy groups. A *friends-of-friends* percolation algorithm was used to detect groups of galaxies in redshift space. This was followed by a trimming step in which a centre, velocity dispersion, σ_1 and r_{200} (\sim virial radius) were estimated and then members were added or deleted within $3 \times \sigma_1$ and $1.5 \times r_{200}$ in 3 rounds of iteration (see Carlberg et al., 2001b). A total sample of over 200 galaxy groups was detected. Although the spectroscopic sample is incomplete, this group sample represents a kinematically-selected sample at intermediate redshifts ($0.12 < z < 0.55$), free from the strong biases present in samples selected by other means.

3.2.3 Deeper LDSS2 data

We used the Multi-Object Spectrograph LDSS2 (Low Dispersion Survey Spectrograph) on the 6.5m Baade Telescope at Las Companas Observatory (LCO) in Chile to obtain a deeper and more complete sample of galaxies in the region of 20 of the CNOC2 groups at $0.3 \leq z \leq 0.55$ located in the 3 out of 4 CNOC2 patches accessible from the latitude of LCO. Masks were designed using an automated selection algorithm to minimise selection bias and maximise the allocation of targets per mask. Due to the proximity on the

sky of some of the CNOC2 groups, the masks were chosen to serendipitously sample a further 11 groups from the Carlberg et al. (2001b) sample, although only 6 of these lie at $z > 0.3$. Targets were prioritised using an automated algorithm which favours brighter objects and objects which lie close together along the mask's spectral axis. This second criterion ensures that the spectral coverage does not vary wildly from object to object in each mask. The data were taken in 4 separate observing runs between May 2001 and November 2002. Each LDSS2 mask covers approximately $6.5' \times 5'$ and in the CNOC2 fields it is normal to fit between 20 and 30 slits onto a mask. Between 1 and 3 masks were observed per target group, depending upon the density of target galaxies in that area of sky. Mask exposures varied from 1 to 4 hours depending on the phase of the moon and observing conditions. For maximum throughput we used the blue-optimised medium resolution grism with a dispersion of 5.3\AA (on the fourth run the red optimised grism was used which has the same dispersion and similar efficiency at wavelengths of interest). The slits have a width = $1.47''$ which corresponds to 8.78\AA of spectral coverage (compared to 6.28\AA in the original CNOC2 masks). Using the CNOC2 photometric classifier from the CNOC2 photometric catalogue, we targeted 634 objects classified as *galaxies*, 102 objects classified as *possible galaxies*. Where there were free spaces on the mask with no galaxies present, we allocated 130 objects classified as *probable stars*. From this last category, 29 out of 130 objects had galaxy-like spectra which yielded redshifts. The remaining 101 were correctly identified as stars. Included in our targets were 35 galaxies which already had redshifts from the initial CNOC2 survey. These were reobserved to form a comparison sample which is used to understand the accuracy of our measurements.

In Table 3.1 we show the number of galaxies targeted in each field and the serendipitous Carlberg et al. (2001b) groups which lie in these fields.

3.3 Measurement of star formation using $\text{EW}[\text{OII}]$

To study the relative levels of star formation in statistical galaxy samples, we use the $[\text{OII}]\lambda 3727$ emission line which lies centrally in the visible window in our CNOC2 redshift range of $0.3 \leq z \leq 0.55$ and at wavelengths of low sky emission. At $z > 0.21$, the $\text{H}\alpha$ emission line disappears entirely from the LDSS2 spectrograph window with the instrument sensitivity dropping in the red with the current optics and detector. At $z \gtrsim 0.1$ measurements of $\text{H}\alpha$ are compromised by the increase in sky line density with increasing wavelength. Hopkins et al. (2003) have recently shown using data from local galaxies

Table 3.1: The number of galaxies targeted in each targeted group and the $0.3 \leq z \leq 0.55$ Carlberg et al. (2001b) groups serendipitous in these fields.

Targeted Group	Number of targeted galaxies	Serendipitous Carlberg et al. (2001b) groups
22	27	23,33
24	51	none
25	54	none
28	95	none
31	44	none
32	23	none
34	61	none
37	27	27,35
38	54	40
39	97	23,33
134	53	132,138
137	58	140
138	60	129,132,133,134
139	31	none
140	68	137
227	59	none
228	22	none
232	27	241
241	24	232
244	43	243

in SDSS that measurements of SFR using [OII] emission are *highly consistent with those from H α and 1.4GHz luminosities*. Also the scatter in the H α -[OII] relationship is primarily luminosity dependent (Jansen et al., 2001) and so in a given luminosity range the systematic error in using the [OII] measurement to infer star formation rates is significantly reduced. Additionally, even at $z < 1$, Flores et al. (2004) place the contribution from dusty starburst galaxies to the total SFR, underestimated by optical emission line measurements at $\lesssim 20\%$. Rather than inferring star formation rates, we deliberately limit our study to direct comparison between [OII] measurements to avoid model dependency in our results. Finally, we restrict our analysis to EW[OII] rather than [OII] flux and star formation rates. Normalisation by the continuum reduces uncertainties related to absorption by dust and aperture bias as well as providing a measure of SFR per unit luminosity.

3.4 Data Processing

3.4.1 Data Reduction

We extracted and calibrated our spectra using mainly *iraf* tools in the *onedspec* and *twodspec* packages. Wavelength calibration was applied using both *iraf* tools and new MOS reduction software written by Dan Kelson in Carnegie (Kelson, 2003). We have tested both these methods to ensure that consistent solutions are obtained. The wavelength calibration is based upon arcs taken during daytime and is secure in the wavelength range $3700\text{\AA} \leq \lambda \leq 8000\text{\AA}$ which corresponds to $z \leq 2.1$ for the [OII] emission line and $z \leq 0.6$ for [OIII] which extends far beyond the redshift range of interest. Around bright skylines, systematic residuals often remain. We interpolated over these regions.

To account for mismatch between the daytime arc and nighttime science observations, we then applied a zero point offset to the wavelength calibration. This is computed by measuring the offset of the 5577\AA skyline in the arc-calibrated frames. Most of these offsets were $< 5\text{\AA}$ and we did not detect any significant non-linearities. The new wavelength solution appears robust, as evidenced in the comparison of LDSS2 and CNOC2 redshifts (see figure 3.1 which is explained in Section 3.4.2.2).

3.4.2 Redshift Measurement

The *iraf* tool *xcsao* in the *rusao* package (Kurtz & Mink, 1998) was used to cross-correlate all the spectra with templates of rest-frame early-type (absorption line) and late-type

(emission line) galaxies. The early-type galaxy template was created by coadding a large number of high signal-to-noise early-type galaxy spectra from the sample, each of which had been shifted to zero redshift.¹ The emission line (Sc) template is a high signal to noise spectrum of NGC4775 from the atlas of Kennicutt (1992) and smoothed to the resolution of LDSS2.² We shall henceforth refer to redshifts obtained using the late-type template as *emission* redshifts and those obtained using the early-type template as *absorption* redshifts.

The peak in the cross-correlation spectrum is selected by *xcsao* to give an estimate of the redshift for each object (Tonry & Davis, 1979). To assess redshift measurements, redshifts attained using the early-type (absorption) and late-type (emission) templates were assessed in each case by manually inspecting the spectra and assigning a redshift quality flag. The quality assessment is based upon the number of believable emission lines in an emission line spectrum. In absorption line spectra, we simply decide whether to *accept* or *reject* a solution. For example, a solution with a visible 4000Å break would be accepted. Spectra containing a single emission line received further checks to ensure the emission is real. Finally, redshifts which became apparent upon visual inspection were applied by setting up that solution as the initial guess in *rvsao*. However, if no peak in the cross-correlation spectrum could be obtained at the correct redshift then the solution was abandoned.

The final redshift of a target was selected by comparing the redshift quality flag from emission and absorption redshifts. Emission redshifts are generally preferred due to their greater accuracy. However, where the emission redshift was not secure and a different, higher quality absorption redshift exists, then the absorption redshift is used. Objects with no acceptable redshift are discounted from the spectroscopic sample.

In total we have 418 redshifts from the LDSS2 data of which 240 are in the range $21 \leq R_c \leq 22$ which dramatically improves the completeness at this depth. In the whole sample, we have 86 new group members from LDSS2 spectroscopy. This increases the total group sample to 295 in 26 groups (see Group Membership section for further details

¹High signal-to-noise early-type galaxy spectra used to create our template are shifted to zero redshift by cross-correlation with a high signal to noise spectrum of NGC3379 from the atlas of Kennicutt (1992).

²Velocity zero points of both Kennicutt (1992) spectral templates have been improved to an accuracy of 30 km s^{-1} (Yee et al., 1996).

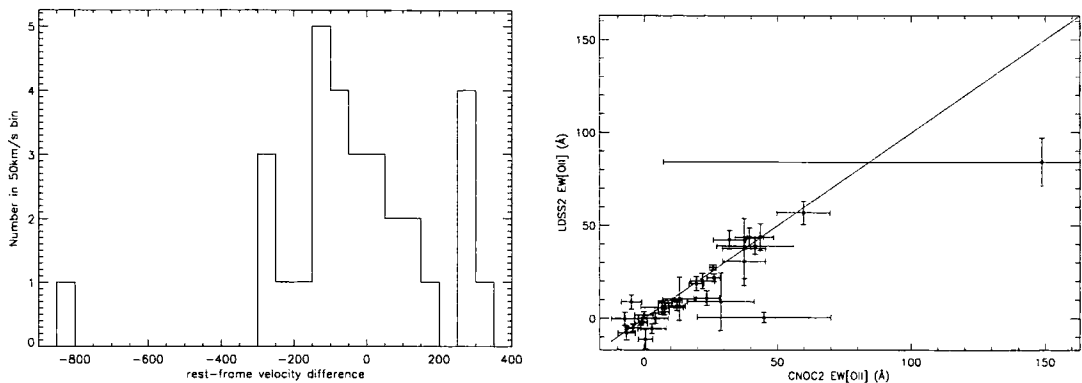


Figure 3.1: A comparison of velocity and EW[OII] measurements in CNOC2 and LDSS2 measurements using the 32 galaxies with matched redshifts in the comparison sample. **Left:** Rest-frame velocity offset, $(cz_{\text{CNOC2}} - cz_{\text{LDSS2}})/(1+z)$ and **Right:** Comparison between rest-frame EW[OII] measurements, for the galaxies in which redshifts and EW[OII] have been obtained from LDSS2 spectra *and* in the original CNOC2 catalogue.

of group allocation). In the magnitude range $21 \leq R_c \leq 22$ and within $150''$ of targeted group centres, we obtained 179 additional redshifts (36 members) on top of the 115 (27 members) existing from the CNOC2 survey. We consider $R_c = 22$ to be our magnitude limit at which we can obtain redshifts for $\sim 60\%$ of objects targeted. However, if we consider all targeted galaxies brighter than $R_c = 22$ then we have a 74% redshift success rate. The selection functions are well understood and targeted galaxies for which we do not manage to obtain a redshift are evenly distributed in colour, suggesting that our sample is unbiased (see Section 3.6.1).

3.4.2.1 Emission Line Equivalent Width Measurements

We measure the [OII] equivalent widths using our own purpose written code. In brief, the equivalent widths are measured over pre-specified “line windows”. The window definition includes two separate continuum regions and a “line” region. We use the definition from Dressler & Shectman (1987) for [OII]. This requires measuring the line region from 3718\AA to 3738\AA and the continuum regions of width 65\AA adjacent to the line region on either side.

3.4.2.2 Comparison with CNOC2 data

In Figure 3.1 we show the common-object comparison between the LDSS2 spectra and the CNOC2 spectra. The redshifts and $\text{EW}[\text{OII}]$ of these objects can be seen in Figure 3.1. It can be seen that the redshifts from these 2 sources are generally in good agreement. Out of 35 galaxies with redshifts from both sources, 4 of the redshifts are discrepant. Three of these are faint objects with low signal-to-noise spectra ($B > 23.5$, $R_c > 21.5$) and are not included in the figure. The other discrepant redshift is offset by $\sim 800 \text{ km s}^{-1}$ (rest-frame). Inspection shows that the LDSS2 redshift provides a better fit to the emission lines. Of the remaining 31 galaxies in this sample, the standard deviation of the rest-frame velocity offsets ($(cz_{\text{CNOC2}} - cz_{\text{LDSS2}})/(1+z)$) is $\sigma_{\text{tot}} = 175 \text{ km s}^{-1}$, with a mean value of only -6 km s^{-1} .

Using duplicate observations Yee et al. (2000) show that the random rest-frame velocity errors in the CNOC2 redshifts is 103 km s^{-1} . As the typical velocity difference in our common-object sample is 175 km s^{-1} , we compute an approximate rest-frame error on LDSS2 spectra of $\Delta(v)_{\text{LDSS2}} = \sqrt{175^2 - 103^2} = 142 \text{ km s}^{-1}$. We expect that the velocity errors are dominated by the CNOC2 astrometrical errors of $\lesssim 1''$ (Yee et al., 2000). Indeed the errors computed using the common-object sample are consistent with an rms astrometrical error of $\sim 0.25''$.

In the right hand panel of figure 3.1, we show that measurements of $\text{EW}[\text{OII}]$ in LDSS2 spectra (measured using our code) are also in excellent agreement with the original CNOC2 survey measurements (Whitaker et al., 2004) within errors, showing that our measurements are consistent with CNOC2. The code used for both sets of measurements is essentially the same and tests show that they provide identical results.

3.4.3 K-corrected rest frame magnitudes

CNOC2 galaxies are k-corrected to give rest-frame absolute magnitudes in the b_J -band. K-corrections have been calculated using no-evolution models; we will explore the sensitivity of our results to the assumed model of galaxy evolution in Chapter 7. We note that k+e corrections are also available for galaxies in the original CNOC2 sample (Shepherd et al., 2001). For each galaxy, we first choose a mixture of observed local SEDs (King & Ellis, 1985) for which the model B-I colour matches the observed colour at the given redshift. Then the rest-frame absolute b_J magnitude can be determined from the models, given the observed R_c magnitude, SED mixture and redshift. The transformation from

observed R_c -band magnitude to rest-frame b_J is chosen because it is closely matched at CNOC2 redshifts and because it directly transforms the CNOC2 spectroscopic selection band to the 2dF selection band, facilitating comparisons with our local group sample (Chapter 5). Luminosities are then corrected for galactic extinction on a patch-to-patch basis, computed by extrapolating from B and V band extinction values obtained from NED (Schlegel et al., 1998, variation within each patch is negligible). We make no correction for internal extinction, also to allow direct comparison with local galaxies in 2dF.

3.4.4 Group Membership

To obtain a consistently selected sample of galaxy groups, we restricted ourselves to examining those groups which were pre-selected from the sample of Carlberg et al. (2001b) and targeted with LDSS2 on Magellan. This provides a sample of 26 targeted and serendipitous Carlberg et al. (2001b) groups in the range $0.3 \leq z \leq 0.55$. Carlberg et al. (2001b) derive r_{200} from the virial theorem, applying a radial cut to groups at $1.5 \times r_{200}$. We convert their derivation to our cosmology, deriving: $r_{200} \sim \frac{1}{11.5H_{75}(z)} \times \sigma(v)$ where $\sigma(v)$ is the velocity dispersion and $H_{75}(z)$ is the Hubble Constant at the group redshift z where $H_{75}(0) = 75 \text{ km s}^{-1} \text{ Mpc}^{-1}$. We emphasize that whilst this determination corresponds to the value of r_{200} derived by Carlberg et al. (2001b), it only strictly corresponds to a true value of r_{200} in their matter-dominated, $\Lambda = 0$ cosmology. However, with this derivation a group with $\sigma(v) = 300 \text{ km s}^{-1}$ has $r_{200} = 0.28h_{75}^{-1} \text{ Mpc}$ at $z = 0.4$, with r_{200} scaling with $\sigma(v)$. The group finding algorithm of Carlberg et al. (2001b) was tuned to identify dense, virialized groups of 3 members or more with the goal of tracing the properties of the underlying dark matter halos. With this in mind, a conservative linking-length ($0.33h_{75}^{-1} \text{ Mpc}$) and the trimming radius of $1.5r_{200}$ in the spatial axes of the groups were selected.

Our objectives differ from those of Carlberg et al. (2001b) in that we wish to understand the global properties of galaxies in groups, not only those galaxies in the virialized group core regions. In order to be more representative of the loose group population, whilst retaining the strict selection criteria of Carlberg et al. (2001b), we choose to relax the projected trimming radius for group members in our redefined group sample. In effect, we find that relaxing this parameter allows the more compact groups to retain the same membership whilst other groups gain extra members.

In Chapter 2 we introduced our membership criteria for local groups in the 2dFGRS

survey. In this case the groups are pre-identified and thus a friends-of-friends algorithm is unnecessary. Our algorithm simply determines whether a galaxy is a group member on the basis of its spatial position and redshift. Interlopers in redshift space are difficult to identify and eliminate so we choose a conservative line-of-sight trimming radius of $2\times$ velocity dispersion. However, to survey a wider spatial region around the group, an axial ratio of 5 is adopted for the trimming volume in redshift space, to compute our spatial trimming radius which will be larger than r_{200} . We find that this provides a stable membership solution for all 26 groups.

The algorithm for defining the final membership of each group in our sample works as follows:

- The group is initially assumed to be located at the latest position in redshift space determined by Carlberg et al. (2001b)³ with an initial observed-frame velocity dispersion, $\sigma(v)_{obs}$, of 500 km s^{-1} .
- The redshift range required for group membership is computed from equation 3.1, which limits membership in the line-of-sight direction to $\pm 2\times$ velocity dispersion:

$$\delta(z)_{max} = 2 \frac{\sigma(v)_{obs}}{c} \quad (3.1)$$

- This is converted into a spatial distance, $\delta(\theta)_{max}$, which corresponds to a redshift space distance $\frac{1}{5}$ the distance computed in the line-of-sight direction. This is computed using equations 3.2 and 3.3.

$$\delta(r)_{max} = \frac{c \cdot \delta(z)_{max}}{b \cdot H_{75}(z)} \quad (3.2)$$

with $b = AspectRatio = 5$.

$$\delta(\theta)_{max} = 206265'' \cdot \left(\frac{\delta(r)_{max}}{h_{75}^{-1} Mpc} \right) \cdot \left(\frac{D_{\theta}}{h_{75}^{-1} Mpc} \right)^{-1} \quad (3.3)$$

where D_{θ} , the angular diameter distance, is a function of z .

- Group Members are selected by applying the redshift and positional limits $\delta(z) = |z - z_{group}| \leq \delta(z)_{max}$ and the angular distance from the group centre, $\delta(\theta) \leq \delta(\theta)_{max}$.

³Note: these positions have been updated since publication

- We recompute the observed velocity dispersion of the group, $\sigma(v)_{obs}$, using the Gapper algorithm (equation 3.4) which is insensitive to outliers and thus gives an accurate estimate of the velocity dispersion for small groups (Beers et al., 1990). The multiplicative factor 1.135 corrects for the 2σ clipping of a gaussian velocity distribution, and the galaxies must be ordered in a monotonic velocity sequence before applying Equation 3.4.

$$\sigma(v)_{obs} = 1.135c \times \frac{\sqrt{\pi}}{n(n-1)} \sum_{i=1}^{n-1} w_i g_i \quad (3.4)$$

with $w_i = i(n-i)$ and $g_i = z_{i+1} - z_i$.

- We also redefine the centre of the group, taking the luminosity-weighted centroid in projected spatial coordinates and the mean redshift to be the new group centre.
- We then recompute the limiting redshift offset $\delta(z)_{max}$ and positional offset $\delta(\theta)_{max}$ using equations 3.1, 3.2 and 3.3. The galaxies are then reassigned to the group as before.
- The whole process is repeated until a stable membership solution is reached. In all 26 groups such a stable solution is found, mostly within 2 iterations although the massive group 138 requires 4 iterations. We finally compute the rest-frame velocity dispersion (equation 3.5) and the intrinsic velocity dispersion. The latter is computed by combining the measurement errors of the component galaxies (equation 3.6) and removing in quadrature from the measured velocity dispersion (equation 3.7).

$$\sigma(v)_{rest} = \frac{\sigma(v)_{obs}}{1+z} \quad (3.5)$$

$$\langle \Delta(v) \rangle^2 = \frac{1}{N} \sum_{i=1}^N \Delta(v)_i^2 \quad (3.6)$$

where $\Delta(v) = 142 \text{ km s}^{-1}$ (LDSS2)

and $\Delta(v) = 103 \text{ km s}^{-1}$ (CNOC2)

$$\sigma(v)_{intr}^2 = \sigma(v)_{rest}^2 - \langle \Delta(v) \rangle^2 \quad (3.7)$$

The combined velocity errors ($\langle \Delta(v) \rangle$) in group 24 exceed the measured velocity dispersion $\sigma(v)_{rest}$ and so an upper limit is placed upon the intrinsic velocity dispersion using Monte-Carlo simulations. We artificially populate a group with the same number of members as group 24, assuming an intrinsic velocity dispersion, $\sigma(v)_{intr}$. We then compute the measured velocity dispersion, $\sigma(v)_{rest}$ in the usual way. This is repeated 10000 times for all values of $\sigma(v)_{intr}$ from 10 km s^{-1} to 350 km s^{-1} in steps of 5 km s^{-1} . The 1σ upper limit for $\sigma(v)_{intr}$ occurs at the value of $\sigma(v)_{intr}$ for which in 15.87% of iterations a value of $\sigma(v)_{rest}$ less than the measured value is obtained from the simulations. This occurs at $\sigma(v)_{intr} = 119.6 \text{ km s}^{-1}$.

In all other groups, the error on the velocity dispersion is computed using the Jackknife technique (Efron, 1982). To compute an error using the Jackknife technique, the required value (in this case the velocity dispersion) is computed for all but 1 group member. This is repeated, on each occasion leaving out each different group member. The error on the velocity dispersion is then computed to be $\left[\frac{N_{tot}}{(N_{tot}-1)} \Sigma(\delta_i^2) \right]^{\frac{1}{2}}$ where N_{tot} = total number of known members and $\delta_i = \sigma(v)_{intr} - \sigma(v)_{intr}$ (excluding i). We note that in groups with few known members (e.g. group 40) the true error on $\sigma(v)_{intr}$ is underestimated using the Jackknife technique in some cases.

In Figure 3.2, we show velocity histograms for 2 of our groups and the redshift space clustering in the region of those groups. The left-hand panels show the rich group 138, possibly even a poor cluster, whilst the right-hand panels show the medium-sized group 241. The overplotted gaussian of width $\sigma(v)_{obs}$ provides a good envelope to the distribution in both cases, which is typical of all 26 groups.

As the group-finding algorithm of Carlberg et al. (2001b) requires CNOC2 redshifts for 3 or more members to be detected, one might expect that at lower redshift the group-finder would find more small, low mass groups than at higher redshift as the survey probes further down the luminosity function. However, figure 3.3 shows that there is no significant bias in our group sample. Nonetheless, the majority of our groups (19/26) lie at the low redshift end of our redshift range ($z \leq 0.45$).

The upper panel of figure 3.4 shows the kinematic offset, (dv), and the projected spatial offset (dr) from the group centre for all group members. The solid line shows how the median of dv (computed over 50 adjacent galaxies in dr) varies with dr . There is a distinct depression of median dv at low dr , corresponding to much more tightly bound galaxies

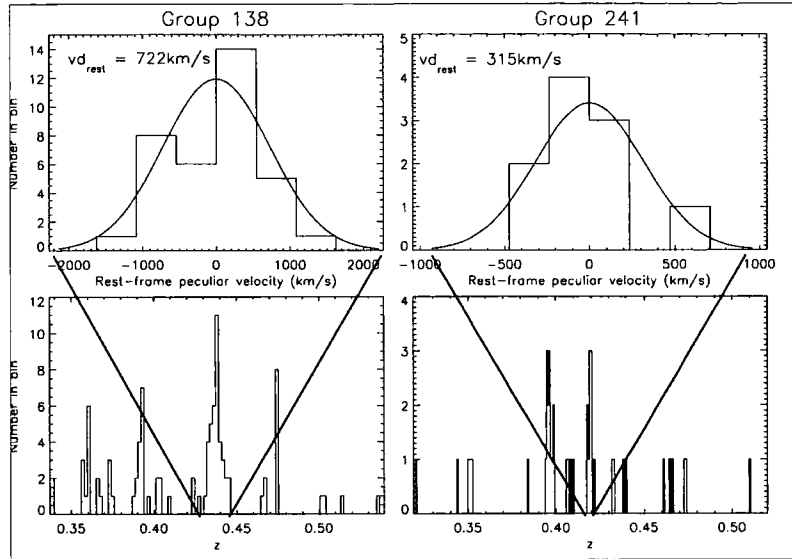


Figure 3.2: Bottom: Redshift Distributions in the regions of 2 groups; Top: Velocity Distribution of the group members; The smooth line represents a gaussian with $\sigma = \sigma(v)_{obs}$.

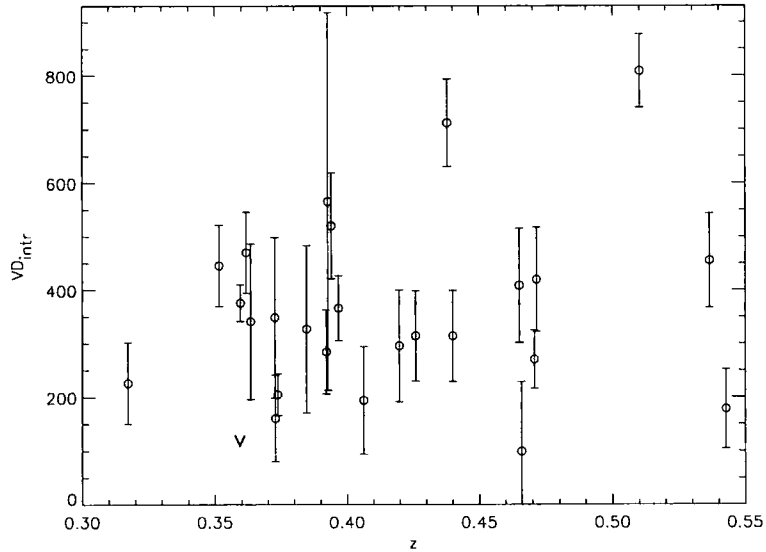


Figure 3.3: The distribution of our CNOC2 groups in $\sigma(v)_{intr}$ - z space. There is no strong correlation, indicating that our highest redshift groups are not necessarily our most massive (highest velocity dispersion) groups.

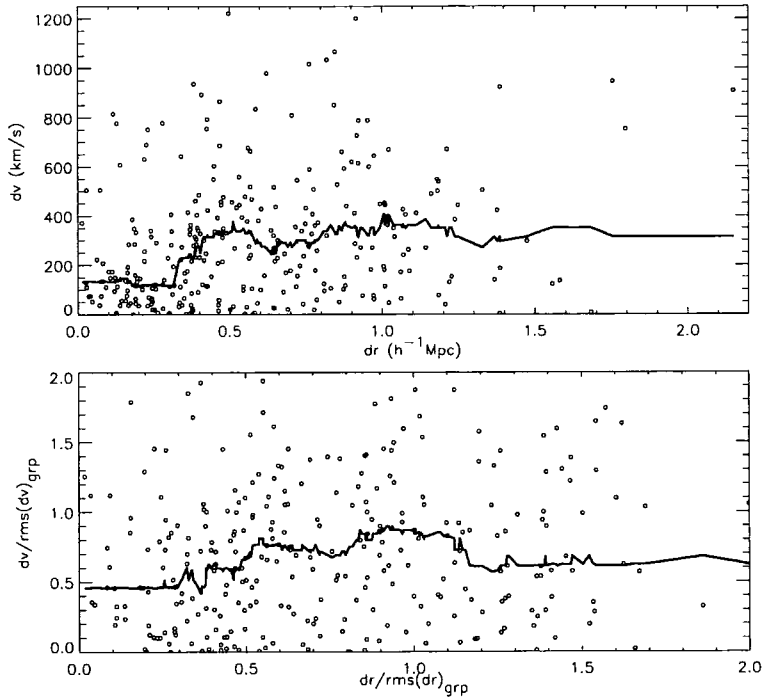


Figure 3.4: **Top:** Kinematic (dv) and projected spatial (dr) offsets from the group centre, as determined by the group membership allocation algorithm (section 3.4.4). The solid line shows the running median of kinematic offset (dv), computed over 50 neighbour-galaxies along the spatial axis. **Bottom:** The same as in the top panel but with the kinematic and spatial offsets each normalised by the rms values of the parent group. This removes any false dv - dr trend originating from the variable physical sizes of the groups.

inwards of $\sim 0.35h_{75}^{-1} \text{Mpc}$. To see if this is merely an effect of superposing groups of different kinematic and spatial extent, the bottom panel shows both dr and dv normalised by the rms values in the group containing each galaxy. The trend mostly disappears, although there is still some indication of a depression in dv inwards of $dr/rms(dr)_{grp} \sim 0.5$. We also see no significant trends in kinematic or spatial offset with galaxy luminosity, indicating that the orbits of group galaxies were independent of the galaxy mass at $z \geq 0.3$, to the accuracy of our data.

Whilst group members lie some distance (up to $\sim 4.5r_{200}$) from the group centre and are included in the calculation of the velocity dispersion, we limit our analysis to galaxies inside a $1h_{75}^{-1} \text{Mpc}$ projected radius at the group redshift ($\sim 3.5r_{200}$ for a group with $\sigma(v)_{intr} = 300 \text{ km s}^{-1}$), where we understand the completeness (see Section 3.6.1). A luminosity $M_{b_j} = -20$ approximates the magnitude limit, $R_c = 22.0$, for most galaxies at $z = 0.55$. We compute N_{mem} , an estimate of the number of group members brighter than

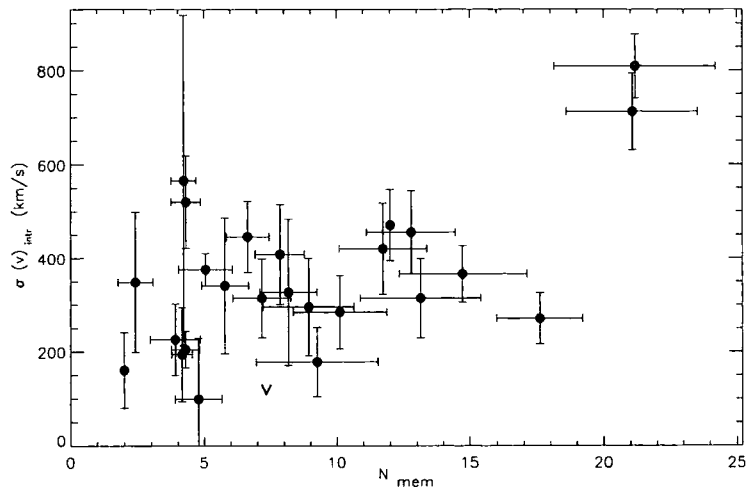


Figure 3.5: Intrinsic Velocity Dispersion of galaxy groups, $\sigma(v)_{intr}$ plotted against the number of galaxy members within 1Mpc and brighter than $M_{b_J} = -20$, corrected for incompleteness (N_{mem}). Errors on N_{mem} represent the Poisson error on the number of candidate members estimated to lie in the group (see Section 3.4.4 for definition).

$M_{b_J} = -20$ and within $1h_{75}^{-1}$ Mpc projected distance from the group centre. N_{mem} is the sum of the number of known members and *candidate members*. The number of candidate members is simply a correction for completeness, computed by multiplying the number of galaxies without redshifts (which would there meet our luminosity and radial cut, at the group redshift), by the fraction of equivalent galaxies with redshifts, which are group members. Figure 3.5 shows N_{mem} plotted against the intrinsic velocity dispersion $\sigma(v)_{intr}$ of each group. Any weak correlation between N_{mem} and $\sigma(v)_{intr}$ is largely masked by a good deal of scatter (excluding the 2 largest systems). This scatter might be attributed to the variation in group structure and the difficulty of obtaining accurate estimates of velocity dispersion with few members. Limiting the membership to galaxies within $0.5h_{75}^{-1}$ Mpc projected radius does not reduce the scatter in this relationship.

Groups often possess a hot gas halo centred on, and often aligned with, a luminous elliptical galaxy (e.g. Mulchaey & Zabludoff, 1998). This suggests that the formation and/or evolution of the central galaxy is linked to the shape of the global group potential. In figure 3.6, we look for a correlation between the optical b_J -band luminosity of the brightest group galaxy (BGG) (within $1h_{75}^{-1}$ Mpc of the group centre), $M_{b_J}(\text{Br})$, and the group velocity dispersion, $\sigma(v)_{intr}$. Any such correlation should support the link between the formation of the BGG and the group properties. There is an indication of a trend

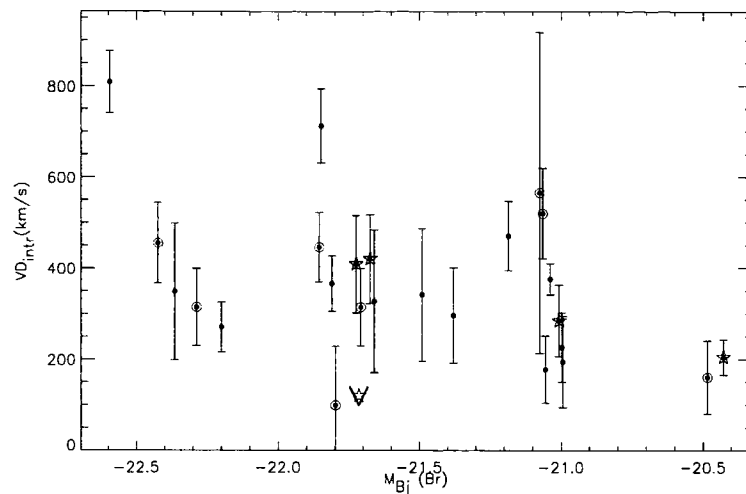


Figure 3.6: The luminosity of the brightest group galaxy (within $1h_{75}^{-1}$ Mpc of the luminosity-weighted group centre) as a function of group velocity dispersion, $\sigma(v)_{intr}$. Some of these groups are keyed on the morphology of the brightest galaxy, where this is known from recent HST imaging (the open symbols). The open circles represent early-type galaxies and the stars represent later galaxy types.

towards brighter BGGs in the most massive (highest $\sigma(v)_{intr}$) groups. Whilst the trend is weak, it suggests that in a hierarchical Universe the formation or mass-assembly of the BGG is linked to the formation and mass of the containing group halo. Using preliminary data from recent HST imaging, we can see no obvious distinction in the $M_{BJ}(\text{Br}) - \sigma(v)_{intr}$ plane between groups with early-type BGGs (open circles) and later-type BGGs (stars).

3.5 Individual Group Analysis

3.5.1 Basic Parameters

In Table 3.2 we present some of the fundamental properties of our CNOC2 group sample including the velocity dispersion, $\sigma(v)_{intr}$ and the number of members of each group (both the total with measured redshifts (N_{tot}) and the number brighter than $M_{BJ} = -20$ and within $1h_{75}^{-1}$ Mpc of the group centre, weighted to account for incompleteness (N_{mem})). The group *class* and parameter f_p are defined in Section 3.5.2. Groups closer to the low redshift limit of $z = 0.3$ are on average complete down to fainter luminosities. Incompleteness over the full luminosity range is also a function of the fraction of targeted objects in the group vicinity.

Table 3.2: *Individual Group Properties*: Including : Luminosity-weighted group centroid positions in spatial coordinates; Mean redshift, z ; Velocity dispersion, $\sigma(v)_{intr}$; Total number of galaxies in each group with redshift, N_{tot} ; The number of members brighter than $M_{b_j} = -20$ and within $1h_{75}^{-1}$ Mpc, weighted to account for incompleteness, N_{mem} ; The manually classified group *class*; The luminosity of the brightest group galaxy (within $1h_{75}^{-1}$ Mpc of the centre), M_{b_j} (Br); The fraction of passive galaxies in the group, f_p (brighter than $M_{b_j} = -20.0$ and within $0.5h_{75}^{-1}$ Mpc of the iteratively determined group centre) Note: Computation of f_p includes resampling to account for galaxies without redshifts in the region of each group (See Section 3.5.2.2).

Group	RA (J2000)	Dec (J2000)	z	$\sigma(v)_{intr}$ (km s $^{-1}$)	N_{tot}	N_{mem}	Class	$M_{B_j}(Br)$	f_p
23	14:49:25.0	+09:30:26	0.351	445 ± 75	13	6.64	C	-21.84	0.67
24	14:49:03.9	+09:06:57	0.359	<119.6	11	7.33	C	-21.7	0.71
25	14:49:40.8	+09:13:43	0.361	470 ± 75	19	12.00	C	-21.17	0.63
27	14:49:49.9	+09:06:38	0.372	348 ± 149	8	2.41	L	-22.35	1.00
28	14:50:22.8	+09:01:13	0.372	160 ± 80	6	2.00	C	-20.47	1.00
31	14:49:12.9	+09:10:09	0.392	565 ± 352	5	4.22	L	-21.06	0.33
32	14:50:01.3	+08:55:57	0.394	519 ± 98	9	4.30	L	-21.05	0.25
33	14:49:36.8	+09:28:48	0.406	194 ± 100	7	4.15	L	-20.98	0.80
34	14:48:43.8	+08:52:02	0.465	408 ± 106	11	7.84	L	-21.71	0.25
37	14:49:29.1	+09:05:33	0.471	419 ± 97	19	11.72	C	-21.66	1.00
38	14:49:27.8	+08:58:12	0.510	808 ± 68	19	21.17	M	-22.58	0.29
39	14:49:23.2	+09:30:24	0.536	454 ± 88	15	12.78	C	-22.41	0.88
40	14:49:20.2	+08:54:57	0.542	177 ± 73	4	9.25	U	-21.04	0.33
129	21:51:03.3	-05:42:23	0.317	225 ± 76	7	3.90	C	-20.98	0.50
132	21:50:25.8	-05:40:53	0.359	375 ± 34	9	5.05	L	-21.02	1.00
133	21:50:48.2	-05:37:33	0.373	204 ± 38	4	4.28	U	-20.41	0.00
134	21:50:24.8	-05:41:29	0.392	284 ± 78	12	10.11	L	-20.99	0.33
137	21:50:37.7	-05:29:18	0.425	314 ± 84	8	7.17	C	-22.27	1.00
138	21:50:48.2	-05:39:53	0.437	711 ± 81	35	21.07	M	-21.83	1.00
139	21:50:25.8	-05:50:20	0.439	314 ± 84	12	13.14	L	-21.69	0.71
140	21:50:41.4	-05:28:38	0.465	98 ± 129	5	4.78	C	-21.78	0.33
227	02:26:29.5	+00:12:08	0.363	341 ± 145	7	5.78	L	-21.49	0.33
228	02:25:05.7	-00:07:12	0.384	326 ± 156	8	8.16	C	-21.66	0.67
232	02:25:50.7	+00:52:17	0.396	366 ± 60	14	14.72	C	-21.81	0.29
241	02:25:58.7	+00:54:21	0.419	295 ± 104	10	8.93	L	-21.38	0.43
244	02:25:45.0	+01:07:30	0.470	270 ± 54	18	17.60	C	-22.20	0.10

3.5.2 Star Formation in the CNOC2 groups

We are motivated by the findings of Strateva et al. (2001), Blanton et al. (2003), Baldry et al. (2004) and Balogh et al. (2004a) who show that galaxy populations have a bimodal distribution in colour and $\text{EW}[\text{H}\alpha]$. Balogh et al. (2004a,b) show that the fraction of red, passive galaxies is strongly dependent upon local galaxy density. The division between passive and star-forming galaxies in the $\text{EW}[\text{H}\alpha]$ distribution occurs at $\sim 4\text{\AA}$ (Balogh et al., 2004a). We do not expect to see such a clear bimodality in $\text{EW}[\text{OII}]$ since $\text{EW}[\text{H}\alpha] = 4\text{\AA}$ typically corresponds to $\text{EW}[\text{OII}] < 2\text{\AA}$, below the measurement error in $\text{EW}[\text{OII}]$ for CNOC2. Greater intrinsic scatter in the $\text{SFR}[\text{OII}]$ relation than in the $\text{SFR}-\text{H}\alpha$ relation also works to mask the division between the two populations. Thus, although we cannot cleanly separate the two populations, we impose an arbitrary division at 5\AA in the CNOC2 data. We expect the population with $\text{EW}[\text{OII}] < 5\text{\AA}$ to be dominated by the passive population⁴ and the population with $\text{EW}[\text{OII}] \geq 5\text{\AA}$ to be dominated by the star-forming population, and this division is sufficient to reveal trends in the data (see e.g. Hammer et al., 1997; Zabludoff & Mulchaey, 2000).

In Section 3.6.4 and Chapter 5 we shall show that an artificial division in $\text{EW}[\text{OII}]$ at 5\AA is sufficient to reveal trends in the fraction of *star-forming galaxies* ($\text{EW}[\text{OII}] \geq 5\text{\AA}$) and *passive galaxies* ($\text{EW}[\text{OII}] < 5\text{\AA}$) in the stacked group. We also create a third category of objects, the *highly star-forming galaxies* with $\text{EW}[\text{OII}] \geq 30\text{\AA}$. By examining the spatial distribution of these types of objects in our 26 groups, we can extract maximal information about the connection between star formation and the local environment of galaxies within each group. Figures 3.7 and 3.8 show the spatial distribution of galaxies in our 26 groups, ordered by their velocity dispersion $\sigma(v)_{\text{intr}}$. Galaxies have been subdivided by star-forming type. Passive galaxies are represented by the open circles; star-forming galaxies by triangles and highly star-forming galaxies by stars. At our high-redshift limit of $z = 0.55$, galaxies brighter than our magnitude limit $R_c = 22$ possess luminosities of $M_{b_j} \lesssim -20$. Therefore group members brighter than this luminosity (*luminous members*) are represented by larger symbols, whilst *faint members* ($M_{b_j} > -20$) are represented by smaller symbols. A limiting radius for our LDSS2 targeting is typically $\sim 240''$ which corresponds to $1h_{75}^{-1}\text{Mpc}$ at the low redshift end of our sample, $z = 0.3$. We represent the $1h_{75}^{-1}\text{Mpc}$ radius centred on the luminosity-weighted centroid of all known members

⁴We note that the shape of the negative side of the 0\AA peak in the $\text{EW}[\text{OII}]$ distribution from the full CNOC2 survey is consistent with a gaussian function, supporting the hypothesis that this peak is dominated by galaxies with no $[\text{OII}]$ emission and normally distributed errors (Whitaker et al., 2004).

in each group, with an overplotted circle. We also compute an iteratively defined centre by throwing out galaxies beyond $1h_{75}^{-1}Mpc$ and recomputing the luminosity-weighted centroid. This is repeated twice, reducing the radial limit to $0.75h_{75}^{-1}Mpc$ and finally to $0.5h_{75}^{-1}Mpc$. A $0.5h_{75}^{-1}Mpc$ radius circle ($\sim r_{200}$ for a $\sigma(v)_{intr} = 500 \text{ km s}^{-1}$ group) centred on this iteratively defined centre is also shown. Finally, it is pertinent to recognise that a small fraction of galaxies in close proximity to the group centre but without redshifts may also be members. Such galaxies which would have luminosities $M_{bj} \leq -20$ should they lie at the group redshift are overplotted as crosses. We call these galaxies *Candidate luminous members*.

As can be seen in figures 3.7 and 3.8, groups come in all shapes and sizes. Judgement about global group properties is reserved for the stacked group which smoothes out the peculiarities of each individual group. This is covered in Section 3.6 and Chapter 5. Some general trends are nonetheless readily apparent in figures 3.7 and 3.8:

- A number of the groups show clumps of either passive or star-forming galaxies. The clumps of passive galaxies would be expected from the star formation - density relation (Balogh et al., 2004a). However, the clumps of star-forming galaxies (seen in for example groups 244, 133, 232) could represent a part of the group system which had not been influenced by the group environment at the redshift of these groups.
- Passive galaxies are not restricted to the most centrally-concentrated, isolated groups and the most massive groups. They are also present in loose and filamentary groups.

3.5.2.1 Trends with group concentration

Figures 3.7 and 3.8 show the wide variety of group structures present in the intermediate-age Universe, from low $\sigma(v)_{intr}$ compact groups (e.g. groups 24 and 28), and more massive groups spanning the gap to poor-clusters (groups 38 and 138) to elongated structures (group 232) and loose groups (e.g. groups 33 and 34). Incompleteness makes the application of any strict quantifiable compactness parameter to the groups difficult. However, for the purpose of studying basic trends in galaxy properties with the overall group structure, we divide the groups into 3 qualitative but readily identifiable categories, hereafter known as the group *class*. These categories are *concentrated* (C), *loose* (L) and *massive* (M). Groups which cannot be classified are labelled *unclassifiable*, (U). The more massive groups 38 and 138 are class M, identifying the more cluster-like environment in these

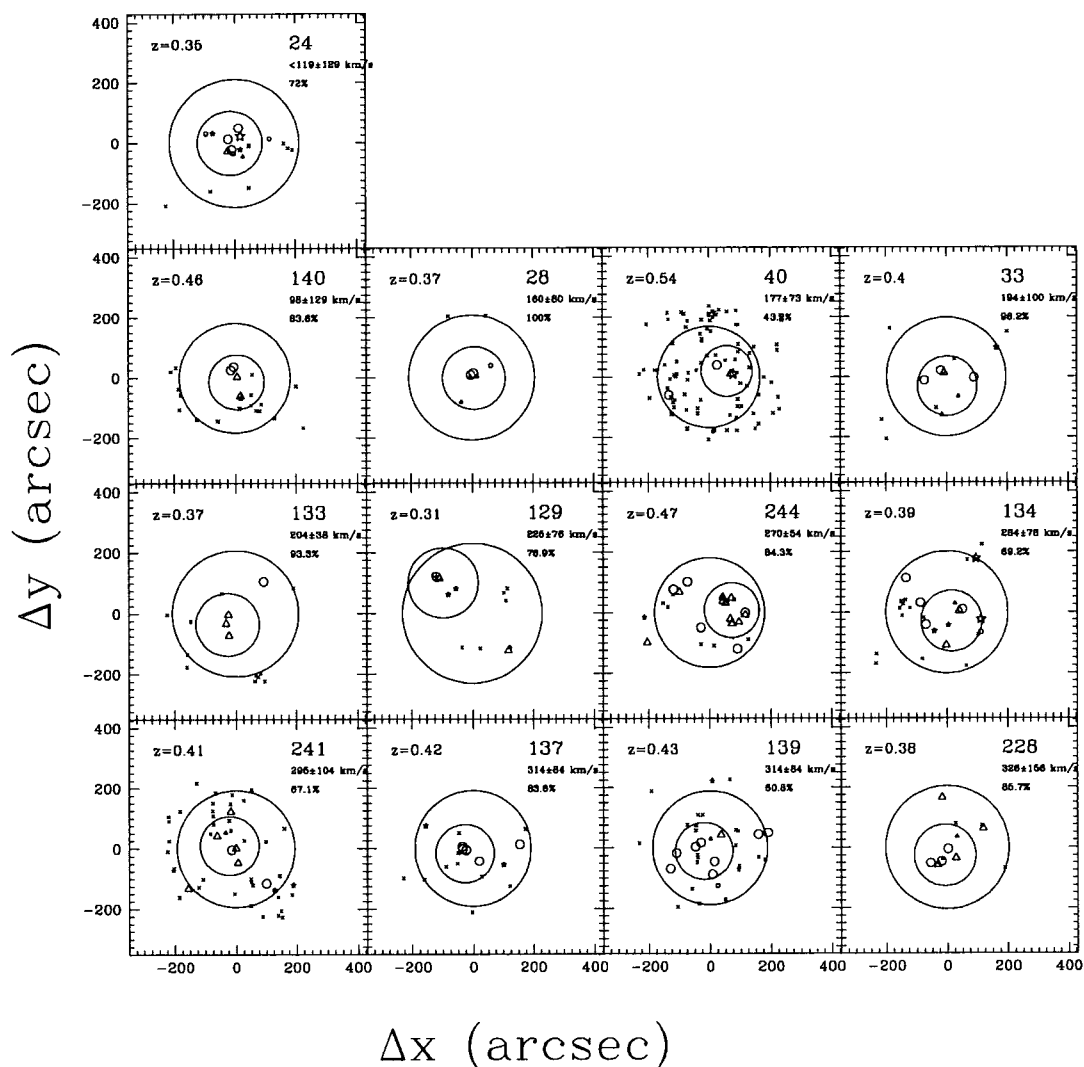


Figure 3.7: The 13 groups with lowest $\sigma(v)_{intr}$. *Passive galaxies, star-forming galaxies* and *highly star-forming galaxies* (defined in the text) are represented by circles, triangles and stars respectively. *Luminous members* are represented by larger symbols than *faint members*. Crosses represent *candidate luminous members*. These are bright galaxies without measured redshifts and whilst in some groups these will be mostly or all foreground / background galaxies, in other groups (preferentially the most massive ones) a significant number may also be group members. The $1h_{75}^{-1} \text{ Mpc}$ radius of each group is also shown centred on the luminosity-weighted centre computed using all known members. We also show a $0.5h_{75}^{-1} \text{ Mpc}$ radius circle, centred on an iteratively defined centre (see Section 3.5.2). With each group, we also display the group redshift, velocity dispersion $\sigma(v)_{intr}$ and completeness within $1h_{75}^{-1} \text{ Mpc}$ and brighter than the R_c -band magnitude required for the galaxy to have a luminosity $M_{bj} \leq -20$ should the galaxy be at the group redshift. Completeness is a function of redshift and the fraction of targeted objects in the group vicinity. Note that groups are ordered by velocity dispersion, $\sigma(v)_{intr}$.

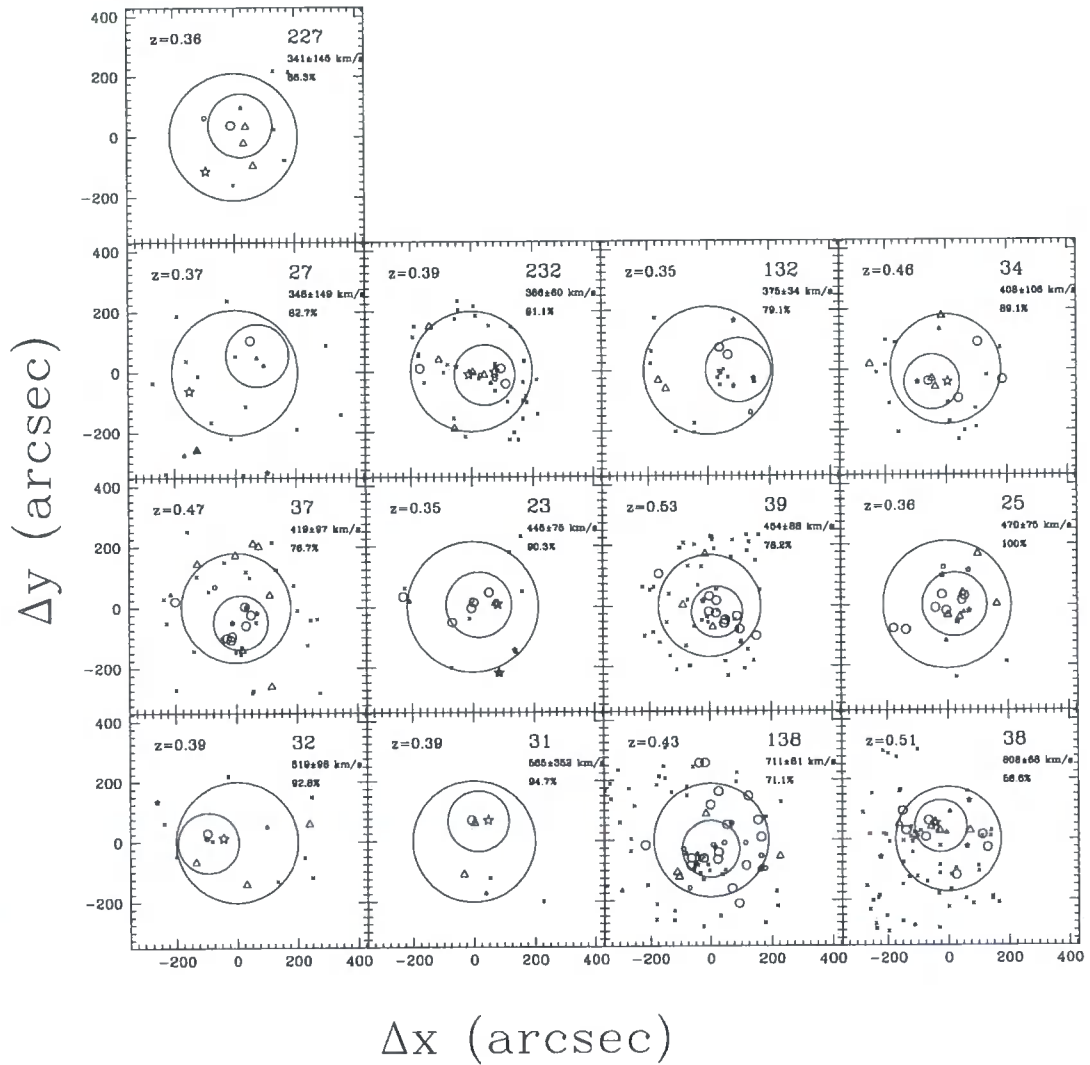


Figure 3.8: As Figure 3.7 for the 13 groups with highest $\sigma(v)_{intr}$.

richer groups. These are selected with velocity dispersion $\sigma(v)_{intr} \geq 600 \text{ km s}^{-1}$ and $N_{mem} \geq 20$. Groups in which galaxies are located in dense clumps (and therefore biased towards higher density in, for example, the morphology-density relation) are classified as class C. More loosely clustered groups are classified as class L and groups 40 and 133 are not classified at all (class U) as each possesses only 4 confirmed members with no structure readily apparent. The class of each group is shown in Table 3.2.

We wish to see how the concentration of group galaxies (i.e. the group structure / state of virialisation) might affect the underlying star-forming properties of the group galaxies.

In Figure 3.9, we show the distributions of EW[OII] in the C-group galaxies (solid histogram) and L-group galaxies (dotted histogram; renormalised to match the number of C-group galaxies). Galaxies are limited to within $0.5h_{75}^{-1} Mpc$ of the iteratively determined group centre (smaller circles in Figures 3.7 and 3.8). In the top panel, galaxies are limited to $M_{b_j} \leq -20.0$ and in the bottom panel we include all group galaxies down to $M_{b_j} \leq -18.5$. The EW[OII] distribution of the L-group galaxy population is well matched to the C-group galaxy population. We ensure that this result is unchanged when the luminosity distributions of the 2 samples are exactly matched, using a *resampling technique*. This involves choosing an L-group galaxy closely matching the luminosity of each C-group galaxy, which results in some L-group galaxies being chosen more than once and others not at all. The dashed histogram in Figure 3.9 represents the resampled L-group galaxy EW[OII] distribution. The resampling process has barely altered the L-group galaxy EW[OII] distribution which is still highly consistent with the C-group galaxy population. Dividing the galaxies once more on their EW[OII] into *passive galaxies* ($EW[OII] < 5\text{\AA}$), *star-forming galaxies* ($5\text{\AA} \leq EW[OII] \leq 30\text{\AA}$) and *highly star-forming galaxies* ($EW[OII] \geq 30\text{\AA}$), we can take the fraction of galaxies in each category directly from Figure 3.9. Table 3.3 shows the fraction of passive galaxies, f_p , and the fraction of highly star-forming galaxies, f_{hsf} , in both the C-group galaxy population, and the L-group galaxy population (raw and resampled) with both luminosity limits applied.

We denote the two luminosity limits applied by appending (1) for $M_{b_j} \leq -20.0$ and (2) for $M_{b_j} \leq -18.5$ to f_p and f_{hsf} . Without resampling (the luminosity functions of C-group and L-group galaxies are not very different), a Kolmogorov-Smirnov test suggests the two populations may be drawn from the same-parent population with a 84% probability ($M_{b_j} \leq -20.0$) or a 96% probability ($M_{b_j} \leq -18.5$), and any indication in Figure 3.9 that we see a slight excess of highly star-forming galaxies in loose groups is not statistically significant.

Table 3.3: The fractions of passive (f_p , $EW[OII] < 5\text{\AA}$) and highly star forming (f_{hsf} , $EW[OII] \geq 30\text{\AA}$) galaxies in C-group galaxies (concentrated into dense clumps), L-group galaxies (looser structure) and resampled L-group galaxies (to match the luminosity distribution of C-group galaxies). Galaxy populations are defined within $0.5h_{75}^{-1}\text{Mpc}$ of the iteratively determined group centre and down to $M_{b_j} = -20.0$ (1) and $M_{b_j} = -18.5$ (2). Statistical errors are computed using the Jackknife technique.

Class	f_p (1)	f_{hsf} (1)	f_p (2)	f_{hsf} (2)
C	$61 \pm 6\%$	$6 \pm 6\%$	$53 \pm 5\%$	$16 \pm 7\%$
L	$51 \pm 9\%$	$11 \pm 5\%$	$39 \pm 7\%$	$18 \pm 4\%$
Resampled L	$55 \pm 6\%$	$12 \pm 6\%$	$42 \pm 5\%$	$20 \pm 5\%$

However the lack of difference between the two classes should not be overinterpreted as the classification is uncertain.

3.5.2.2 Trends with group velocity dispersion

The value of f_p in each group is computed for all known group galaxies within $0.5h_{75}^{-1}\text{Mpc}$ of the iteratively determined group centre and brighter than $M_{b_j} = -20.0$. We also include candidate members in the sample (see Section 3.4.4 for definition). For each candidate member we assign the properties (redshift, $EW[OII]$) of a similar (in $(B - R_C)$ colour and R_C magnitude) galaxy with a measured redshift (a *measured- z galaxy*). This galaxy must also lie in the projected region of the group and a galaxy 0.5mags different in R_C is considered an equally good match to one 0.25mags different in $(B - R_C)$ colour. In this way a high redshift group (where a $M_{b_j} = -20.0$ galaxy has $R_C \sim 22.0$) is evenly sampled in luminosity despite incompleteness at faint magnitudes. Nonetheless, we find that every group f_p is highly consistent with the value computed from known members only. Values of f_p for each group are also shown in Table 3.2. f_p is plotted against group velocity dispersion, $\sigma(v)_{\text{intr}}$ in Figure 3.10. Groups are also keyed on their class. There is no clear trend of f_p with $\sigma(v)_{\text{intr}}$ and the scatter in the individual values is large because of the small number of galaxies in each group. In order to improve the statistics in this plot, we bin the groups in velocity dispersion. The average f_p in each bin shows no systematic evidence for variation with $\sigma(v)_{\text{intr}}$. In general, there is little trend of f_p with group class. Only for systems with $\sigma(v)_{\text{intr}} > 400 \text{ km s}^{-1}$ velocity dispersion is there a suggestion

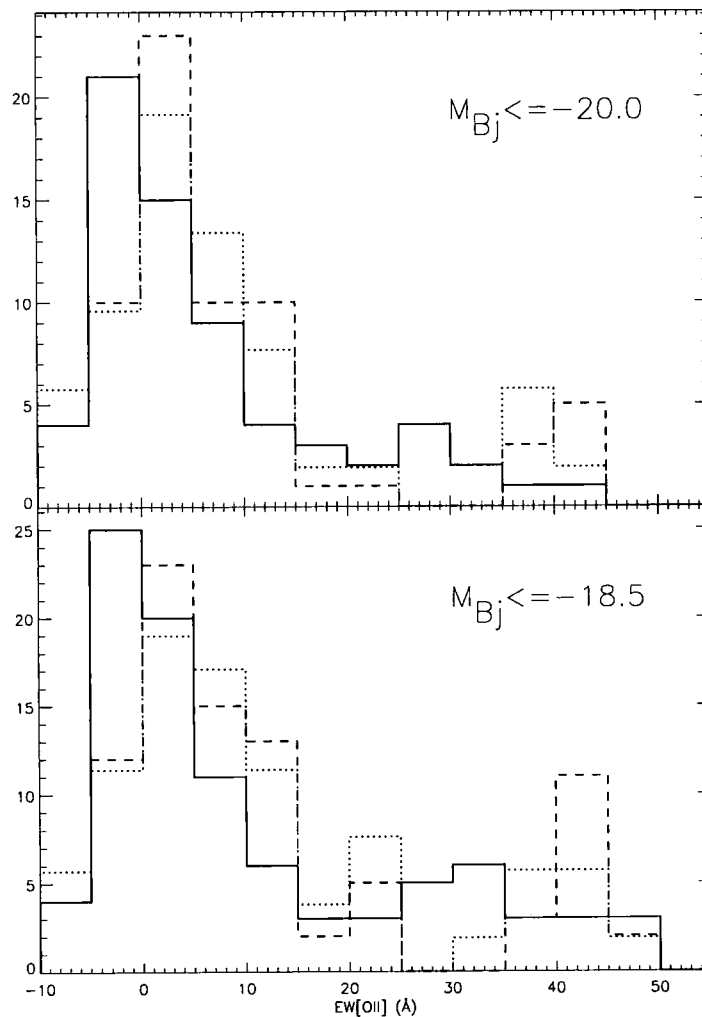


Figure 3.9: **Top:** The distribution of EW[OII] for the C-group galaxies (solid histogram), L-group galaxies (dotted histogram, renormalised to match the number of C-group galaxies) and the L-group galaxies, resampled to match the luminosity distribution of galaxies in the concentrated groups (dashed histogram - method described in text). The sample is limited to galaxies brighter than $M_{b_j} \leq -20.0$ and to within $0.5h_{75}^{-1} Mpc$ of the iteratively determined group centre (smaller circles in Figures 3.7 and 3.8). **Bottom:** The same as above, but incorporating all galaxies down to the fainter limit of $M_{b_j} \leq -18.5$.

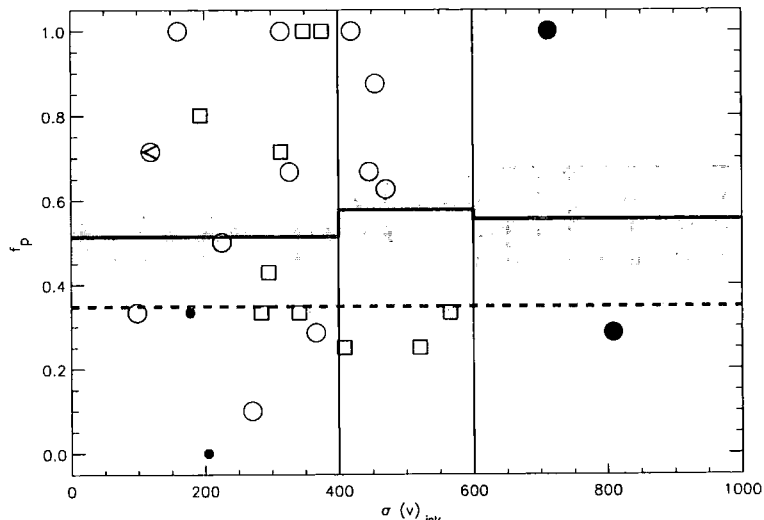


Figure 3.10: The fraction of passive galaxies f_p (brighter than $M_{b_j} \leq -20.0$ and within $0.5h_{75}^{-1}$ Mpc of the iteratively determined group centre), in each group as a function of the group velocity dispersion, $\sigma(v)_{intr}$. The galaxies in each group without redshift measurement (candidate members) are resampled from the measured- z galaxies in the same region of sky, on the basis of their luminosity and $(B - R_c)$ colour. Groups are also keyed on the allocated group-class with open circles to represent concentrated groups, squares to represent loose groups, large filled circles to represent massive groups and small filled circles to represent unclassified groups. The arrow indicates an upper limit on the velocity dispersion of group 28. We also show the value of f_p in combined groups for 3 bins of $\sigma(v)_{intr}$ (solid line) and for the field (dashed line). The shaded area represents the error on these values computed using the Jackknife technique. There is no clear trend of f_p with $\sigma(v)_{intr}$ in groups for galaxies brighter than $M_{b_j} \leq -20.0$.

that the concentrated groups have higher f_p than the loose systems. We note that f_p also shows no correlation with group redshift within the sample.

3.6 The Stacked Group

We have shown that there are no significant differences between groups of different class or velocity dispersion, so we now consider their properties when combined. We co-add the data from our 26 groups to form a stacked group. We then possess the statistical tools necessary to investigate the global properties of group galaxies and to make a comparison with the field at intermediate redshift ($0.3 \leq z \leq 0.55$). The stacked group sample contains a total of 282 galaxies above our magnitude limit of $R_C = 22.0$. Each galaxy is

weighted by a combined selection weight W_C to correct for the stacked group selection functions. These are well understood and are discussed in detail in Section 3.6.1. However, we only trust the weights when applied to a large sample as incompleteness varies from group to group. Whilst the application of this weight is strictly correct, we find the results from Section 3.6.4 are consistent with and without the galaxy weightings.

We also define a field sample to contrast with our stacked group sample. Field galaxies are defined to include all galaxies *not in the Carlberg et al. (2001b) group sample*, with $0.3 \leq z \leq 0.55$ and within $240''$ of the targeted group centre (where the radial selection function is understood). The field sample contains a total of 334 galaxies above our magnitude limit of $R_C = 22.0$.

3.6.1 Completeness in the stacked group

Despite the greater depth and spectroscopic completeness achieved in the region of the groups with our Magellan targeting, it was still necessary to adopt a sparse sampling strategy due to the high density of targets, especially close to our new magnitude limit of $R_c = 22$. In this section, we investigate the selection functions for the spectroscopic sample, seeking a representative means of stacking the data. The CNOC2 photometric catalogue is complete to $R_c \sim 23$ and so the probability that we possess a redshift of any galaxy brighter than this limit can be easily understood. In Section 3.6.2 we assume that our Magellan data reach sufficient depth to be unbiased at magnitudes $R_c \leq 22$. We then describe a simple weighting scheme which accounts for targeting bias in both CNOC2 and Magellan spectroscopic samples. This scheme differentiates between galaxies with redshifts from each source which have different selection functions. In Section 3.6.3 we test our assumption of unbiased redshift completeness in the Magellan data and show that this assumption holds within the limits of tests using current data.

3.6.2 Selection Functions

To understand the selection functions for the spectroscopic sample, it must first be split into its component CNOC2 and Magellan subsets as selection depends critically on the observing strategies and facilities used. Target selection in the CNOC2 spectroscopic survey was primarily dependent upon apparent R_c -band magnitude. However, below the nominal spectroscopic limit of $R_c = 21.5$ in that survey, galaxies with redshifts become biased towards strong EW[OII] with respect to those obtained using Magellan. In contrast target selection with Magellan is dependent upon both magnitude and angular distance

from the targeted group centre. However there appears to be no strong bias towards emission redshifts brighter than our magnitude limit of $R_c = 22$ (see Section 3.6.3). Therefore we can implement a simple weighting scheme which simulates a 100% complete survey and removes targeting bias and CNOC2 redshift incompleteness bias simultaneously:

The weighting scheme requires a radial selection function and a magnitude-dependent selection function. For each galaxy in the spectroscopic sample, a radial weight W_{rad} and a magnitude-dependent weight, W_{mag} , are computed in such a way that the total weight of all galaxies with redshifts (*measured-z galaxies*) $\Sigma_1^{N_{spec}}(W_{rad} \cdot W_{mag}) = N_{phot}$, the total number of galaxies in the photometric sample brighter than $R_c = 22$. We denote galaxies with redshifts from the original CNOC2 survey with the suffix (C_z) and those with Magellan LDSS2 redshifts with the suffix (L_z).

We begin by looking at the radial selection function, S_{rad} . The fraction of galaxies with CNOC2 redshifts shows no significant dependence upon angular distance from the centre of the nearest group and so we choose $W_{rad}(C_z) = 1$ for all these galaxies. However, there is a strong dependence on angular radius for the fraction of Magellan redshifts (or Magellan targets). In Figure 3.11, the fraction of galaxies in the CNOC2 photometric catalogue ($R_c \leq 22$) targeted by Magellan, $S_{rad}(L_{obs})$ (triangles), where redshifts were obtained, $S_{rad}(L_z)$ (filled circles) and including the fraction with CNOC2 redshifts, $S_{rad}(L_z) + S_{rad}(C_z)$ (diamonds) is shown as a function of angular radius. Most untargeted galaxies lie in the magnitude range $21.5 \leq R_c \leq 22$. We apply a final cut to stacked data at $240''$ which is the approximate limiting radius for LDSS2 targeting. This corresponds to $1h_{75}^{-1} Mpc$ at the low redshift end of our sample, $z = 0.3$. The linear spline through the filled circles ($S_{rad}(L_z)$) represents the radial selection function $S_{rad}(L_z)$ from which the value of S_{rad} is linearly interpolated for any galaxy targeted with Magellan. For these galaxies, the radial weight is then simply computed to be $W_{rad}(L_z) = S_0(L_z)/S_{rad}(L_z)$, normalised so that galaxies located at the group centre receive a weighting $W_{rad} = 1$. We note that a galaxy at $240''$ receives a weighting of $W_{rad} \sim 4.47$.

In Figure 3.12, we show the magnitude-dependent selection function. Galaxies are limited to within $240''$ and galaxies with redshifts are weighted by W_{rad} . As in Figure 3.11, we plot the fraction of galaxies with Magellan redshifts, $S_{mag}(L_z)$ (filled circles) and the fraction with Magellan or CNOC2 redshifts, $S_{mag}(L_z) + S_{mag}(C_z)$ (diamonds). W_{mag} must weight the galaxies such that $\Sigma_1^{N_{spec}}(W_{rad} \cdot W_{mag}) = N_{phot}$ in each magnitude bin and the combined weight of all galaxies must accurately emulate the properties of the entire galaxy population. In each bin of magnitude we normalise the total *weighted* frac-

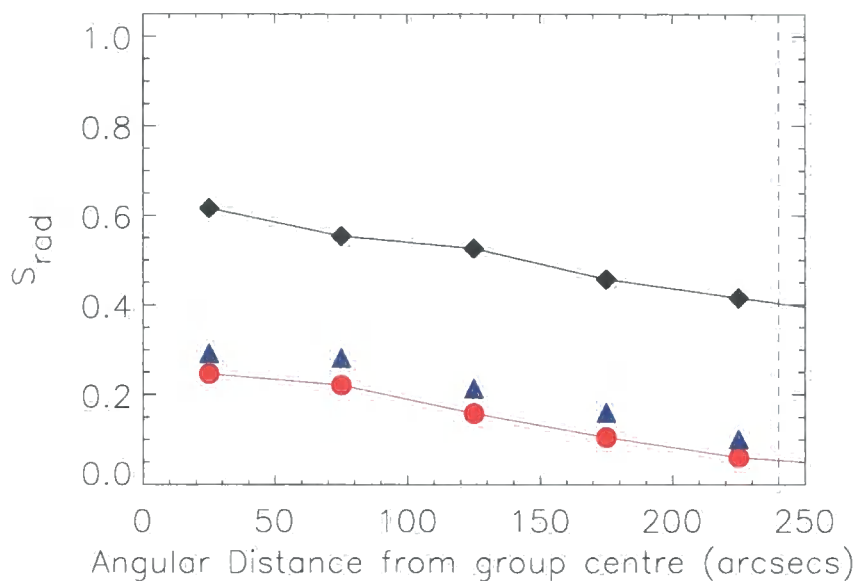


Figure 3.11: Radial selection function of the stacked data as a function of angular distance from the target group centre. Filled circles represent the fraction of galaxies with Magellan redshifts ($S_{rad}(L_z)$); triangles represent the fraction of galaxies targeted by Magellan ($S_{rad}(L_{obs})$) and diamonds represent galaxies with CNOC2 or Magellan redshifts ($S_{rad}(L_z) + S_{rad}(C_z)$). Only galaxies within $240''$ and with $R_C \leq 22.0$ are considered in our analysis.

tion of CNOC2 redshifts to be equal to the fraction of CNOC2 redshifts in the *unweighted* sample, $S_{mag}(C_z)$. We know that in the entire population, that fraction at least will have the properties of CNOC2 spectroscopic galaxies, regardless of CNOC2 redshift incompleteness. Magellan targets come from the remaining galaxies without CNOC2 redshifts (ignoring a tiny comparison sample) and these have properties typical of that population at any given magnitude (based upon our assumption of unbiased redshift completeness in the Magellan data - see Section 3.6.3). Therefore the remainder of the combined weight required to match the total number of galaxies in any magnitude bin (N_{phot}) is spread amongst the galaxies with Magellan redshifts. Thus W_{mag} is computed independently for galaxies with CNOC2 redshifts and Magellan redshifts using equations 3.8 and 3.9 (which simplify to equations 3.10 and 3.11). We note that each quantity is computed *at a given R_c -band magnitude* (or across each magnitude bin).

$$W_{mag}(C_z) = 1 + \frac{[N_{phot} - N_{C_z} - \Sigma(W_{rad}(L_z))]}{N_{phot}} \quad (3.8)$$

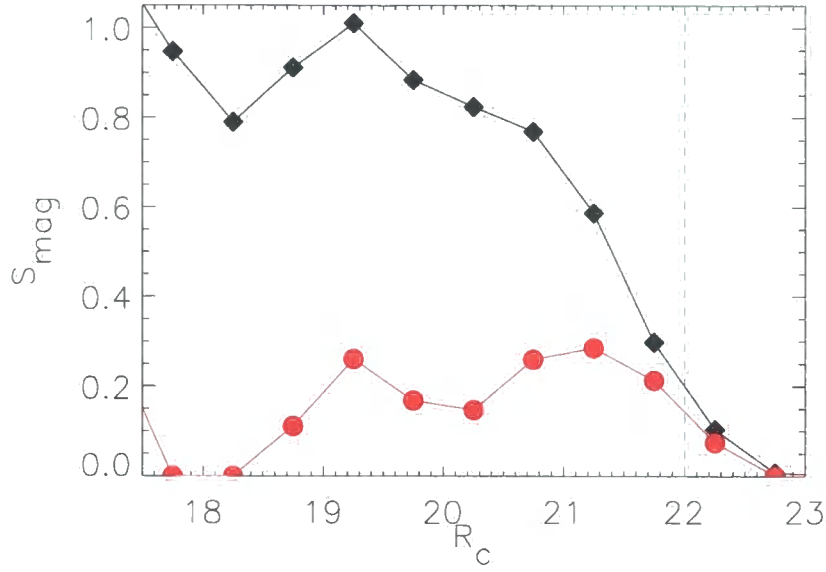


Figure 3.12: Selection functions of the stacked group sample as a function of R_c -band magnitude. Filled circles represent the fraction of galaxies with Magellan redshifts, weighted by $W_{rad}(S_{mag}(L_z))$ and diamonds represent galaxies with CNOC2 or Magellan redshifts ($S_{mag}(L_z) + S_{mag}(C_z)$). Only galaxies brighter than $R_c = 22$ are considered in our analysis.

$W_{mag}(L_z) = 1 + \alpha$ where

$$\alpha = \frac{[N_{phot} - N_{C_z} - \Sigma(W_{rad}(L_z))]}{N_{phot}} \times \frac{N_{phot} - N_{C_z}}{\Sigma(W_{rad}(L_z))} \quad (3.9)$$

In terms of $S_{mag}(C_z)$ and $S_{mag}(L_z)$ these become:

$$W_{mag}(C_z) = 1 + [1 - S_{mag}(C_z) - S_{mag}(L_z)] \quad (3.10)$$

and α in equation 3.9 becomes:

$$\alpha = [1 - S_{mag}(C_z) - S_{mag}(L_z)] \times \frac{1 - S_{mag}(C_z)}{S_{mag}(L_z)} \quad (3.11)$$

where $S_{mag}(C_z)$ and $S_{mag}(L_z)$ is computed by linear interpolation through the points in Figure 3.12. The combined weight for each galaxy is computed using equation 3.12.

$$W_C = W_{rad} \times W_{mag} \quad (3.12)$$

We note from Figure 3.12 that in the magnitude bin at $21.5 \leq R_c \leq 22$ the fraction of galaxies with redshifts is down to $\sim 30\%$. However, it is at magnitudes below $R_c = 21$ that

the Magellan data comes to dominate the statistics and the greater depth of the larger telescope allows us to achieve unbiased and highly successful redshift determination down to $R_c = 22$. This fainter galaxy population is expected to be more star-forming than the brighter population in the local Universe (e.g. Brinchmann et al., 2004). Therefore by reaching this depth, we can begin to probe the evolution of group galaxy properties significantly below L_* , to reach this interesting population of mainly star-forming galaxies at intermediate redshift.

3.6.3 Magellan Redshift Completeness

To investigate redshift incompleteness in the galaxies targeted with Magellan, we examine the distribution of targeted galaxies in colour-magnitude ($(B - R_c), R_c$) space (Figure 3.13). If there were a bias associated with preferentially losing absorption-line (early-type) galaxies, then one would expect those galaxies for which we could not measure redshifts to be clustered mainly towards the red end of the colour range. In Figure 3.13 we compare the colour and magnitude distributions of objects for which we could not measure redshifts (bottom panel - hereafter referred to as *lost* objects) with those for which we have emission redshifts (top panel) and absorption redshifts (centre panel). We restrict this analysis to fainter than $R_c = 19.5$ where not all targets are successful. Open symbols represent objects with redshifts outside our range of interest, $0.3 \leq z \leq 0.55$ or below the luminosity range considered in the analysis, $M_{b_j} \geq -18.5$. Lost objects are not concentrated in the red ($B - R_c \gtrsim 2.0$), absorption redshift dominated region, as might be expected if we were preferentially losing absorption line (\sim early-type) galaxies. Indeed, the lost galaxies are spread quite evenly across the full colour range, suggesting no colour bias due to redshift-incompleteness (and thus no bias in star-forming properties). Nonetheless, we are cautious in evaluating any such bias as it will impact directly upon our results. Therefore we perform two further checks.

The first check involves making a detailed analysis of the lost objects. We begin by making a manual examination of the spectra for the 19 lost objects with magnitudes $R_c \leq 21$. Six of these objects are stars misclassified as galaxies and are removed from the catalogue. A further 10 of the objects have noisy, low signal spectra, which could represent Low Surface Brightness (LSB) galaxies or astrometric offsets from the brightest galaxy regions. Most of these objects have extended morphology, as assessed from the CNOC2 imaging. We also characterise the objects by measuring the signal in a significant part of the spectrum. We measure the combined signal (total counts, *cts*) from the wavelength

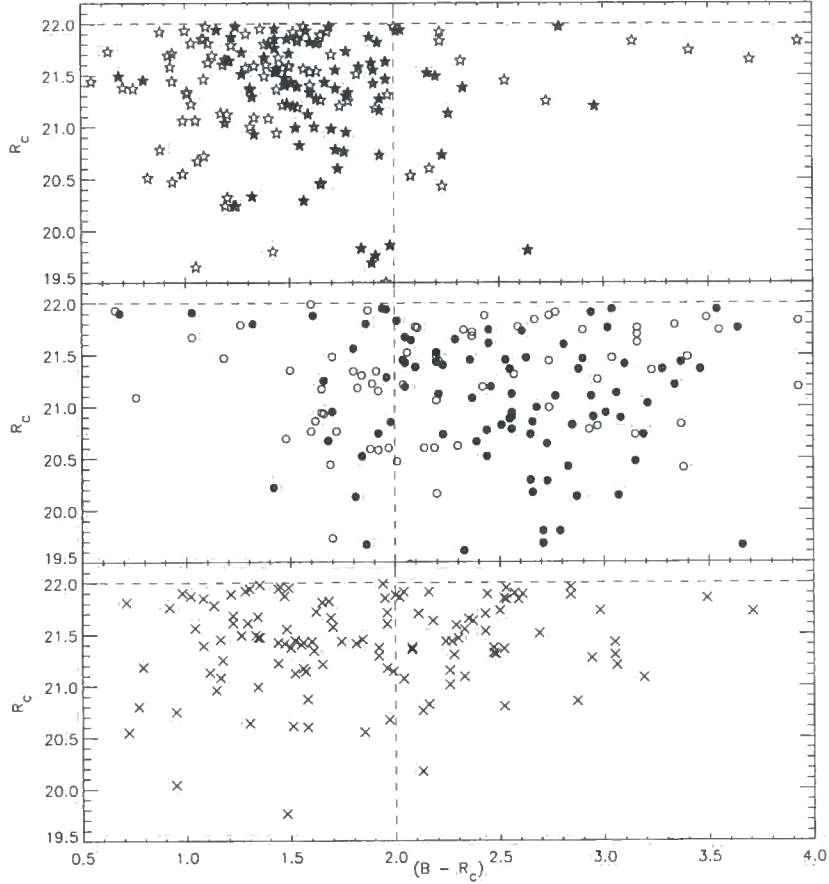


Figure 3.13: $B - R_c$ colour vs R_c magnitude for $R_c \leq 22$ objects targeted with Magellan. The top panel (stars) and middle panel (circles) show the positions of the 187 emission redshift objects and 196 absorption redshift objects in this plane respectively. Filled symbols represent objects which make the redshift and luminosity cuts for our analysis ($\sim 50\%$ of all objects in the range $0.3 \leq z \leq 0.55$; $M_{b_j} \geq -18.5$). The bottom panel locates in the colour-magnitude plane the 124 objects targeted with Magellan which failed to yield redshifts. The magnitude limit ($R_c = 22$) and a rough division in colour at $B - R_c = 2.0$ are also shown (dotted lines).

ranges $5300\text{\AA} - 5530\text{\AA}$ and $5645\text{\AA} - 5820\text{\AA}$ which spans the most efficient region of the grism, eliminating the strong night sky lines. From 13 lost objects with $cts \geq 3 \times 10^4$, there are 8 stars, 1 quasar, 1 BL Lac, 1 LSB galaxy, 1 highly noisy spectrum and 1 unclassifiable object. In the low signal range, most objects with $cts \leq 10^4$ are lost, although there are also some relatively low signal to noise galaxies with clear absorption redshifts. Finally, lost objects in the intermediate $10^4 \leq cts \leq 3 \times 10^4$ range tend to have noisy spectra, often lacking emission lines. However, *all* blue galaxies ($B - R_c \lesssim 2.0$) with redshifts in this region possess emission lines and so it seems possible that the blue lost objects in this region lie at low redshift where [OII] falls out of the spectral window. Alternatively, it is possible that those galaxies without redshifts do not for some reason possess emission lines despite their blue colours. However, red ($B - R_c \gtrsim 2.0$) lost objects with this signal range simply appear noisier and with less obvious absorption features than their counterparts with redshifts.

The second check involves computing a redshift incompleteness weight, W_{NoZ} , which is computed by distributing the weight of the lost object across its 5 nearest neighbours with redshifts in colour ($B - R_c$) - magnitude (R_c) space. Nearest neighbours are computed by equating 1 magnitude in R_c to 0.5 magnitudes in colour. Then the combined weight of each galaxy is computed to be $W = W_{rad} \times W_{mag} \times W_{NoZ}$. We note that Wilson et al. (2002) have performed a similar correction to compensate for galaxies in their sample for which they could not obtain redshifts. In Figure 3.14 we show the fraction of passive galaxies in the sample f_p (at $0.3 \leq z \leq 0.55$) as a function of apparent magnitude R_c without applying this additional weight W_{NoZ} (solid line) with statistical errors computed using the Jackknife method. We show how this uncorrected version changes when we apply the redshift incompleteness weight (W_{NoZ}) to all galaxies (dashed line) and when we apply it to red galaxies only ($B - R_c \geq 2.0$, dotted line). The latter correction assumes that all lost blue galaxies lie outside our redshift range whilst lost red galaxies are lost simply due to low signal-to-noise spectra. This is the most biased scenario we can imagine, yet even in the faintest bin, the difference made to f_p is comparable with the statistical error. Therefore we consider the LDSS2 redshift incompleteness to be unbiased at $R_C \leq 22.0$, to the best of our knowledge.

3.6.4 The properties of stacked group galaxies

In this section we investigate how galaxy properties in the stacked group differ from the field population.

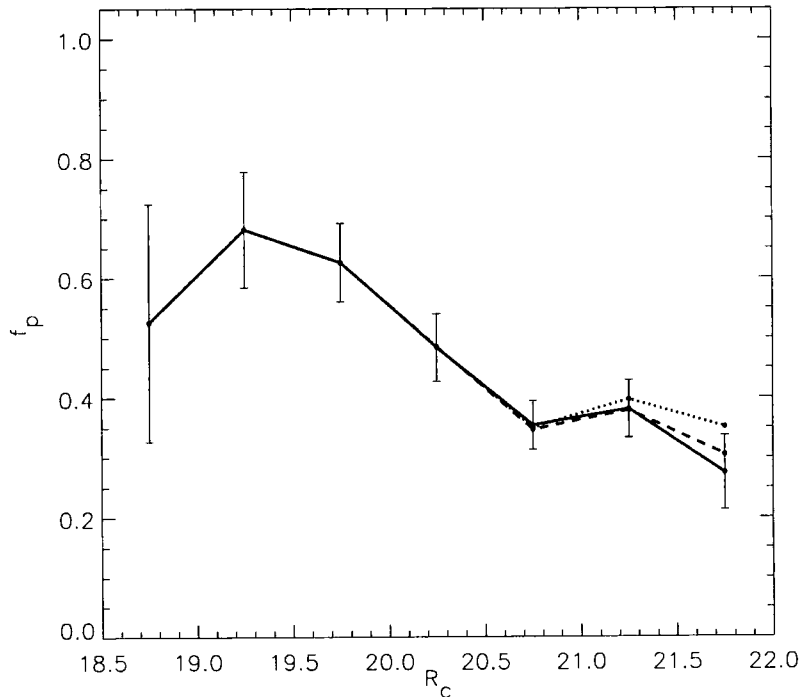


Figure 3.14: The fraction of passive galaxies, f_p , as a function of apparent magnitude for all galaxies in the range $0.3 \leq z \leq 0.55$. Galaxies are weighted by W_C to account for selection bias. The solid line does not make any correction to account for bias in Magellan redshift incompleteness. Jackknife errors are computed in this case. The dashed line represents the case where galaxies with Magellan redshifts have also been weighted by an additional weight W_{NoZ} , effectively resampling Magellan *lost* galaxies (no redshifts) in colour-magnitude space. The dotted line case applies this additional weight only to red ($B - R_c \geq 2$) galaxies.

3.6.4.1 The fraction of passive galaxies in the stacked group

In Figure 3.15 we show how the fraction of passive galaxies, f_p , depends upon galaxy b_J -band luminosity in the stacked group and in the field. This should be distinguished from f_p computed for each individual group in Section 3.5 and Figure 3.10. In the top panel of Figure 3.15, we limit the group sample to galaxies within $0.5h_{75}^{-1} Mpc$ of the iteratively determined group centre (corresponding to r_{200} for $\sigma(v)_{intr} \sim 500 \text{ km s}^{-1}$ groups). There is a clear enhancement of f_p in the group galaxies with respect to the field, especially in the luminosity range $-22.0 \leq M_{b_J} \leq -19.0$. In the lower panel, we include all galaxies within $1h_{75}^{-1} Mpc$ of the original centroid computed in Section 3.4.4 (the luminosity-weighted centre of *all* confirmed group members). There is no significant change in f_p as a function of luminosity when the radial constraint is loosened apart from an improvement in the sample statistics. Combining all galaxies within the luminosity range $-22.5 \leq M_{b_J} \leq -18.5$, the enhancement in groups of f_p is of better than 3σ significance and this trend is still evident if the massive groups 38 and 138 are excluded from the sample. However we note that brighter than $M_{b_J} = -21.0$ the value of f_p is only enhanced in groups of higher velocity dispersion ($\sigma(v)_{intr} \gtrsim 400 \text{ km s}^{-1}$). During the remainder of our analysis we limit the galaxy sample to those within $1h_{75}^{-1} Mpc$ from the luminosity-weighted centre of all confirmed group members.

In the top panel of Figure 3.16, we plot f_p as a function of group-centric radius ($\delta(r)$) for all group galaxies brighter than $M_{b_J} = -18.5$. We have used a physical distance scale since virial radii in groups are uncertain due to the low number of galaxies and often irregular group morphologies. The horizontal solid line and dashed lines represent the field f_p and $\pm 1\sigma$ uncertainties respectively. There is a weak trend of f_p with group-centric radius ($\delta(r)$) and a significant enhancement over the field is seen out to $1.0h_{75}^{-1} Mpc$. The lack of strong trend is unsurprising: the groups are not relaxed, spherical systems and often have multiple concentrations within the fiducial $1.0h_{75}^{-1} Mpc$ radius (see Figures 3.7 and 3.8). To see if any trend becomes more obvious when the group is centred on the BGG (Brightest Group Galaxy, chosen from within $1h_{75}^{-1} Mpc$ of the luminosity-weighted group centre), we recalculate the radial trend placing the group centre on the BGG. This enhances f_p in the innermost bin, but does not otherwise strengthen the radial gradient. In Figure 3.17 we show the dependence of f_p on the distance to the nearest confirmed group galaxy. This measure of density has the advantage that it can be applied to systems with few members and irregular spatial distribution. In this plot, f_p is significantly reduced

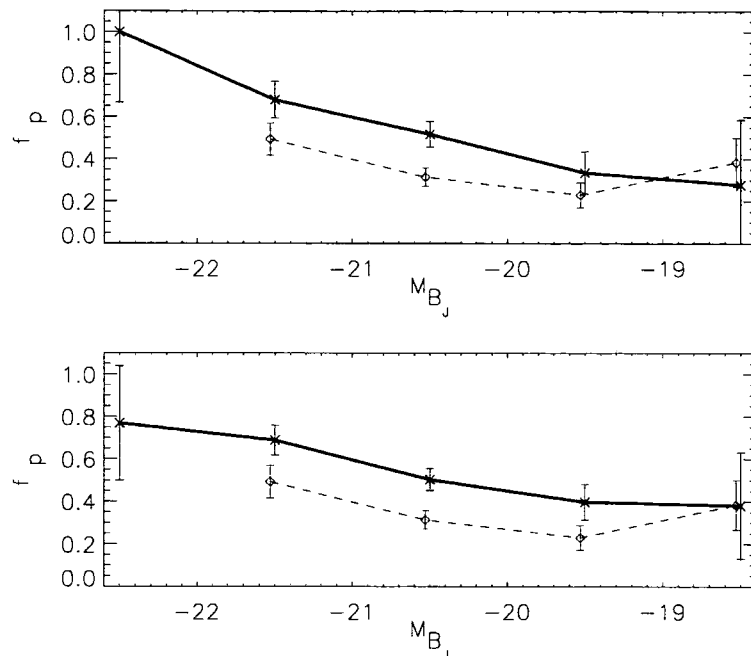


Figure 3.15: **Top:** The fraction of passive galaxies, f_p , in the stacked group within $0.5h_{75}^{-1} \text{ Mpc}$ of the iteratively determined group centre (solid line) and the field (dashed line) as a function of galaxy luminosity, M_{b_j} . The field symbols are offset slightly in luminosity for clarity. Statistical errors on f_p are computed using a Jackknife method. **Bottom:** The same as above, except including all galaxies within $1h_{75}^{-1} \text{ Mpc}$ of the original centroid computed in Section 3.4.4 (the luminosity-weighted centre of all confirmed group members).

at large separations, indicating that the high passive fraction seen in Figure 3.17 at large $\delta(r)$ is related to the clumpy distribution of group galaxies. We note, however, that there is no dependence on separation less than $\sim 0.4h_{75}^{-1} \text{ Mpc}$.

3.6.4.2 Environmental dependencies in the luminosity function of galaxies

In Figure 3.18 we show how the luminosity function of the stacked group (solid histogram) compares with that of the field (dashed histogram) over the same redshift range ($0.3 \leq z \leq 0.55$). For a full discussion of evolution in the CNOC2 field luminosity function, see Lin et al. (1999); here we concentrate on the comparison with the groups. The field luminosity function has been scaled to match the number of galaxies seen in the group luminosity function over the range $-21.0 \leq M_{b_j} \leq -20.0$. The vertical line represents the luminosity limit of galaxies where $R_c = 22.0$ at $z = 0.55$ ($M_{b_j} = -19.75$), our high

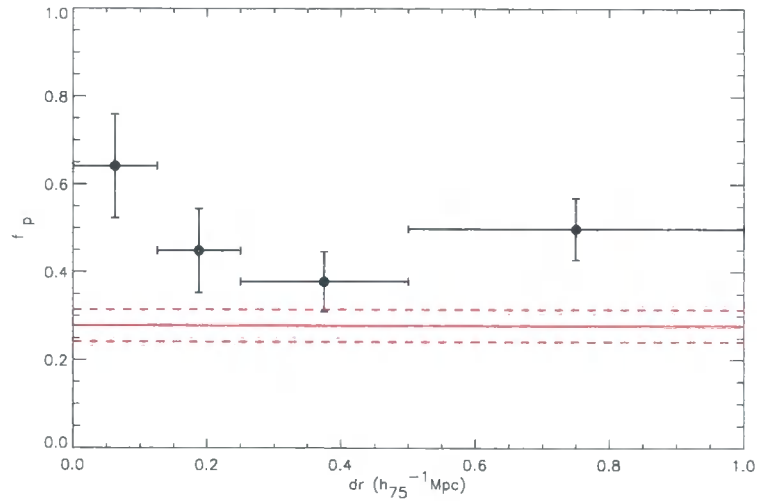


Figure 3.16: f_p ($M_{b_j} \leq -18.5$) in the stacked group as a function of physical distance from the group centre where the group centre is defined to be the luminosity-weighted centre of all confirmed group members. The horizontal solid line and dashed lines represent the field f_p and $\pm 1\sigma$ uncertainties respectively (The luminosity limit is deeper than in Figure 3.10 and so f_p is reduced). All errors on f_p are computed using the Jackknife method.

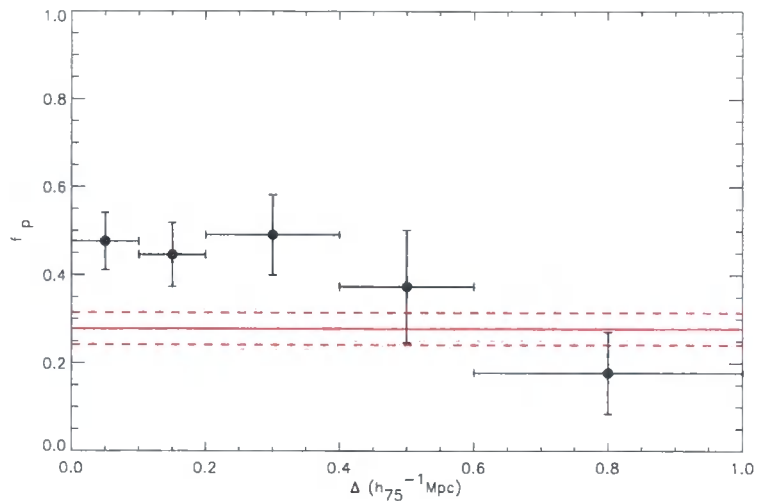


Figure 3.17: f_p ($M_{b_j} \leq -18.5$) in the stacked group as a function of the projected distance to the nearest neighbour (Δh_{75}^{-1} Mpc). The horizontal solid line and dashed lines represent the field f_p and $\pm 1\sigma$ uncertainties respectively. All errors on f_p are computed using the Jackknife method. We find a correlation between f_p and Δ where group galaxies located in more overdense regions ($\Delta \lesssim 0.4 h_{75}^{-1}$ Mpc) have an enhanced likelihood of being passive.

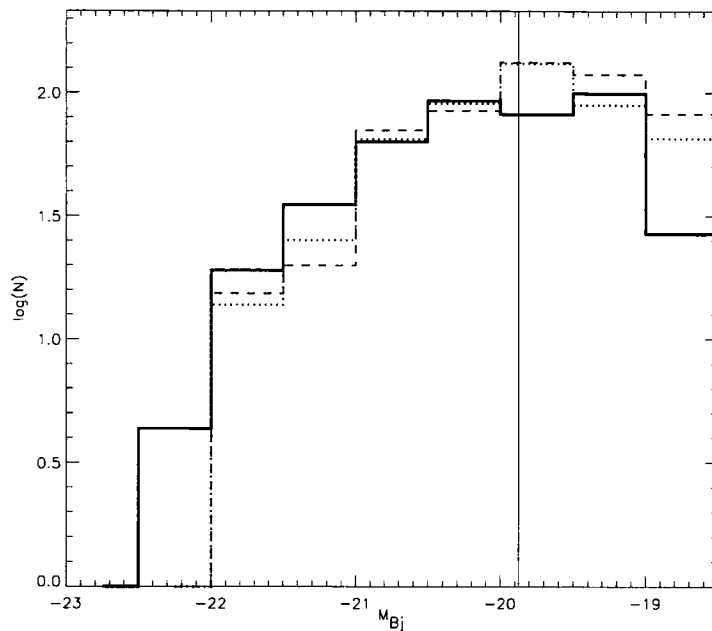


Figure 3.18: The luminosity functions for group (solid line), field (dotted line) and redshift-weighted field (dashed line) galaxies weighted by selection, W_C and within our redshift range ($0.3 \leq z \leq 0.55$). The vertical line represents the approximate luminosity limit of the sample at the redshift limit $z = 0.55$.

redshift limit, for galaxies with mean K-corrections. At the low redshift limit $z = 0.3$ the corresponding luminosity limit is $M_{b_j} = -17.93$. For the galaxies with the largest K-corrections, these limits become $M_{b_j} = -18.06$ at $z = 0.3$ and $M_{b_j} = -20.07$ at $z = 0.55$. Figure 3.18 suggests that there may be a slight excess of bright ($M_{b_j} \leq -21.0$) galaxies in the groups with respect to the field.

A concern with this comparison is that the field galaxies have a different redshift distribution from the group galaxies. This is a particular concern at the faint end of the luminosity function where the selection effect has the greatest impact. In order to see if this can account for the difference between the field and group luminosity functions, we apply an additional weighting to the field galaxies to match the redshift distribution of the group galaxies. The luminosity functions of the redshift-weighted field is shown as a dashed line in Figure 3.18. Within our luminosity range the field luminosity function remains relatively unaltered by the redshift weighting. The comparison with the group luminosity function is qualitatively unchanged.

Figure 3.18 suggests that there is an excess of bright galaxies and a deficit of faint galaxies in the groups compared to the field. To investigate the statistical significance

of this apparent excess of bright galaxies in groups, we split the luminosity functions into three bins of luminosity: bright ($M_{b_j} \leq -21.0$), control ($-21.0 \leq M_{b_j} \leq -20.0$; which encompasses the local value of $M_* \sim -20.3$ from Norberg et al. 2002, corrected to $H_0 = 75 \text{ km s}^{-1} \text{ Mpc}^{-1}$) and faint ($-20.0 \leq M_{b_j} \leq -18.5$). We prefer this approach over fitting a Schechter function to the luminosity function, since it avoids degeneracy between the cut-off parameter, M_* , and the faint-end slope parameter, α . We define two new indices to measure the relative abundances of galaxies in each of these luminosity bins. The bright-to-faint galaxy ratio, $R_{(B/F)}$, is defined as the logarithm of the ratio of galaxies in the bright bin to that in the faint bin. The bright-to-control galaxy ratio, $R_{(B/C)}$ is similarly the logarithm of the ratio of galaxies in the bright bin to that in the control bin. The values of $R_{(B/C)}$ and $R_{(B/F)}$ in the field are shown in Table 3.4. $R_{(B/C)}$ only utilises data for which galaxies are brighter than the magnitude limit at all redshifts, while $R_{(B/F)}$ spans a wider range of luminosity (and thus has more leverage to measure changes in the luminosity function) but requires us to correct by the redshift weighting (ie., to compare with the dashed line in Fig. 3.18. We estimate the significance of the difference in the field and group ratios by bootstrap resampling two mock samples using the field data-set alone, and comparing the difference between the two resampled values. This indicates the likelihood that the observed difference between the group and the field occurs by random sampling from the same underlying distribution.

A comparison between the group and field luminosity functions can now be made by computing $R_{(B/C)}$ and $R_{(B/F)}$. The result of this process is summarised in Table 3.5. We compute values of $R_{(B/C)} = -0.425$ for the group galaxy population and $R_{(B/C)} = -0.600$ for the field galaxy populations, indicating a larger fraction of bright galaxies in the groups. We compute a difference between the group and field of $\Delta R_{B/C} = +0.175$; however, this result has low significance. The computed significance level for the difference $\Delta R_{B/C}$ is $S_{B/C} = 85.6\%$ (there is a $\sim 15\%$ chance that the luminosity functions are the same). For BF we find $R_{(B/F)} = -0.551$ in the group galaxy population and $R_{(B/F)} = -0.976$ in the redshift-weighted field population, again indicating a much larger ratio of bright to faint galaxies in the groups than in the field ($\Delta R_{B/F} = +0.425$). In this case, the difference has much higher statistical significance, $S_{B/F} = 99\%$ (we can be 99% confident that the difference is real).

Table 3.5 also explores whether the field and group luminosity functions are significantly different for passive and actively star-forming types, and whether they differ as a

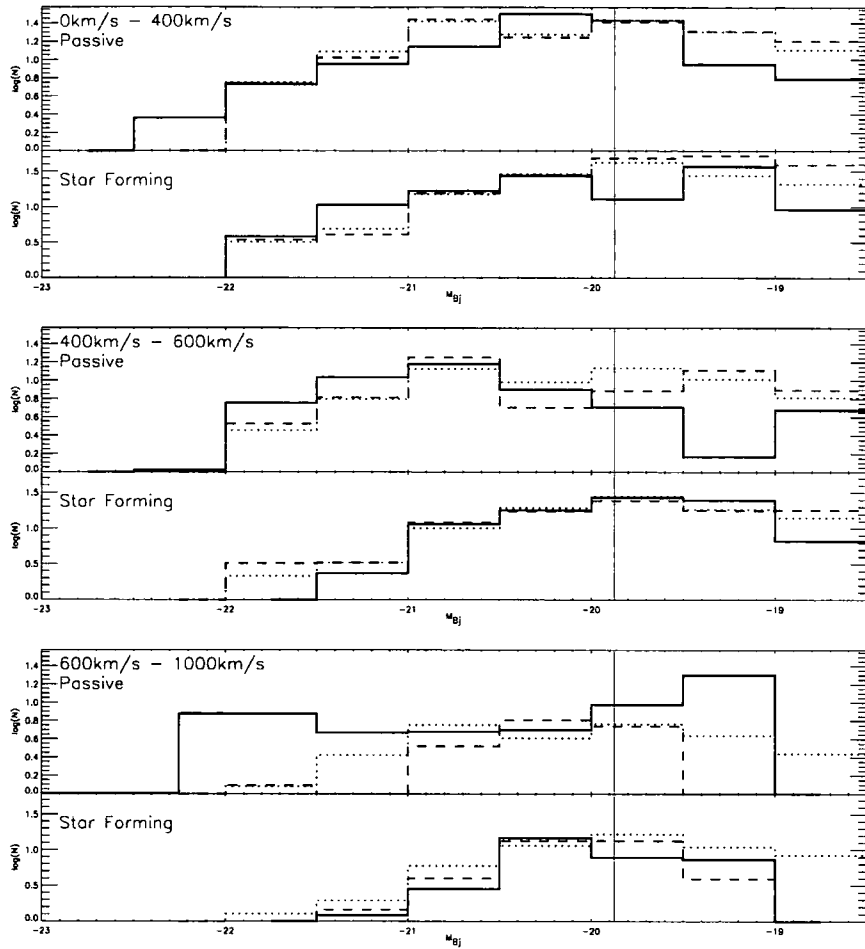


Figure 3.19: As Figure 3.18 but with group galaxies split into 3 bins of velocity dispersion, $\sigma(v)_{intr}$ going from low $\sigma(v)_{intr}$ (**top 2 panels**) to high $\sigma(v)_{intr}$ (**bottom 2 panels**); and with star-forming and passive galaxies shown separately in the upper and lower panels of each plot.

function of group velocity dispersion. Within the uncertainty of the small sample size, the difference in $R_{(B/F)}$ appears to be evident in both the star-forming and passive populations. While the excess of the brightest passive galaxies appears to be most prevalent in the groups with highest velocity dispersion, the depression in the faint galaxy population is most evident in the lower velocity dispersion groups. Only in low velocity dispersion groups is a population of bright star-forming galaxies still common. These trends are shown graphically in Fig. 3.19.

Table 3.4: **Field Luminosity Function Properties:** The Bright to Control ($R_{(B/C)}$) and Bright to Faint ($R_{(B/F)}$) ratios of the galaxy populations in the CNOC2 field:

$R_{(B/C)}$			$R_{(B/F)}$		
All	Passive	Star-Forming	All	Passive	Star-Forming
-0.600	-0.401	-0.733	-0.865	-0.525	-1.049

Table 3.5: **Group Luminosity Function properties:** The Bright to Control ($R_{(B/C)}$) and Bright to Faint ($R_{(B/F)}$) ratios of the passive and star-forming galaxy populations in the CNOC2 groups and the redshift-weighted field ($R_{(B/F)_{wf}}$) and the enhancement of $R_{(B/C)}$ or $R_{(B/F)}$ in the groups relative to the field with associated error ($\Delta R_{B/C} \pm \sigma(R_{(B/C)})$, $\Delta R_{B/F} \pm \sigma(R_{(B/F)})$) and significance of each enhancement ($S_{B/C}$, $S_{B/F}$).

$\sigma(v)_{intr} (\text{ km s}^{-1})$	p/sf	$R_{(B/C)}$	$\Delta R_{B/C}$	$\sigma(R_{(B/C)})$	$S_{B/C}$	$R_{(B/F)}$	$R_{(B/F)_{wf}}$	$\Delta R_{B/F}$	$\sigma(R_{(B/F)})$	$S_{B/F}$
All	All	-0.425	0.18	0.12	85.6%	-0.551	-0.971	0.43	0.13	99.0%
All	p	-0.29	0.12	0.16	53.1%	-0.31	-0.52	0.21	0.18	79.1%
All	sf	-0.64	0.10	0.19	40.4%	-0.85	-1.14	0.30	0.19	88.8%
0-400	p	-0.434	-0.03	0.19	13.6%	-0.402	-0.593	0.19	0.22	64.9%
0-400	sf	-0.453	0.28	0.22	80.3%	-0.581	-1.269	0.69	0.23	99.7%
400-600	p	-0.118	0.28	0.23	78.3%	0.191	-0.459	0.65	0.26	97.7%
400-600	sf	-1.098	-0.35	0.29	72.9%	-1.394	-0.963	-0.43	0.31	78.3%
600-1000	p	0.129	0.53	0.26	95.4%	-0.348	-0.424	0.08	0.30	20.2%
600-1000	sf	-1.159	-0.41	0.26	91.8%	-1.095	-0.971	-0.12	0.39	30.6%

3.6.4.3 Discussion

In this chapter, we set out to present the properties of galaxies in the CNOC2 group sample. The primary result of this chapter has been to compare the level of star formation in the $z \sim 0.4$ groups with that in the intermediate redshift field. The significant enhancement of f_p over the field level, even in the smallest groups in our sample, indicates that the galaxy population is less star-forming in the group environment than in the field, even at intermediate redshift. This could be related to either a different formation history in the group environment, intragroup environmental processes accelerating galaxy evolution to the passive state, or a combination of these two effects. In Chapter 5 we will make a more detailed comparison with the properties of our low redshift 2dF group sample.

We have investigated how this deficit of star-forming galaxies depends on the group properties. The correlations we find are relatively weak. Whilst there is little overall trend of f_p with group velocity dispersion, there is a suggestion that f_p is higher in the more

concentrated systems with $\sigma(v)_{intr} > 400 \text{ km s}^{-1}$. We examined the radial dependence of f_p , finding a weak trend with radius. Comparing f_p with the nearest neighbour distance, the passive fraction declines significantly at large separations, suggesting a relation to the substructure within groups. Taking into account the low numbers of galaxies in each system, these trends are qualitatively similar to those reported in local group samples (e.g. Hashimoto et al., 1998; Gómez et al., 2003; Girardi et al., 2003; Balogh et al., 2004a). The correlations of passive fraction with environment also mimic the dependence of morphology on environment in local groups (e.g. Postman & Geller, 1984; Zabludoff & Mulchaey, 1998, 2000; Tran et al., 2001). A detailed comparison will be made with galaxy morphologies in Chapter 4.

We also investigate how the luminosity function of galaxies depends on their environment: local studies have shown that luminosity is at least as important as environment in determining whether a galaxy is passive or star-forming at the present day (Balogh et al., 2004a, see Chapter 2). Our data suggest that the intermediate redshift group galaxy population is enhanced in bright galaxies and that lower velocity dispersion groups ($\sigma(v)_{intr} \lesssim 400 \text{ km s}^{-1}$) have a deficit of faint galaxies compared to the intermediate redshift field. However, only in the more massive groups is the enhanced bright population primarily passive (f_p also enhanced).

It is instructive to see how these trends compare with similar studies at low redshift in the literature. The variation in the shape of the global luminosity function measured from survey to survey is worryingly large (Driver & De Propris, 2003) and so it is important to use data from the same survey where possible in studies of how the luminosity function depends upon environment. Data from SDSS and 2dFGRS suggests that in regions of higher density the local galaxy population is biased towards a brighter characteristic magnitude and steeper faint-end slope (De Propris et al., 2003a; Blanton et al., 2003; Croton et al., 2004). This density dependence appears to be dominated by the relative abundance of early-type passive galaxies and may not be obvious in each individual cluster (e.g. the Coma cluster, Mobasher et al., 2003). In local groups there may also be a correlation between group velocity dispersion and the faint-end slope, driven by the population of faint, early-type galaxies (Zabludoff & Mulchaey, 2000; Christlein, 2000). The large population of faint passive galaxies in the most massive groups ($\sigma(v)_{intr} \gtrsim 600 \text{ km s}^{-1}$, see Figure 3.19) suggests that we might be seeing the same trends at $z \sim 0.45$, although there appears to be a deficit of faint galaxies in less massive groups, relative to the field. The generation of this faint passive galaxy population is relevant to downsizing in the red

sequence of cluster galaxies, with recent observations indicating that it does not extend faintwards of $\sim M_* + 2$ at $z \sim 1$ (Kodama et al., 2004b; De Lucia et al., 2004).

3.7 Conclusions

We have used the LDSS2 spectrograph on the Magellan telescope at LCO to obtain 418 new galaxy redshifts in the regions of 26 CNOC2 groups at intermediate redshift ($0.3 \leq z \leq 0.55$). Of these, 86 are group members. With the depth of Magellan, we are highly complete and unbiased down to $R_C = 22.0$ and out to $240''$ ($\sim 2r_{200}$ for a 500 km s^{-1} group at $z = 0.3$). The primary purpose of this chapter is to present this data set.

We have investigated the fraction of star-forming galaxies in the groups compared to the field at the same redshift. We find that the fraction of passive galaxies (f_p , defined as the fraction of galaxies with $\text{EW}[\text{OII}] < 5\text{\AA}$) is higher in the groups than in the field at the same redshift. We have qualitatively divided the groups into massive (M), concentrated (C), loose (L) and unclassifiable (U) classes. We find no significant difference in the overall $\text{EW}[\text{OII}]$ distribution of concentrated and loose groups. Although the fraction of passive galaxies shows no strong relationship with group velocity dispersion, $\sigma(v)_{intr}$, the data suggest that the fraction may be most enhanced in the compact groups with the highest $\sigma(v)_{intr}$.

We have coadded the data to provide a well-understood stacked group sample and a stacked field sample over the same redshift range ($0.3 \leq z \leq 0.55$). We use this sample to investigate the dependence of f_p on galaxy luminosity. We find that f_p is greatly enhanced in group galaxies with respect to the field down to at least $M_{b_j} \sim -19.0$. In the brightest galaxies ($M_{b_j} \lesssim -21.0$) this trend is strongest in the higher velocity dispersion systems ($\sigma(v)_{intr} \gtrsim 400 \text{ km s}^{-1}$). We find only a weak trend of f_p with radius; this trend becomes stronger when we compute the local density based upon the distance to the nearest group member.

We use the stacked data-set to compare the luminosity function of the group galaxies with the surrounding field. The group luminosity function shows a significant excess in the ratio of bright to faint galaxies relative to the field population, analogous to low redshift studies (De Propris et al., 2003a; Blanton et al., 2003; Croton et al., 2004). We divided the groups into 3 bins of group velocity dispersion and the group and field populations into passive and star-forming samples. Compared to the field, the data suggest that

the intermediate redshift groups are enhanced in bright ($M_{b_j} \lesssim -21.0$) galaxies but only lower velocity dispersion groups ($\sigma(v)_{intr} \lesssim 400 \text{ km s}^{-1}$) have a deficit of faint galaxies compared to the intermediate redshift field.

Chapter 4

The Morphological Composition of Galaxy Groups at $0.3 \leq z \leq 0.55$

4.1 Introduction

In this chapter we examine how the group environment at $z \sim 0.4$ has influenced the morphological composition of group members. With deep HST ACS (Hubble Space Telescope - Advanced Camera for Surveys) observations of 16 of our CNO2 groups (and 4 more targets to be observed in Autumn 2004) we have the resolving power to classify galaxy morphology to well below the magnitude limit of our spectroscopy. In this way we can isolate the morphological transformations which may be driving galaxy evolution in groups at intermediate redshift.

Much of extragalactic astronomy is built on the bedrock of the Hubble Sequence. First identified as extragalactic objects by Edwin Hubble, it was quickly recognized that “extragalactic nebulae” (galaxies) fall into a distinct sequence of morphological types. This sequence of galaxies can be depicted in a “tuning fork diagram” (Figure 4.1) which shows the sequence of smooth elliptical galaxies (left), through lenticular S0 type galaxies which possess a smooth disk and a large bulge, to the populous spiral (and barred spiral) galaxy population (right) of decreasing bulginess and widening spiral arms as one moves from Sa (SBa) through to Sd (SBd) types and beyond (de Vaucouleurs, 1959; Sandage, 1961; Sandage & Bedke, 1994). There is also a category for irregular type galaxies with a more chaotic morphology which do not fit neatly onto this Hubble Sequence of galaxy morphological types.

Studies of galaxy evolution often centre upon how galaxy formation and evolution have

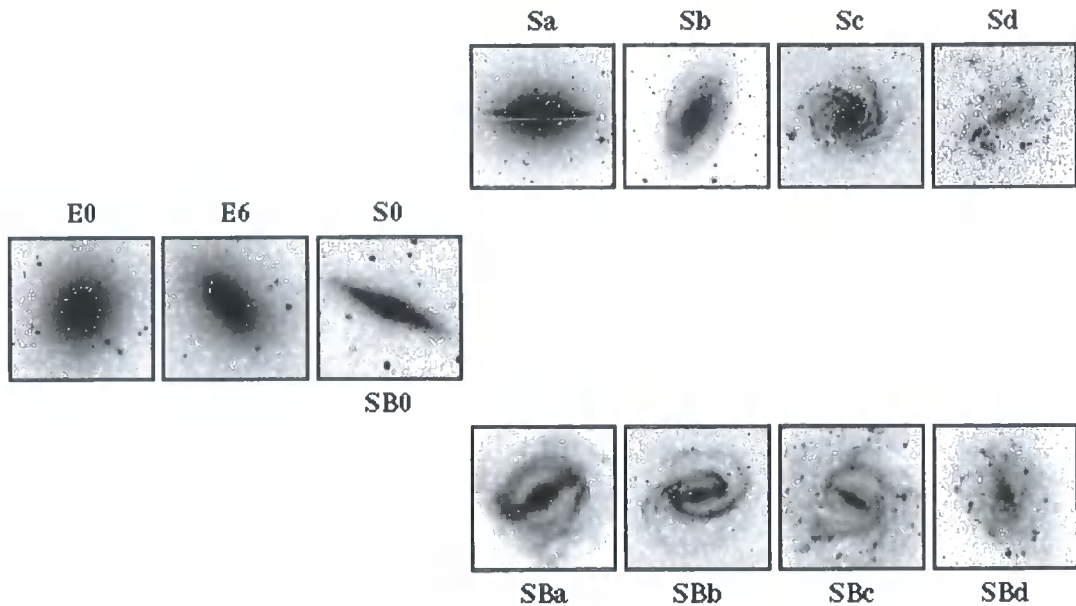


Figure 4.1: The “tuning fork” diagram depicting the Hubble Sequence of galaxy morphological types. This figure derives from the diagram found at:

<http://www.iitk.ac.in/ac/right/mag/galaxy.htm>. We note that we consider the galaxy here denoted ‘Sa’ to be closer to an edge-on ‘S0’ type, due to the large bulge.

progressed to build up the regular Hubble Sequence of galaxies seen today. The resolving power of modern telescopes, in particular the Hubble Space Telescope (HST), has allowed us to examine the morphological properties of galaxies at much higher redshift. It seems that at earlier epochs the population of peculiar / irregular galaxies was much larger than it is today suggesting that many galaxies have evolved onto the Hubble Sequence since $z \sim 1 - 2$ (e.g. van den Bergh, 2002; Conselice et al., 2004). At redshifts greater than ~ 2 the fraction of galaxies with merger signatures becomes so great that it is suggested that merger-induced starbursts may dominate the global star formation rate of the Universe (van den Bergh, 2002).

Morphology is also tightly correlated with environment. The morphology-density relation links morphology to the local density of galaxies over several decades of local density (Dressler, 1980). There is a continuous transition from the low density regimes where most galaxies have a spiral morphology to the highest density cluster cores which are dominated by elliptical and S0 types. There is also evidence that this relation is evolving, with an increasing fraction of S0 type galaxies in clusters since $z \sim 0.5$ (by a factor of 2-3) and a corresponding decrease in spiral fraction (Dressler et al., 1997). The

low redshift isolated early type galaxy sample of Stocke et al. (2004) has a much higher relative proportion of elliptical galaxies than in low redshift groups and clusters where S0s are more common. These results all indicate that S0 galaxy formation is related to processes of galaxy transformation which are more likely to occur in groups and/or clusters and which can dramatically alter the population of S0s in clusters since $z \sim 0.5$. The direct link between the morphological composition of a galaxy population and its local environment was contested by Whitmore & Gilmore (1991) and Whitmore et al. (1993) who claim a more direct relation between morphology and cluster-centric radius. They find that the fraction of S0 galaxies falls rapidly in the inner ~ 0.2 Mpc of clusters. More recent work suggests that global cluster conditions may be more important in the extreme conditions of the dense cluster core whilst the local environment is more important in the cluster outskirts, corresponding to the infalling groups (Domínguez et al., 2001; Balogh et al., 2002; Treu et al., 2003).

We know that galaxy morphology is also affected by the group environment at low redshift. Tran et al. (2001) show that the fraction of bulge dominated systems is higher in groups than in the field, and that it decreases with group-centric radius or local density. Coziol et al. (2004) show that more massive groups possess a more evolved galaxy population (with early type morphology and no star formation), consistent with hierarchical evolution. In the CNOC2 groups at $z \sim 0.4$ we might therefore expect to see an excess of early type galaxies already in place in groups at this redshift, corresponding to the excess population of passive galaxies (Chapter 3).

Alternatively, we might have isolated the epoch and environment at which the morphology-density relation is embedded in the galaxy population via regular transformations of infalling field galaxies as they are subject to the group environment for the first time. Smith et al. (2004) suggest that most of the evolution of the fraction of early type galaxies in groups has taken place since $z \sim 0.5$. In this case we might expect to see a population of transitory galaxies exhibiting signatures of transformation. These might include morphological signatures of mergers or interactions with another galaxy or an unusual combination of spectral and morphological types such as passive spiral galaxies or starbursting early types. Passive spiral galaxies have been shown to exist preferentially in intermediate density regimes ($\sim 1 Mpc^{-2}$) such as cluster outskirts (Goto et al., 2003; Yamauchi & Goto, 2004). They also regularly exhibit signs that they have completed their last major episode of star formation $1 - 2 Gyr$ prior to observation (i.e. the $k+a$ spectroscopic type) (Couch et al., 1998; Dressler et al., 1999; Poggianti et al., 1999). Together

this suggests that the mechanism responsible for truncating the star formation of a spiral galaxy in intermediate density regimes does not necessarily lead to a transformation of morphology on a timescale of $\lesssim 1Gyr$.

In Section 4.2 we introduce our HST imaging of 16 of the CNOC2 groups. We then discuss the visual classification scheme used and compare the classifications of Augustus Oemler Jnr. (AO) and myself in Section 4.3. In Section 4.4 we then attempt to answer some of the fundamental questions of galaxy evolution by combining our morphological and spectroscopic data. Finally these results are discussed in the context of the growing evidence in the literature in Section 4.5.

4.2 Data

4.2.1 The Observations:

We achieve reasonable coverage of the CNOC2 groups in the ACS field of view: $202'' \times 202''$. The angular distance of $202''$ corresponds to $1.3h_{75}^{-1}Mpc$ at $z = 0.55$ and $0.9h_{75}^{-1}Mpc$ at $z = 0.3$, extending well beyond than the virial radius of a typical group ($\sim 0.28h_{75}^{-1}Mpc$ for a 300 km s^{-1} group at $z = 0.4$). So that comparisons can be made with other HST observations of intermediate redshift clusters and X-ray-selected groups, we needed to achieve comparable depth in a similar bandpass. We chose the F775W filter which is the ACS bandpass most similar to the WFPC2 F702W filter most commonly used in earlier work. To reach the same depth as the MORPHS collaboration ($R_C \sim 23.9 \sim M_* + 3$) (Smail et al., 1997) we calculated that an exposure time of $\sim 2000s$ was required. Including overhead and readout time this was possible inside 1 orbit per group ($\sim 2800s$ at the declination of CNOC2) with low sky background. To date we have data from 16 of the 20 targeted groups (1 orbit per group). 4 raw images were taken per group in 2 dithered positions. This allows optimal extraction of cosmic rays during data processing and to cover the gap between CCDs.

4.2.2 HST-ACS Data Processing

Our HST imaging is processed in the usual way using the ACS pipeline (Pavlovsky et al., 2004). This reduction produces a fully astrometrically calibrated and undistorted image from the highly distorted ACS focal surface. Other basic calibration procedures which have been applied automatically before we retrieved the data include bias and dark subtraction and flat fielding. To create a suitable final image with cosmic rays and hot pixels

removed we reapply the *Multidrizzle* task in *pyraf* (Chapter 4.5 of Pavlovsky et al. (2004)) which recombines the dithered images into an undistorted and well-sampled median image in WCS coordinates. This task provides cosmic ray rejection and sky subtraction which is applied easily by setting optimal values for *Multidrizzle* parameters. The final images look clean and galaxies can be easily identified below the CNOC2 photometric catalogue magnitude limit of $R_C \sim 23.2$.

4.2.3 Galaxy Identification

To identify galaxies from the CNOC2 catalogue in the HST imaging, we apply an algorithm which selects the galaxies in CNOC2 which lie inside the HST field of view. The algorithm then computes the corresponding ACS pixel coordinates of each CNOC2 galaxy using the ACS astrometrical solution and the *wcstools* package. The galaxy positions are centroided using the *digiphot* package in *iraf*. In Figures 4.2 to 4.17 we mark the locations of group galaxies on the field which targets that group. Note that members of other groups in our CNOC2 sample are often serendipitously located in the HST imaging, as are many field galaxies. These are not marked in these figures. Group members are marked with a symbol which indicates their level of [OII] emission. Circles represent passive galaxies ($EW[\text{OII}] < 5\text{\AA}$); triangles represent star-forming galaxies ($5\text{\AA} \leq EW[\text{OII}] \leq 30\text{\AA}$) and stars represent highly star-forming galaxies ($EW[\text{OII}] \geq 30\text{\AA}$). We also label each galaxy with its CNOC2 ID and $EW[\text{OII}]$. In this way it is possible to examine the links between the position of a galaxy within a group and its morphology and $EW[\text{OII}]$ (star-forming activity).

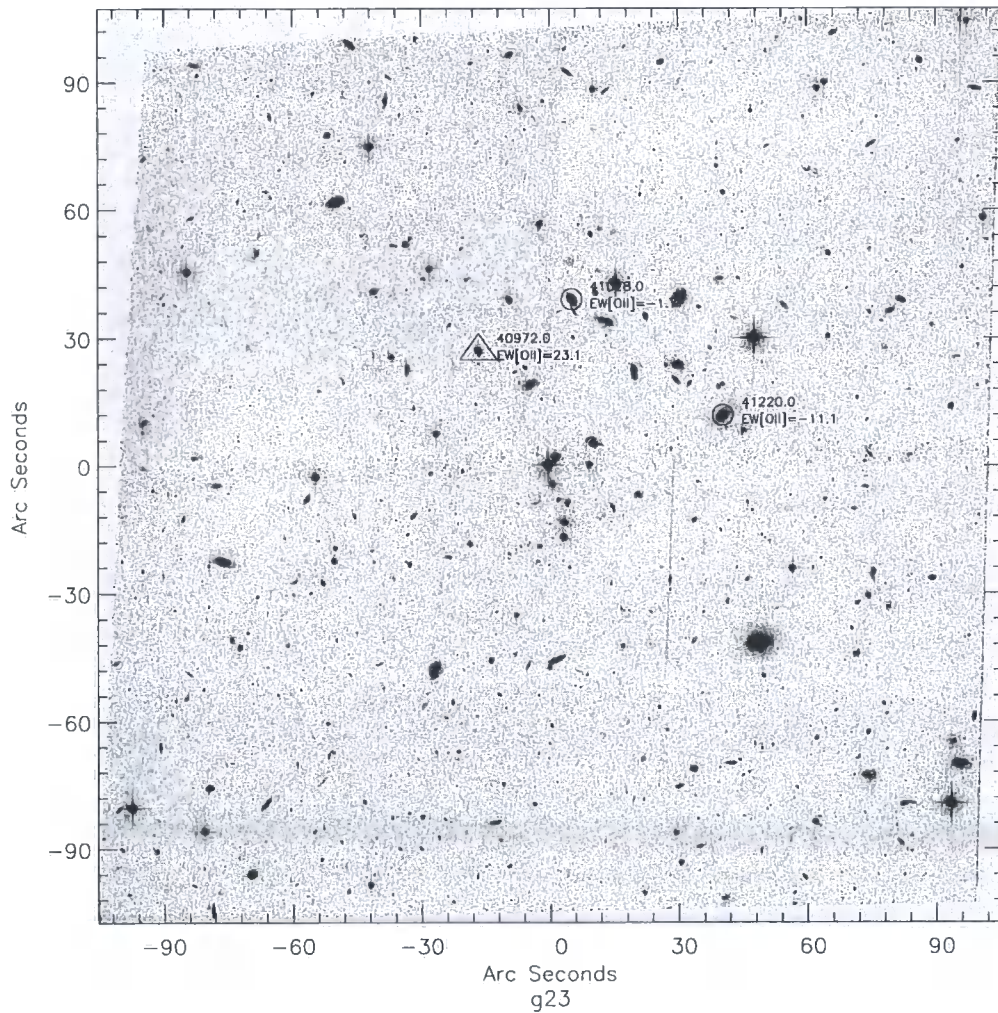


Figure 4.2: HST field 23 and members of group g23 at $z = 0.351$ ($445 \pm 75 \text{ km s}^{-1}$). Circles represent passive galaxies ($\text{EW}[\text{OII}] < 5 \text{ \AA}$); Triangles represent star-forming galaxies ($5 \text{ \AA} \leq \text{EW}[\text{OII}] \leq 30 \text{ \AA}$) and stars represent highly star-forming galaxies ($\text{EW}[\text{OII}] \geq 30 \text{ \AA}$)

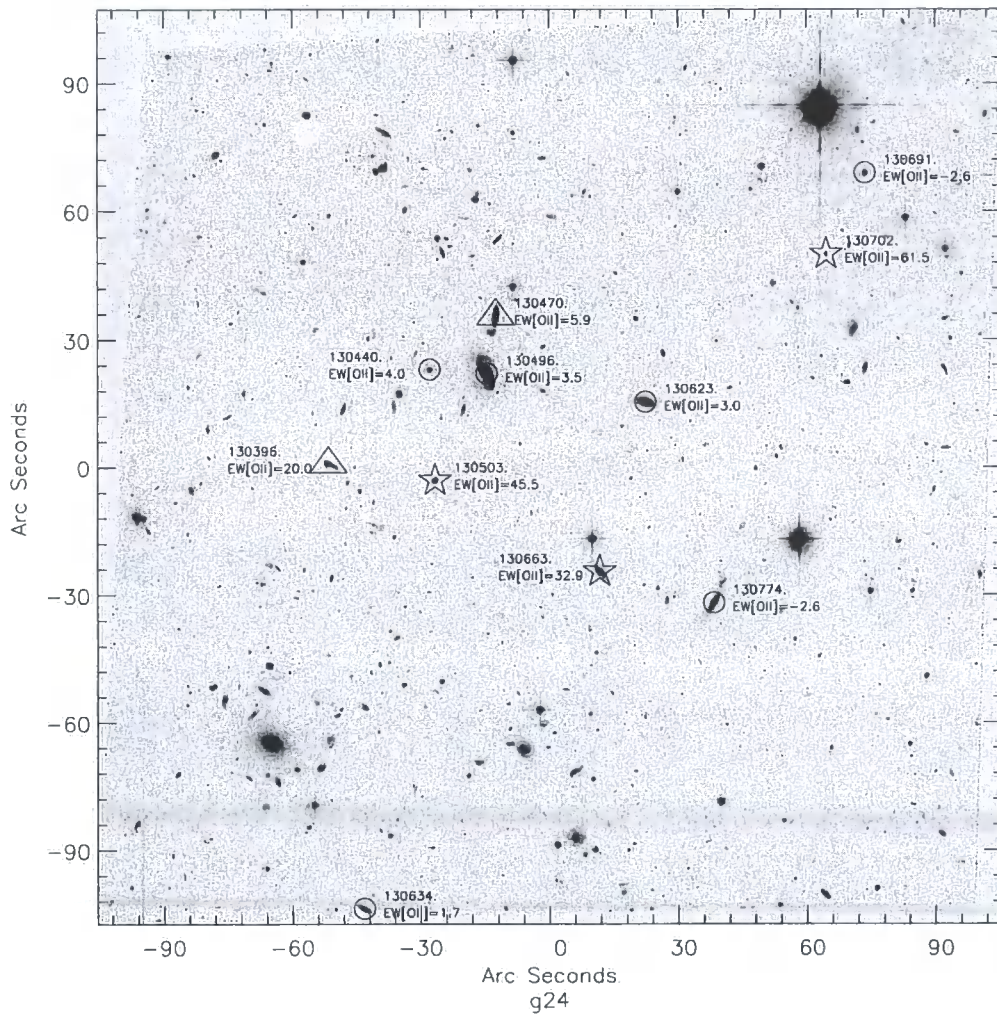


Figure 4.3: HST field 24 and members of group g24 at $z = 0.359$ ($<119.6 \text{ km s}^{-1}$).

Symbols are the same as for figure 4.2

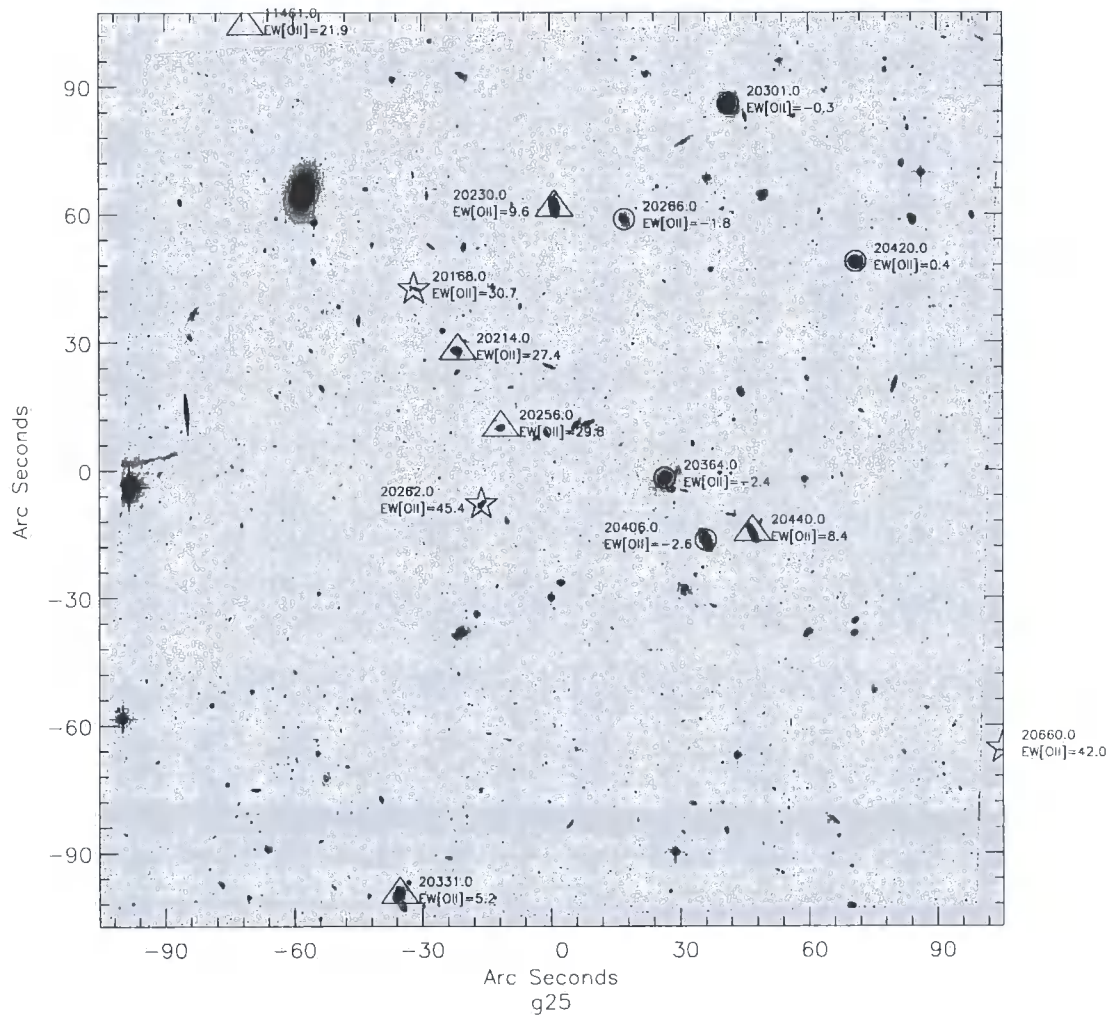


Figure 4.4: HST field 25 and members of group g25 at $z = 0.361$ ($470 \pm 75 \text{ km s}^{-1}$).

Symbols are the same as for figure 4.2

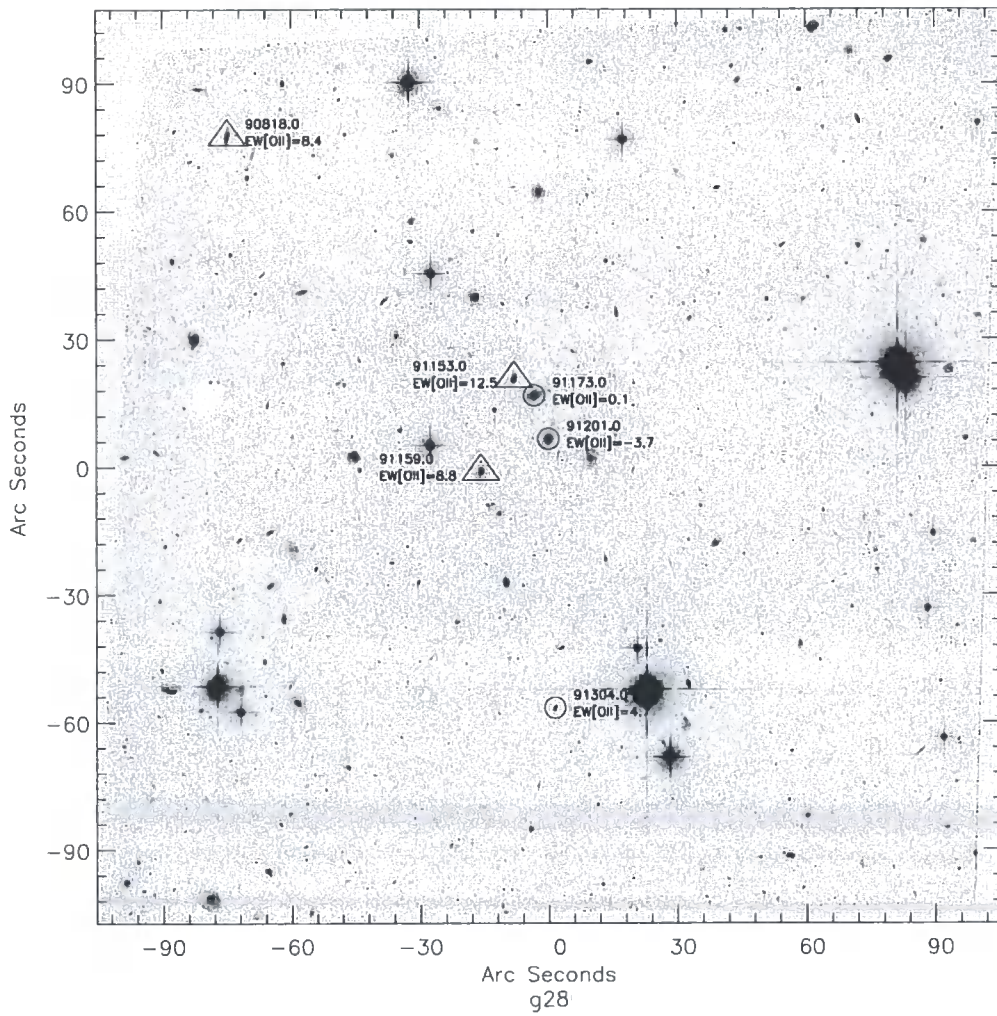


Figure 4.5: HST field 28 and members of group g28 at $z = 0.372$ ($160 \pm 80 \text{ km s}^{-1}$).

Symbols are the same as for figure 4.2

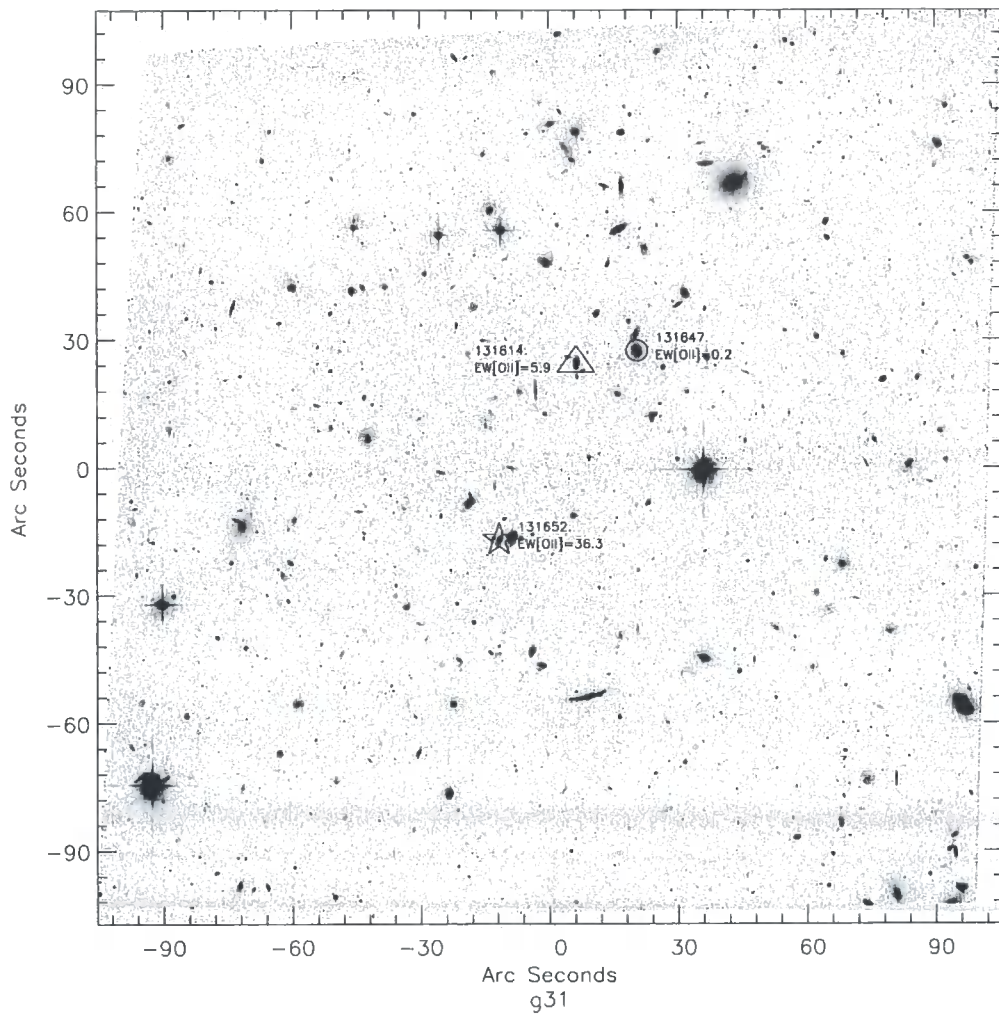


Figure 4.6: HST field 31 and members of group g31 at $z = 0.392$ ($565 \pm 352 \text{ km s}^{-1}$). Symbols are the same as for figure 4.2

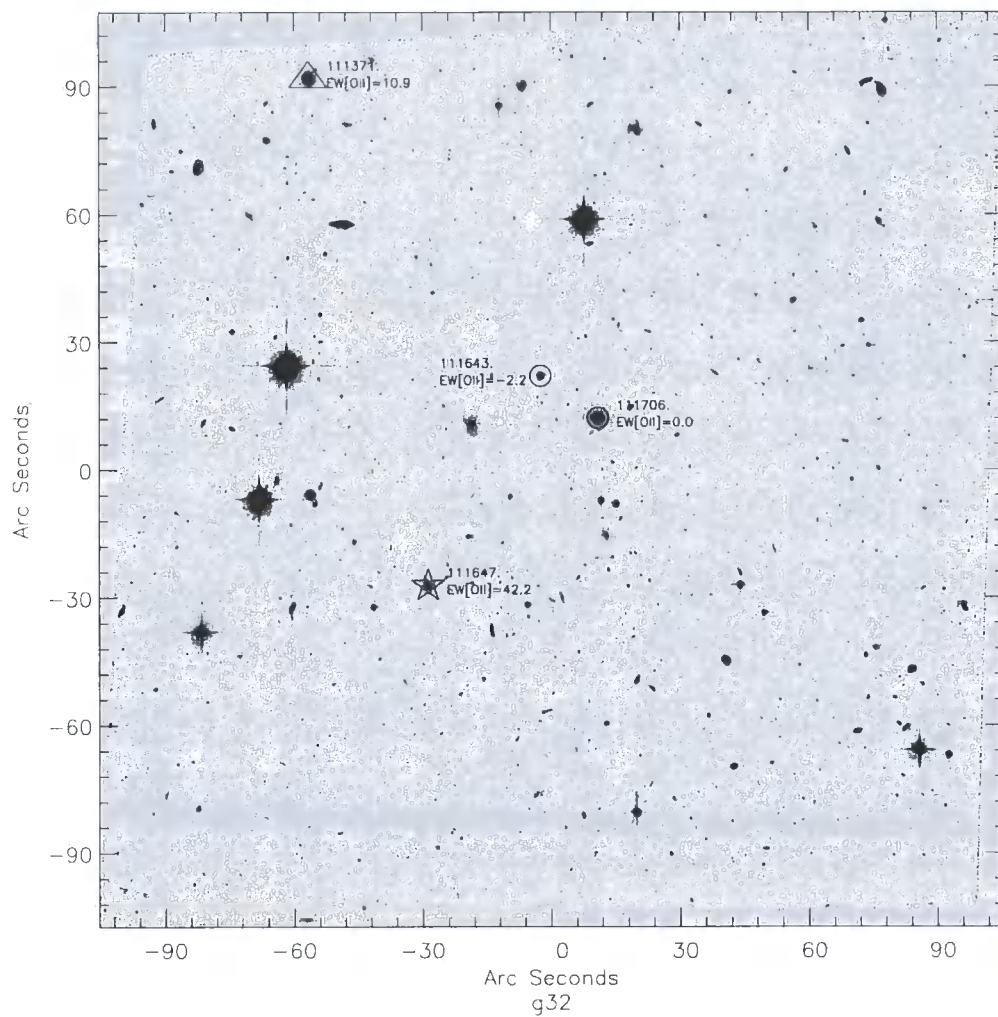


Figure 4.7: HST field 32 and members of group g32 at $z = 0.394$ ($519 \pm 98 \text{ km s}^{-1}$).

Symbols are the same as for figure 4.2

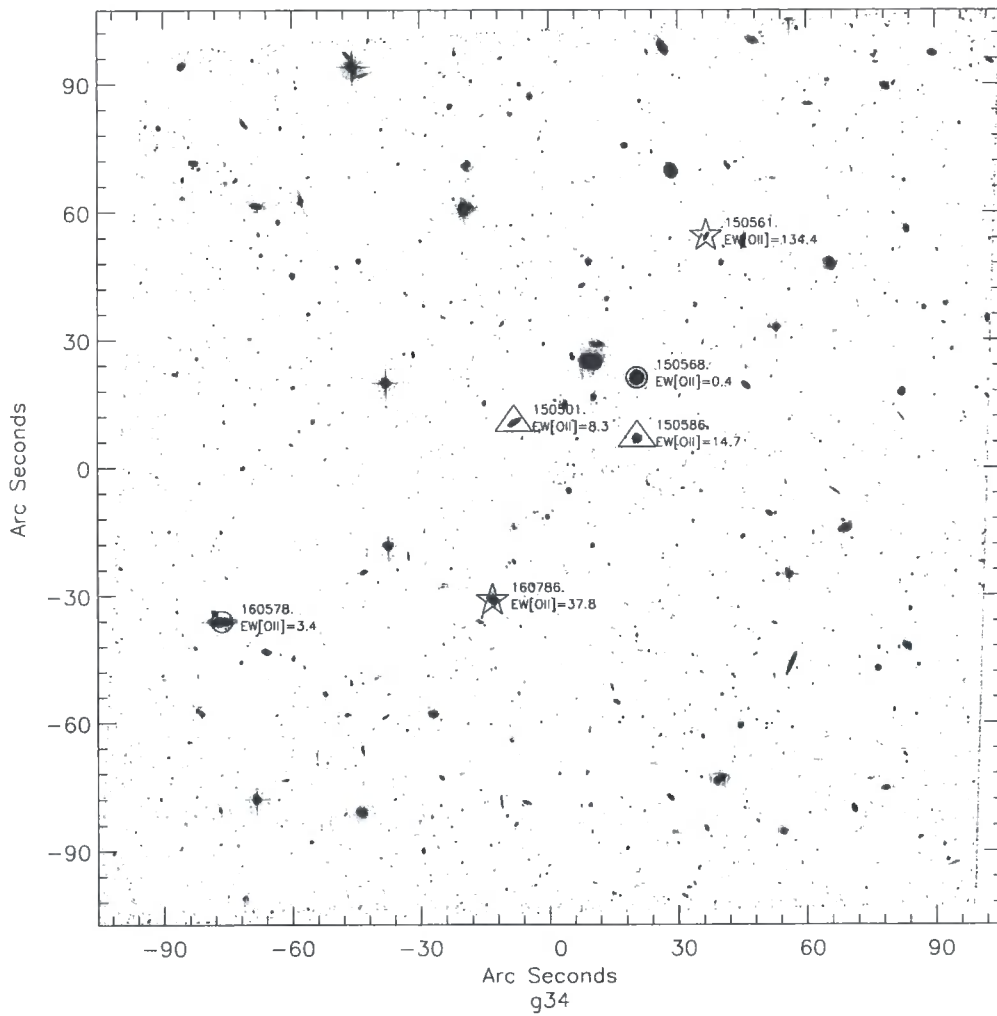


Figure 4.8: HST field 34 and members of group g34 at $z = 0.465$ ($408 \pm 106 \text{ km s}^{-1}$). Symbols are the same as for figure 4.2

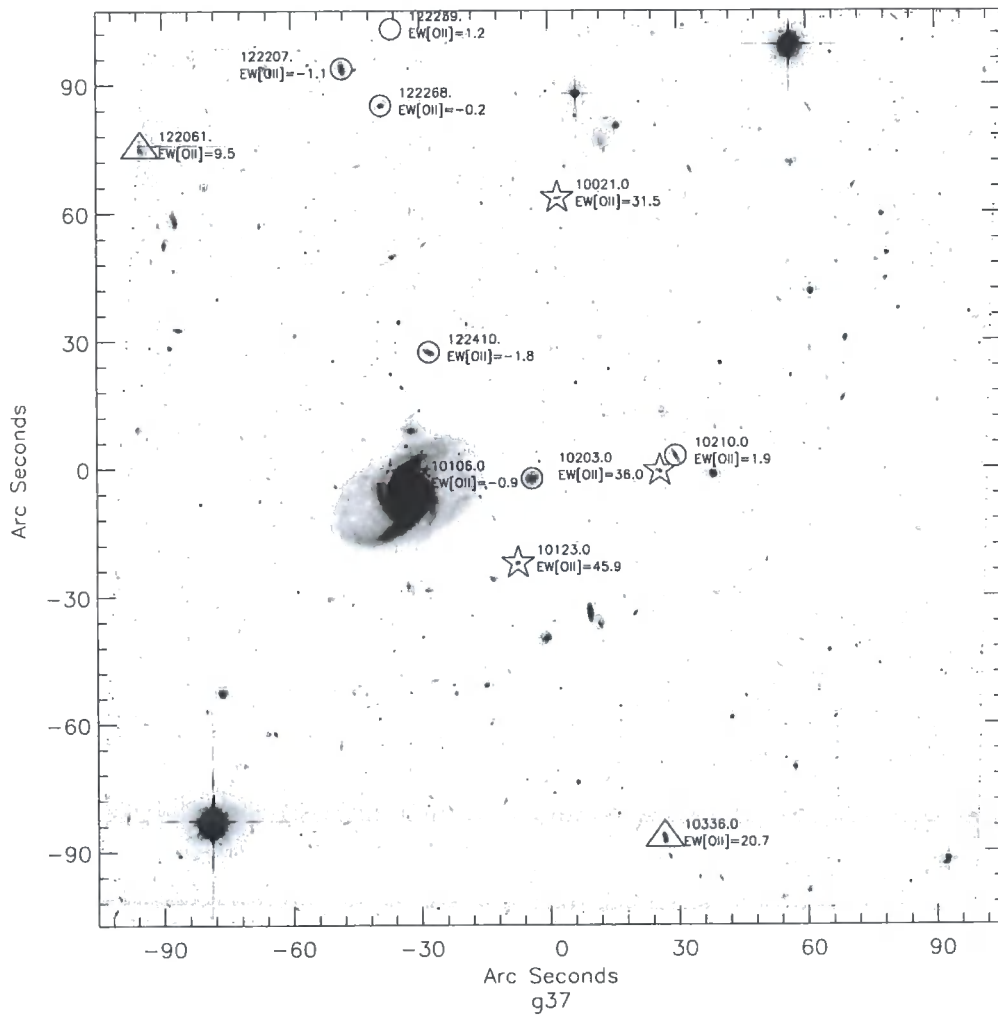


Figure 4.9: HST field 37 and members of group g37 at $z = 0.471$ ($419 \pm 97 \text{ km s}^{-1}$). Symbols are the same as for figure 4.2

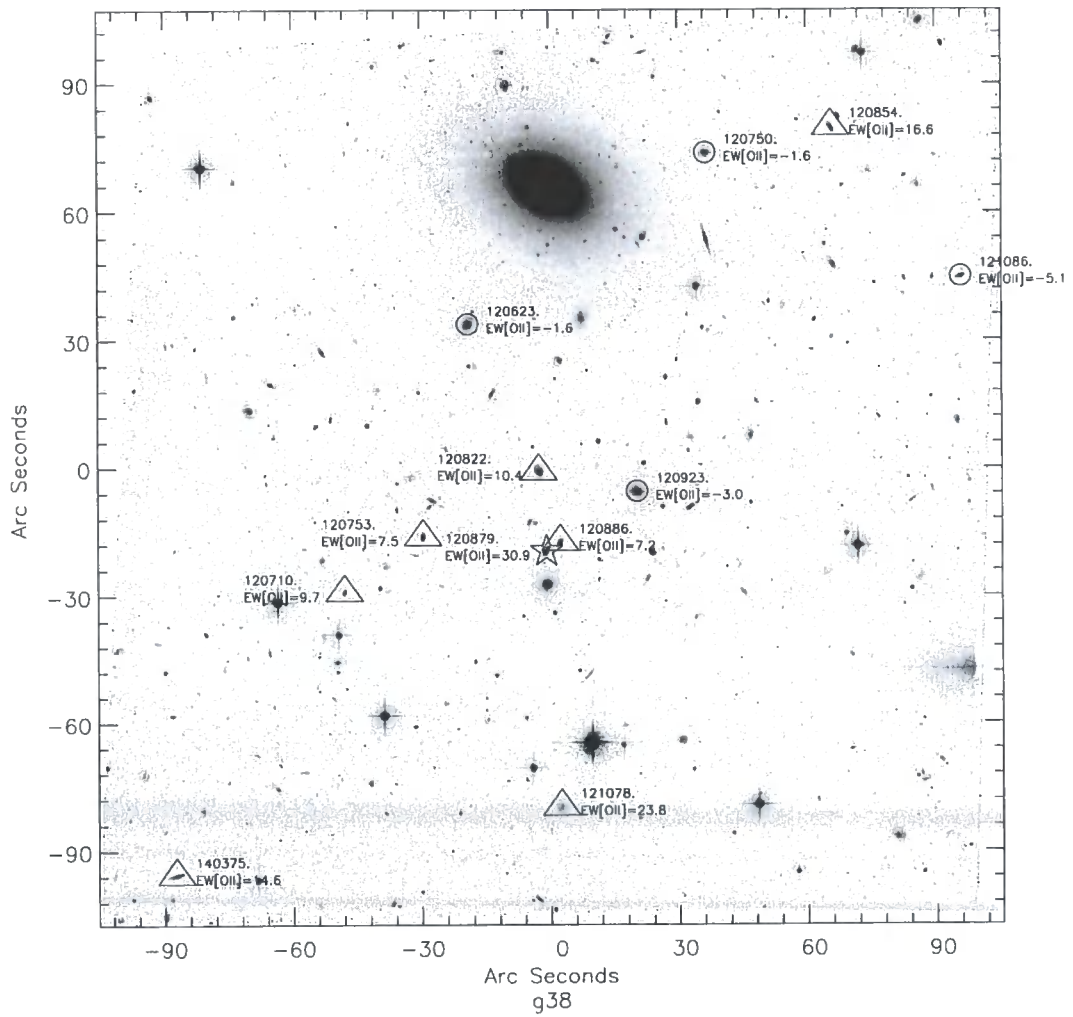


Figure 4.10: HST field 38 and members of group g38 at $z = 0.51$ ($808 \pm 68 \text{ km s}^{-1}$). Symbols are the same as for figure 4.2

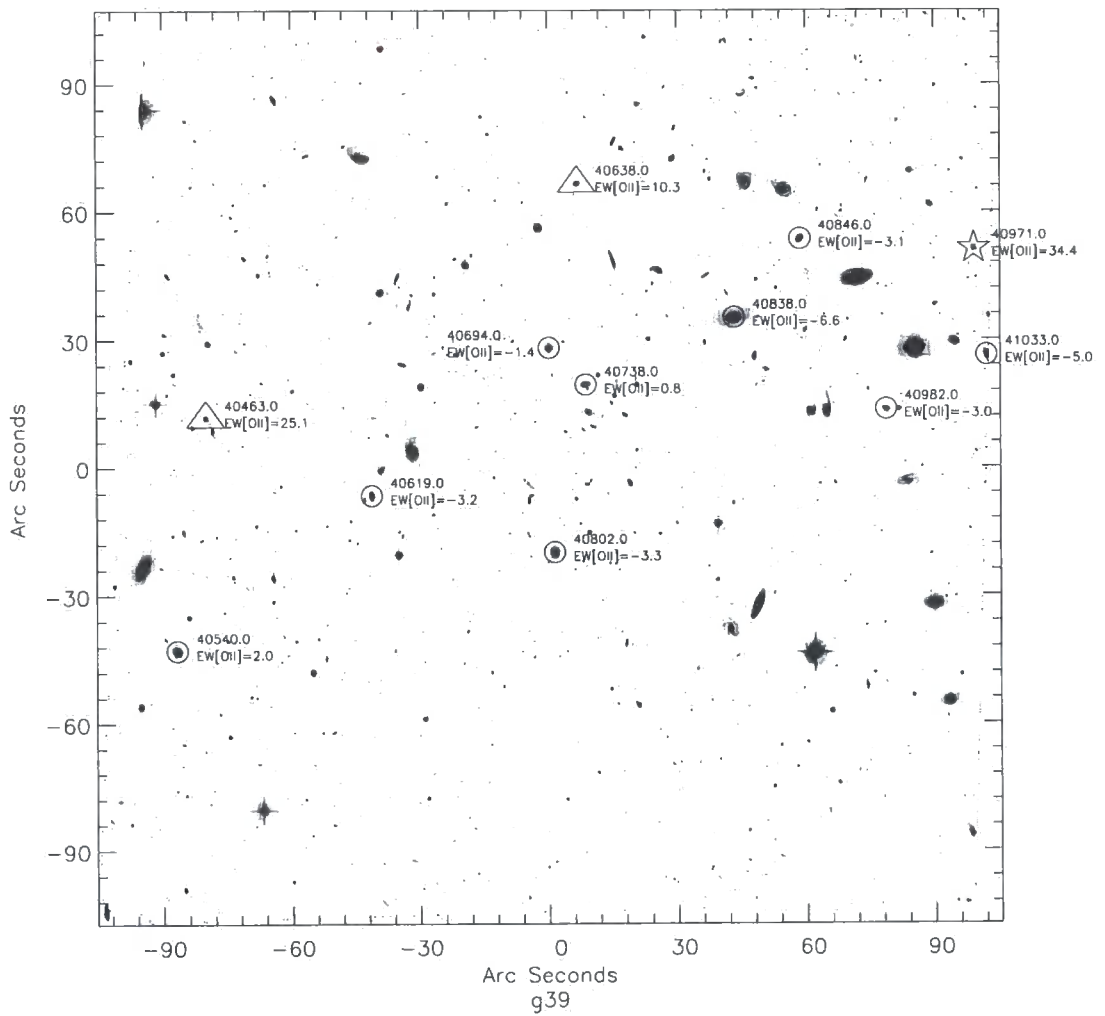


Figure 4.11: HST field 39 and members of group g39 at $z = 0.536$ ($454 \pm 88 \text{ km s}^{-1}$). Symbols are the same as for figure 4.2

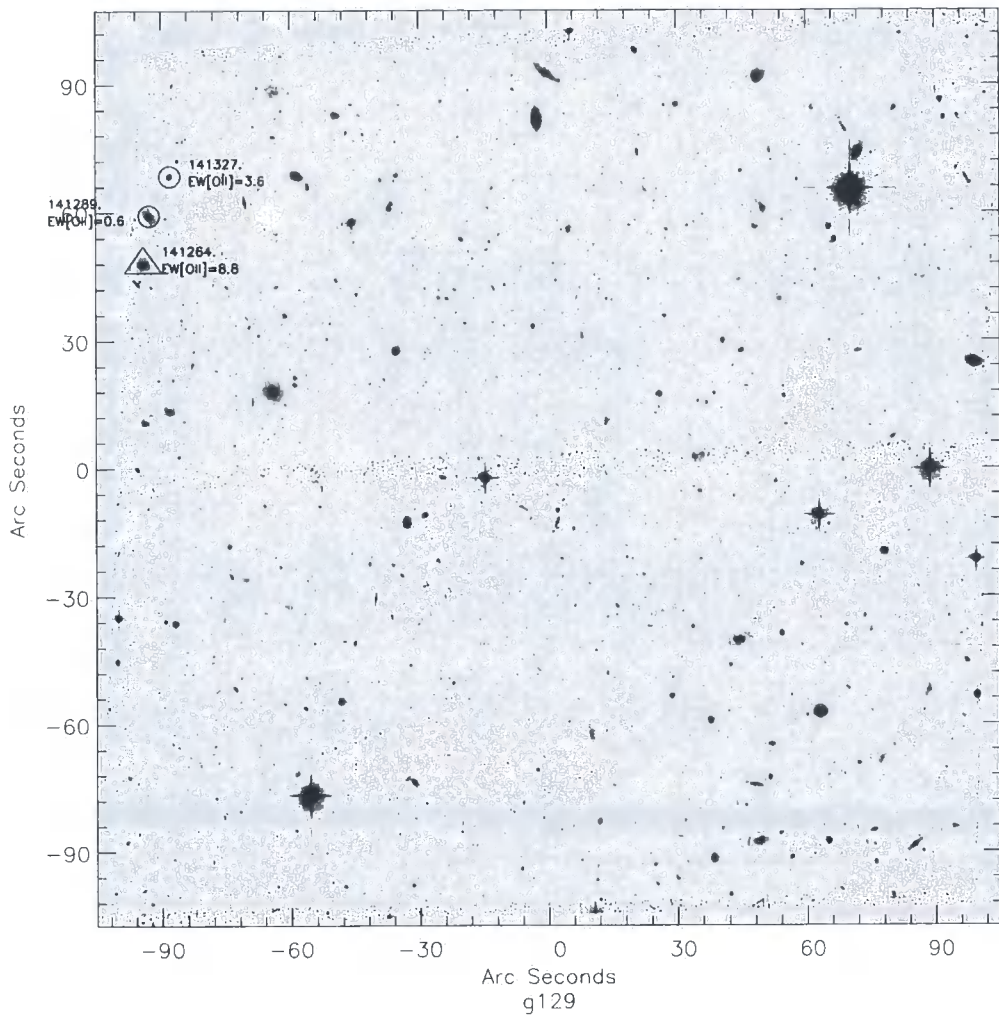


Figure 4.12: HST field 129 and members of group g129 at $z = 0.317$ ($225 \pm 76 \text{ km s}^{-1}$).

Symbols are the same as for figure 4.2

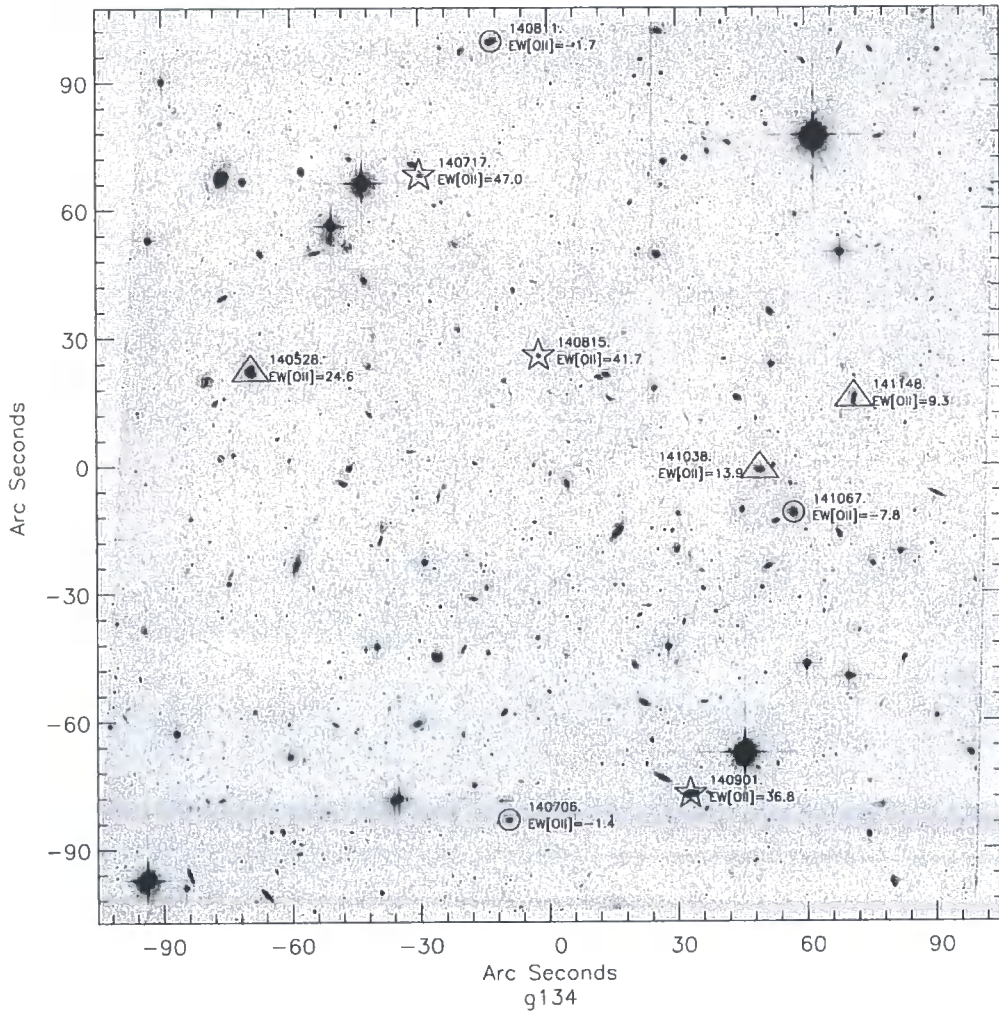


Figure 4.13: HST field 134 and members of group g134 at $z = 0.392$ ($284 \pm 78 \text{ km s}^{-1}$).

Symbols are the same as for figure 4.2

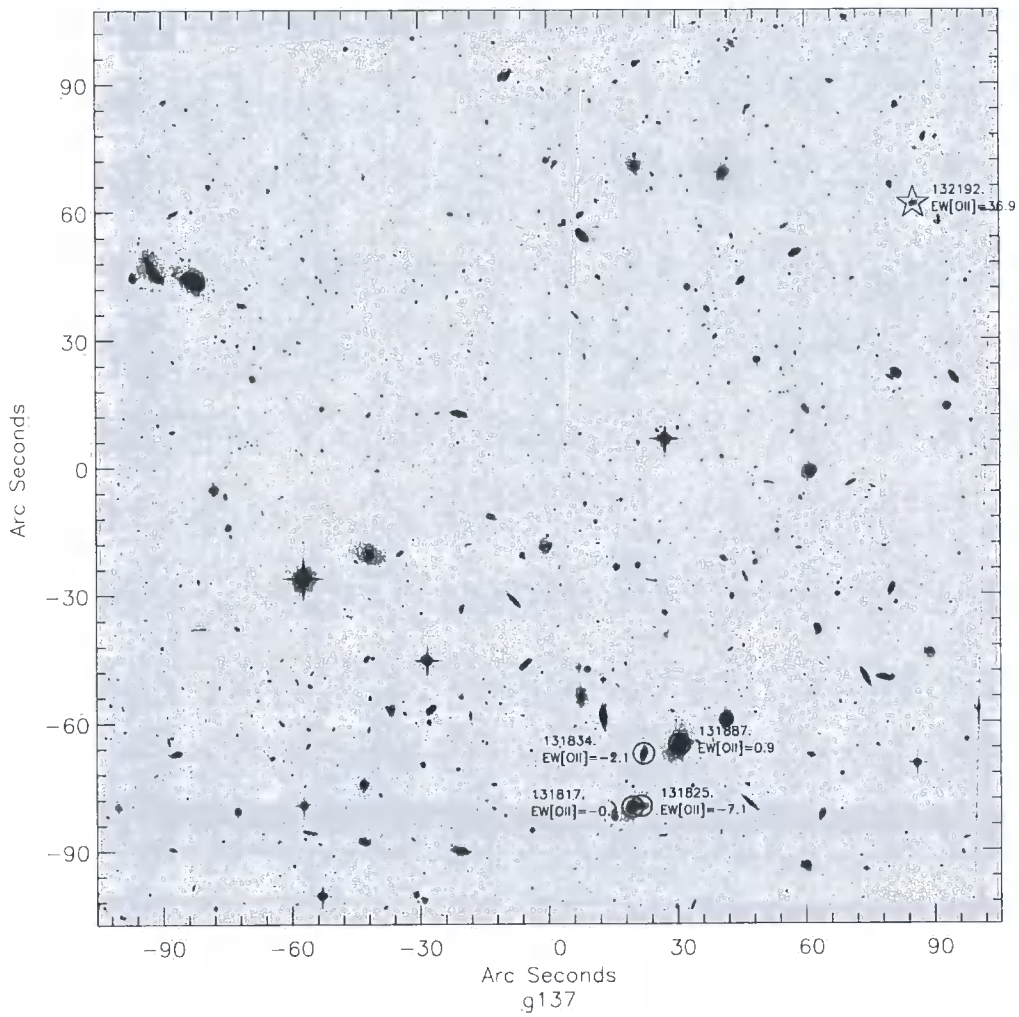


Figure 4.14: HST field 137 and members of group g137 at $z = 0.425$ ($314 \pm 84 \text{ km s}^{-1}$).

Symbols are the same as for figure 4.2

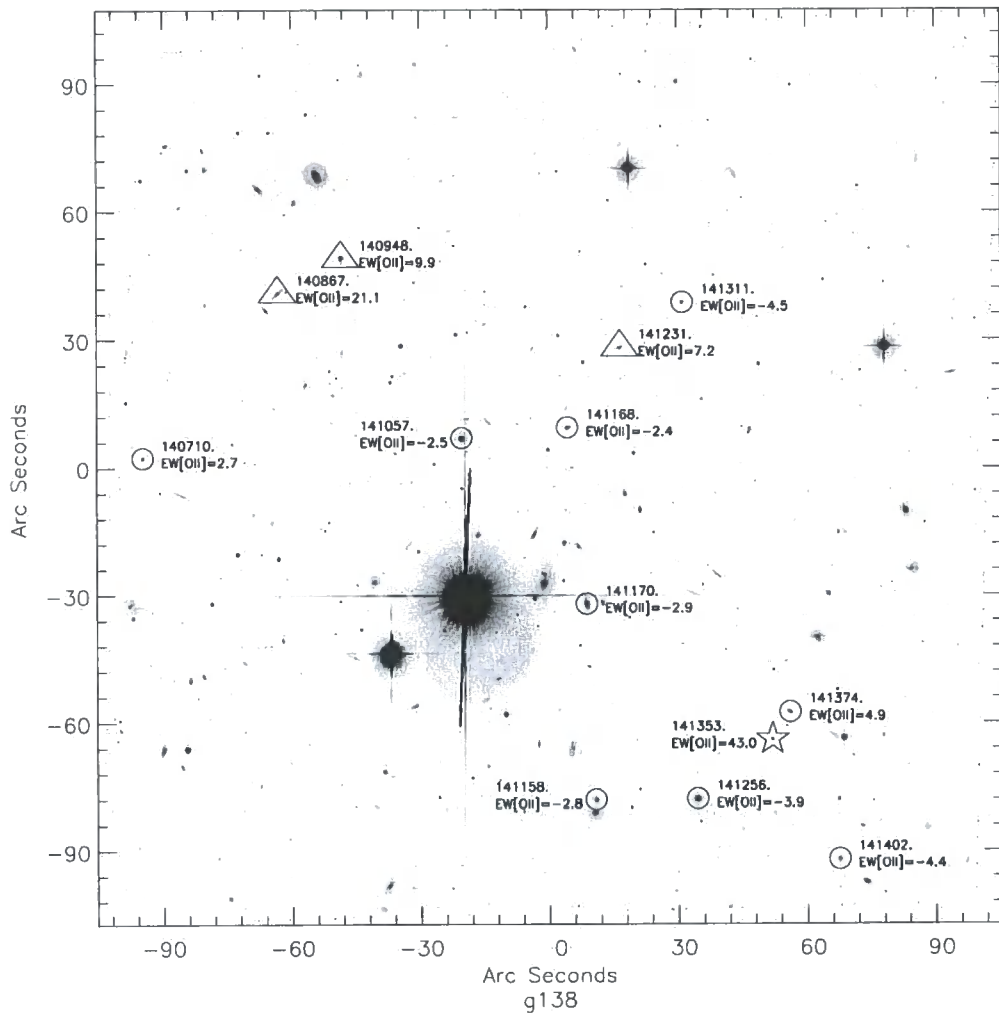


Figure 4.15: HST field 138 and members of group g138 at $z = 0.437$ ($711 \pm 81 \text{ km s}^{-1}$). Symbols are the same as for figure 4.2

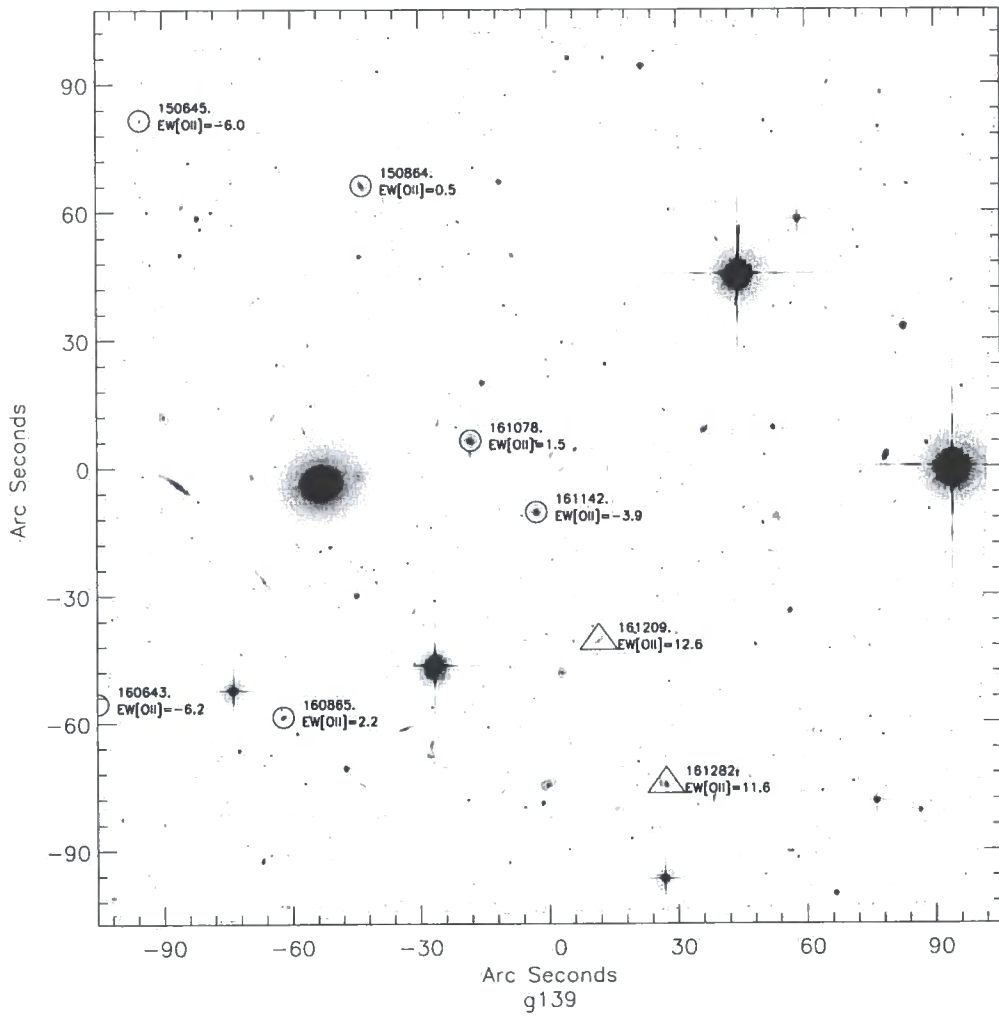


Figure 4.16: HST field 139 and members of group g139 at $z = 0.439$ ($314 \pm 84 \text{ km s}^{-1}$).

Symbols are the same as for figure 4.2

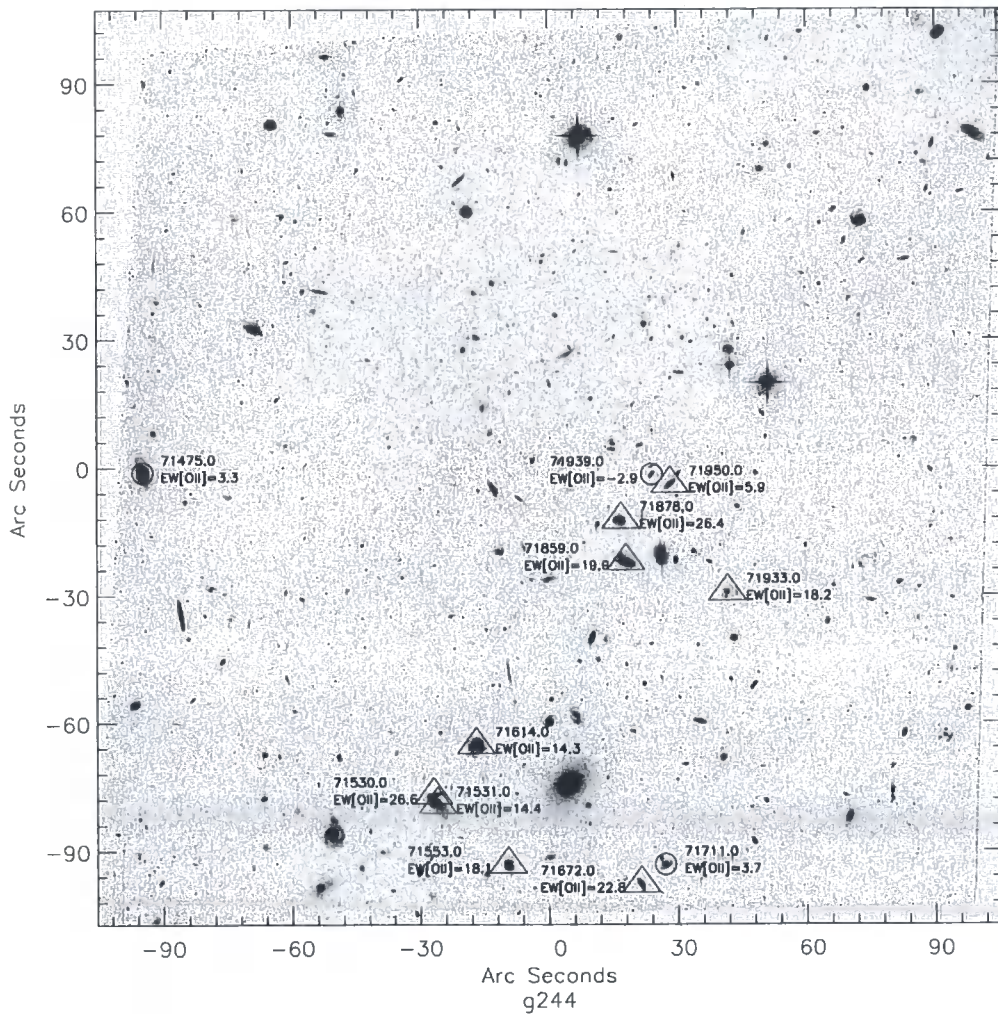


Figure 4.17: HST field 244 and members of group g244 at $z = 0.47$ ($270 \pm 54 \text{ km s}^{-1}$). Symbols are the same as for figure 4.2

The resulting HST galaxy sample contains 282 galaxies with known redshifts in the range $0.3 \leq z \leq 0.55$. These include 158 group members and 124 field galaxies.

4.3 Morphological Classification

The development of fully automated methods for the morphological classification of galaxies is a subject which has received a lot of interest in recent years (e.g. Abraham et al., 1994; Simard et al., 2002; Goderya & Lolling, 2002; Conselice, 2003). The ability to accurately quantify the morphology of a galaxy has the obvious advantage of removing the human bias of visual classification schemes. Most methods have centred on quantifying the bulge to disk ratio using a two-dimensional bulge+disk surface brightness model (e.g. Schade et al., 1996; Simard et al., 2002). Whilst this method can safely decompose luminous spiral and elliptical galaxies into well-defined bulge and disk components, it is based upon a priori assumed morphological characteristics which do not necessarily apply to all galaxies. Irregular and asymmetric galaxies in particular do not match this assumed light profile which is a particular problem at high redshift where these galaxies are more common (van den Bergh, 2002). Conselice (2003) reviews the subject of light decomposition and suggests a new scheme based upon the concentration, asymmetry and clumpiness of a galaxy's stellar light distribution. Other possibilities include the use of a neural network which can learn to recognise galaxy morphology (e.g. Goderya & Lolling, 2002).

Whilst there is undoubtedly progress being made in this field, automated methods of classification are controversial and not well understood. Conversely astronomers are highly experienced at visual classification of galaxy morphology along the Hubble sequence. This method may not allow a galaxy's morphology to be easily quantified but previous studies have shown that the human eye is very good at detecting the subtle differences in galaxies of different morphology, with classifications regularly reproduced by different authors to better than one class (e.g. Smail et al., 1997). Our goal is to understand the nature of galaxy evolution by examining the morphological composition of the CNOC2 groups and field. We consider this can be done most easily using a visual classification scheme which will produce results which are easier to interpret. This method also allows a more direct comparison with the morphological composition of the galaxy population in different environments and at different redshifts (e.g. Dressler et al., 1997).

All galaxies in our HST sample were visually classified by myself and Augustus Oemler Jr. (AO). Our HST observations are calculated to reach the same depth as Smail et al.

(1997) who determine that visual classification is possible down to a limiting magnitude of $R_{702} \leq 23.5$ which corresponds to $R_C \leq 23.9$. As our current limit for obtaining redshifts is $R_C = 22.0$, we should easily be able to classify our full HST sample of galaxies with redshifts.

As I have no prior experience in the visual classification of galaxies, I first spent some time examining a random sample of galaxies with 2 collaborators (John Mulchaey and Richard Bower). I also decided to classify according to a simple scheme with just 4 categories of galaxy:

- **Early-Type:** This category includes everything with obvious elliptical morphology and includes S0s. We recognise an early-type by the dominance of the bulge so that a galaxy with a disk and a luminous, extended bulge will be categorised as an early-type whilst a similar disk with a smaller more compact bulge will be categorised as a spiral galaxy.
- **Spiral:** This category includes all galaxies with an obvious disk which are not dominated by the bulge emission. Later type spirals are expected to show some signs of spiral arms.
- **Irregular:** This category includes every galaxy of unusual morphology which cannot be classified as spiral or early-type, and shows no obvious sign of merging activity. Irregular types are typically cloudy structures with evidence for knots of star formation. They may be disturbed systems, or simply galaxies in the process of formation which are not yet pressure or rotationally supported.
- **Merger:** This category includes everything believed to show morphological signatures of present or recent merging activity. This includes galaxies with double nuclei and / or signatures of tidal interaction between 2 components / companion galaxies.

As a much more experienced classifier (e.g. Oemler, 1974; Dressler et al., 1994; Oemler et al., 1997; Smail et al., 1997) AO classified our sample according to the MORPHS classification method (Smail et al., 1997). This method provides a detailed classification of galaxies onto the Revised Hubble Type system and in addition provides a disturbance index (D) and a subjective interpretation of the possible cause of any disturbance (anomaly index, I). We refer the reader to Smail et al. (1997) for a detailed description of this classification scheme. We expect that most classifications are robust to within ~ 1 Hubble Type as in that paper. However to improve the statistical significance of our results we

will group the galaxies into broader morphological classes for our analysis (Section 4.4). This will also reduce uncertainties relating to the unreliability of classifications.

4.3.1 Galaxy Classifications

To classify galaxies we used a script written for the *iraf* package by Lori Lubin for this purpose. Each galaxy was displayed as a postage stamp-sized image at 2 scalable stretch levels. This allows us to identify faint features on the galaxy outskirts as well as morphological signatures residing in the galaxy's nuclear regions. For each galaxy the classifier allocates a morphological type and other parameters according to the chosen scheme, as well as some comments recording the features which led to the classification and more uncertain features. We classified all galaxies with redshifts in the range $0.3 \leq z \leq 0.55$ in the HST fields. The order of classification is random so that the classifier has no prior knowledge of group membership. Therefore we were also simultaneously creating an unbiased comparison between group and field samples.

Figures 4.18 to 4.37 show postage stamp images of all the group galaxies located in the HST images. Each image is overlaid by the classifications of myself (left) and AO (right). AO classifications include values for disturbance index and the nature of any anomaly, I. Anomaly types include T (I=1, tidal arms but no obvious counterpart), I (I=2, visible interaction with another object) and M (I=3, merger). We also show the galaxy's CNOC2 ID, the R_C -band magnitude, $(B - R_C)$ colour, EW[OII] and EW[H δ] where available from Magellan spectra.

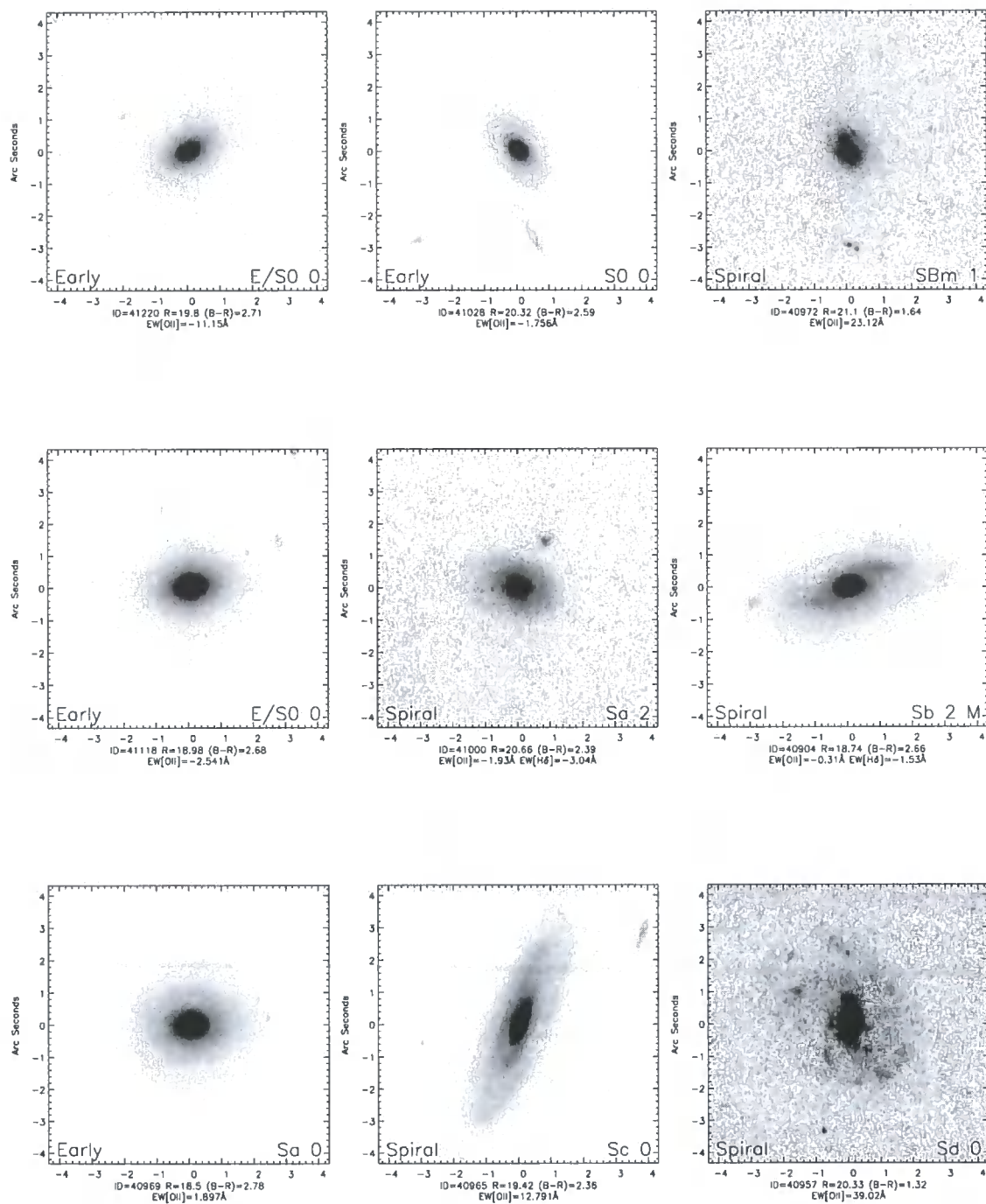


Figure 4.18: Members of group g23 at $z = 0.351$ ($445 \pm 75 \text{ km s}^{-1}$). Galaxies are labelled as described in the text.

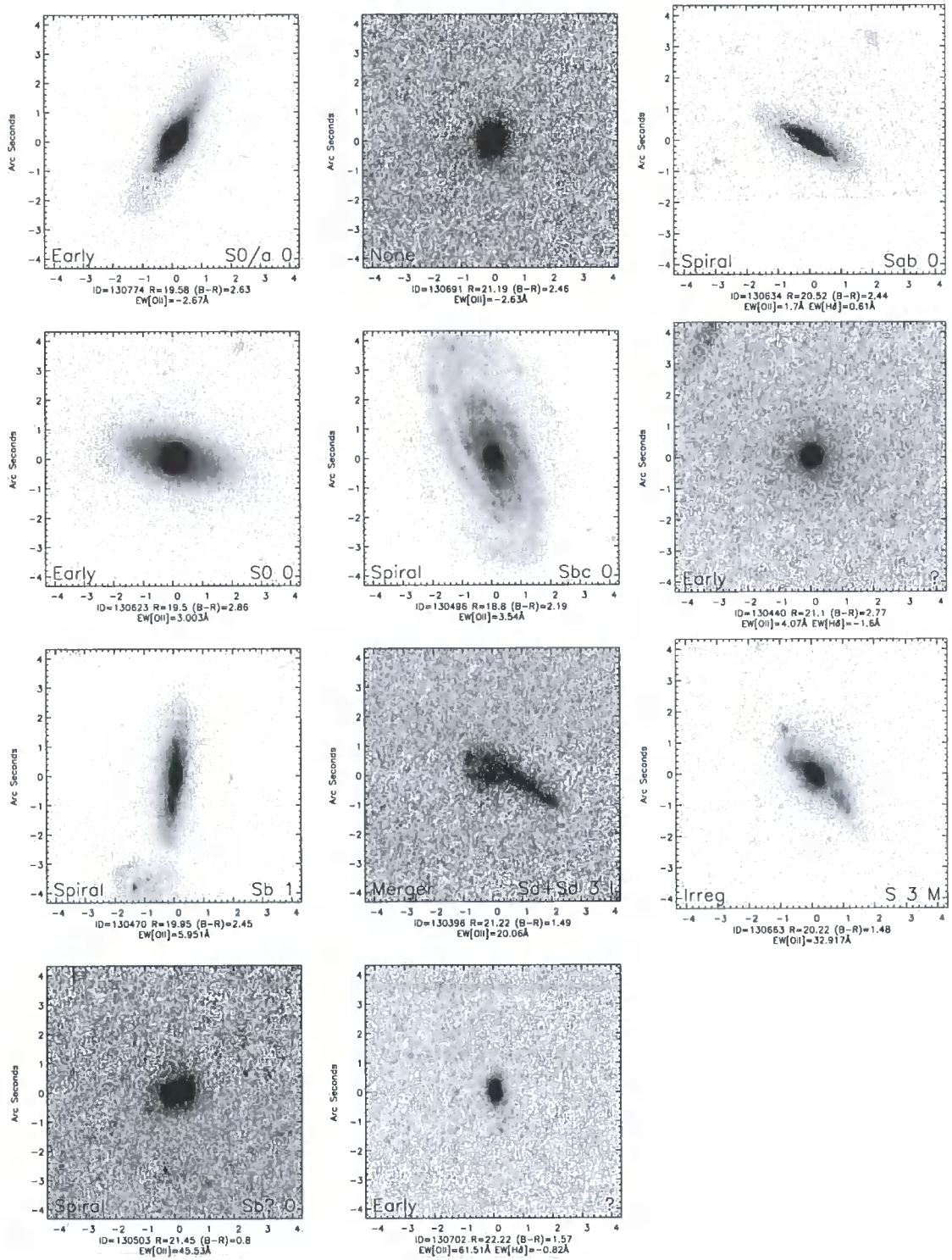


Figure 4.19: Members of group g24 at $z = 0.359$ ($< 119.6 \text{ km s}^{-1}$). Galaxies are labelled as described in the text.

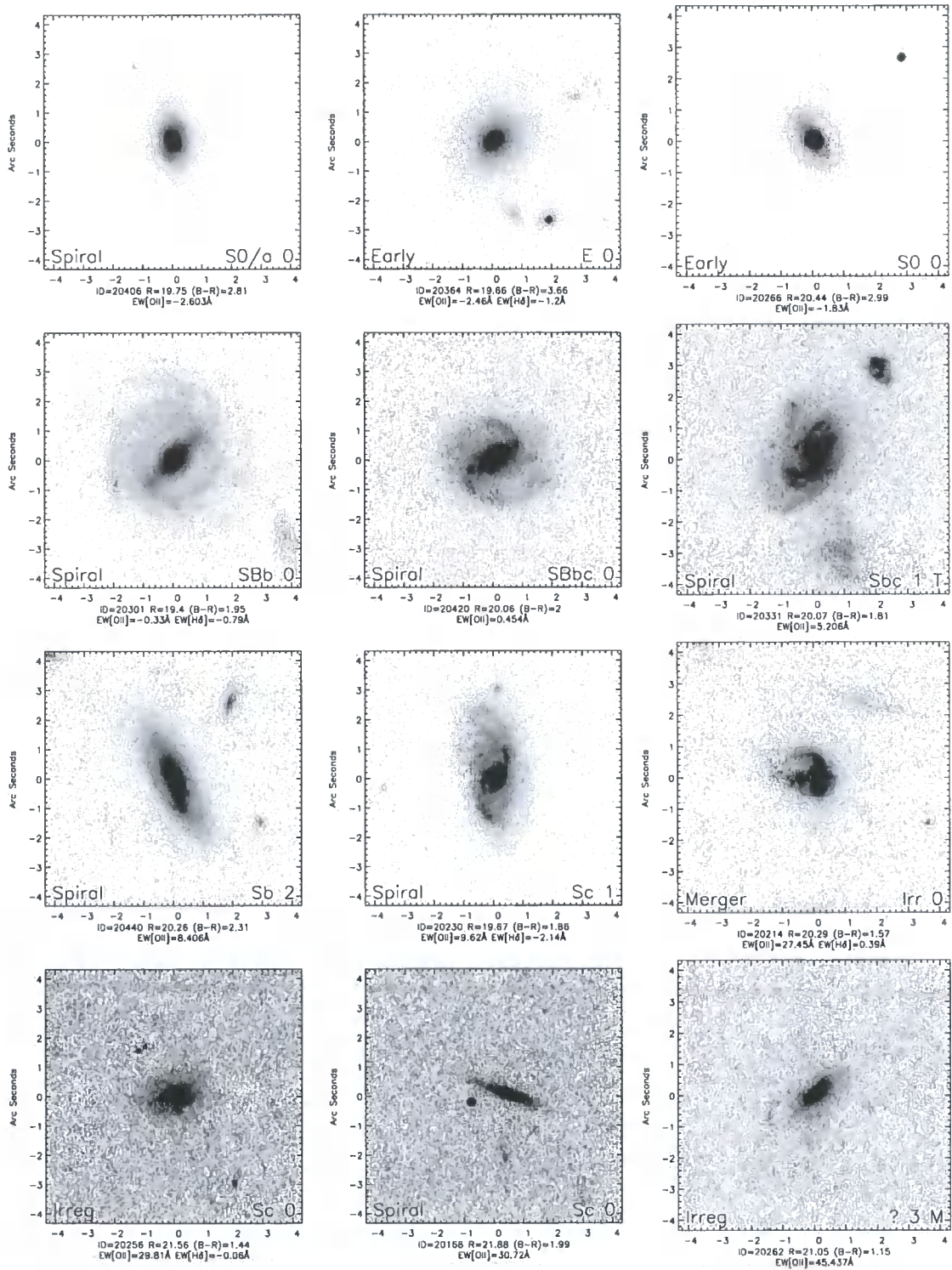


Figure 4.20: Members of group g25 at $z = 0.361$ ($470 \pm 75 \text{ km s}^{-1}$). Galaxies are labelled as described in the text.

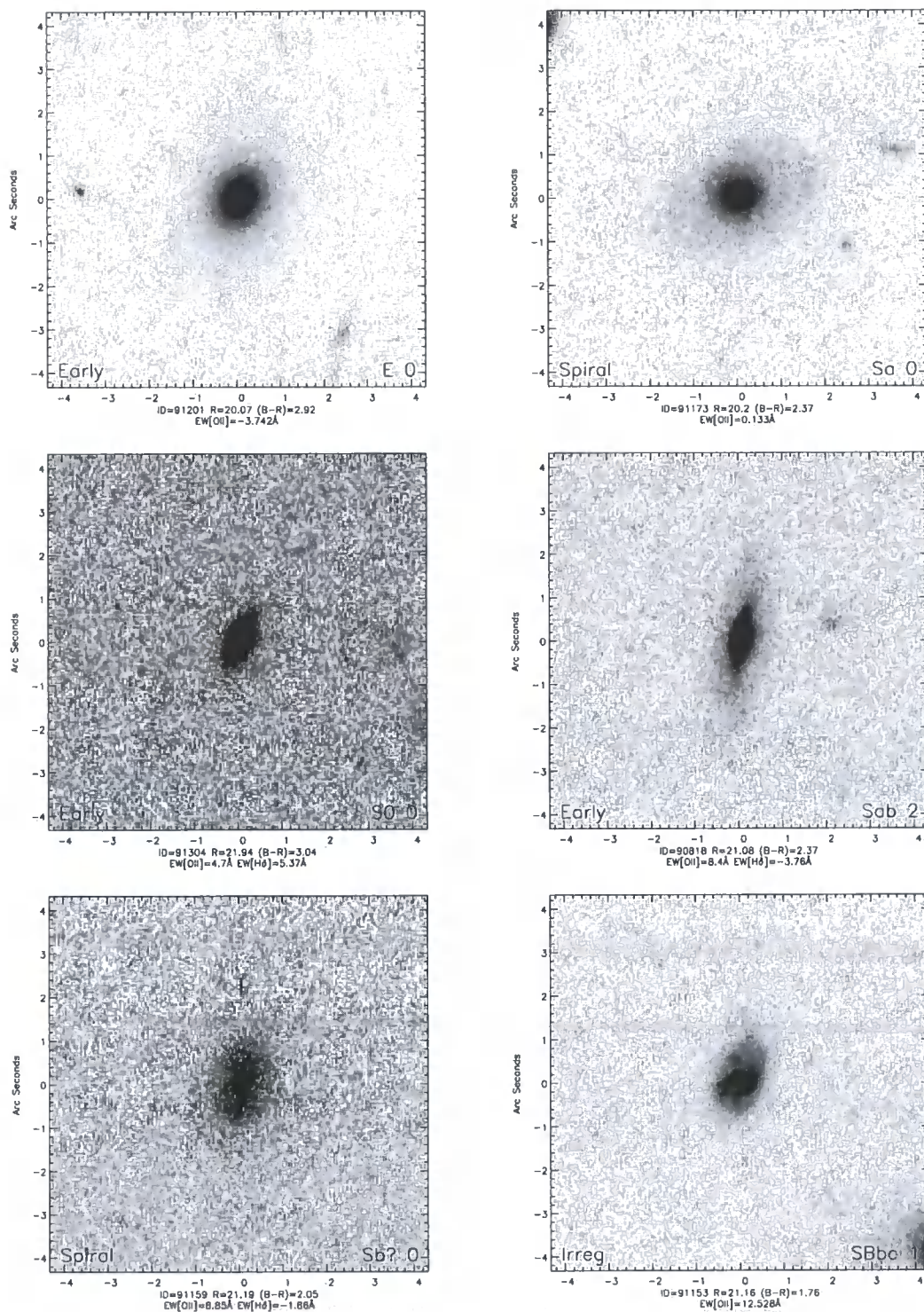


Figure 4.21: Members of group g28 at $z = 0.372$ ($160 \pm 80 \text{ km s}^{-1}$). Galaxies are labelled as described in the text.

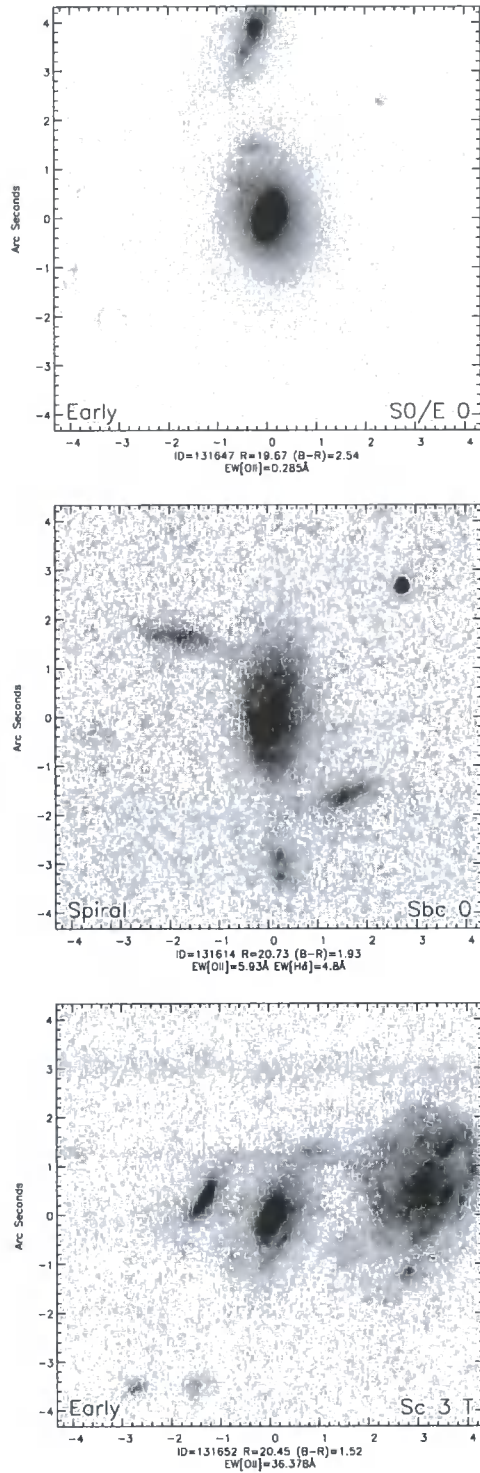


Figure 4.22: Members of group g31 at $z = 0.392$ ($565 \pm 352 \text{ km s}^{-1}$). Galaxies are labelled as described in the text.

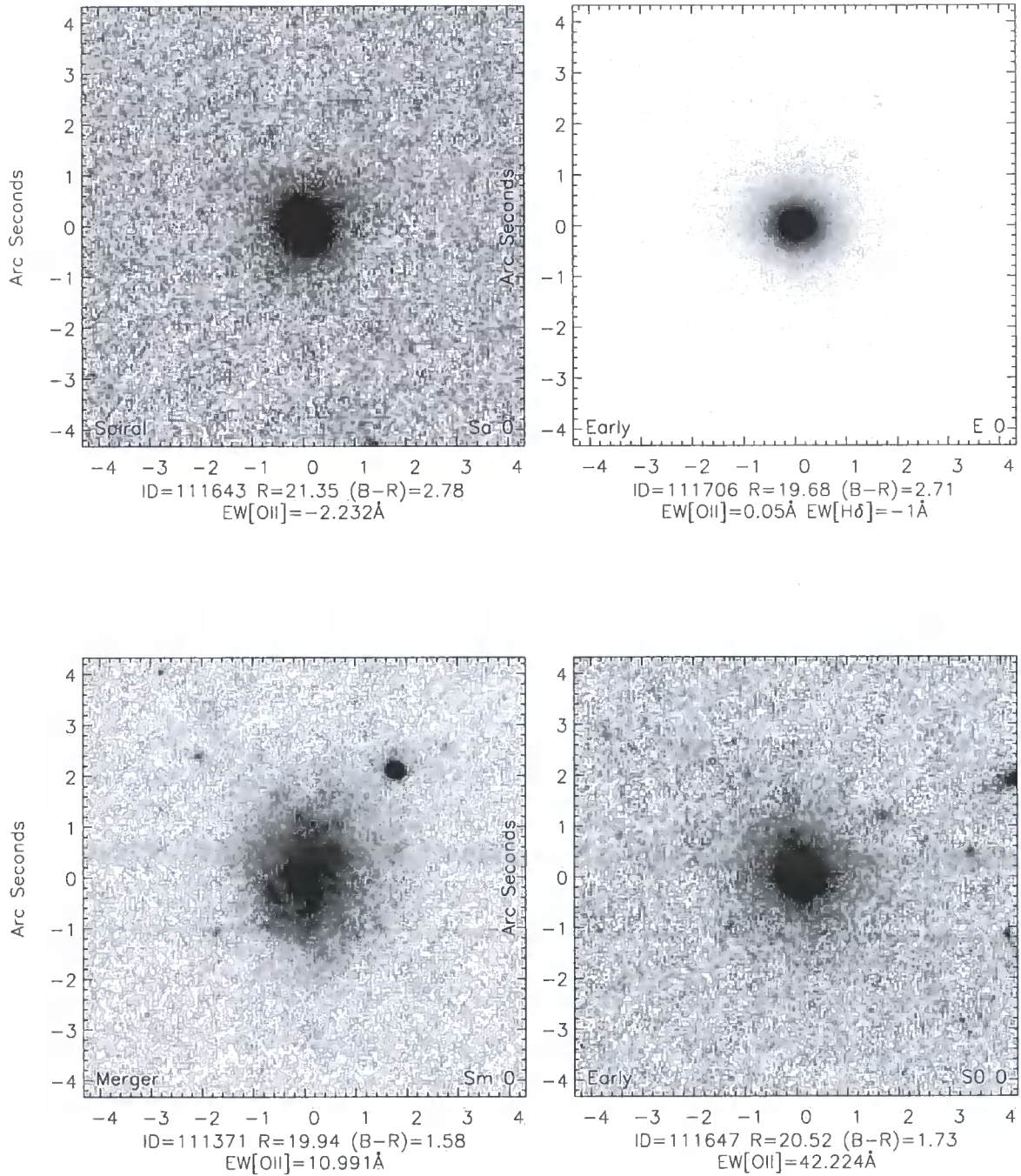


Figure 4.23: Members of group g32 at $z = 0.394$ ($519 \pm 98 \text{ km s}^{-1}$). Galaxies are labelled as described in the text.

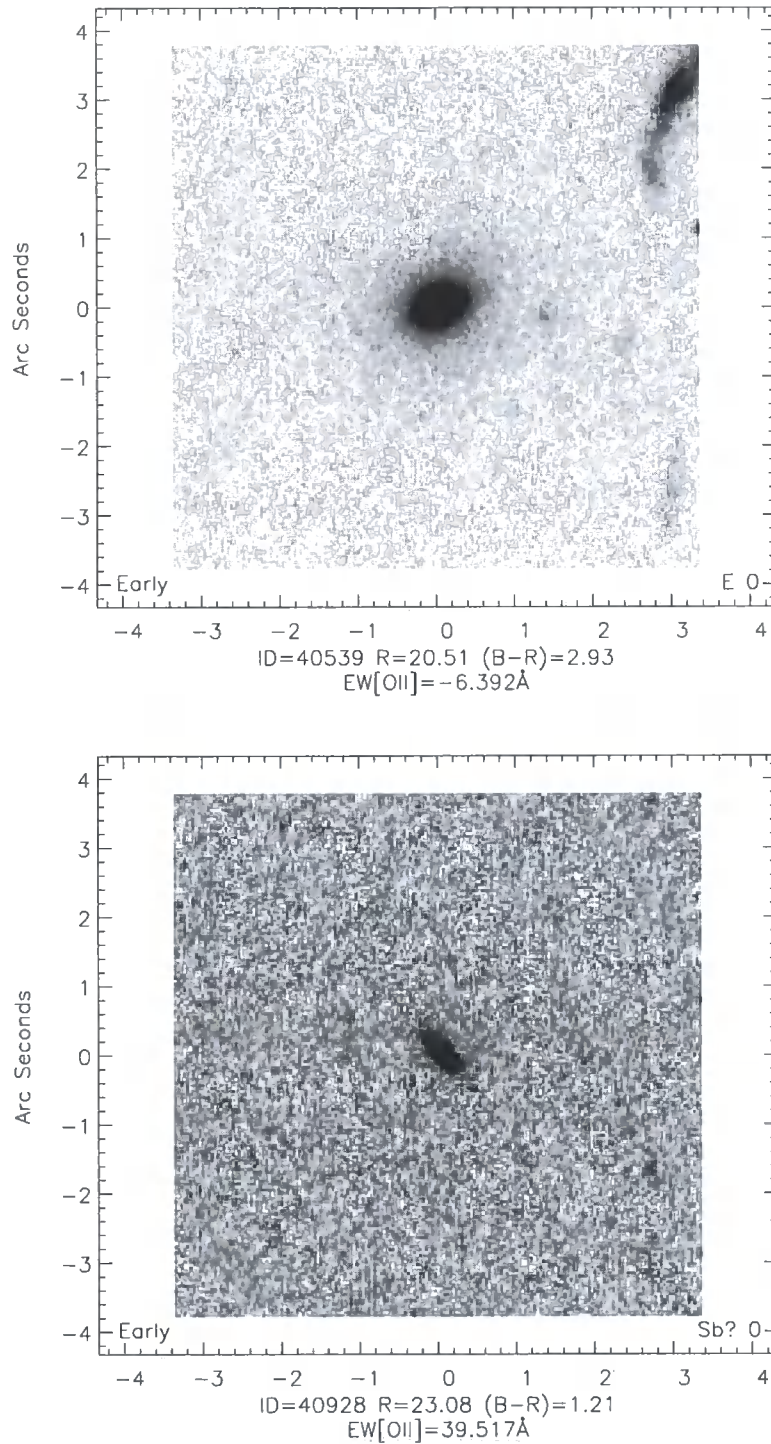


Figure 4.24: Members of group g33 at $z = 0.406$ ($194 \pm 100 \text{ km s}^{-1}$). Galaxies are labelled as described in the text.

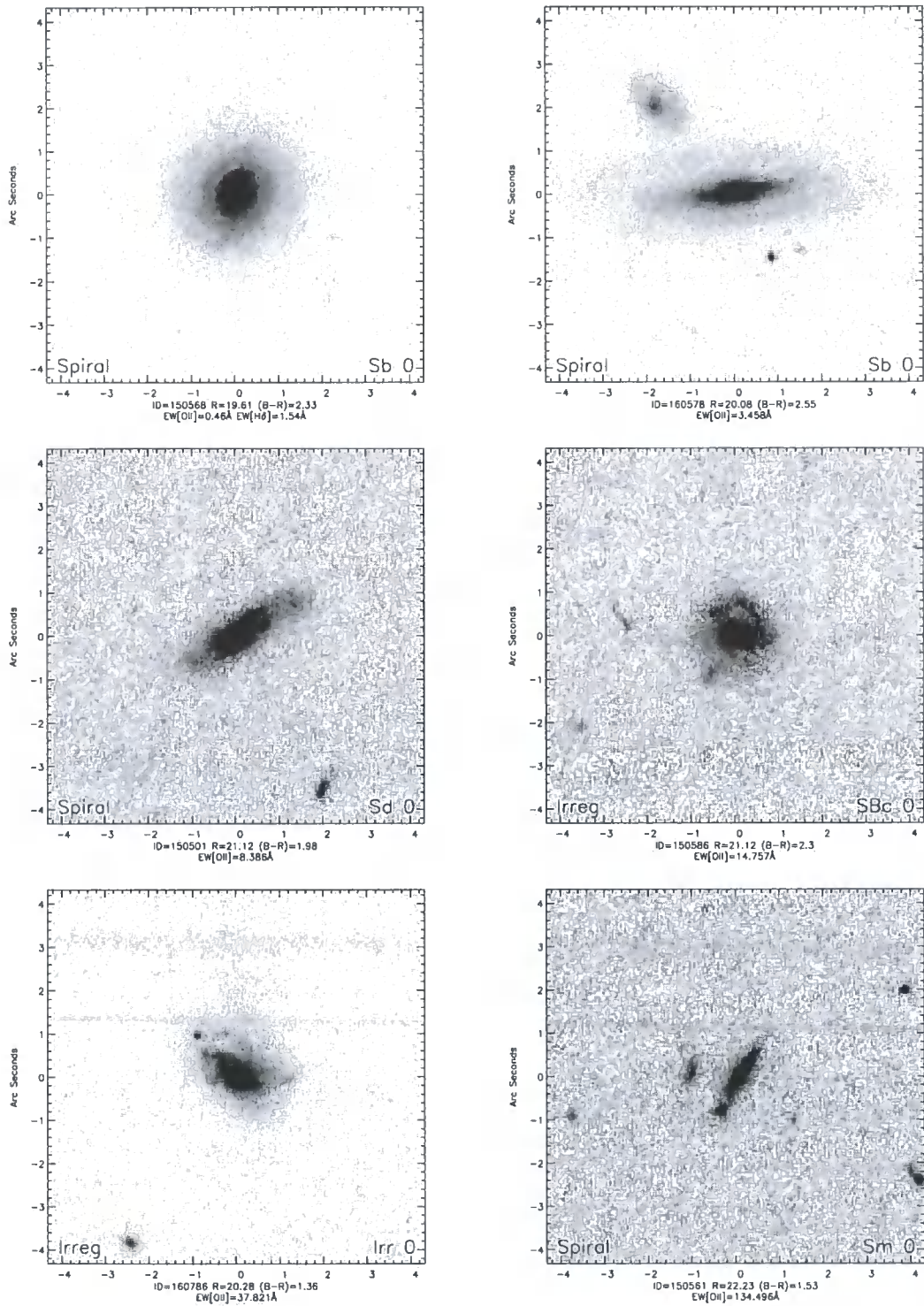


Figure 4.25: Members of group g34 at $z = 0.465$ ($408 \pm 106 \text{ km s}^{-1}$). Galaxies are labelled as described in the text.

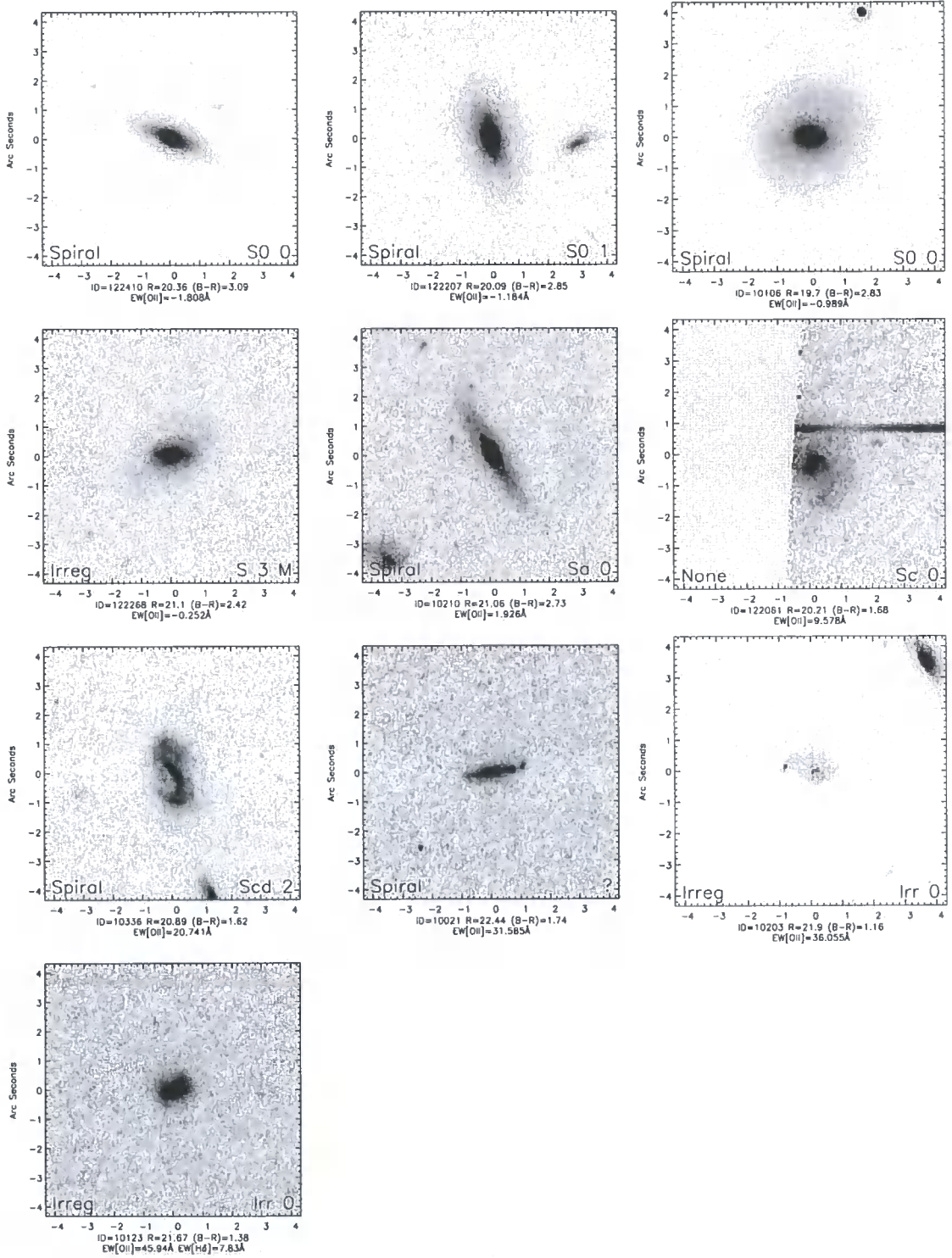


Figure 4.26: Members of group g37 at $z = 0.471$ ($419 \pm 97 \text{ km s}^{-1}$). Galaxies are labelled as described in the text.

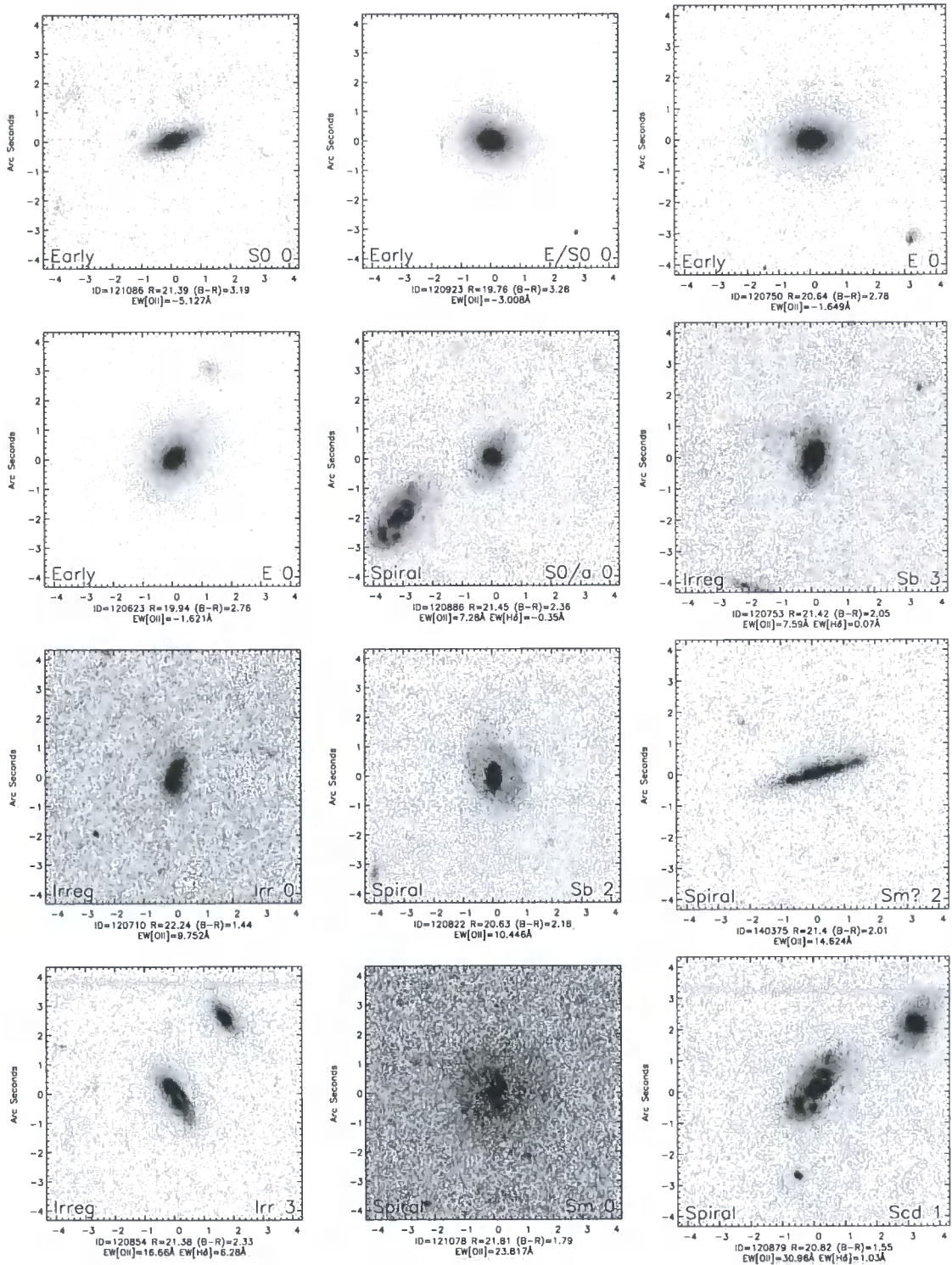


Figure 4.27: Members of group g38 at $z = 0.51$ ($808 \pm 68 \text{ km s}^{-1}$). Galaxies are labelled as described in the text.

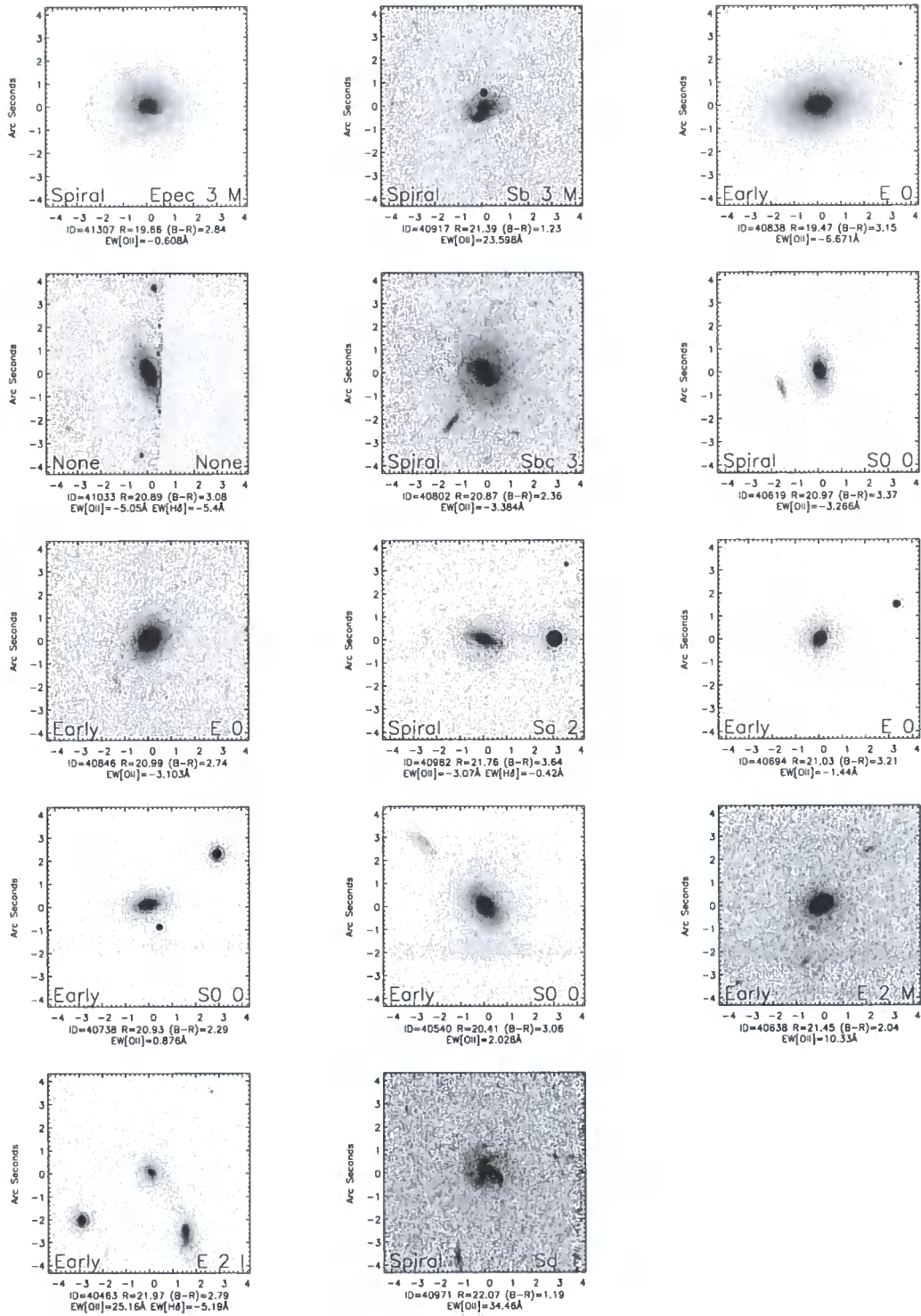


Figure 4.28: Members of group g39 at $z = 0.536$ (454 ± 88 km s $^{-1}$). Galaxies are labelled as described in the text.

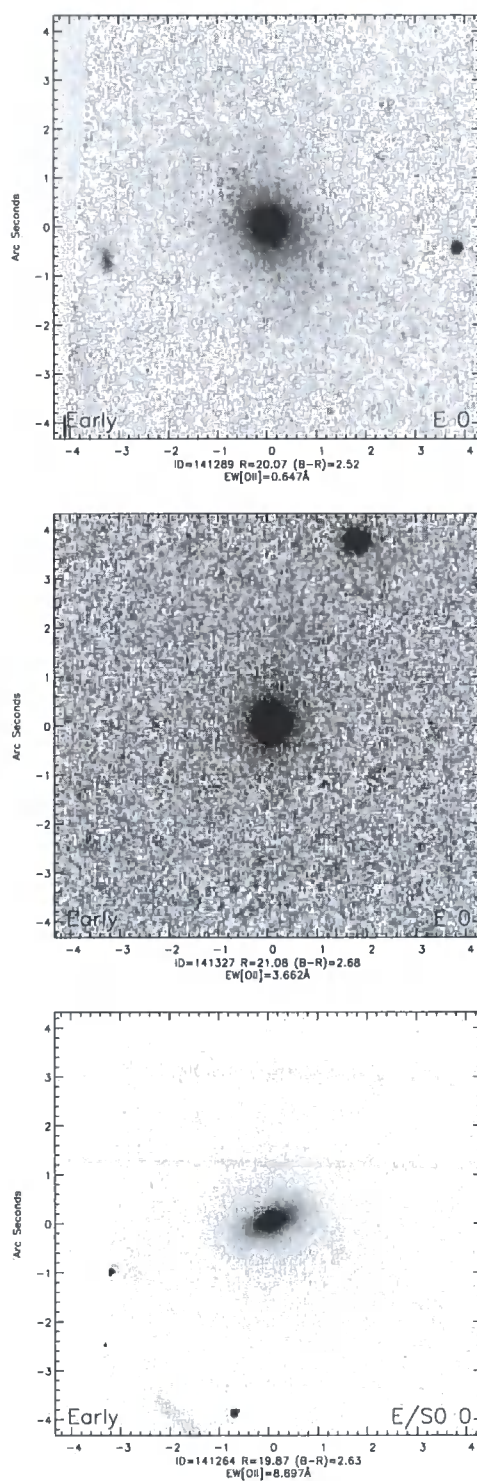


Figure 4.29: Members of group g129 at $z = 0.317$ ($225 \pm 76 \text{ km s}^{-1}$). Galaxies are labelled as described in the text.

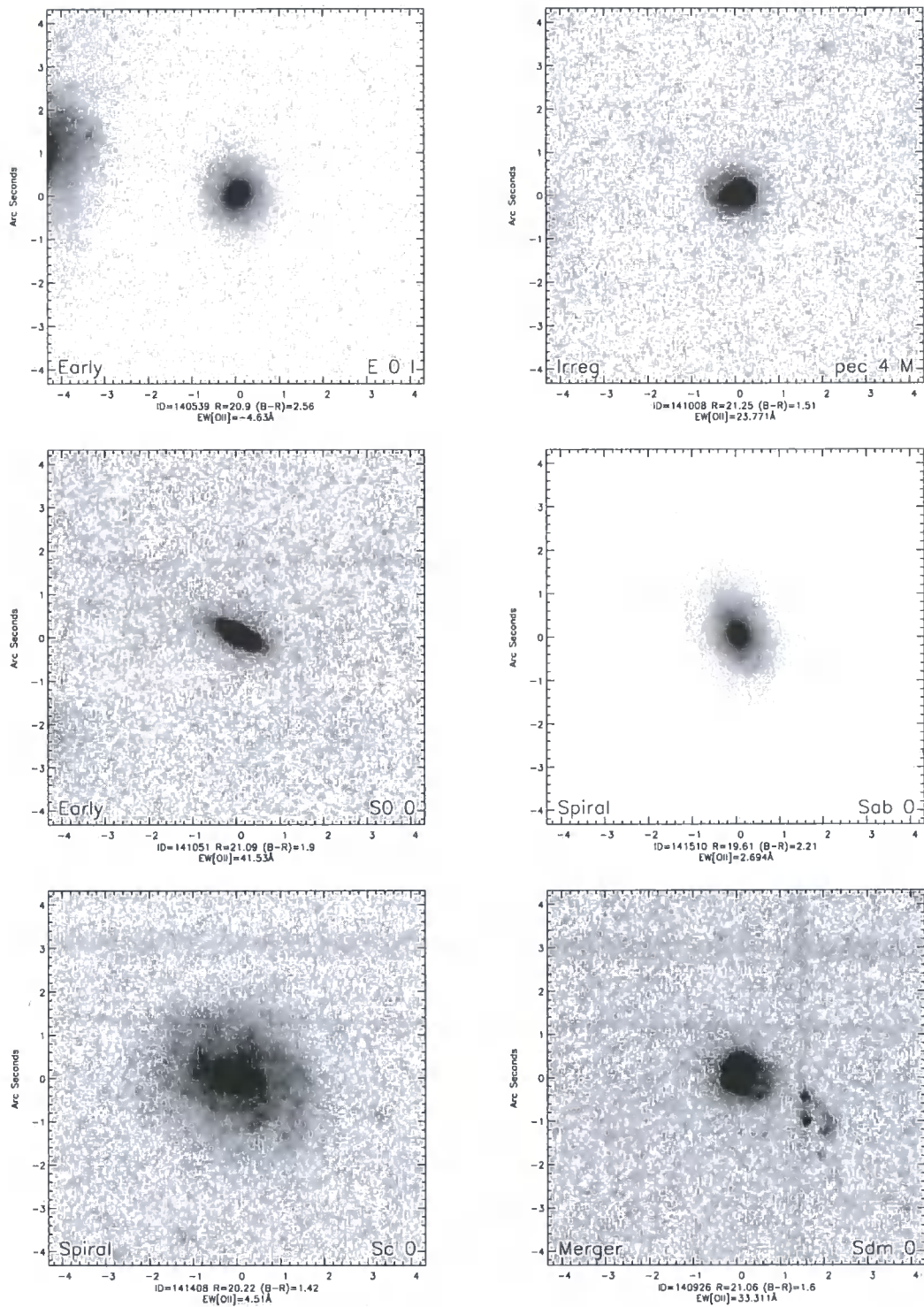


Figure 4.30: Members of group g132 at $z = 0.359$ ($375 \pm 34 \text{ km s}^{-1}$). Galaxies are labelled as described in the text.

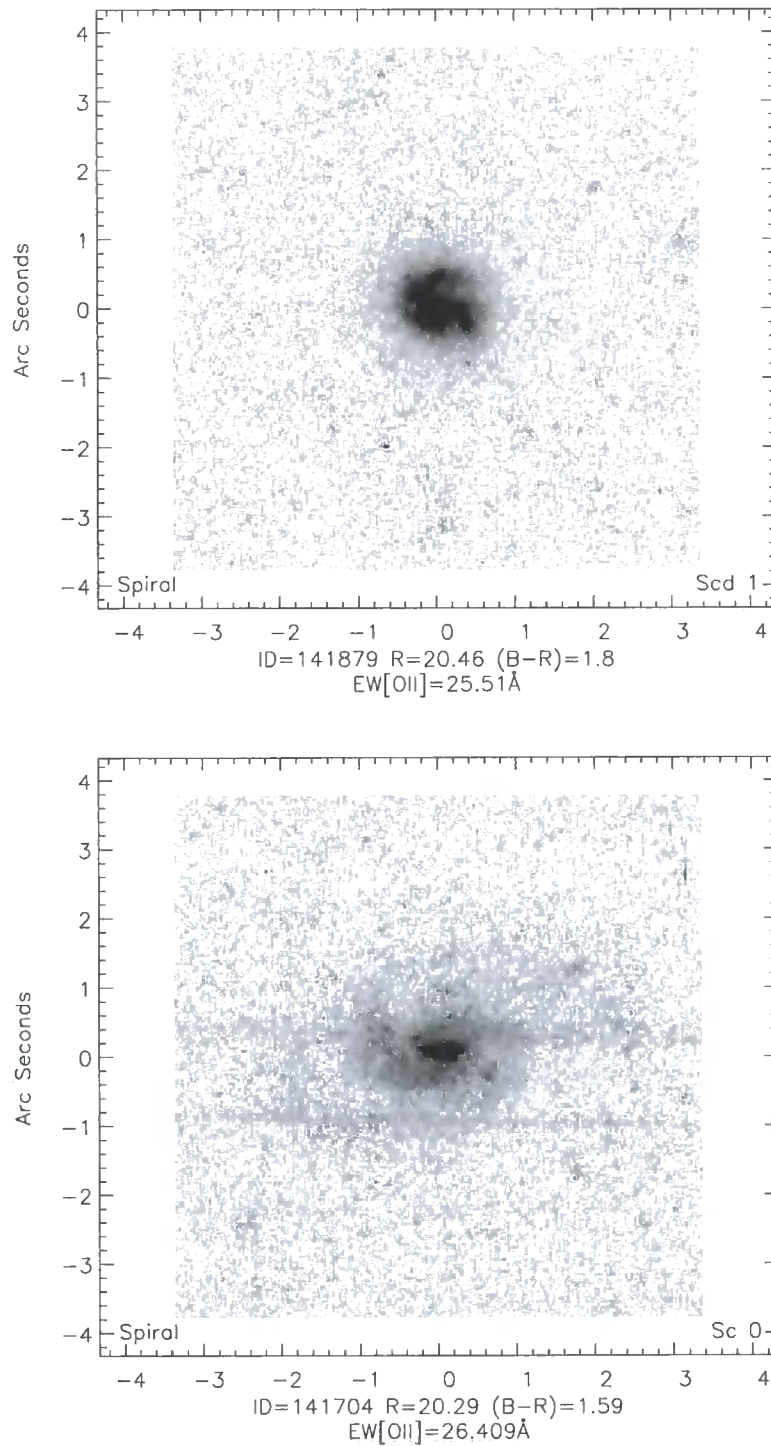


Figure 4.31: Members of group g133 at $z = 0.373$ ($204 \pm 38 \text{ km s}^{-1}$). Galaxies are labelled as described in the text.

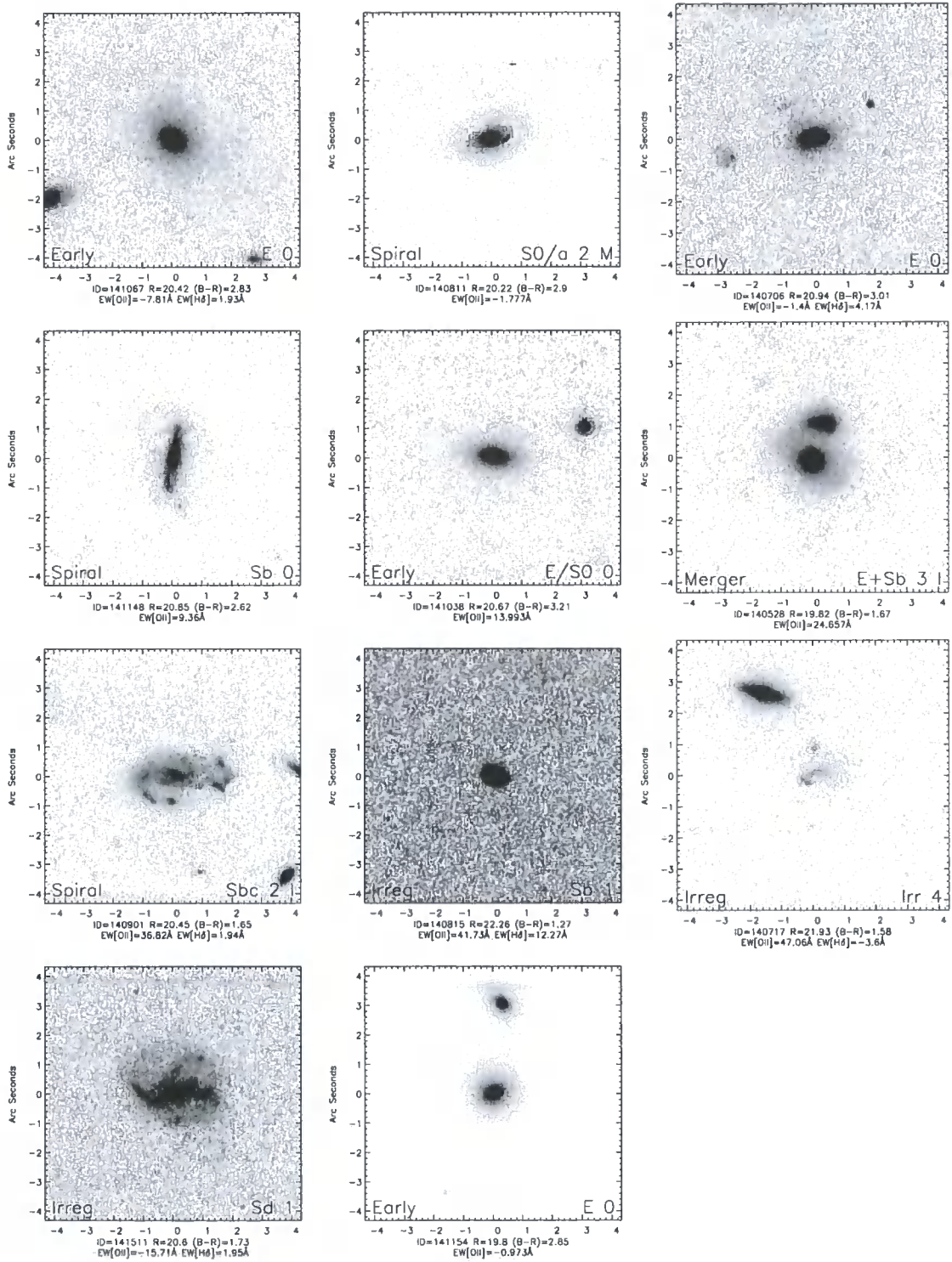


Figure 4.32: Members of group g134 at $z = 0.392$ ($284 \pm 78 \text{ km s}^{-1}$). Galaxies are labelled as described in the text.



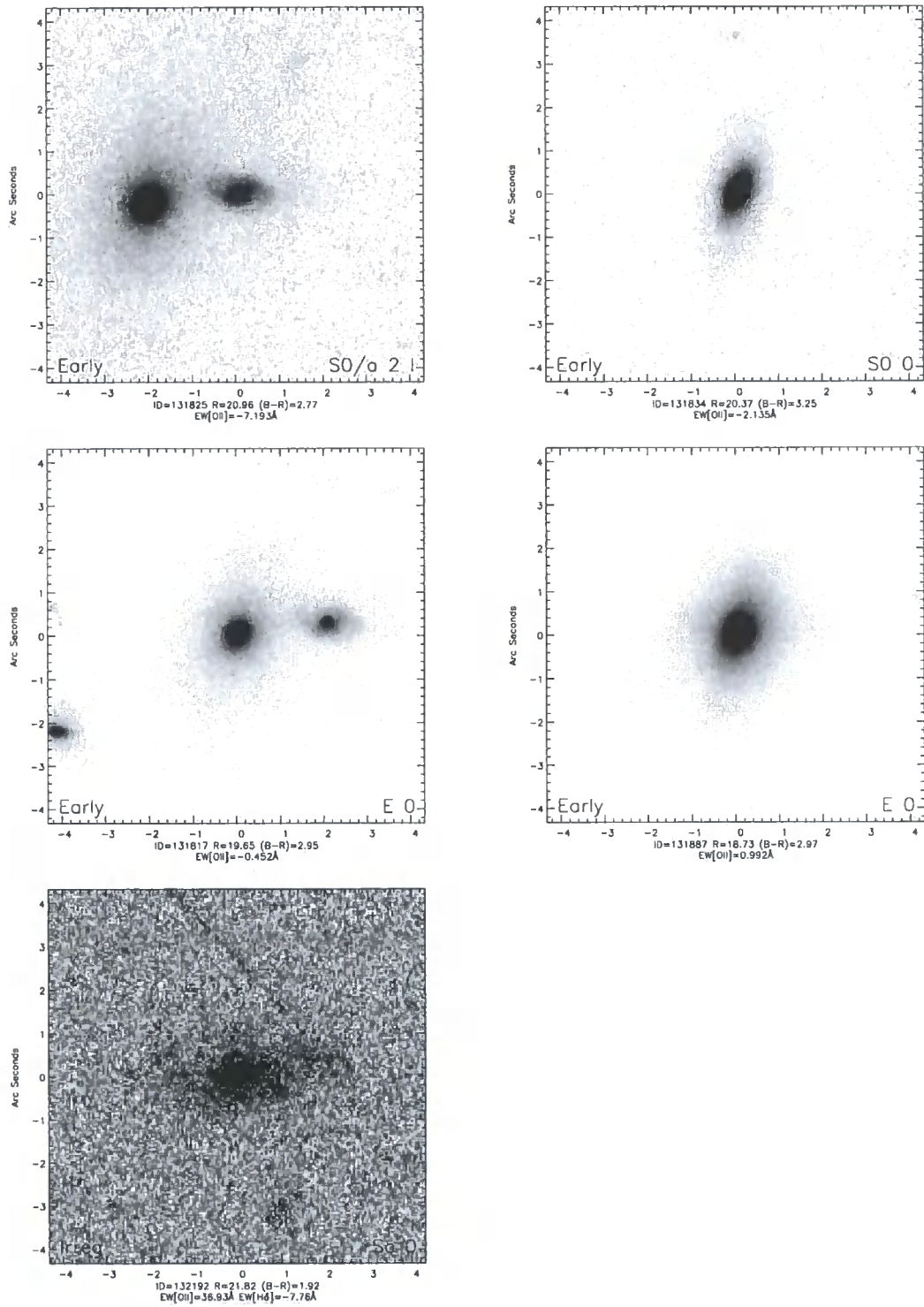


Figure 4.33: Members of group g137 at $z = 0.425$ ($314 \pm 84 \text{ km s}^{-1}$). Galaxies are labelled as described in the text.

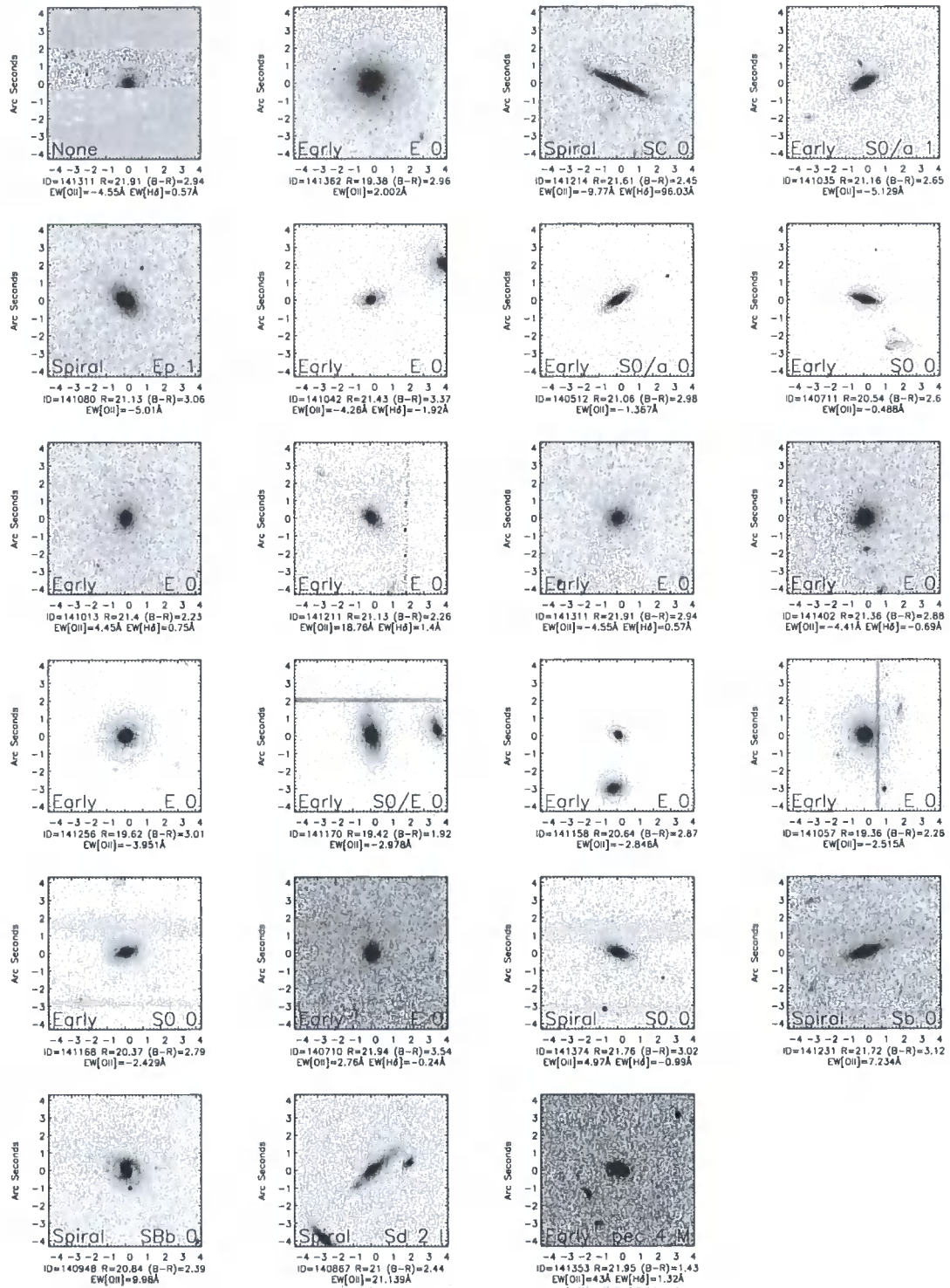


Figure 4.34: Members of group g138 at $z = 0.437$ ($711 \pm 81 \text{ km s}^{-1}$). Galaxies are labelled as described in the text.

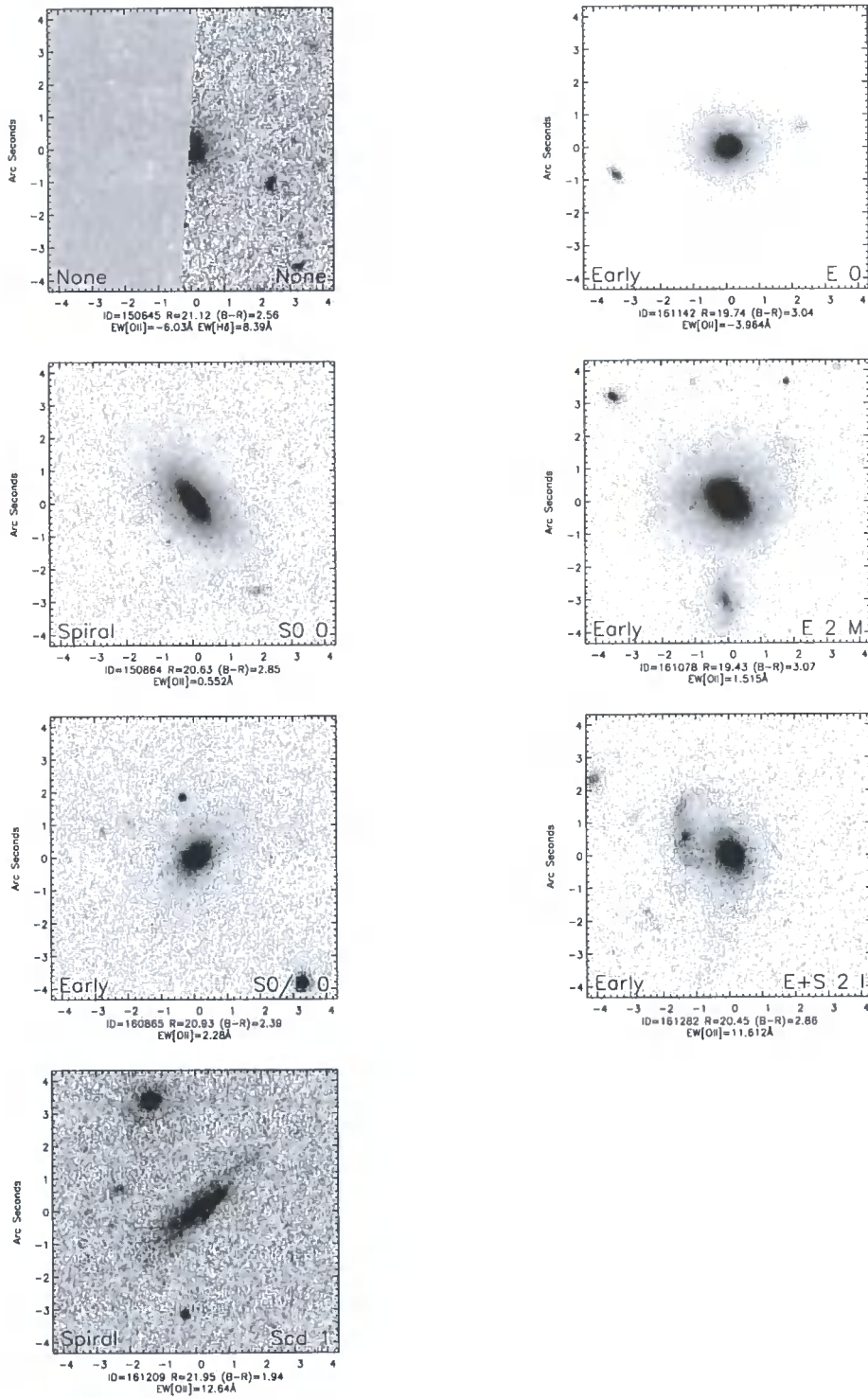


Figure 4.35: Members of group g139 at $z = 0.439$ ($314 \pm 84 \text{ km s}^{-1}$). Galaxies are labelled as described in the text.

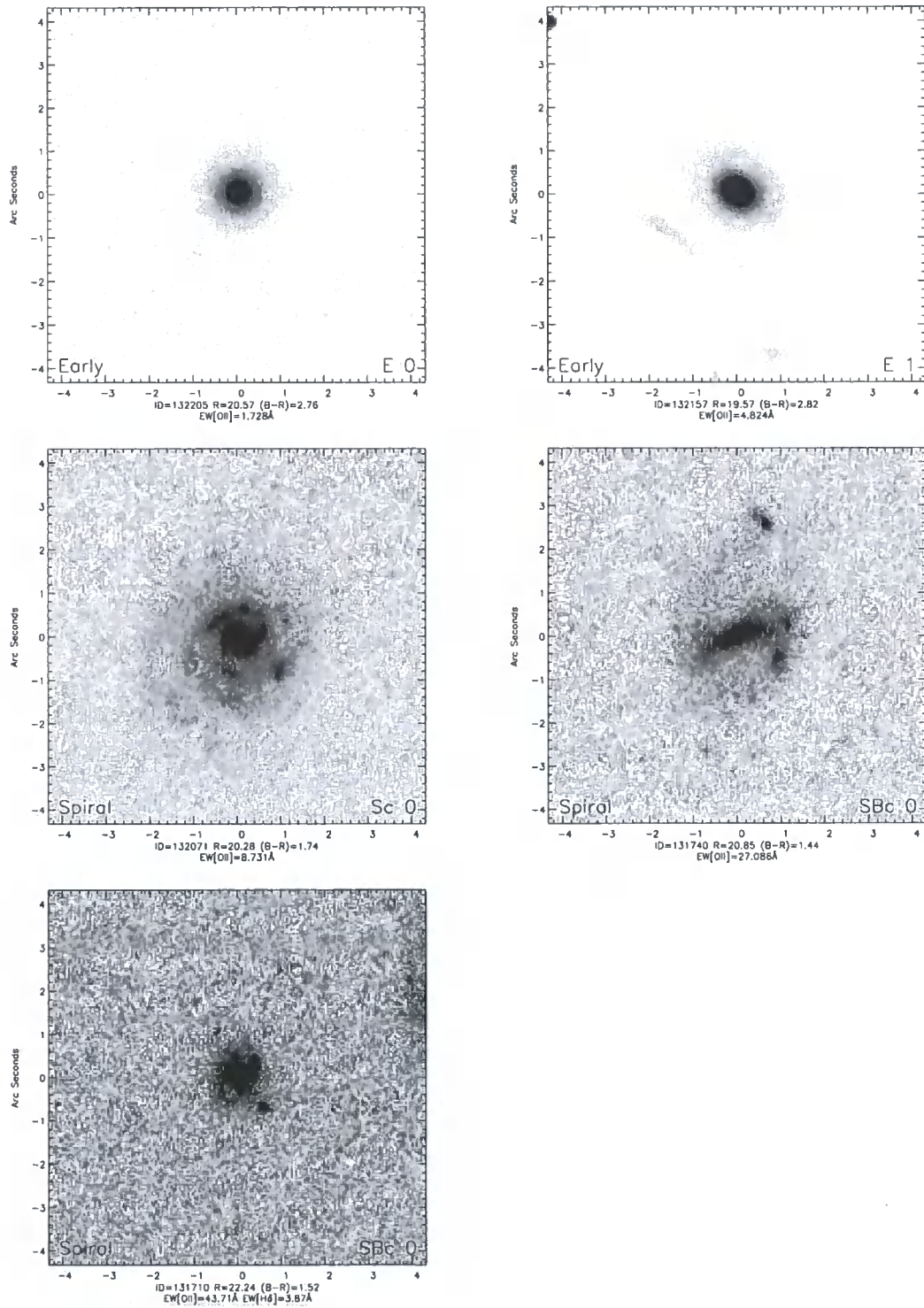


Figure 4.36: Members of group g140 at $z = 0.465$ ($98 \pm 129 \text{ km s}^{-1}$). Galaxies are labelled as described in the text.

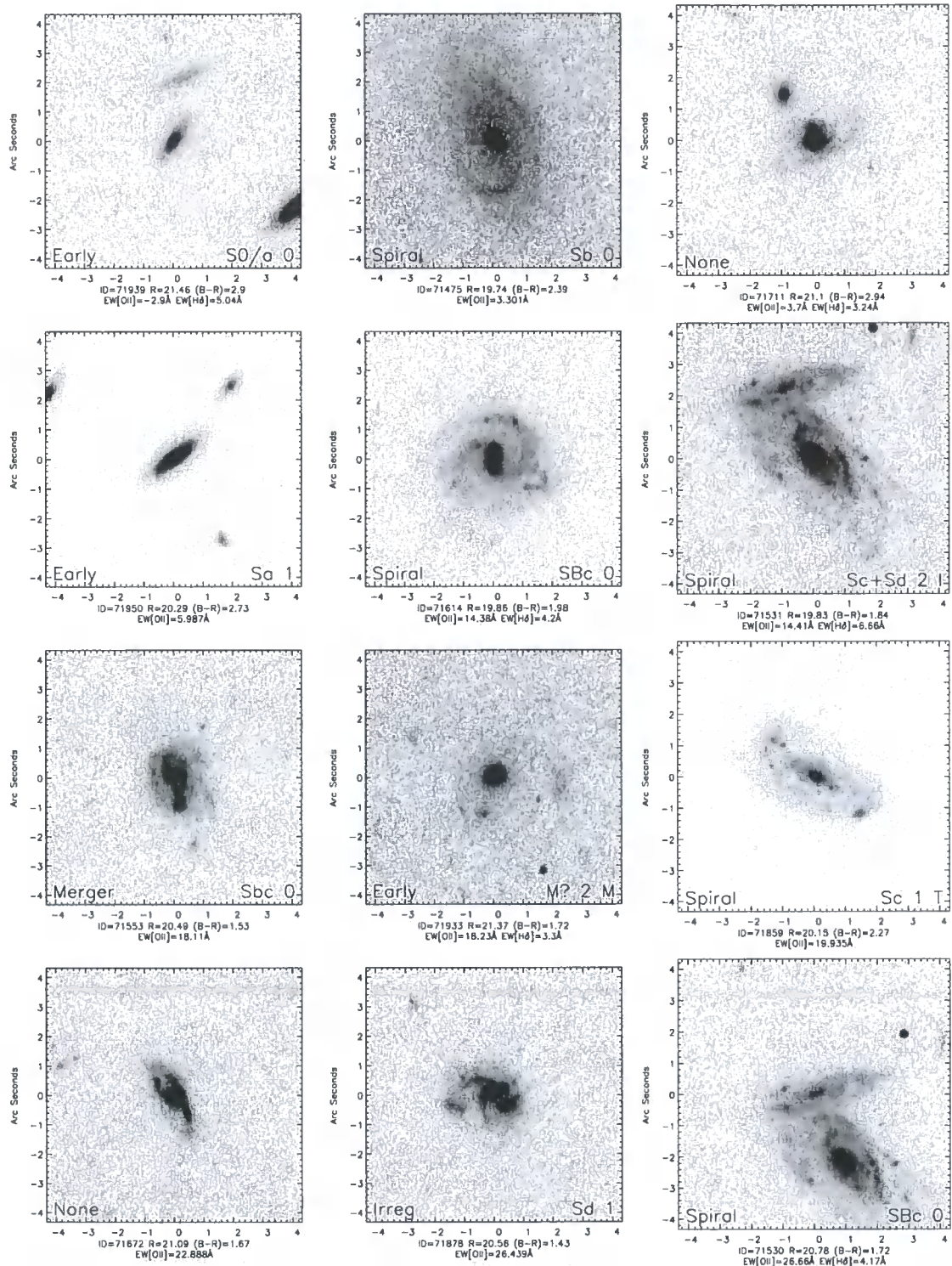


Figure 4.37: Members of group g244 at $z = 0.47$ ($270 \pm 54 \text{ km s}^{-1}$). Galaxies are labelled as described in the text.

4.3.2 Comparison of morphological classifications

My classifications led to a final sample of 99 early-types, 122 spirals, 49 irregulars and 12 mergers.

We compare the classifications of myself and AO, aiming to demonstrate the level of agreement and uncertainty within the classified sample. In Table 4.1, we show the number of galaxies with each combination of my classification and AO classification. The AO Type Code in column 2 is simply used as a numeric identifier of each AO classification type. The occasional galaxies with an extremely rare classification by AO (e.g. Ep) or with 2 components (e.g. E+Sb), have been grouped together with similar classifications.

Table 4.1 shows that the classifications of myself and AO are mostly compatible. From the AO classifications of probable S0s (AO Type Codes 4,6 and 7), my classifications include 24 as early-type (intended to include S0s) and 13 as spirals (not intended). This suggests that I am misidentifying $\sim 35\%$ of S0s as spiral galaxies. However, the 13 galaxies which I identified as early-type and which AO identified as spirals represent an equivalent sample of galaxies with mis-matched classifications in the opposite direction. Therefore the total number of early-type galaxies is similar in both sets of classification. AO identifies 153 spiral galaxies in total (AO Type Codes 8-22). From this sub-sample I identify 100 as spirals, 13 as early-types, 31 as irregulars (all of AO type Sb - Sm) and 7 as mergers (2 galaxies I do not classify as they overlap the edge of the HST image). Overall in my classifications, this leads to an overestimate of the number of irregular type galaxies and an underestimate of the number of spiral galaxies relative to AO. This effect is unsurprising: an inexperienced classifier is likely not to recognise the wide variety of spiral structures which are present in the Universe. As an example, galaxy 141511 in group 134 (the bottom-right panel of Figure 4.32) is classified by AO as a Sd type galaxy, where I classified it as an irregular type.

4.4 Results

As the more experienced classifier and with the more detailed morphological classifications, we choose the classifications of AO for further interpretation. We have shown that they are generally consistent with my own more straightforward classification system. However, we recognise that these results are still preliminary and will be subject to a more thorough treatment with detailed classifications from a greater number of authors before publication in a journal.

Table 4.1: The number of galaxies with each combination of my classification and AO classification.

AO Type	AO Type Code	My Type				
		None	Early	Spiral	Irregular	Merger
None	0	N/A	0	0	0	1
X	1	0	3	0	0	0
E	2	0	46	1	0	0
E/S0	3	0	8	0	0	0
S0/E	4	0	4	0	0	0
Ep E+S Epec E+Sb	5	0	1	2	0	1
S0	6	0	15	10	0	0
S0/a	7	0	5	3	0	0
Sa SA	8	0	5	9	0	0
Sab	9	0	1	8	0	0
Sb Sb?	10	1	3	20	7	0
SBb	11	0	0	2	0	0
Sbc Sb+Sc	12	0	0	15	3	2
SBbc	13	0	0	1	1	0
Sc SC Sc? Sc??	14	1	2	22	6	1
SBc	15	0	0	4	1	0
Scd Sc+Sd	16	0	0	5	0	0
Sd Sd+Sd	17	0	1	9	6	1
Sdm	18	0	0	0	2	1
Sm Sm?	19	0	0	3	3	1
SBm	20	0	0	1	0	0
S	21	0	1	0	2	1
SB	22	0	0	1	0	0
M	23	0	0	1	1	1
M? M?Irr?	24	0	1	2	1	0
Irr Irr? pec	25	0	1	1	10	2
? ??	26	0	2	2	6	0

To investigate how galaxy morphology relates to the group environment and to other galaxy properties, it is necessary to group the fine MORPHS morphological classes into somewhat broader bins of morphology. In this way the properties of group galaxies which are different from the field can be deduced to a higher degree of significance. We group the galaxies into broad morphological classes as follows:

- **Ellipticals:**

The elliptical class includes everything initially classed as compact (X), elliptical (E) and elliptical / S0 (E/S0).

- **S0s:**

The S0 class includes everything initially classed as S0, S0 / elliptical (S0/E) or S0/Sa.

- **Spirals:**

The spiral class includes everything on the Hubble Sequence from Sa to Sm including barred spirals. We have also created 3 sub-classes of spiral galaxies:

1. **Early-type spirals:** This includes everything initially classed as Sa, Sab, Sb, SBb, S or SB.
2. **Late-type spirals:** This includes everything initially classed as Sbc, SBbc, Sc, SBc or Sd.
3. **Latest-type spirals:** This includes everything initially classed as Sdm, Sm or SBm.

- **Irregular and Merger types:** This includes everything classified as Irregular, peculiar, unusual (?) and merger (M). These individual classes have too few members to detect any significant trends. Therefore we have combined them to form a population of “unusual” objects. However for some purposes we have also divided this into 2 sub-classes:

1. **Irregulars:** This includes everything initially classed as Irr, pec, ? or ??.
2. **Mergers:** This includes everything initially classed as M or M/Irr?

In the following sections we will investigate how galaxy properties are influenced by the group environment, with particular emphasis on the galaxy morphology.

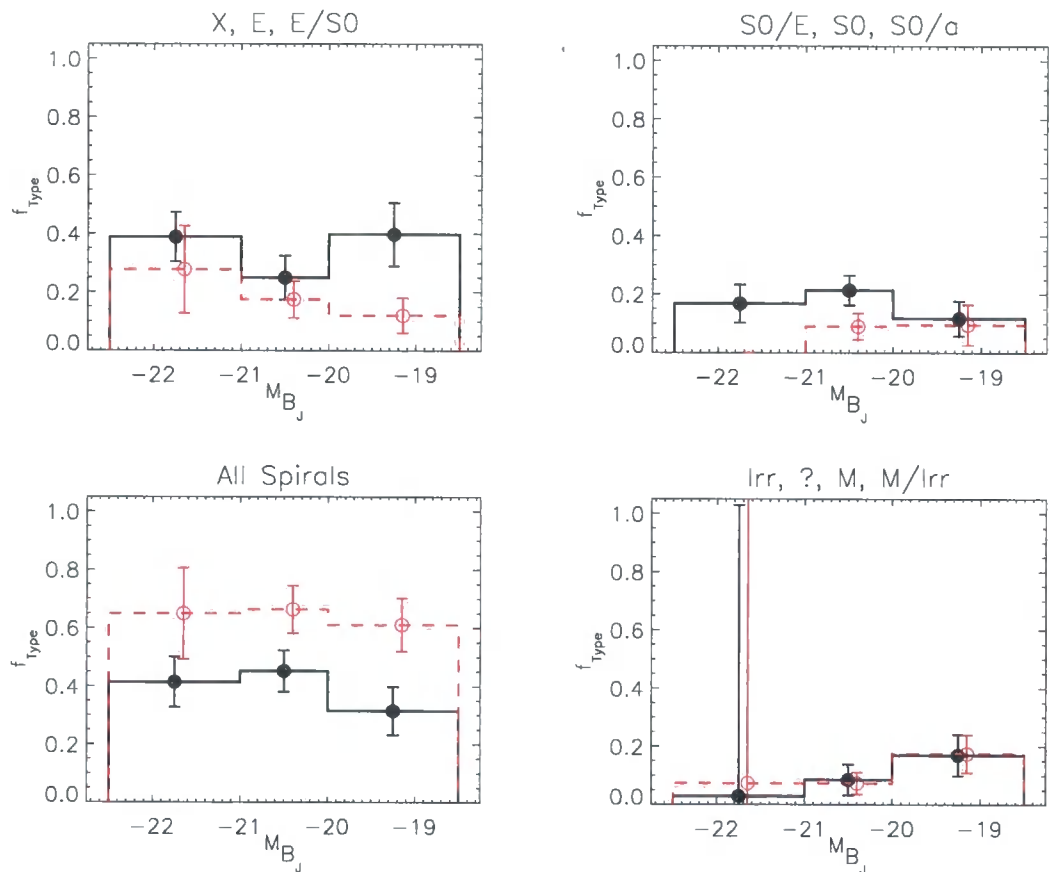


Figure 4.38: The fraction of each morphological type of galaxy, f_{type} , in 3 bins of luminosity: Bright ($M_{b_j} < -21.0$), Control ($-21.0 \leq M_{b_j} < -20.0$) and Faint ($-20.0 \leq M_{b_j} \leq -18.5$). The solid line with the filled circles represents the group galaxy population and the dashed line with the open circles represents the field population. Errors are estimated using the Jackknife technique and field points are offset slightly in M_{b_j} for clarity. This figure clearly shows that the CNOC2 groups possess a larger fraction of early galaxy types (elliptical and S0) than the field, in place of spiral galaxies, more common in the field.

4.4.1 Are early-type galaxies more prevalent in groups than in the field?

We begin by examining the morphological composition of the group and field galaxy populations. In Figure 4.38 we show the fraction of galaxies of each morphological type, f_{type} in 3 bins of luminosity ($M_{b_J} < -21.0$, $-21.0 \leq M_{b_J} < -20.0$, $-20.0 \leq M_{b_J} \leq -18.5$). The solid line with the filled circles represents the group galaxy population and the dashed line with the open circles represents the field population. Errors are estimated using the Jackknife technique (Efron, 1982) and we also use these errors to estimate the significance of each result. It shows that whilst spiral galaxies dominate the field galaxy population, there is a significant deficit of spirals in galaxy groups (3σ computed for all galaxies $M_{b_J} \leq -18.5$). In the place of these spirals, there is an excess of early-type galaxies in groups. There is a 2.7σ excess of ellipticals and a 1.3σ excess of S0 type galaxies in total. Figure 4.38 indicates that the elliptical excess is most significant at faint luminosities, where the field elliptical population is less important. However at brighter $\lesssim -20.0$ luminosities, the S0 population seems to become very important in groups. Down to our magnitude limit of $R_C = 22.0$ we believe that the elliptical versus S0 classification is robust, since galaxy classification should be possible down to $R_C = 23.9$ (Smail et al., 1997).

4.4.2 Star Formation across the Hubble Sequence

We now examine the basic properties ($\text{EW}[\text{OII}], M_{b_J}$) of each morphological class of galaxies. Figure 4.39 shows the distribution of $\text{EW}[\text{OII}]$ for each morphological class in group galaxies (solid line) and field galaxies (dashed line). In each case the histogram represents the fraction of galaxies of each morphological class (including sub-classes) and bin of $\text{EW}[\text{OII}]$ from the whole population of either group or field galaxies.

From Figure 4.39 it is clear that later galaxy types (spirals, irregulars) are much more highly star-forming (higher $\text{EW}[\text{OII}]$) than earlier types (ellipticals, S0s). This is unsurprising as we know that morphology is strongly correlated with star formation and galaxy colour (See Chapter 1). However it is more interesting to note that early spirals seem to be more frequently passive in groups than in the field. We will investigate this trend in more detail.

Figure 4.40 shows the b_J -band luminosity distribution of galaxies divided in the same way into bins of morphology and environment. The top two panels show that there is a particular excess of bright early-type galaxies in groups (ellipticals and S0s). This

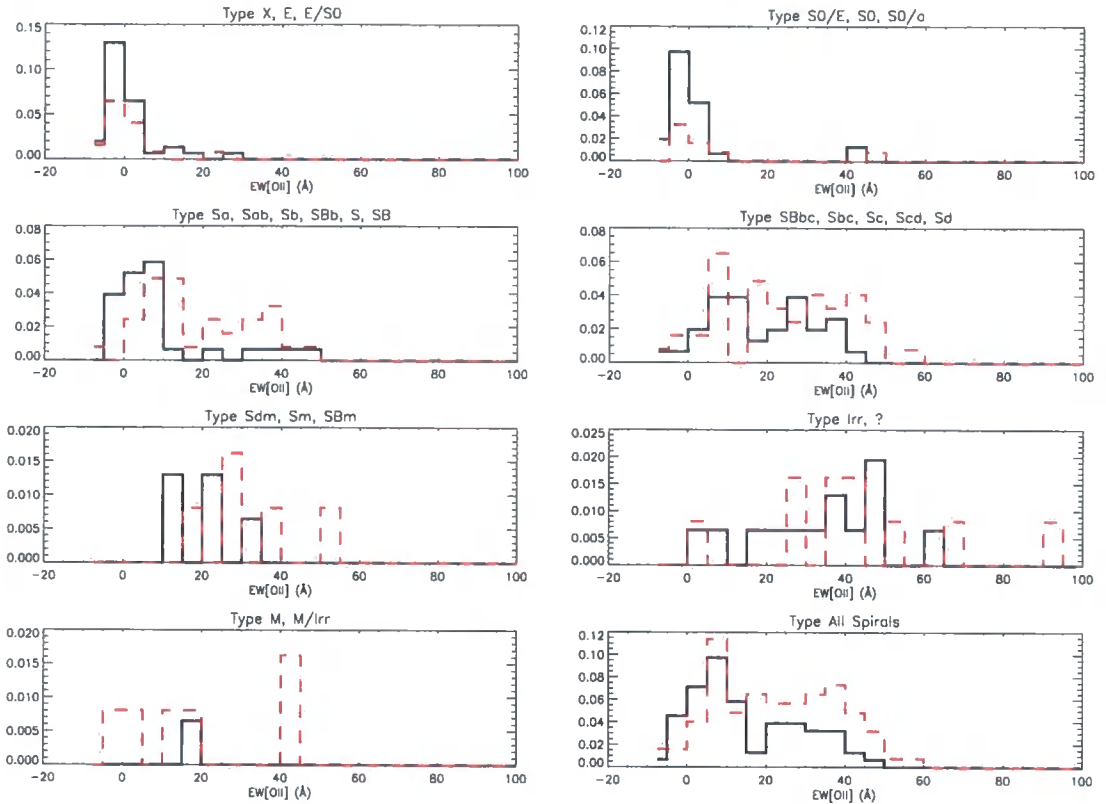


Figure 4.39: The distribution of $\text{EW}[\text{OII}] (\text{\AA})$ of field (dashed line) and group (solid line) galaxies, for classified galaxies of each morphological class. Galaxies of later morphological type are more frequently star-forming, as expected.

suggests that the suppression of star formation in groups might simply be a consequence of a top-heavy galaxy mass distribution, in line with the excess of bright galaxies in groups (Chapter 3). This is likely to be related to an extended history of major and minor mergers for group galaxies. To test this theory, we resample the field galaxy population to match the b_J -band luminosity distribution of group galaxies. For each group galaxy, we select the field galaxy of the same morphological type which matches the group galaxy most closely in luminosity.

Figure 4.41 shows a comparison of the $\text{EW}[\text{OII}]$ distribution in group and field galaxies of each morphological type. On this occasion, the field has been resampled as described above to match the luminosity distribution of group galaxies. The distribution of $\text{EW}[\text{OII}]$ is now well matched in the group and field populations for each morphological type other than early-type spiral galaxies. In the field, there is no population of passive spirals analogous to that found in groups, even when it is resampled to match the group luminosity distribution. Whilst we note that we are limited by the small number of bright field spiral

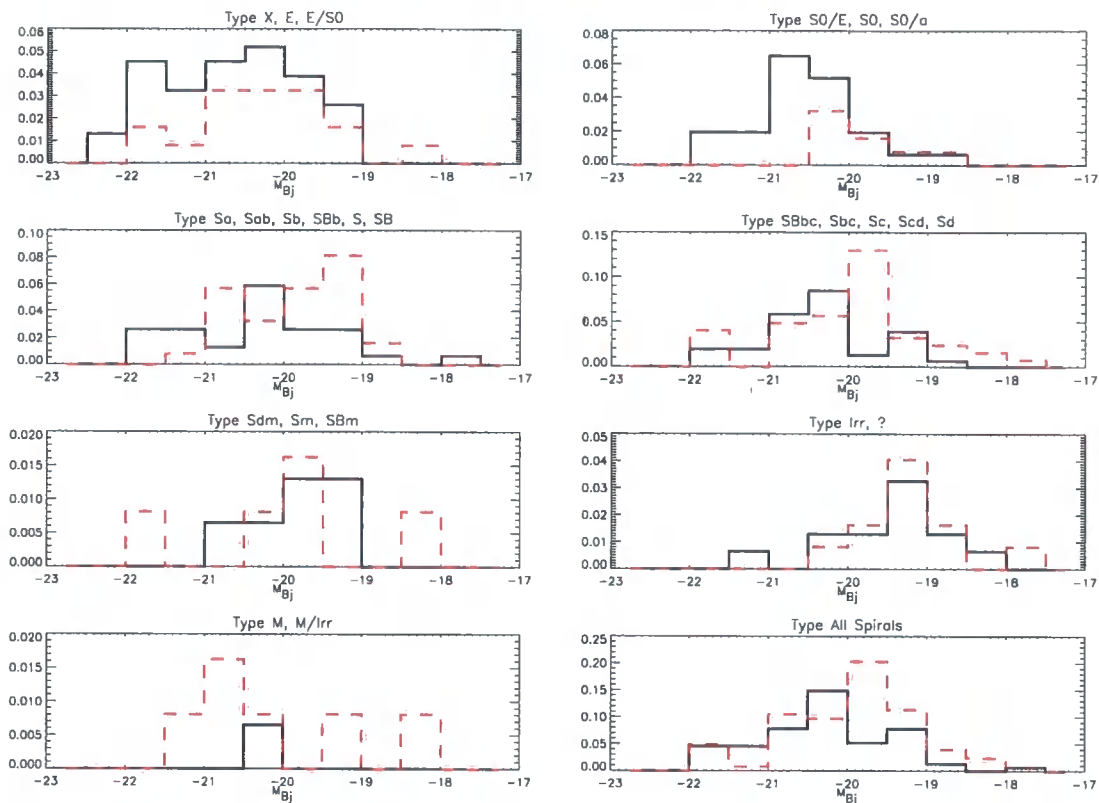


Figure 4.40: The luminosity (M_{b_j}) distribution of field (dashed line) and group (solid line) galaxies, for classified galaxies of each morphological class. Early-type galaxies (ellipticals and S0s) are often more luminous in groups than in the field.

galaxies for resampling, this result is analogous to that of Balogh et al. (1998) who find a small excess of passive disk-dominated galaxies in galaxy clusters with respect to the field. We shall investigate the passive nature of group spirals in Section 4.4.4.

4.4.3 Are S0 type galaxies significantly more common in groups?

In Section 4.4.1 we computed a significance of 1.3σ for the excess of S0 galaxies in the group environment. However Figure 4.38 shows us that this excess is of greater significance in brighter galaxies, where the field S0 population disappears completely. In Figure 4.42 we show the luminosity function of S0 galaxies in groups (solid line) and the field (dashed line). Galaxies are weighted by W_C to account for the spectroscopic selection functions (see Section 3.6.1). It is clear that there is an excess population of S0 galaxies in groups brighter than $M_{b_j} \lesssim -20.5$ where there are 16 group and 0 field S0 type galaxies with measured redshifts in the range $0.3 \leq z \leq 0.55$. We compute the fraction of S0 galaxies

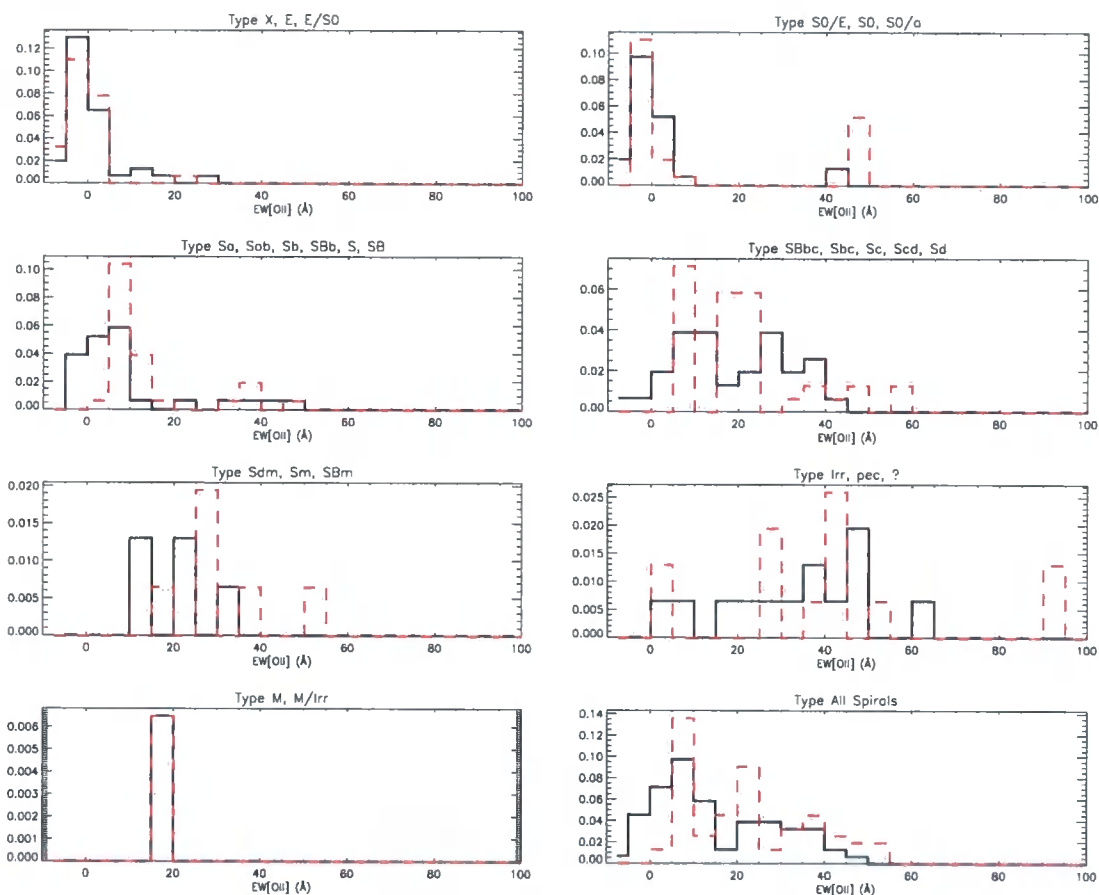


Figure 4.41: As figure 4.39 except with the field sample resampled to match the luminosity distribution of the group galaxies for each morphological class. The resampled field galaxies do not include a passive population of early-type spirals to match that found in groups.

in this luminosity range to be $f_{S0} = 0.23$ in the groups. A bootstrap-resampling technique is then used to estimate the significance of this excess with respect to $f_{S0} = 0$ in the field. By selecting a population of galaxies the size of the total bright field galaxy population ($M_{b_j} \leq -20.5$) from the groups 10^5 times we determine that on only 0.027% of occasions do we obtain $f_{S0} = 0$ (99.973% confidence that the group and field do not share the same parent population). From a one-tailed gaussian distribution, this is equivalent to a $\sim 3.5\sigma$ result. We note that it is necessary to repeat this process as many as 10^5 times, to obtain $f_{S0} = 0$ on a significant number of occasions. It is interesting to see if S0 galaxies are especially prevalent in groups of a certain size. In Figure 4.43 we divide the group luminosity function into 3 bins of group velocity dispersion $\sigma(v)_{intr}$. Strikingly, the population of bright S0 galaxies is concentrated in the groups with velocity dispersions in the range 400 km s^{-1} to 600 km s^{-1} . Using the same resampling technique, we estimate the significance of the S0 population excess in these groups at 99.996% ($\sim 4\sigma$). Out of the 8 confirmed bright S0 group members in these groups, 3 lie in group 37 and 3 lie in group 39 suggesting that these groups represent a good environment for the formation of bright S0 galaxies. In both cases, the galaxies are in quite close proximity and lie along a straight line across the sky. Finally we note that S0 galaxies are predominately passive as we would expect (see Figure 4.39). In fact there are no star-forming S0 galaxies in the sample brighter than $M_{b_j} = -20.5$.

4.4.4 Are spiral galaxies more passive in groups?

In Section 4.4.2 we identified a population of passive spiral galaxies in groups which does not exist in our field sample. In this section we look at this population in more detail.

To examine the population of spiral galaxies in groups and the field, we firstly examine the luminosity functions of group and field spirals (Figure 4.44). A large number of galaxies have been classed as spirals including 67 confirmed group members and 68 field spirals (brighter than our spectroscopic magnitude limit of $R_C = 22.0$). Galaxies are weighted by the spectroscopic selection weight W_C and renormalised to match the same total number of spiral galaxies. There is clearly an excess of bright spiral galaxies in the group sample, and so it is logical to suppose that these galaxies might differ somehow from the field population. Therefore we divide our sample into 3 bins of luminosity: Bright ($M_{b_j} < -21.0$), Control ($-21.0 \leq M_{b_j} < -20.0$) and Faint ($-20.0 \leq M_{b_j} \leq -18.5$). For each luminosity bin we compute the value of f_p (the fraction of galaxies with $\text{EW}[\text{OII}] < 5\text{\AA}$) in groups and the field.

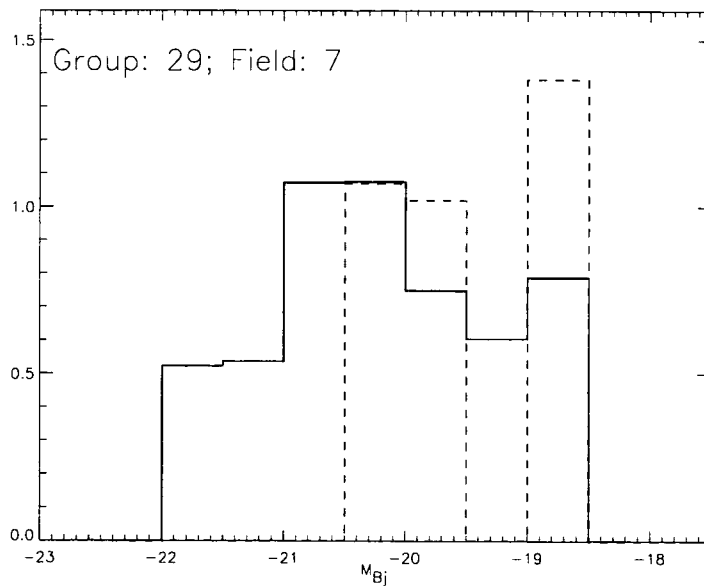


Figure 4.42: Luminosity Functions of S0 galaxies. The solid and dashed lines represent the group and field galaxy populations respectively. Galaxies are weighted by the selection weight W_C . We show the unweighted number of group and field galaxies in each sample in the top left hand corner of the plot. This figure shows that there is a significant (3.5σ) excess of bright ($M_{B_j} \leq -20.5$) S0 galaxies in groups.

Figure 4.45 shows f_p in our 3 bins of luminosity in groups (solid line, filled circles) and the field (dashed line, open circles). The population of spiral galaxies is clearly more passive in groups at brighter luminosities ($M_{B_j} \leq -20.0$). Visual inspection of this population of bright passive galaxies suggests that they are not misclassified S0-type galaxies.

Transformation mechanisms which can truncate the star formation of a galaxy without destroying its spiral structure are likely to operate preferentially in certain environmental regimes. For example, there are known populations of passive spirals in galaxy clusters (e.g. Couch et al., 1998; Dressler et al., 1999; Poggianti et al., 1999). Therefore in Figure 4.46 we examine the dependence on group velocity dispersion ($\sigma(v)_{intr}$) of this passive fraction in brighter galaxies ($M_{B_j} \leq -20.0$). We do this by dividing our groups into 3 bins of group velocity dispersion: $\sigma(v)_{intr} < 400 \text{ km s}^{-1}$, $400 \text{ km s}^{-1} \leq \sigma(v)_{intr} < 600 \text{ km s}^{-1}$ and $\sigma(v)_{intr} > 600 \text{ km s}^{-1}$. It is clear that the excess of passive galaxies in the CNOC2 groups is limited to the smaller groups ($\sigma(v)_{intr} \leq 600 \text{ km s}^{-1}$). We will discuss this apparent contradiction with cluster work in the Discussion (Section 4.5).

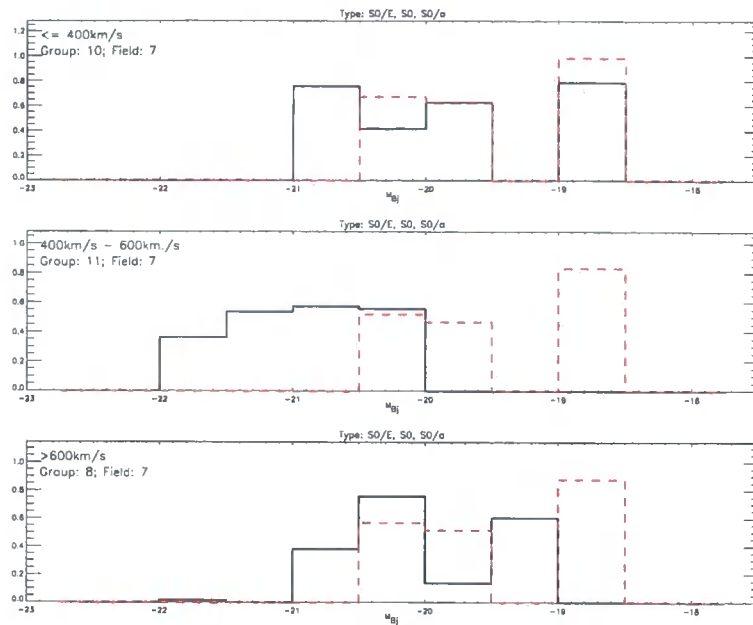


Figure 4.43: Luminosity Functions of S0 galaxies for group (solid line) and field (dashed line) samples divided into 3 bins of group velocity dispersion $\sigma(v)_{intr}$. **Top:** The least massive group sample ($\sigma(v)_{intr} \leq 400 \text{ km s}^{-1}$); **Middle:** The intermediate mass group sample ($400 \text{ km s}^{-1} < \sigma(v)_{intr} \leq 600 \text{ km s}^{-1}$) and **Bottom:** The most massive group sample ($\sigma(v)_{intr} > 600 \text{ km s}^{-1}$). The bright S0 population is clearly concentrated in the intermediate mass groups.

To estimate the significance of the excess passive fraction of bright ($M_{bJ} \leq -20.0$) spiral galaxies in smaller groups ($\sigma(v)_{intr} \leq 600 \text{ km s}^{-1}$), we use a similar procedure to that used to estimate the significance of the excess S0 population in groups (Section 4.4.3). On this occasion we bootstrap-resample the group (limited to $\sigma(v)_{intr} \leq 600 \text{ km s}^{-1}$) and field populations from the combined sample, with the null hypothesis that they are sampled from the same parent population. We determine that in 99.9% of occasions the difference between f_p in the resampled group and field populations is less than the measured difference of $\Delta f_p = 0.32$. This is the equivalent of a 3.2σ result. In Section 4.4.2 the excess of passive spiral galaxies in groups does not appear to be merely a result of groups containing brighter galaxies. However, to ensure this is not the case, we weight each field galaxy by a luminosity-dependent weight computed to force the luminosity distributions of the weighted group and field samples to match. We then redetermine the significance that f_p is larger in the group population and find that it actually increases to 3.3σ in agreement with our earlier analysis.

Finally in Figure 4.47, we examine whether the likelihood that a group spiral is passive

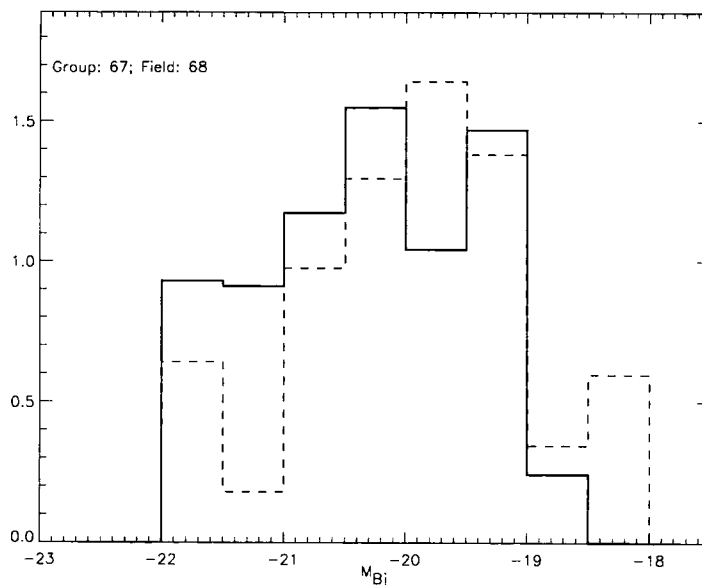


Figure 4.44: Luminosity Functions of spiral galaxies. The solid and dashed lines represent the group and field galaxy populations respectively. Galaxies are weighted by the selection weight W_C . We show the unweighted number of group and field galaxies in each sample in the top left hand corner of the plot. We see an excess of bright spiral galaxies in the group population.

has any dependence upon its position within the group. We limit ourselves to spiral galaxies brighter than $M_{bj} = -20.0$ and show how, for this subsample, f_p depends upon group-centric radius, dr (top panel). Despite the large error bars, it is clear that a larger fraction of spiral galaxies are passive towards the group centre, with a radial dependence of f_p at least as strong as for the whole galaxy population (Figure 3.16). To ensure that we are not simply reproducing the preference for passive spirals to lie in less massive groups, we also show how f_p depends upon group-centric radius, normalised by the rms value of the parent group (bottom panel). The relation stands, indicating that processes leading to the cessation of star formation in bright spiral galaxies are tightly related to the group environment.

4.4.5 How can we characterise the excess of elliptical galaxies in groups?

Figure 4.38 shows that the excess of ellipticals in groups exists largely in the faint galaxy population ($-20.0 < M_{bj} \leq -18.5$). This is in direct contrast to the excess of S0 type galaxies which appears mostly in brighter galaxies ($M_{bj} \leq -20.0$). We note that the

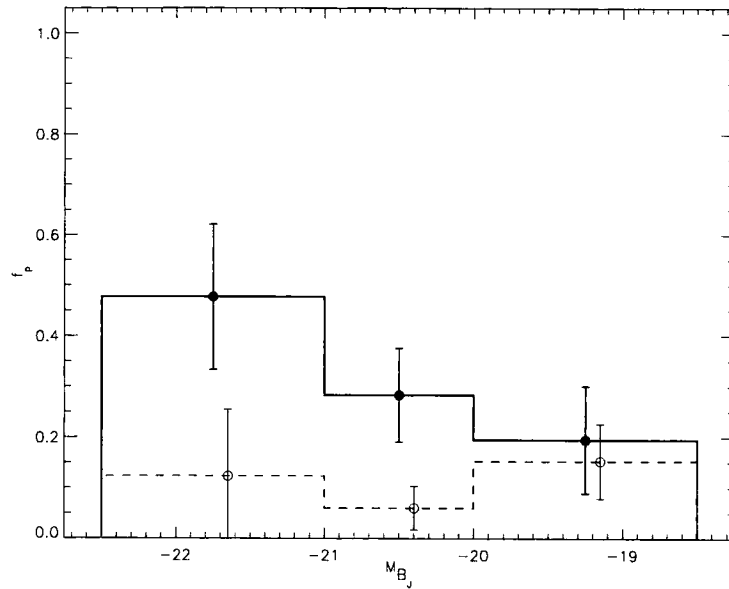


Figure 4.45: The fraction of spiral galaxies which are passive, f_p , in groups (solid line, filled circles) and in the field (dashed line, open circles) in 3 bins of luminosity: Bright ($M_{b_j} < -21.0$), Control ($-21.0 \leq M_{b_j} < -20.0$) and Faint ($-20.0 \leq M_{b_j} \leq -18.5$). Errors are estimated using the Jackknife technique. The passive fraction in group spirals is only significantly greater than in the field brighter than $M_{b_j} = -20.0$.

presence of a similar population of faint S0s in groups and in the field suggests that the faint elliptical population in groups does not simply represent a mis-identified population of faint S0s. In Figure 4.48 we show the fraction of elliptical galaxies f_E ($M_{b_j} \leq -18.5$) in the field (dashed horizontal line) and in groups split into 3 bins of group velocity dispersion: $\sigma(v)_{intr} < 400 \text{ km s}^{-1}$, $400 \text{ km s}^{-1} \leq \sigma(v)_{intr} < 600 \text{ km s}^{-1}$ and $\sigma(v)_{intr} > 600 \text{ km s}^{-1}$. f_E is consistent with a constant excess in all groups, although it is particularly evident in the most massive groups ($\sigma(v)_{intr} > 600 \text{ km s}^{-1}$). Errors are again estimated using the Jackknife technique.

As we know the excess of elliptical galaxies is most prevalent at $-20.0 < M_{b_j} \leq -18.5$, in Figure 4.49 we show the fraction of elliptical galaxies at these luminosities in the field (dashed line) and our 3 bins of group velocity dispersion. The number of confirmed and morphologically-classified group galaxies in each bin of velocity dispersion is not sufficient to identify any significant trend of f_E with $\sigma(v)_{intr}$ (20, 9 and 11 in small, intermediate and massive groups respectively). However, we note that the fraction of faint elliptical galaxies is most significant in the most massive groups ($\sigma(v)_{intr} > 600 \text{ km s}^{-1}$). This

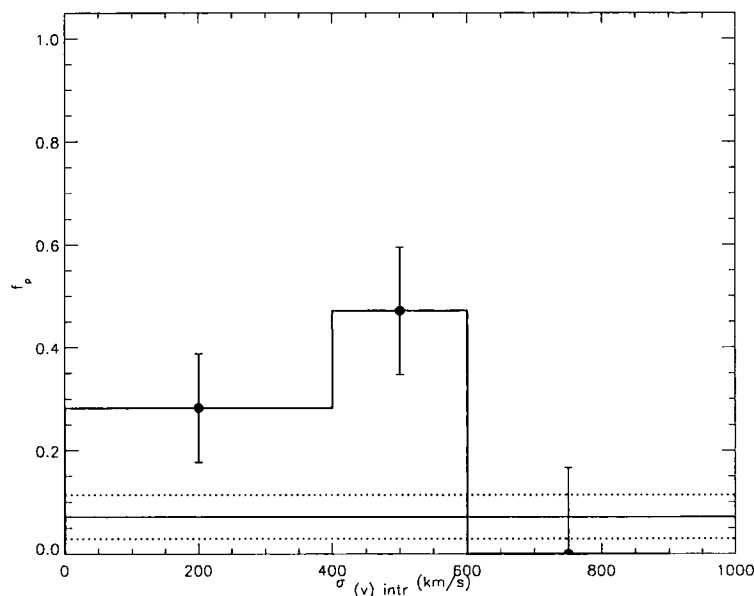


Figure 4.46: The fraction of spiral galaxies brighter than $M_{b_j} = -20.0$ which are passive, f_p , in the field (solid horizontal line) and in 3 bins of group velocity dispersion, $\sigma(v)_{intr}$ ($\sigma(v)_{intr} < 400 \text{ km s}^{-1}$, $400 \text{ km s}^{-1} \leq \sigma(v)_{intr} < 600 \text{ km s}^{-1}$, $\sigma(v)_{intr} > 600 \text{ km s}^{-1}$) with errors estimated using the Jackknife technique (or Poisson errors in the case of the massive groups). The passive galaxies are found mostly in smaller groups ($\sigma(v)_{intr} \leq 600 \text{ km s}^{-1}$).

is in agreement with the excess in faint passive galaxies seen most prominently in these most massive groups (Chapter 3 - Figure 3.19) as we know that most elliptical galaxies are also passive (see Figure 4.39).

Using a similar resampling procedure to that described in Section 4.4.3, we resample the combined group and field population of faint galaxies ($-20.0 < M_{b_j} \leq -18.5$) to estimate the significance of the excess faint elliptical population in groups. We determine that on 99% of occasions the difference in f_E between the resampled group and field populations is less than that seen. The excess of faint passive elliptical galaxies in groups is therefore significant at the 2.4σ level.

4.4.6 Other Morphological trends

Whilst the deficit of spiral galaxies in groups is a reflection of the other trends, it is still interesting to investigate. In Figure 4.50 we show the fraction of spiral galaxies, f_{sp} , in the field (solid horizontal line) and in 3 bins of group velocity dispersion: $\sigma(v)_{intr} < 400 \text{ km s}^{-1}$, $400 \text{ km s}^{-1} \leq \sigma(v)_{intr} < 600 \text{ km s}^{-1}$ and $\sigma(v)_{intr} > 600 \text{ km s}^{-1}$. Whilst

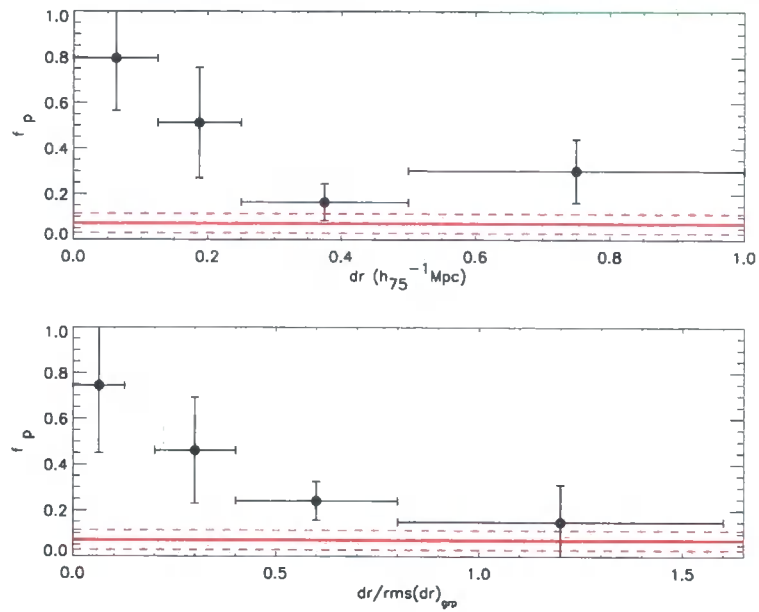


Figure 4.47: The fraction of spiral galaxies brighter than $M_{b_j} = -20.0$ which are passive, f_p , in the field (solid horizontal line) and in groups as a function of (**Top:**) group-centric radius, dr , and (**Bottom:**) group-centric radius, normalised by the rms value of the parent group. Errors are computed using the Jackknife technique. The likelihood that a spiral galaxy is no longer forming significant numbers of stars is a clear function of its position in the group.

groups of all sizes have a deficit of spiral galaxies, this is easily most significant in the most massive groups ($\sigma(v)_{intr} > 600 \text{ km s}^{-1}$). By resampling from the massive group and field population (again using the technique described in Section 4.4.3) we determine that f_{sp} is lower in the massive groups than in the field with 99.97% significance (3.4σ). To ensure that the difference in group and field luminosity distributions has no influence, we weight the field population to match the group luminosity distribution. However, we find that the deficit of spiral galaxies in these massive groups is now even more significant at the 3.5σ level.

In Figure 4.51 we show the luminosity function of star-forming spiral galaxies in small groups ($\sigma(v)_{intr} < 400 \text{ km s}^{-1}$ - solid line) and in the field (dashed line). The luminosity function for the 59 star-forming spiral galaxies in the field is renormalised to match the area of the luminosity function of the 23 star-forming spiral galaxies in the small groups. We notice what appears to be an excess of bright star-forming spiral galaxies in these smallest groups. This might correspond to an excess of bright star-forming galaxies which is apparent in Section 3.6.4.2 (although it is difficult to distinguish this from a deficit of

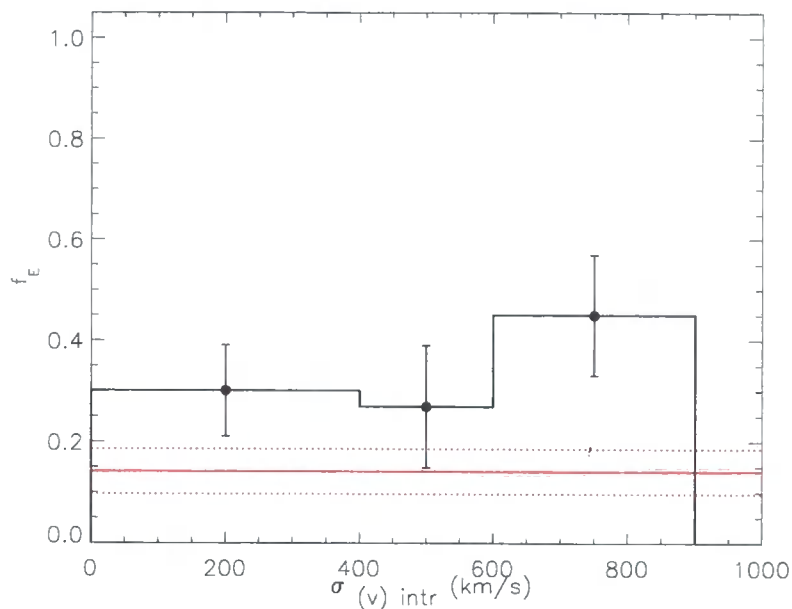


Figure 4.48: The fraction of elliptical galaxies, f_E , in the field (solid horizontal line) and in 3 bins of group velocity dispersion, $\sigma(v)_{intr}$ ($\sigma(v)_{intr} < 400 \text{ km s}^{-1}$, $400 \text{ km s}^{-1} \leq \sigma(v)_{intr} < 600 \text{ km s}^{-1}$, $\sigma(v)_{intr} \geq 600 \text{ km s}^{-1}$) with errors estimated using the Jackknife technique. The excess of elliptical galaxies in groups is most evident in the most massive groups ($\sigma(v)_{intr} > 600 \text{ km s}^{-1}$).

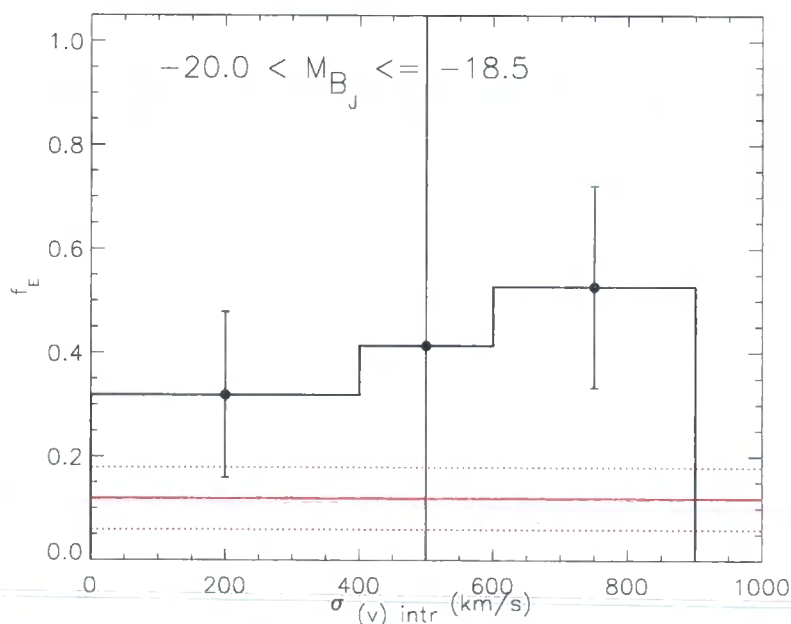


Figure 4.49: As Figure 4.48 but only for faint galaxies ($-20.0 < M_{B_j} \leq -18.5$).

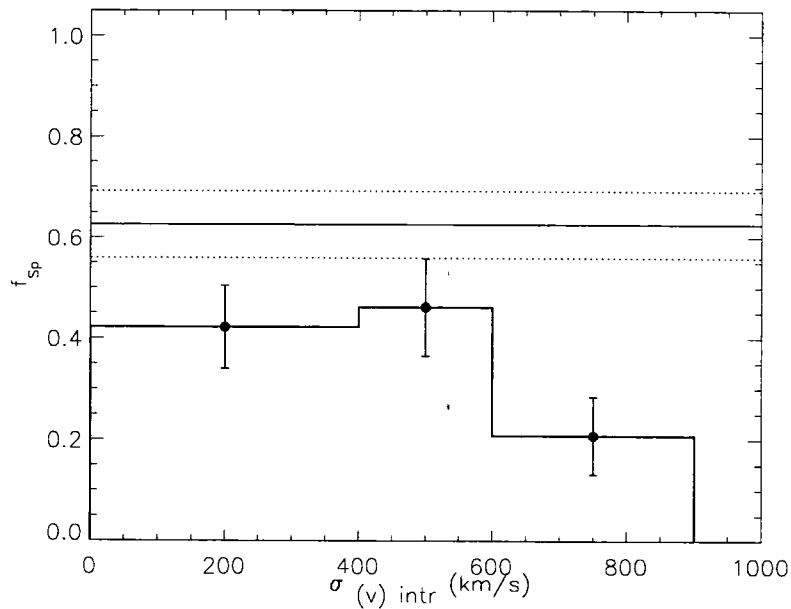


Figure 4.50: The fraction of spiral galaxies, f_{sp} in the field (solid horizontal line) and in 3 bins of group velocity dispersion, $\sigma(v)_{\text{intr}}$ ($\sigma(v)_{\text{intr}} < 400 \text{ km s}^{-1}$, $400 \text{ km s}^{-1} \leq \sigma(v)_{\text{intr}} < 600 \text{ km s}^{-1}$, $\sigma(v)_{\text{intr}} > 600 \text{ km s}^{-1}$) with errors estimated using the Jackknife technique. There is a deficit of spiral galaxies in groups, most prominent in the most massive groups ($\sigma(v)_{\text{intr}} > 600 \text{ km s}^{-1}$).

faint star-forming galaxies). As this represents an overall excess of bright galaxies as opposed to an increase in the fraction of a particular type of galaxy, we estimate the significance of this result using the parameter $\Delta R_{\text{B/C}}$ (the bright to control galaxy ratio in the groups normalised by the field level) as was defined and used in Section 3.6.4.2. Using the same technique to estimate $\Delta R_{\text{B/C}}$ and its significance, $S_{\text{B/C}}$ we find that the excess of bright star-forming spiral galaxies is $\Delta R_{\text{B/C}} = 0.41 \pm 0.36$ with a significance of only $S_{\text{B/C}} = 73.4\%$ ($\sim 1.1\sigma$). This is not therefore a significant result. We suspect that despite the low significance of the result, it is still suggestive of a population of bright spirals forming preferentially in low mass groups which can explain a significant excess of bright star-forming galaxies. A larger sample of galaxies would allow us to reduce the error on this measurement.

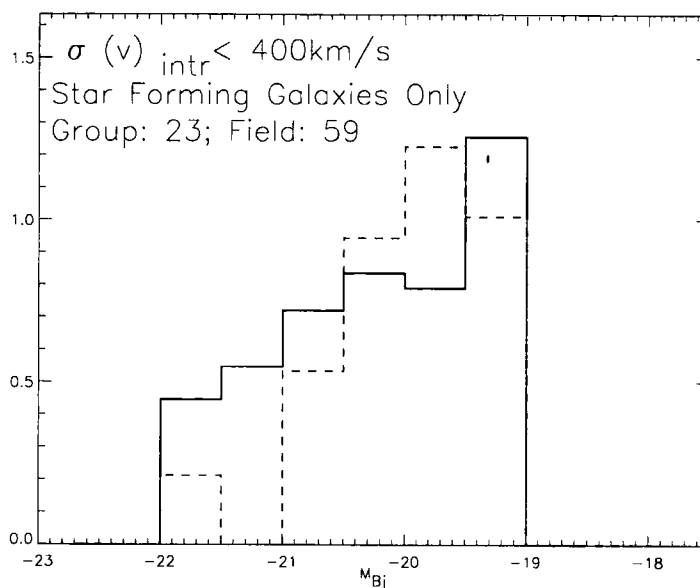


Figure 4.51: Luminosity Functions of star-forming spiral galaxies in small groups ($\sigma(v)_{intr} < 400 \text{ km s}^{-1}$ - solid line) and the field (dashed line). Galaxies are weighted by the selection weight W_C and the field luminosity function is renormalised to match the area of the group luminosity function. We show the unweighted number of group and field galaxies in each sample in the top-left-hand corner of the plot. There appears to be a brighter population of spiral galaxies in the small groups than is seen anywhere in the field. However this is not a significant result.

4.4.7 Peculiar and Interacting galaxies

4.4.7.1 Are peculiar or interacting galaxies more common in groups?

In the lower right panel of Figure 4.38 we can see that the fraction of Irregular and Merger-type galaxies shows little or no dependence on environment and decreases with increasing galaxy luminosity. This is surprising as the group environment is believed to provide ideal conditions for frequent galaxy mergers and interactions (Hashimoto et al., 1998; Severgnini & Saracco, 2001). However, the MORPHS classification system used by AO also provides 2 additional indices used to classify the morphological characteristics of galaxies. The disturbance index D indicates the level of peculiarity of a galaxy morphology on a scale of 0 - 4. In Figure 4.52 we show the fraction of galaxies in groups (solid circles) and in the field (open circles) with each value of D . The fraction of galaxies with $D=0$ is much higher in groups than the field (by $\sim 5\sigma$). This indicates that there is a significantly lower probability that CNOC2 group galaxies have peculiar morphological characteristics

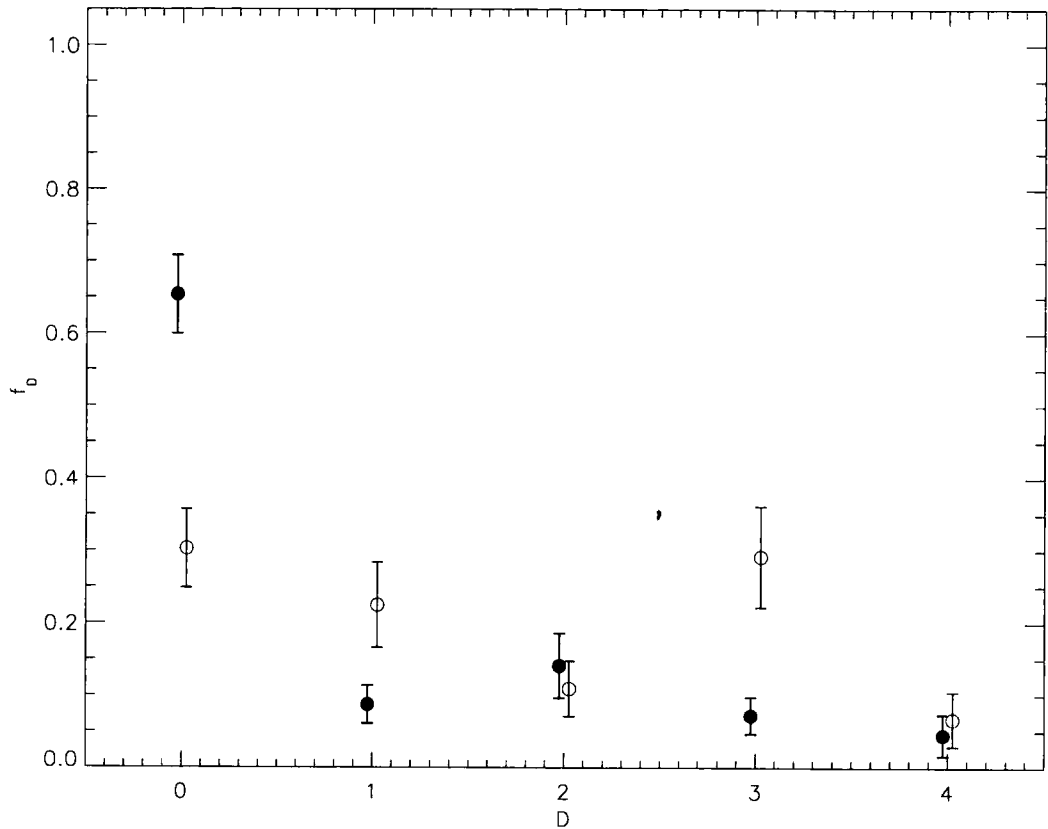


Figure 4.52: The fraction of galaxies with disturbance index D which possess each value of D . $D = 0$ infers a galaxy contains no peculiar features and progressively larger values of D infer more peculiar features. The solid circles represent the group galaxy population and the open circles represent the field galaxy population. Errors are estimated using the Jackknife technique and points are horizontally offset slightly for clarity. The likelihood that group galaxies have a peculiar morphology is significantly lower than for field galaxies.

than field galaxies at the same epoch.

The classification scheme also provides a visual determination of galaxies which are clearly undergoing some form of interaction or merger. For plotting purposes, we encode these classifications with a parameter I which can take integer values between 1 and 3. A value of $I = 1$ indicates that a galaxy has tidal arms but no obvious counterpart. $I = 2$ galaxies have visible interaction with another object and $I = 3$ galaxies have visible signs of undergoing a recent merger. In Figure 4.53 we show the fraction of galaxies with each value of anomaly index I , f_I in the groups (solid circles) and in the field (open circles). The number of galaxies classified in this way is sufficiently low that the errors on f_I (estimated using the Jackknife technique) are large. However, there is an indication that galaxies

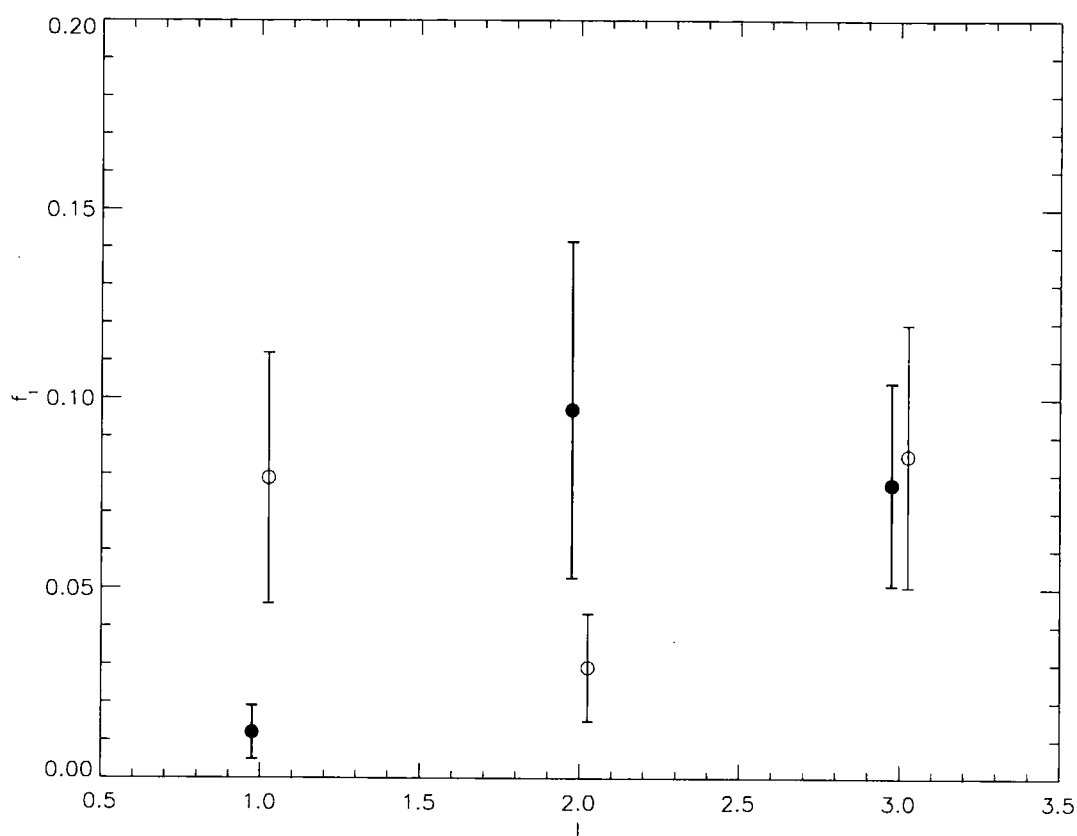


Figure 4.53: The fraction of all classified galaxies which possess each value of anomaly index, I . $I = 1$ galaxies have tidal arms but no obvious counterpart; $I = 2$ galaxies have visible interaction with another object and $I = 3$ galaxies have visible signs of undergoing a recent merger. The solid circles represent the group galaxy population and the open circles represent the field galaxy population. Errors are estimated using the Jackknife technique and points are horizontally offset slightly for clarity. Whilst galaxies undergoing visible interaction with another object are more common in the group population, the fraction with visible signs of undergoing a recent merger is consistent with the field value.

with tidal arms but with no obvious counterpart ($I = 1$) are more common in the field whilst galaxies undergoing visible interactions with another object are more common in groups. The fraction of galaxies with visible signs of undergoing a recent merger is similar in the groups and the field, in direct contradiction with other evidence indicating that mergers are predominantly a group phenomenon (Hashimoto & Oemler, 2000; Severgnini & Saracco, 2001).

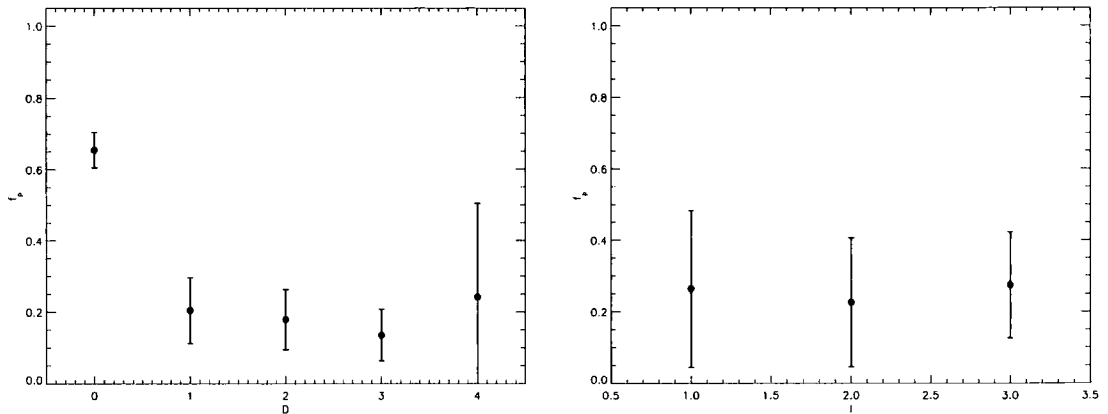


Figure 4.54: The fraction of passive galaxies in the combined sample for each disturbance index D (left) and anomaly index I (right). $D = 0$ implies a galaxy contains no peculiar features and progressively larger values of D imply more peculiar features. $I = 1$ galaxies have tidal arms but no obvious counterpart; $I = 2$ galaxies have visible interaction with another object and $I = 3$ galaxies have visible signs of undergoing a recent merger. Errors are estimated using the Jackknife technique.

4.4.7.2 Do galaxies with peculiar morphologies form more stars than an average galaxy?

With the combined information on galaxy morphology and star formation, we can examine whether there is a correlation between the peculiarity of a galaxy's morphology and the star-forming properties of those galaxies. As interacting and merging galaxies are observed to regularly lead to an increased level of star formation (starbursts - e.g. Joseph & Wright, 1985; Borne et al., 2000), this is a very relevant question. Figure 4.54 shows the fraction of passive galaxies, f_p , of the galaxies with each peculiarity index, D and anomaly index I . Normal looking galaxies with $D = 0$ are clearly much more likely to be passive than galaxies with some level of peculiarity ($D > 0$). However, there appears to be no dependence of f_p on the galaxy anomaly type I , although the number of galaxies classified in this way is low.

Figure 4.55 shows the fraction of highly star-forming galaxies, f_{hsf} , ($\text{EW}[\text{OII}] \geq 30\text{\AA}$) of the galaxies with each peculiarity index, D and anomaly index I . There is an indication that this fraction is larger in galaxies with the highest level of peculiarity ($D = 4$) although the numbers are low (only 8 confirmed galaxies with $D = 4$, much lower than the number with other values of D). Also the number of highly star-forming galaxies seems to be higher

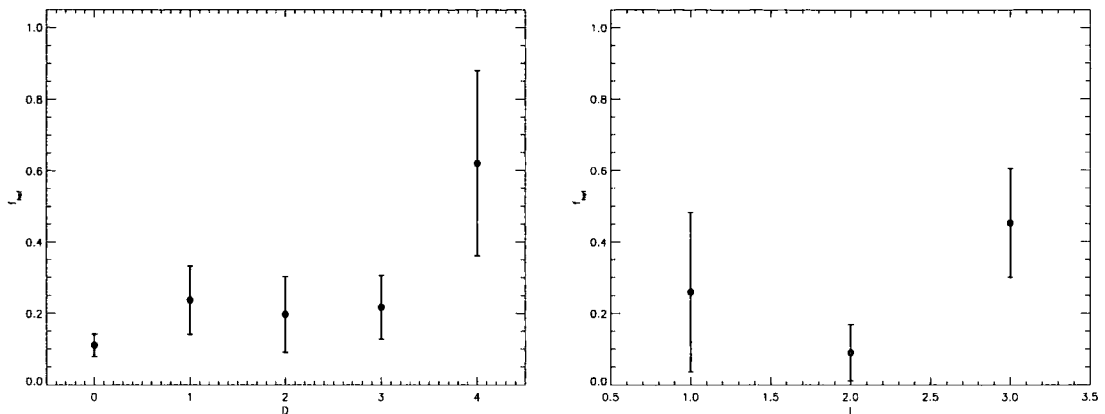


Figure 4.55: As Figure 4.54 but showing the fraction of highly star-forming galaxies, f_{hsf} as a function of disturbance index D (left) and anomaly index I (right).

in merging galaxies ($I = 3$) than in those merely interacting with a visible counterpart ($I = 2$). Whilst this is a very marginal result it supports the link between galaxy mergers and starbursting activity and suggests that this link is not so strong in galaxy-galaxy interactions. However, the number of galaxies classified in this way is also low (10 with $I = 1$, 14 with $I = 2$, 21 with $I = 3$). A larger sample of galaxies would be necessary to confirm any of these trends.

4.5 Discussion

We have found a significant excess of early-type galaxies in the CNOC2 groups at $0.3 \leq z \leq 0.55$. The fraction of ellipticals plus S0s in these groups is $f_{\text{early}} \sim 0.55$ compared with $f_{\text{early}} \sim 0.3$ in the field. This is similar to the fraction of bulge-dominated galaxies in the low-redshift X-ray detected groups of Tran et al. (2001) who find $f_{\text{early}} \sim 0.5$ compared to a field level of $f_{\text{early}} \sim 0.2$, and slightly lower than Helsdon & Ponman (2003) who find $f_{\text{early}} \sim 0.6$ in their X-ray bright group sample. It is greater than the fraction found by Zabludoff & Mulchaey (1998) who find $f_{\text{early}} \sim 0.25 - 0.55$ in low redshift groups. At $z \sim 0.25$ Balogh et al. (2002) also find $\sim 55\%$ of galaxies are bulge-dominated in low X-ray luminosity clusters with higher fractions in more X-ray luminous clusters. Direct comparisons with the literature are difficult because of the different galaxy luminosity ranges and group types sampled as well as different classification schemes. However, a comparison with the $z \sim 0.5$ MORPHS cluster sample of Dressler et al. (1997) suggests that our groups match the morphological composition of the irregular MORPHS clusters

($\sim 40\%$ spirals, $\sim 40\%$ ellipticals and $\sim 20\%$ S0s) even though our groups lie in a much lower density regime (mean density to the MORPHS luminosity limit within $1h_{75}^{-1}Mpc$ is $\sim 1.6Mpc^{-2}$). Conversely, the fraction of S0 galaxies found by Dressler (1980) and at low redshift ($f_{S0} \gtrsim 0.4$ at all local densities in clusters, extended to groups by Postman & Geller (1984)) is inconsistent with the fraction of S0s found in our groups. Therefore it seems likely that more S0 galaxies remain to be formed as the CNOC2 groups are encompassed into the groups and clusters of the local Universe. At $z \sim 0.4$ we have isolated the environment in which bright, passive S0 type galaxies are found. In both groups 37 and 39 we identify 3 bright S0 type galaxies ($M_{b_j} \leq -20.5$). In common between these 2 systems is the group velocity dispersion ($400 - 500 \text{ km s}^{-1}$) and the location of the S0 galaxies, in quite close proximity and along a straight line on the sky. This might suggest a common history for these galaxies both in terms of their dynamics and their evolution.

At faint magnitudes ($M_{b_j} \gtrsim -20.0$) we find the most significant excess of elliptical galaxies in groups. We have shown that this population is particularly evident in the most massive groups ($\sigma(v)_{intr} > 600 \text{ km s}^{-1}$). This shows that the faint passive galaxy population seen primarily in massive groups (Chapter 3 - Figure 3.19) also have predominantly elliptical morphology. This is in agreement with the local compact group analysis of Coziol et al. (2004). Other studies have found that the population of faint passive galaxies becomes more important as one moves up the mass scale from small groups to rich clusters (Christlein, 2000; Zabludoff & Mulchaey, 2000; Christlein & Zabludoff, 2003; De Propris et al., 2003a; Croton et al., 2004). One way in which such a population of faint elliptical galaxies can be created is by galaxy harassment in which galaxies interact with the global group potential and pass through the disturbed spiral stage to become dwarf ellipticals (Moore et al., 1996). This would also explain the apparent correlation between group mass and the size of the faint elliptical galaxy population (e.g. Christlein, 2000).

The fraction of bright spiral galaxies ($M_{b_j} \leq -20.0$) which are passive is significantly higher in the CNOC2 groups than in the surrounding field. Whilst we have found no such passive spirals in the most massive groups ($\sigma(v)_{intr} \geq 600 \text{ km s}^{-1}$) we note that our HST imaging is limited to sampling mainly the inner regions of the most massive groups (poor clusters). Since passive galaxies seem to be found predominantly at the outskirts of clusters (Goto et al., 2003), then we expect passive spirals to be found in environments typical of smaller systems and the outskirts of clusters. Examining the locations of passive spirals in the CNOC2 groups we find that they are preferentially located towards the

centre of groups. In some cases they are tightly clustered together (e.g. 3 passive spirals in group 23) whilst in others, they are in close proximity to bright S0-type galaxies (groups 37 and 39). This paints an interesting picture in which the truncation of star formation in group spirals is intimately related to the local group environment and might possibly represent an intermediate stage in the transformation of spiral to S0-type galaxies. The strong dependence upon group-centric radius suggests a truncation process related to interactions with the intra-group medium (IGM). Recent evidence for spatially truncated HI and H α emission in the disks of cluster spirals suggests that the star-forming cold gas in disks can be lost in clusters through interactions with the intra-cluster medium (ICM) (Vogt et al., 2004a,b; Koopmann & Kenney, 2004; Kenney et al., 2004; Vollmer et al., 2004). Simulations show that ram pressure stripping is only effective in regions of high gas density such as cluster cores (Quilis et al., 2000). However, given the evidence for stripping of outer disks in the Virgo cluster (e.g. Koopmann & Kenney, 2004), a relatively poor cluster, one might speculate that spiral galaxies might be subject to additional stripping processes when subject to unusual conditions of the ICM or IGM. Alternatively the cold gas disks in our passive spiral galaxies may have been starved of replenishment from their hot gas halo as that is stripped away in a process of strangulation (e.g. Balogh et al., 2000; Diaferio et al., 2001; Cole et al., 2000). However, if interactions with the IGM are responsible for truncating star formation in spiral galaxies, we would expect to find a higher fraction of passive group spirals at fainter magnitudes, since less massive galaxies are expected to lose their gas more easily. This is contrary to the observations. Galaxy mergers and interactions with other galaxies are expected to be common in groups in which the low velocity dispersion can lead to numerous encounters between galaxies (Zabludoff & Mulchaey, 1998; Barnes, 1985; Hashimoto & Oemler, 2000). We have found no substantial evidence that galaxy mergers are any more common in groups than in the field but there is an indication that the frequency of galaxy-galaxy interactions is higher in groups. Therefore star formation in spiral galaxies might also be truncated during an encounter with another group galaxy. Mergers and interactions are expected to be most common amongst the more massive, brighter galaxy population (due to their greater gravitational potential). This suggests that a history of interactions and minor mergers with other galaxies, which should lead to the segregation of galaxy types in groups and clusters, is a more likely candidate. We note that none of the 6 passive group spirals for which we have measured EW[H δ] in Magellan spectra have strong H δ absorption which would indicate strong recent star formation.

The excess of bright galaxies ($M_{b_j} \leq -21.0$) in groups and clusters with respect to the field is seen in numerous studies (Blanton et al., 2003; De Propris et al., 2003a; Christlein & Zabludoff, 2003; Croton et al., 2004). In Chapter 3 we showed that this excess extends to bright galaxies in our smallest CNOC2 groups ($\sigma(v)_{intr} \leq 400 \text{ km s}^{-1}$), many of which are still star-forming. In this chapter we have seen that many of the bright star-forming galaxies in these groups have spiral morphology. Whilst this is not a significant result in itself, it is in agreement with the work of Varela et al. (2004) who find that isolated disk galaxies are on average smaller, fainter, bluer, less barred, of a later Hubble type and less evolving than non-isolated disk galaxies (selected to have at least 1 companion). A population of more massive star-forming galaxies in the group environment than in the field could be explained in either of the nature or nurture scenarios of galaxy evolution. In the nature scenario, the more massive galaxies form preferentially in the deeper potential wells of what will become clusters and groups. Hierarchical evolution requires that galaxies are built from smaller building blocks in a process of regular galaxy mergers. Minor mergers are likely to leave a galaxy disk intact or even enhance it whilst supplementing the mass of a galaxy (Bertschik & Burkert, 2002). Therefore the nurture scenario can also explain the observed excess of massive star-forming spirals in groups and clusters via a long history of minor mergers in this dense environment.

This study has isolated a number of important galaxy populations which are preferentially found in the group environment. Whilst we can speculate about how they came to be, only direct observations of galaxy interactions (of which there are relatively low numbers in our sample), or sophisticated high resolution simulations of galaxy interactions will finally tell us which mechanisms are responsible for creating these populations.

4.6 Summary

We have found a number of significant differences in the morphological composition of group and field galaxy populations:

- The CNOC2 groups are composed of $\sim 40\%$ elliptical, $\sim 40\%$ spiral and $\sim 20\%$ S0 type galaxies (ignoring irregular and merger types which contribute negligibly at bright magnitudes). Compared to $\sim 30\%$ E+S0 and $\sim 70\%$ spiral galaxies in the field, this represents a significant enhancement of early-type galaxies in groups, with respect to field levels at $z \sim 0.45$.

- There is a significant excess of bright ($M_{b_j} \leq -20.5$) S0 galaxies over the field, notably in groups 37 and 39 (both with velocity dispersions $400 - 500 \text{ km s}^{-1}$ and with bright S0 galaxies spatially in close proximity to one another).
- Below M_* (~ -20.3 at $z \sim 0$ (Norberg et al., 2002)) the elliptical population becomes especially prevalent in groups, driving the excess of faint passive galaxies in the more massive groups.
- Less massive groups ($\sigma(v)_{intr} \lesssim 600 \text{ km s}^{-1}$) also contain a significant excess of bright passive spiral galaxies ($M_{b_j} \leq -20.0$), often located towards the centre of these groups and in close proximity to one another and to S0 galaxies. This suggests a common formation mechanism in the group environment and at the outskirts of clusters (Goto et al., 2003).
- The CNOC2 group galaxies appear less frequently disturbed than field galaxies and we find no evidence that galaxy mergers are any more common in groups than in the field. However there is an indication that the frequency of galaxy-galaxy interactions is higher in groups.

Chapter 5

Evolution in Galaxy Groups

5.1 Introduction

One way to directly observe the influence of galaxy groups is to trace their redshift evolution. The evolution of the galaxy populations in rich clusters has been the subject of much debate, centred upon the strong evolution in blue galaxy fraction (e.g. Butcher & Oemler, 1984; Margoniner et al., 2001), emission line fraction (Dressler et al., 2004) and lenticular S0-type galaxy fraction (Dressler et al., 1997). Globally, there is known to be a strong evolution in emission line fraction (Hammer et al., 1997) and morphological types (van den Bergh, 2002). However the level of evolution in groups is poorly understood, with only tentative evidence of evolution in the blue galaxy fraction of rich groups (Allington-Smith et al., 1993) within the significant statistical limitations of photometric data and the bias of radio selection. It is therefore important to repeat this study using a redshift-space selected sample of spectroscopically confirmed groups.

In this chapter, we contrast the properties of our intermediate redshift CNOC2 group sample (Carlberg et al., 2001b, Chapter 3) with our large sample of 2dFGRS galaxy groups at low redshift (Eke et al., 2004, Chapter 2). In Chapter 3 we found that the properties of galaxies in intermediate redshift groups are significantly different from those of coeval field galaxies, in that group galaxies are significantly less likely to have ongoing star formation than their field counterparts, and groups also contain a significant excess of bright galaxies ($M_{b_j} \leq -21$). By contrasting with the properties of galaxies in nearby groups we will be able to examine the evolution of galaxies in the critical group environment with purely spectroscopic data and over a significant range of redshift.

In Section 5.2 we ensure a fair comparison between these two populations and the surrounding field by examining the luminosity functions and EW[OII] distributions. In Section 5.3, we present our results in which we assess the environmental and evolutionary

dependencies of $\text{EW}[\text{OII}]$ as well as the dependence on other parameters such as galaxy luminosity. We then discuss the scientific implications of these results in section 5.4. Finally in Section 5.5 we present our conclusions.

As a reminder, the low redshift 2dF group sample contains 5490 galaxies within $1h_{75}^{-1}Mpc$ of the group centre and the field sample contains 50981 galaxies. The intermediate redshift CNOC2 group sample contains 240 galaxies within $1h_{75}^{-1}Mpc$ of the group centre and the field sample contains 334 galaxies.

5.2 Data

The CNOC2 and 2dF group and field samples are well matched. The b_J -band spectroscopic selection of 2dFGRS is similar to the $z \sim 0.45$ R_c -band selection of CNOC2 and Magellan spectroscopy. The CNOC2 group detection algorithm (Carlberg et al., 2001b) requires more bright members in close proximity to each other, and therefore likely suffers from less contamination than 2dF groups. We find that the range of group velocity dispersion for 2dF groups matches that seen in the CNOC2 group sample. Therefore the 2dF sample appears to be unbiased by the requirement for at least 10 confirmed 2dF members, even though no such requirement is applied to CNOC2 groups. The CNOC2 field excludes those galaxies assigned to the targeted group to avoid biasing the field towards the group environment. The final CNOC2 field sample should therefore be representative of the Universe in the $0.3 \leq z \leq 0.55$ redshift range. Since the 2dF groups were untargeted, the 2dF field definition (all galaxies in the 2dF catalogue in the $0.05 \leq z \leq 0.1$ redshift range) is as close to our CNOC2 field definition as can be reasonably achieved. However, we note that this is a potential source of uncertainty, when interpreting evolution in the field.

5.2.1 The galaxy luminosity function in groups and the field

5.2.1.1 Luminosity limits

Figure 5.1 shows the superimposed luminosity functions of the 2dF and CNOC2 group and field samples. The volume-limited 2dF sample is $> 90\%$ complete for $M_{b_J} \leq -19$ and so we apply no completeness correction. The Schechter function computed for the 2dF survey (Nörberg et al., 2002) is shown for comparison. The CNOC2 galaxies are weighted by W_C to correct for the selection function. For comparison between 2dF and CNOC2 group and field samples, the data are normalised so that there is the same number of weighted

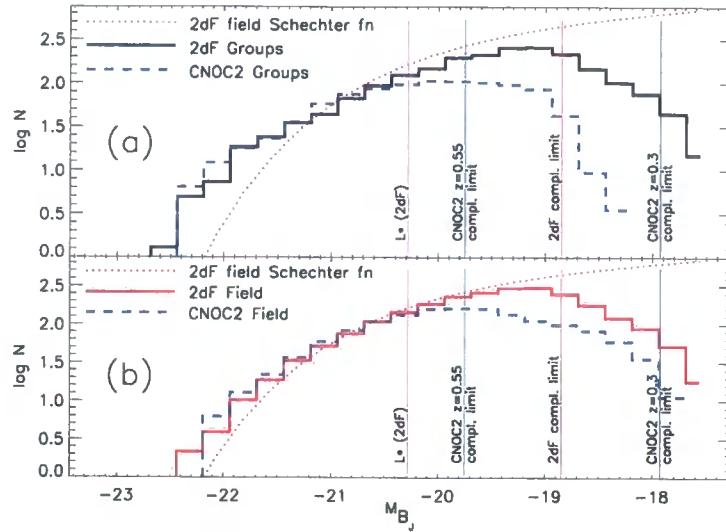


Figure 5.1: Luminosity functions of the group galaxies (top) and field galaxies (below) for 2dF and CNOC2. Field and Group CNOC2 data are each normalised to match total number in CNOC2 sample for $M_{b_J} < -20.25$

galaxies brighter than $M_{b_J} = -20.25$. At these magnitudes, neither sample suffers any incompleteness due to falling below the apparent magnitude limit in the redshift range considered. We note that the enhanced bright to faint galaxy ratio seen in CNOC2 groups relative to the field (Chapter 3) is also seen in the local 2dF groups.

Also shown in Figure 5.1 are some critical values of luminosity. The value of M_* in Norberg et al. (2002), appropriate to our cosmological model, is ~ -20.28 , and the 2dF data are complete down to -18.85 , or equivalently $\sim M_* + 1.5$. Our CNOC2 data span a wide range in redshift and thus the luminosity limit corresponding to our apparent magnitude limit of $R_c=22$ is redshift dependent. At the upper limit of our redshift range, $z = 0.55$, a $R_c=22$ galaxy with a mean K-correction will transform to a rest-frame luminosity $M_{b_J} = -19.75$ and at the lower redshift limit of $z = 0.3$, the same galaxy would transform to $M_{b_J} = -17.93$. In the case of the reddest galaxies with larger K-corrections, these limits would lie at $M_{b_J} = -20.07$ ($z = 0.55$) and $M_{b_J} = -18.06$ ($z = 0.3$), so we are incomplete below these magnitudes.

Most galaxies in our CNOC2 and 2dF galaxy catalogues lie below the brightest CNOC2 luminosity limit of $M_{b_J} = -20.07$. To enable us to compare the 2dF and CNOC2 galaxy samples independently of differences in the luminosity function (which may be partly intrinsic but is mostly due to selection effects), we choose to apply an additional luminosity weighting to the CNOC2 galaxies. This weighting is calculated within each bin in

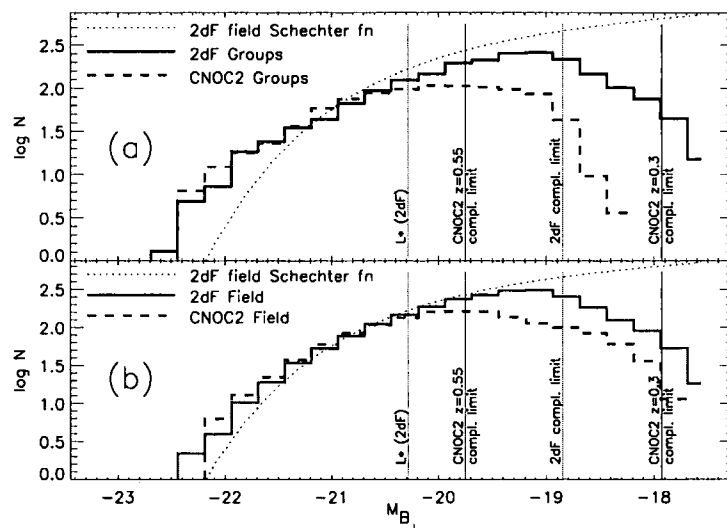


Figure 5.1: Luminosity functions of the group galaxies (top) and field galaxies (below) for 2dF and CNOC2. Field and Group CNOC2 data are each normalised to match total number in CNOC2 sample for $M_{b_j} < -20.25$

galaxies brighter than $M_{b_j} = -20.25$. At these magnitudes, neither sample suffers any incompleteness due to falling below the apparent magnitude limit in the redshift range considered. We note that the enhanced bright to faint galaxy ratio seen in CNOC2 groups relative to the field (Chapter 3) is also seen in the local 2dF groups.

Also shown in Figure 5.1 are some critical values of luminosity. The value of M_* in Norberg et al. (2002), appropriate to our cosmological model, is ~ -20.28 , and the 2dF data are complete down to -18.85 , or equivalently $\sim M_* + 1.5$. Our CNOC2 data span a wide range in redshift and thus the luminosity limit corresponding to our apparent magnitude limit of $R_c=22$ is redshift dependent. At the upper limit of our redshift range, $z = 0.55$, a $R_c=22$ galaxy with a mean K-correction will transform to a rest-frame luminosity $M_{b_j} = -19.75$ and at the lower redshift limit of $z = 0.3$, the same galaxy would transform to $M_{b_j} = -17.93$. In the case of the reddest galaxies with larger K-corrections, these limits would lie at $M_{b_j} = -20.07$ ($z = 0.55$) and $M_{b_j} = -18.06$ ($z = 0.3$), so we are incomplete below these magnitudes.

Most galaxies in our CNOC2 and 2dF galaxy catalogues lie below the brightest CNOC2 luminosity limit of $M_{b_j} = -20.07$. To enable us to compare the 2dF and CNOC2 galaxy samples independently of differences in the luminosity function (which may be partly intrinsic but is mostly due to selection effects), we choose to apply an additional luminosity weighting to the CNOC2 galaxies. This weighting is calculated within each bin in

luminosity using the formula:

$$W_{lum} = N_{2dF} / \sum_{i=1}^{N_{CNOC2}} W_C \quad (5.1)$$

which corresponds to the difference between the field luminosity functions. It is applied in the range $-20.25 \leq M_{b_j} \leq -18.5$ at which magnitudes the CNOC2 data become incomplete at the high redshift end. The choice of a faint final luminosity limit of $M_{b_j} = -18.5$ ($\sim M_* + 1.75$) makes maximal use of the data and allows the properties of faint galaxies to be compared with those of brighter galaxies. We emphasise that whilst we are incomplete at $M_{b_j} \gtrsim -19.75$ at $z = 0.55$ in CNOC2 and $M_{b_j} \gtrsim -18.85$ in 2dFGRS, this has no impact on any analysis of galaxy properties as a function of luminosity or on comparisons between the group and field galaxy populations. Also by studying galaxy properties as a function of luminosity, the analysis is independent of CNOC2 galaxy weighting, including little effect from weighting by the selection function.

5.2.2 EW[OII] in 2dF and CNOC2

Details of the CNOC2 equivalent width measurement process are given in Chapter 3. In 2dFGRS, the equivalent widths of [OII] are measured in a similar way to H α using a completely automated fitting procedure, (see Lewis et al., 2002a, for details). In the fitting of the [OII] emission line, many 2dF measurements are classified as *no line present*. In our analysis, these are set to 0Å and then *all* 2dF measurements are smoothed with a gaussian kernel of width 2Å to match the mean error on CNOC2 EW[OII] measurements (much greater than the 2dF line measurement error). We note that the fraction of galaxies with $EW[OII] > 5\text{Å}$ is unchanged by this smoothing to $< 1\%$. Figure 5.2 shows the distribution of EW[OII] in our 2dF and CNOC2 group and field galaxy catalogues. We limit the group data to within $1h_{75}^{-1}\text{Mpc}$ (projected) of the group centre in all cases (see Chapter 3 for explanation). The CNOC2 galaxies are weighted by a combined completeness and luminosity weighting to match the 2dF luminosity function, $W_{tot} = W_C \times W_{lum}$. The CNOC2 galaxies are limited to $R_c \leq 22$ and all galaxies are limited to $M_{b_j} \leq -18.5$. Finally, the distribution of 2dF EW[OII] is normalised to provide an equal number of galaxies to that found in CNOC2, for presentation only. This is done independently for the group and field populations.

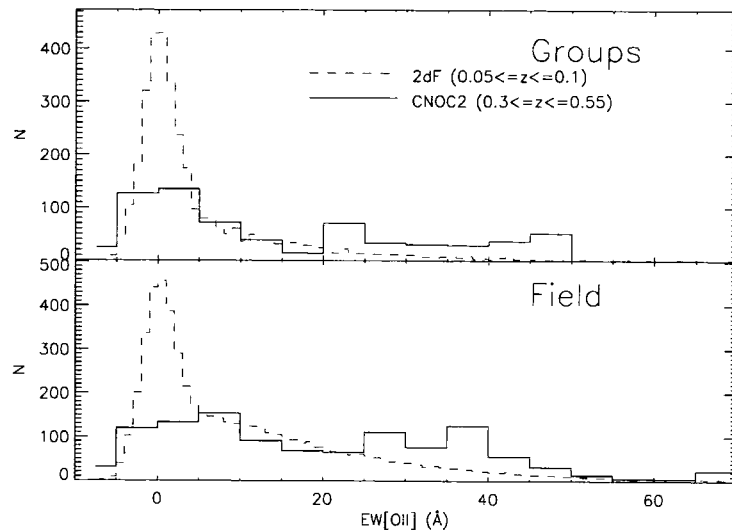


Figure 5.2: Normalised distributions of $\text{EW}[\text{OII}]$ of the group and field galaxies in 2dF ($0.05 \leq z \leq 0.1$) and CNOC2 ($0.3 \leq z \leq 0.55$) samples where $M_{b_j} \leq -18.5$. The data is normalised to match the total number of galaxies in the CNOC2 analysis.

5.2.2.1 Diagnostics of Star Formation for a Galaxy Population

To assess the relative normalisation of the 2 populations, f_p measures the *fraction of passive galaxies* as defined in Chapter 3. The level of [OII] emission in the star-forming galaxies is measured using $\langle \text{EW}[\text{OII}] | \text{SF} \rangle$ which records the **median EW[OII] only for star-forming galaxies**.

5.2.2.2 Aperture bias

Systematic effects on the measurements of $\text{EW}[\text{OII}]$ can be induced by the relative aperture sizes used in the 2dFGRS and CNOC2 spectroscopy. In particular, the 2dF fibres generally sample light from a smaller physical radius than the CNOC2 slits, and this might lead to an overestimate of f_p by excluding the star-forming regions in face-on disk galaxies. In Chapter 6, we use SDSS resolved photometry to estimate the effects of aperture bias across our magnitude range. We find that the fraction of galaxies found in the red peak of the bimodal colour distribution is no greater when considering colours measured inside $3''$ SDSS fibres, rather than the total colour. This is because both red and blue galaxies have similar colour gradients, likely due to metallicity rather than star formation. Thus we conclude that the effects of aperture bias do not strongly affect our measurements of f_p .

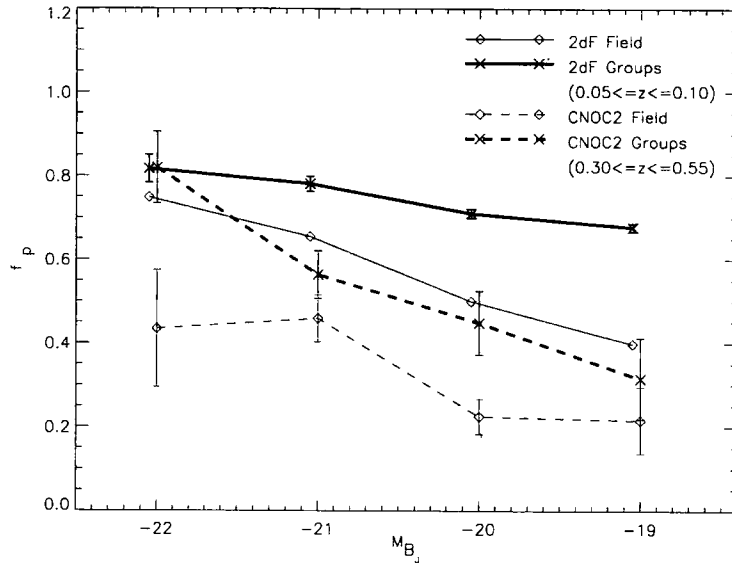


Figure 5.3: Fraction of galaxies with $\text{EW}[\text{OII}] < 5 \text{ \AA}$ (the passive population), f_p , in 2dF and CNOC2 groups (within 1 projected Mpc of group centre) and field, as a function of M_{B_j} . The 2dF points are slightly offset in M_{B_j} for clarity.

5.3 Results

A comparison of the 2dF and CNOC2 $\text{EW}[\text{OII}]$ distributions in Figure 5.2 shows that the fraction of galaxies in the 0 \AA peak depends on both epoch and environment. In particular, the 0 \AA peak in the 2dF data is much more prominent than in the CNOC2 survey, for both field and groups. At both epochs, however, the group galaxy population is more biased towards the 0 \AA peak than the corresponding field population. We now explore these trends in more detail.

5.3.1 The dependence of f_p on redshift, environment and luminosity

In Figure 5.3, the fraction of passive galaxies, f_p , is plotted against rest-frame M_{B_j} luminosity. Statistical errors are estimated using a Jackknife resampling method (Efron, 1982). We can see that:

- In all samples, f_p is a strong function of luminosity with fainter galaxies far more likely to be star-forming than brighter galaxies at equivalent redshifts. This is consistent with many previous results, e.g. Kauffmann et al. (2003).
- f_p is significantly greater in the galaxy groups than in the field at both low and intermediate redshift and also right across the luminosity range investigated.

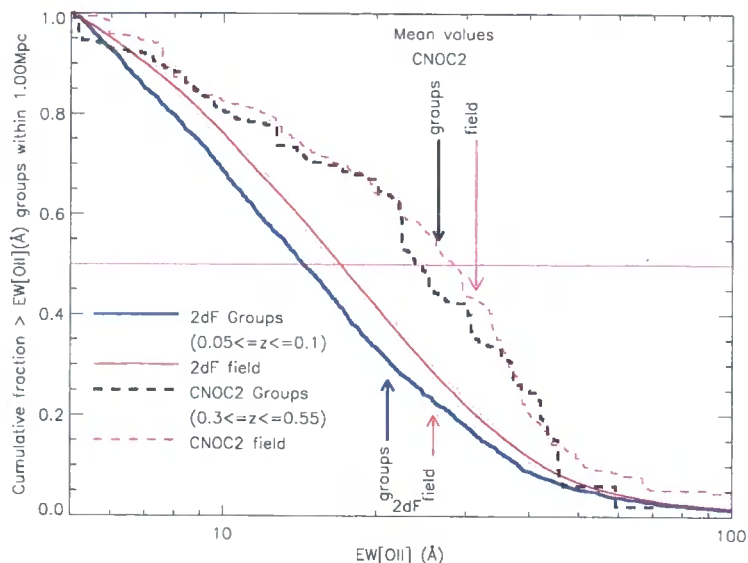


Figure 5.4: Cumulative distributions of $\text{EW}[\text{OII}]$ in star-forming galaxies in the field and group galaxies of 2dF ($0.05 \leq z \leq 0.1$) and CNOC2 ($0.3 \leq z \leq 0.55$) samples. The arrows indicate the mean values of $\text{EW}[\text{OII}]$ for star-forming galaxies in each sample.

- f_p is strongly redshift dependent, both in the field and in galaxy groups. At brighter magnitudes than $M_{b_j} = -18.5$ ($\sim M_* + 1.75$ in 2dF), f_p in groups evolves from $\sim 42\%$ at $0.3 \leq z \leq 0.55$ in CNOC2 to $\sim 71\%$ at $0.05 \leq z \leq 0.1$ in 2dF. In our field samples (defined to represent the global population), f_p evolves from $\sim 25\%$ to $\sim 47\%$ over the same redshift interval. The observed field evolution is consistent with the equivalent strong evolution in the fraction of passive galaxies in the Canada-France Redshift Survey (Hammer et al., 1997) and the global decline in star formation rate since $z \sim 1$ (e.g. Madau et al., 1998). We refer to Whitaker et al. (2004) for a more detailed and thorough discussion of the evolution of star formation rate in the global CNOC2 population. This provides a clear analogy at lower densities to the observed evolution of the blue galaxy fraction in clusters (Butcher & Oemler, 1984) and to similar evolution in rich groups, estimated by Allington-Smith et al. (1993) using photometric data.

5.3.2 The properties of the star-forming population

Figure 5.4 shows the cumulative distribution of $\text{EW}[\text{OII}]$, for star-forming galaxies only, in the 2dF and CNOC2 group and field samples. Interestingly, the shape of the distribution at a particular epoch (i.e. 2dF or CNOC2) is approximately independent of environment, consistent with earlier analysis of the $\text{EW}[\text{H}\alpha]$ distribution (Balogh et al., 2004a). In

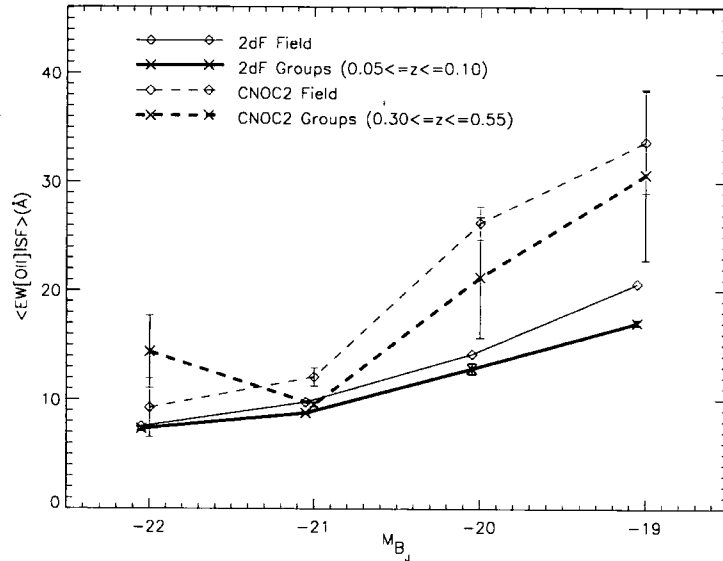


Figure 5.5: The median $\text{EW}[\text{OII}]$ (\AA) of star-forming galaxies, $\langle \text{EW}[\text{OII}] | \text{SF} \rangle$, in the 2dF and CNOC2 galaxies in the groups (within 1 projected Mpc of group centre) and field, as a function of M_{B_j} . The 2dF points are slightly offset in M_{B_j} for clarity.

the CNOC2 sample, the distribution shows a small enhancement in highly star-forming galaxies ($\text{EW}[\text{OII}] \gtrsim 30 \text{\AA}$) relative to the 2dF galaxies in both groups and the field. The mean values of $\text{EW}[\text{OII}]$ for each sample are indicated by the arrows in Figure 5.4. These values of 26.4\AA (groups) and 31.3\AA (field) in CNOC2 are within ~ 20 per cent of the mean values in the 2dF (20.9\AA in groups and 25.8\AA in the field). This difference is much smaller than the evolution in f_p , which is almost a factor of two. Therefore, the evolution of the total star formation rate is driven more by the evolution of f_p than by evolution of the mean properties of star-forming galaxies.

In Figure 5.5 we show the median $\text{EW}[\text{OII}]$ among star-forming galaxies, $\langle \text{EW}[\text{OII}] | \text{SF} \rangle$, as a function of luminosity in the CNOC2 and 2dF group and field samples. Errors are again computed using a Jackknife resampling method. The median $\text{EW}[\text{OII}]$ is significantly larger for fainter galaxies than for bright galaxies. Furthermore, the evolution in the $\text{EW}[\text{OII}]$ distribution is largely manifested as an increase in $\langle \text{EW}[\text{OII}] | \text{SF} \rangle$ in galaxies with $M_{B_j} \gtrsim -21.5$.

5.3.3 Dependence of f_p in groups upon group-centric radius and velocity dispersion

In Figure 5.6 we plot f_p as a function of the projected physical distance, dr , from the group centre. It is clear that even in the better sampled 2dF groups, the total fraction

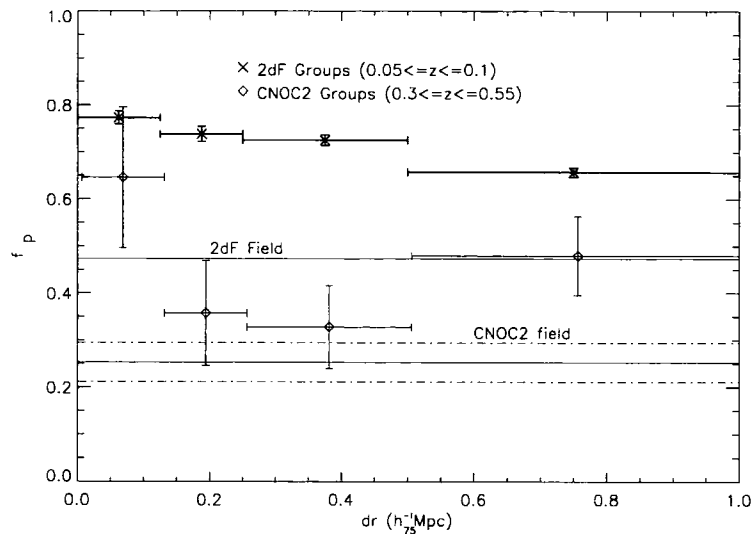


Figure 5.6: The fraction of galaxies with $\text{EW}[\text{OII}] < 5\text{\AA}$ (the passive population) (f_p) in 2dF and CNOC2 groups, as a function of physical radius. The field level is overplotted and only galaxies where $M_{bJ} \leq -18.5$ are considered.

of passive galaxies, f_p , merely declines from ~ 0.76 in the innermost $0.125 h_{75}^{-1}$ Mpc bin to ~ 0.65 in the $0.5 h_{75}^{-1}$ Mpc $< \delta(r) \leq 1 h_{75}^{-1}$ Mpc bin. This is a weak, but statistically significant trend. The value of f_p for the total 2dF field population is ~ 0.47 , much lower than in the groups. Similarly, in the CNOC2 field, $f_p = 0.25$ is much smaller than that in the combined group population where $f_p = 0.42$. We only see a trend with dr in the inner regions of the CNOC2 group population, as shown in Paper I. However, a trend as weak as that seen in 2dF group galaxies would be masked by the statistical errors.

We have also investigated how the star formation properties of galaxy groups¹ depend upon the group velocity dispersion, $\sigma(v)_{intr}$. In Paper I we found that there is little dependence of f_p on $\sigma(v)_{intr}$ when computed over a wide range of galaxy luminosity. Figure 5.7 shows f_p in CNOC2 and 2dF groups as a function of $\sigma(v)_{intr}$. There are no clear trends visible in Figure 5.7 other than the evolution from lower f_p in CNOC2 groups to that seen in 2dF groups. It is also noticeable that there are very few 2dF groups with high velocity dispersion ($> 400 \text{ km s}^{-1}$) and low f_p (< 0.4), which is a common regime for CNOC2 groups. We note that the enhancement of f_p in CNOC2 groups over the CNOC2

¹We note that whilst f_p in CNOC2 groups is computed with each galaxy weighted by its combined completeness and luminosity weighting W_{tot} (strictly only applicable when the full stacked group is considered) we find that f_p is insensitive to this weighting and very close to the value obtained with no weighting applied.

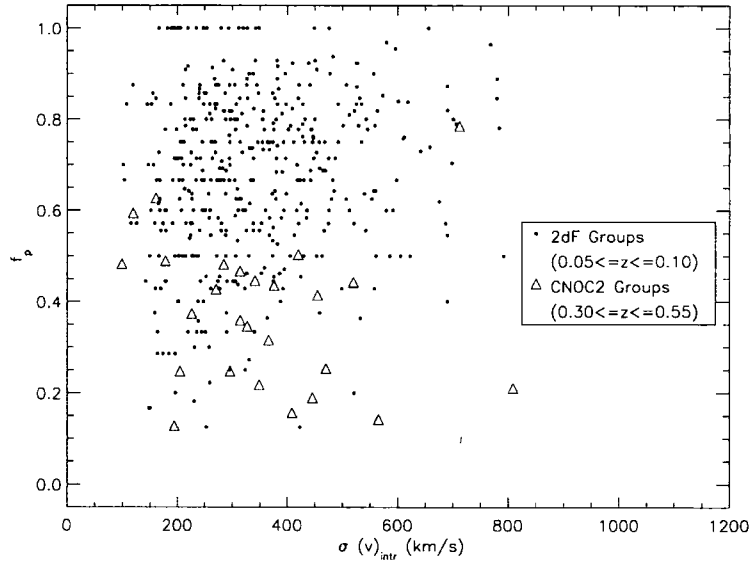


Figure 5.7: Fraction of galaxies with $\text{EW}[\text{OII}] < 5\text{\AA}$ (passive galaxies) (f_p) in 2dF and CNOC2 groups, as a function of group line of sight velocity dispersion. The points represent 2dF groups and the triangles represent CNOC2 groups.

field holds when we exclude the 2 groups with velocity dispersion $> 600\text{ km s}^{-1}$ (for more details see Paper I). The only CNOC2 group with $f_p > 0.7$ (group 138) is characterised by a high number of confirmed members (35 compared to 19 in the group with the next highest $\sigma(v)_{intr}$) and might better be considered a poor cluster (see e.g. Nakata et al., 2004, for the behaviour of f_p in clusters).

5.4 Discussion

5.4.1 Implications

We have detected a strong evolution in the fraction of passive galaxies, f_p (defined as the fraction of galaxies with $\text{EW}[\text{OII}] < 5\text{\AA}$), in both groups and the field since the Universe was $\sim 1/3$ its current age. Thus, the Butcher–Oemler effect (e.g. Butcher & Oemler, 1984; Margoniner et al., 2001; De Propris et al., 2003b) is not strictly a cluster phenomenon, but is seen both in the general field and in small groups, as previously found by Allington-Smith et al. (1993). These results represent clear evidence that a significant proportion of galaxies in both environments have ceased forming stars since $z \sim 0.5$. A simple argument, neglecting density and luminosity evolution, sees 50% of star-forming group galaxies and 35% of star forming field galaxies at $z \sim 0.4$ (CNOC2) becoming passive galaxies by $z \sim 0.1$ (2dF). This evolution is modelled in more detail in Chapter 7.

In contrast, while we find significant redshift evolution in the shape of the EW[OII] distribution for star-forming galaxies, there is little or no dependence on environment. This suggests that this evolution results from very local (i.e. internal to the galaxy) processes that drive an evolution in SFR or metallicity, rather than external, environmental influences. We caution however that amongst star-forming galaxies, it is not possible with current data to rule out an aperture bias in the measurement of EW[OII], which might lead to underestimation of EW[OII] in 2dFGRS star-forming galaxies.

In Chapter 7 we make a first attempt to quantitatively decouple the environmental dependence of galaxy evolution from the global SFR evolution. To fully understand this, we require a homogeneous sample over a large range of environments. We are currently working on providing a fair comparison study in cluster cores (Nakata et al., 2004) using spectroscopic data over an equivalent redshift range. Understanding the importance of galaxy evolution in groups with respect to cluster cores will help to isolate the environments in which galaxy evolution is most active. Complementary studies of the evolution in isolated galaxies would be of especially great benefit to understand the role of environment in driving galaxy evolution, and in particular, the evolution of f_p .

5.5 Conclusions

In this chapter, we have examined the evolution of galaxies and the effects of the group environment in kinematically-selected groups from the CNOC2 (Carlberg et al., 2001b, supplemented with new and deeper Magellan spectroscopy) and 2dFGRS (Eke et al., 2004) surveys. The data span the redshift range $0.05 \leq z \leq 0.55$ and luminosities down to $M_{b_j} \leq -18.5$ (locally $\sim M_* + 1.75$). Motivated by the apparently fundamental differences between the blue, star-forming and the red, passive populations of galaxies (Balogh et al., 2004a; Blanton et al., 2003) we have arbitrarily divided our galaxies into *passive* ($\text{EW}[\text{OII}] < 5\text{\AA}$) and *star-forming* ($\text{EW}[\text{OII}] \geq 5\text{\AA}$) populations. We have then shown that the fraction of passive galaxies f_p is a strong function of:

- **redshift:** f_p declines strongly with redshift, both in groups and the field and over the full luminosity range to at least $z \sim 0.45$. This is equivalent to a Butcher-Oemler trend in the emission line properties of group galaxies and in the global population.
- **environment:** f_p is significantly higher in groups than the field across the full luminosity range, both locally and at $z \sim 0.45$.

- **luminosity:** f_p increases steeply with luminosity across our range ($M_{b_j} \lesssim -18.5$) in groups and the field up to at least $z \sim 0.45$.

A better understanding of the environmental influence on galaxy properties will be made possible by comparisons with semi-analytic models (Chapter 7), galaxies in other environments (e.g. Nakata et al., 2004) and higher redshift galaxy systems.

Chapter 6

Aperture Effects and the Origin of Colour Gradients in Galaxies

The 2dF galaxies are observed spectroscopically through 2.1'' diameter fibres at low redshift, corresponding to between $\sim 1.9\text{kpc}$ ($z = 0.05$) and 3.6kpc ($z = 0.1$). The CNOC2 galaxies are observed through 1.3'' (CNOC2) and 1.47'' (LDSS2) slits at much higher redshift corresponding to between $\sim 5.5\text{kpc}$ and 8.8kpc . Therefore, significantly more flux will be lost from a large galaxy in the low redshift 2dF sample than would be lost in its CNOC2 counterpart. The use of emission line equivalent widths rather than fluxes reduces serious aperture effects by normalising to the continuum level. However, a remaining worry is the existence of any bias towards sampling primarily bulge light in the smaller apertures. Baldry et al. (2002) show that measurements of EW[OII] in 2dFGRS are relatively insensitive to aperture size in repeat observations with significant differences in seeing (differing by a factor of > 2). There is also no significant variation in the distribution of EW[OII] over the redshift range $0.05 \leq z \leq 0.1$ over which we sample little evolution but a factor of 2 in aperture diameter. However, the variation in aperture size considered in this paper is somewhat larger and so we have looked for clues in the SDSS for which resolved, digital photometry exists.

Differences in selection method between SDSS and 2dFGRS are not important when considering the aperture corrections to galaxies in the same redshift range ($0.05 \leq z \leq 0.1$). Brinchmann et al. (2004) estimate aperture bias measurements of SFR per unit luminosity (SFR/L) by constructing a likelihood distribution to determine the probability of a given SFR/L for a given set of colours ((g-r),(r-i)) based on the photometry within the fibre aperture. They then apply this likelihood distribution to the galaxy population given the total galaxy colours. The main assumption present in this technique is that the distribution of SFR/L for a given colour is similar inside and outside the fibre. However, we know that colour gradients can also be driven by metallicity (Hinkley & Im, 2001;

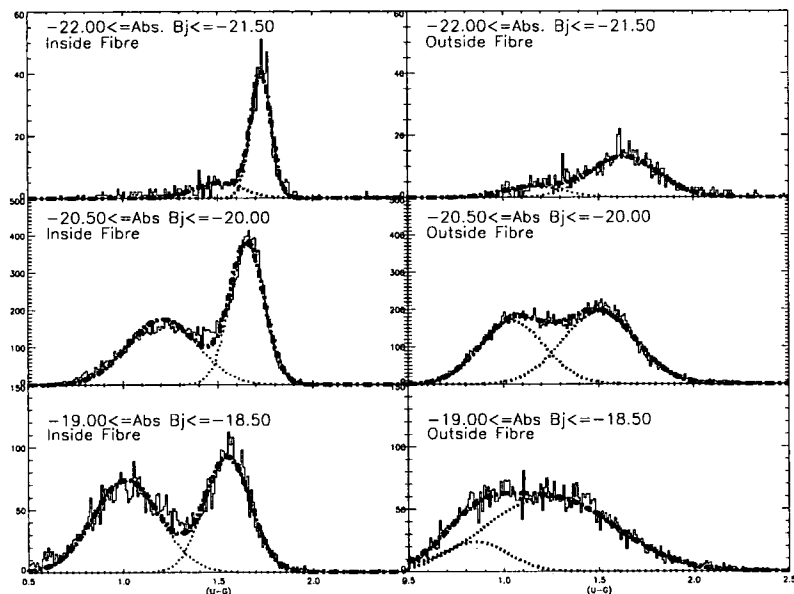


Figure 6.1: $(u-g)$ colour distribution of SDSS galaxies *inside* (left) and *outside* (right) the fibre for *bright* ($-22 \leq M_{b_j} \leq -21.5$) galaxies (top), *intermediate brightness* ($-21 \leq M_{b_j} \leq -20.5$) and *faint* ($-19 \leq M_{b_j} \leq -18.5$) galaxies (below). Each colour distribution is fitted by a double gaussian representing the bimodal populations of galaxies (thick line).

Mehlert et al., 2003; Tamura & Ohta, 2003). Therefore it is important that we understand the origin of the colour gradients in the SDSS galaxy population before interpreting the level of aperture bias in our data.

We approximate the total galaxy colour of SDSS galaxies using their Petrosian magnitudes. The fibre magnitudes measure the flux within a SDSS spectroscopic fibre of diameter $3''$. We estimate the colour of galaxies outside the fibre to be the Petrosian flux minus the fibre flux. More details on the SDSS magnitude system can be found in Stoughton et al. (2002). Whilst these fibres are larger than the 2dF fibres, the poor seeing of 2dFGRS observations (a median seeing of about $1.5''$) means that the 2dF fibres sample galaxy light from a similar radius. We find that many SDSS galaxies with $0.05 \leq z \leq 0.1$ do show significantly bluer colours outside of the fibre than inside (see Figure 6.1).

We interpret the colours of galaxies in terms of the bimodal distribution of red passive galaxies and blue star-forming galaxies (as seen by Balogh et al., 2004a; Blanton et al., 2003; Baldry et al., 2004). Baldry et al. (2004) find that the colour distribution of the SDSS galaxy population is well represented by a double gaussian model and so we choose a similar method to fit the colour distribution of galaxies both inside and outside the fibre. To make direct comparisons with our 2dFGRS galaxy samples easier, we estimate the rest frame Petrosian b_j -band absolute magnitude of all SDSS galaxies in the range

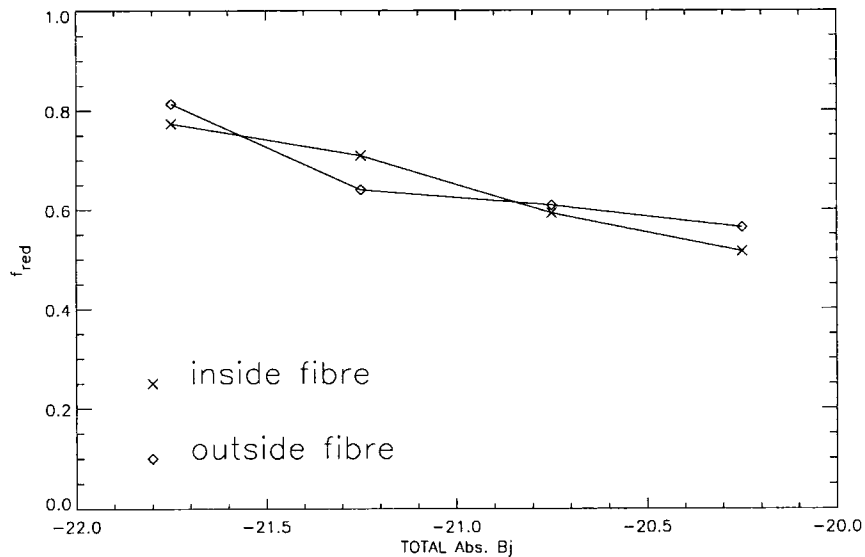


Figure 6.2: The fraction of galaxies located in the red peak of the bimodal distribution (f_{red}) as a function of luminosity, both inside and outside the fibre. The crosses represent the fibre colour distribution and the diamonds the colour distribution outside the fibre.

$0.05 \leq z \leq 0.1$ using the transformation $b_J = g + 0.15 + 0.13(g - r)$ where g and r have been k -corrected (Norberg et al., 2002). The double gaussian model is fit to the galaxy population using a gradient-expansion algorithm to compute a non-linear least squares fit. Fits to 3 of these bins of luminosity, spanning the full significant luminosity range can be seen in Figure 6.1. The wider peaks seen outside the fibre can be attributed to the measurement errors on the galaxy magnitudes. These errors are roughly twice as large in computed magnitudes outside the fibre than in fibre magnitudes. Fainter than $M_{b_J} = -20$, the median measurement error of $\gtrsim 0.15\text{mag}$ outside the fibre (and up to $\sim 0.5\text{mag}$ in some galaxies) smoothes out the double gaussian distribution, as can be seen in the bottom-right panel of Figure 6.1. The double gaussian fit to the colour distribution is then poorly constrained. Therefore, we only consider the galaxy population brighter than $M_{b_J} = -20$ in this analysis (aperture effects should be less important for the less luminous galaxies, anyway).

Figures 6.2 and 6.3 respectively, show the variation with luminosity, inside and outside the fibre, of the fraction of galaxies located inside the red peak (f_{red}), and the mean (u-g) colour of the red peak (μ_{red}) and blue peak (μ_{blue}). In particular, Figure 6.2 shows that the fraction of galaxies located in the red peak f_{red} outside the fibre is consistent with f_{red} inside the fibre. This indicates that no aperture corrections are necessary to account for the fraction of red, passive galaxies in the sample.

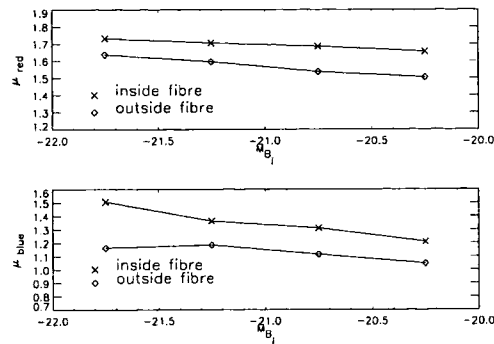


Figure 6.3: The central position (mean) of the red peak (**Top**, μ_{red}) and the blue peak (**Bottom**, μ_{blue}) of the bimodal distribution as a function of luminosity, both inside and outside the fibre. The crosses represents the fibre colour distribution and the diamonds the colour distribution outside the fibre.

Figure 6.3 shows a bluewards shift of μ_{red} as we move to fainter magnitudes both inside and outside the fibre. However, a radial colour gradient exists at all luminosities, such that μ_{red} is $\sim 0.1 - 0.15$ magnitudes bluer in the outer regions. A comparable colour gradient is seen in the blue peak (the blue population of galaxies). The similarity of the colour gradient in both the blue galaxies and in the red, passive galaxies (in which no star formation is expected) suggests that it may arise from a metallicity gradient rather than an age gradient, and explains why we observe no trend in f_{red} with aperture.

This interpretation is supported by the observations of metallicity gradients (and the lack of age gradients) in early-type galaxies (e.g Hinkley & Im, 2001; Mehlert et al., 2003; Tamura & Ohta, 2003; Wu et al., 2004). The colour differences we observe inside and outside the fibre are $\delta(u - g) \sim 0.15$, consistent with the average (u-g) colour gradient of 0.18 found in 36 early type SDSS galaxies analysed by Wu et al. (2004).

Chapter 7

Modelling Galaxy

Evolution and

Environmental Effects

In this chapter we take two completely opposite approaches to model the evolution of galaxy populations in groups and the field. In Section 7.1 we begin with the observed evolution in the fraction of passive galaxies f_p (see Chapter 5). We then try and match this behaviour using a simple model in which the evolution of broad-band luminosity and line emission from a galaxy is predetermined only by its star formation history. Then in Section 7.2 we take a “mock” catalogue of galaxies, each with a model spectrum, generated from simulations using a semi-analytic model of galaxy formation (GALFORM, Cole et al., 2000). Semi-analytic modelling is designed to reproduce a variety of galaxy observables through the application of physically motivated properties to galaxies and the dark matter haloes in which they are embedded. Therefore, comparison of the emission line properties of group and field galaxies at $z \sim 0$ and $z \sim 0.4$, with the properties of galaxies in the mock catalogue, provides a new and independent test of how well the most recent iteration of GALFORM mimics the real Universe.

7.1 Simple Models of Galaxy Evolution

In Chapter 5 we discovered a strong evolution in the fraction of passive galaxies f_p in groups and in the field since $z \sim 0.45$. In this section, we seek to determine whether this evolution can be matched without regular transformation, or “truncation” events (in which the SFR of a galaxy drops to zero over a short timescale).

We assume that CNOC2 galaxies represent a population equivalent to the progenitors of the 2dF population; therefore, using the stellar population models of Bruzual & Charlot (2003) it is possible to create mock-2dF populations by evolving the CNOC2 galaxies to the mean redshift of 2dF galaxies ($z_{2dF} = 0.08$) in accordance with a chosen set of model

parameters. We present two model methods with different evolutionary scenarios but similar basic methodology. Both models allow us to estimate the evolution of EW[OII] and M_b , within a given set of parameters. The *quiescent evolution* scenario is characterised by the lack of environmental evolution (i.e. group galaxies were always group galaxies). There are no sudden events which drastically alter a galaxy's star formation. Bright star-forming galaxies simply decline exponentially in their star formation with a constant e-folding timescale and thus fade in luminosity. In the *truncation* scenario, we incorporate into our evolution model a probability of each galaxy undergoing a truncation event, in which it suddenly ceases star formation. In this model, there is also a probability that a high redshift field galaxy can infall onto a galaxy group to become a local group galaxy.

7.1.1 The Quiescent Evolution Scenario

7.1.1.1 The Modelling Procedure

A quiescent evolution scenario is characterised by the lack of sudden events which drastically alter a galaxy's star formation. In this scenario, the star formation rate (SFR) in any galaxy declines internally with an e-folding timescale, τ . This timescale is short in the case of massive early-type galaxies, and much longer in the case of later types. The environmental dependence of star formation can then be invoked using a nature-origin scenario in which more early-type galaxies form in more densely clustered regions of the Universe.

To test whether this model can explain the strong evolution seen in our data, we must first model the ways in which galaxy luminosity and EW[OII] depend upon the star formation history of a galaxy. We do this by modelling the spectrophotometric evolution of CNOC2 galaxies (Bruzual & Charlot, 2003) with different forms of star formation history. By accounting for this evolution, we can understand how f_p in CNOC2 galaxies can be compared with the equivalent values of f_p locally in the 2dF data. This model also requires no density evolution which means that group galaxies remain as group galaxies and field galaxies remain as field galaxies. The model evolution contains the parameters $[IMF, z_{form}, Z, dust]$ and is applied in the following way:

1. Each model galaxy is given an IMF, redshift of formation, z_{form} , characteristic timescale, τ and metallicity Z^1 . We also choose either a model with no dust or with a Granato et al. (2000) Milky Way dust extinction law applied.

¹Note: The galaxy metallicity, Z is capitalised to distinguish it from redshift, z

2. Bruzual & Charlot (2003) model SEDs are used to model the spectrum of a galaxy with the chosen parameter set at various steps in redshift up to $z = 0.55$.
3. The rest-frame b_J -band luminosity evolution between two different redshifts is modelled by convolving the filter transmission function with the model spectrum (normalised to a fixed stellar mass) at each redshift and calibrating to Vega as in 2dFGRS.
4. The evolution of EW[OII] is measured by computing the model Lyman continuum flux in each spectrum and artificially reprocessing this as [OII] flux using the HII region models of Stasinska (1990) at the chosen metallicity, Z . We assume 1 ionising star per HII region with effective temperature 45000K and a HII region electron density of 10cm^{-3} . The equivalent width is then simply measured by computing the continuum luminosity at the wavelength of the [OII] emission line and normalising the line flux by its continuum level. We have successfully tested our model by reproducing the results of Poggianti & Barbaro (1996) for an elliptical galaxy with a recent starburst.

At a given redshift and for a given IMF, Z , z_{form} and dust option, we can determine a value of τ at which $\text{EW}[\text{OII}] = 5\text{\AA}$. By measuring $\tau = \tau_{lim}$ at low redshift (in the 2dF redshift range), we can then determine the equivalent value of EW[OII] for the same galaxy (with $\tau = \tau_{lim}$) at higher redshift (i.e. at CNOC2 redshifts). This value we then call x , in units of \AA .

In this way, we determine the dependence of x on all the relevant parameters. Higher values of x imply greater evolution in a galaxy's SFR and so the most extreme example of quiescent evolution will occur with a parameter set in which x is chosen to be as large as realistically possible:

- x is approximately 1/3 larger for a Salpeter IMF than for a Kennicutt IMF (Kennicutt, 1983).
- x decreases when dust is included.
- x is at a peak where the metallicity, Z , is approximately solar ($= 0.02$) or slightly sub-solar (down to $Z \sim 0.004$). Both at lower and higher metallicities, the value of x decreases.
- On the whole, x decreases as z_{form} increases.

- x generally increases for larger choices of CNOC2 redshift (i.e. up to $z = 0.55$).
- x increases for lower choices of 2dFGRS redshift (i.e. down to $z = 0.05$).

The rest-frame b_J -band luminosity evolution of a CNOC2 galaxy is computed by determining the value of τ which best reproduces the value of EW[OII] for that galaxy at z_{CNOC2} . Then the fading of that galaxy by z_{2dF} is computed using $\delta M_{b_J} = M_{b_J}(z_{2dF}) - M_{b_J}(z_{\text{CNOC2}})$ for those model parameters.

7.1.1.2 The Influence of Quiescent Evolution on f_p

The obvious problem is that this model would predict very different EW[OII] distributions at $z = 0$ and $z = 0.45$ (not observed - see Chapter 5). Here, we examine the influence on f_p .

To investigate the effects of quiescent evolution on f_p , we choose a control model and an extreme model. For our control model we choose a Kennicutt IMF, a galaxy formation redshift $z_{\text{form}} = 10$ and solar metallicity. We also incorporate a basic dust prescription into the model. For our extreme model, we deliberately choose model parameters which achieve maximal evolution in f_p (as discussed in Section 7.1.1.1). We choose a Salpeter IMF, $z_{\text{form}} = 3$, solar metallicity and we ignore the effects of dust.

The mean redshifts of the 2dFGRS and CNOC2 samples are $z \sim 0.08$ and $z \sim 0.45$ respectively. The values of τ_{lim} and x in our 2 test cases (see main text) are then:

- **Control model:** With a Kennicutt IMF, $z_{\text{form}} = 10$ and solar metallicity and the Granato et al. (2000) dust prescription, $\tau_{\text{lim}} = 2.93\text{Gyrs}$ and $x = 7.04\text{\AA}$.
- **Extreme model:** With a Salpeter IMF, $z_{\text{form}} = 3$, solar metallicity and no dust, $\tau_{\text{lim}} = 1.74\text{Gyrs}$ and $x = 9.86\text{\AA}$.

Figure 7.1 shows f_p as a function of luminosity in the observed CNOC2 and 2dF samples, together with the equivalent trend in the evolved CNOC2 population obtained using this model. The evolution of f_p in the model significantly underestimates the trend seen in the real data. This is partly because galaxies which become passive also tend to fade into a fainter bin of luminosity, leaving the trend of f_p with luminosity approximately unchanged.

Figure 7.2 shows the same 2dF and CNOC2 data as in Figure 7.1 but this time overplotted with the evolved CNOC2 population obtained using this extreme model. In this case, galaxies fainter than $\sim M_* - 0.5$ still show a significant deficit of passive galaxies

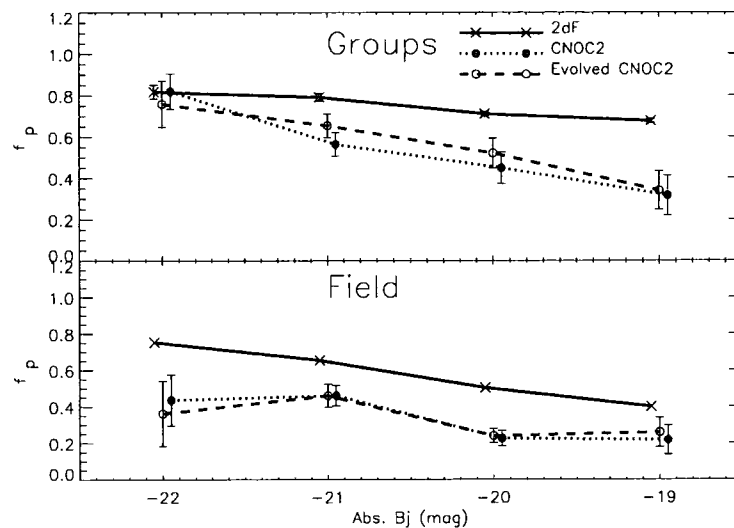


Figure 7.1: The fraction of passive galaxies, f_p , in the 2dF (solid line) and CNOC2 group (within 1 projected h_{75}^{-1} Mpc of group centre) and field galaxy populations, as a function of M_{b_j} . The CNOC2 galaxies are shown as observed (dotted-line), and evolved to z_{2dF} using a quiescent model with a Kennicutt IMF, $z_{form} = 10$, solar metallicity and dust extinction (dashed-line). The 2dF points are slightly negatively offset, and the CNOC2 data points slightly positively offset in M_{b_j} for clarity.

(low f_p) in the evolved CNOC2 galaxies when compared to the data. This provides strong evidence that transformations are required to reproduce the observed evolution in f_p both in groups and in the global (field) population.

7.1.2 The Truncation Scenario

7.1.2.1 The Modelling Procedure

Next we consider a model in which galaxies undergo transformations that cause them to cease forming stars. We have shown in Section 7.1.1 that some form of galaxy transformation appears to be required to reproduce our observed evolution in f_p . Here, we constrain the probability of the transformations required to match the observed evolution in f_p and its dependence upon galaxy luminosity and environment.

In this scenario, a CNOC2 galaxy either continues with its e-folding decline in star formation, or has its star formation truncated instantaneously with a probability P_{trunc} per Gyr, at a random point during its evolution to $z_{2dF} = 0.08$. This acts as a simple way to enhance the decline of star formation, and in particular to turn a star forming galaxy

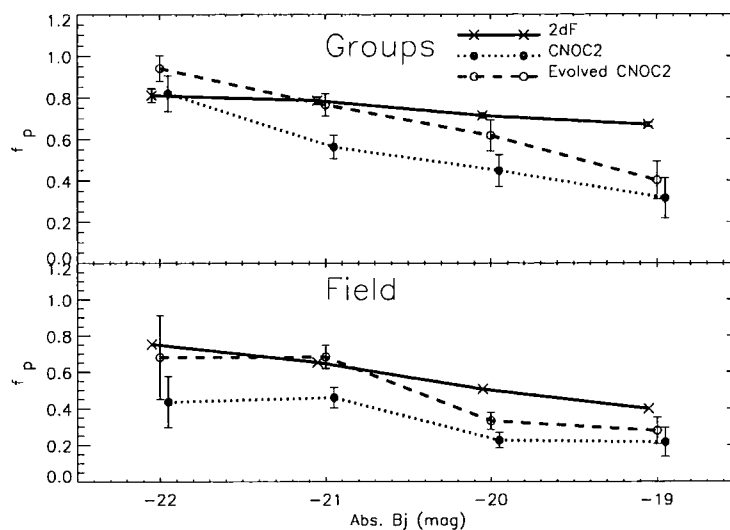


Figure 7.2: Similar to Figure 7.1, but assuming an extreme quiescent evolution model for the CNOC2 population, with a Salpeter IMF, $z_{form} = 3$, solar metallicity and no dust extinction (dashed-line). This represents the maximum evolution expected from any realistic quiescent model. The 2dF points are slightly negatively offset, and the CNOC2 data points slightly positively offset in M_{b_j} for clarity.

into a passive galaxy, independent of its initial star formation. We neglect the possibility that some transformations are accompanied by a strong starburst or involve the merging of galaxies as either of these possibilities cannot be constrained by simply considering the evolution in f_p . A detailed modelling of spectral and photometric parameter space would be necessary to constrain these elements of the model with enough accuracy. The timescale of the transformation is likely to have little effect on the evolution of f_p . Here, we concentrate on matching the value of f_p as defined using the value of $EW[OII]$ over a range of M_{b_j} luminosity. This is enough information to constrain the probability of transformations using a simple model, similar to our quiescent evolution model described in section 7.1.1.1. In Section 7.2 we will consider our data in the context of semi-analytic models.

The probability of truncation (P_{trunc}) is constrained as a function of local luminosity in groups and the field by randomly choosing an evolution to z_{2dF} of star formation for each CNOC2 galaxy with a range of truncation probabilities. The CNOC2 galaxies are then evolved appropriately in M_{b_j} and $EW[OII]$ using Bruzual & Charlot (2003) models and the resulting f_p for the evolved population is compared with the local values obtained from 2dF

data, thus constraining P_{trunc} . Density evolution is incorporated by requiring local groups to contain ξ_{gr} % CNOC2 group members and $(1 - \xi_{\text{gr}})$ % CNOC2 field galaxies. The model contains the spectrophotometric evolution parameters $[P_{\text{trunc}}, \text{IMF}, z_{\text{form}}, Z, \text{dust}]$ and the density evolution parameter ξ_{gr} . However, this is simplified by maintaining a consistent and reasonable spectrophotometric model. We choose a realistic set of basic parameters governing the spectrophotometric evolution: a Kennicutt IMF, redshift of formation, $z_{\text{form}} = 10.0$, and solar metallicity. We also incorporate a constant dust prescription in the model (Granato et al., 2000). We note from experimentation that changing these parameters does not strongly affect our conclusions (dependencies on these parameters can be seen in the section 7.1.1.1). Our model is implemented as follows:

1. A fiducial set of model parameters is chosen. These include IMF, redshift of formation z_{form} , metallicity Z and presence (or not) of dust extinction.
2. For the chosen set of parameters, galaxy spectra are constructed for a variety of star formation histories, using Bruzual & Charlot (2003) model SEDs. The star formation histories are parameterised with characteristic timescale τ and redshift of truncation, z_{trunc} , allocated via a 2D grid of discrete values for ease of computation. We compute histories combining $\tau = [1000, 15, 12, 10, 9, 8, 7, 6, 5, 4, 3, 2, 1, 0.5]$ Gyrs and z_{trunc} corresponding to 12 equally spaced intervals in time between $z = 0.55$ and $z = 0.05$, given our cosmology. One set of models histories with no truncation is also computed.
3. The evolution in rest-frame b_J -band luminosity and EW[OII] are computed using the same method as described in the quiescent evolution model.
4. At the redshifts $z = [0.55, 0.5, 0.45, 0.4, 0.35, 0.3, 0.08]$ we determine the values of rest-frame b_J -band luminosity per unit stellar mass, EW[OII] and the ratio of stellar mass to present day stellar mass for all possible combinations of τ and z_{trunc} . This covers the CNOC2 redshift range and the mean 2dF redshift ($z_{2dF} = 0.08$).
5. For each star forming history (i.e. each value of τ and z_{trunc}), we compute the evolution in M_{b_J} and EW[OII] from $z_{\text{CNOC2}} = [0.55, 0.5, 0.45, 0.4, 0.35, 0.3]$ to $z_{2dF} = 0.08$. For intermediate z_{CNOC2} we simply interpolate between these values.
6. For each galaxy in the CNOC2 sample, a value of τ is chosen which best matches the EW[OII] of the CNOC2 galaxy at the redshift of that galaxy. This involves making a 2D interpolation over the τ models in EW[OII] and z_{CNOC2} .

7. The probability of a galaxy having its star formation truncated in 1 Gyr is P_{trunc} . For a given value of P_{trunc} , the CNOC2 galaxies are evolved to redshift $z = 0.08$ for comparison with 2dF galaxies. This evolution consists of randomly selecting a truncation redshift, z_{trunc} , where $z_{\text{CNOC2}} > z_{\text{trunc}} > 0.08$ with a probability equivalent to the product of P_{trunc} and the timestep in Gyr, for each z_{trunc} . Each galaxy can only experience one truncation and if it has not undergone any truncation by $z = 0.08$ then we select the evolution model with no truncation. The values of M_{b_j} and EW[OII] for the evolved CNOC2 galaxy at $z = 0.08$ are then assigned in a consistent manner from the computed evolution models.
8. This evolution is repeated with a range of values of P_{trunc} to create a series of mock catalogues of CNOC2 galaxies evolved to $z = 0.08$. We allow P_{trunc} to vary between 0.0 and 0.8 in steps of 0.005.
9. A density evolution model is assumed. In this model, CNOC2 field galaxies become 2dF field galaxies and CNOC2 group galaxies become 2dF group galaxies. However, a CNOC2 field galaxy may also become a 2dF group galaxy, with a probability $P_{f:g}$ (which is computed such that local groups comprise $\xi_{\text{gr}}\%$ CNOC2 group members and $(1 - \xi_{\text{gr}})\%$ CNOC2 field galaxies), mimicking the clustering of large scale structure in the Universe. Realisations of dark matter halo merger trees suggest that the actual fraction of 2dF group galaxies in groups by $z = 0.45$ was $\sim 80\%$ ($\xi_{\text{gr}} = 80\%$) (Lacey & Cole, 1993)
10. Given our choice of density evolution, for each evolved CNOC2 mock catalogue (each choice of P_{trunc}) we compute $f_p(\text{mock})$ as a function of luminosity in the group and field samples. These values are then compared with the locally measured values $f_p(2\text{dF})$ and a best fit value of P_{trunc} is chosen for each luminosity bin in each sample using a polynomial function to fit $f_p(\text{mock})$ as a function of P_{trunc} .
11. Errors on P_{trunc} are determined by first determining the errors in $f_p(\text{mock})$ and $f_p(2\text{dF})$ and then combining these in quadrature and converting to an error in P_{trunc} in each bin. Errors in $f_p(\text{mock})$ include the statistical errors in the CNOC2 population and its evolution and the error in EW[OII] leading to an error in the distribution of τ models selected. Errors in $f_p(2\text{dF})$ include the statistical error in the population and the error due to random smoothing (by 2\AA) of the 2dF galaxies' EW[OII]. These errors are all estimated using a resampling method.

Table 7.1: Values assigned to truncation model parameters, whether kept constant or allowed to vary. We note that the parameters IMF, z_{form} , metallicity Z , dust and the choice of τ for each galaxy have little effect on the results. This is because the evolution of f_p to $z_{2dF} = 0.08$ mostly depends upon P_{trunc} .

Parameter	Value(s)
Initial Mass Function of stars, IMF	Constant: Kennicutt IMF (Kennicutt, 1983).
Redshift of galaxy formation, z_{form}	Constant: $z_{form} = 10.0$.
Galaxy Metallicity, Z	Constant: solar metallicity.
Galaxy internal extinction by dust	Constant: Granato et al. (2000) prescription.
Probability that star formation is truncated per Gyr, P_{trunc}	Varied: A $z_{2dF} = 0.08$ mock population is created for each value from 0.0 and 0.8 in steps of 0.005.
Percentage of galaxies in local groups, in groups at z_{CNOC2} , ξ_{gr}	Two values: $\xi_{gr} = 100\%$ (All local group galaxies in groups at z_{CNOC2}) and $\xi_{gr} = 0\%$ (No local group galaxies in groups at z_{CNOC2}).
e-folding time of SFR decline in each galaxy, τ	Fixed for CNOC2 each galaxy, to match the observed value of EW[OII].
Redshift at which a galaxy has its star formation truncated, z_{trunc}	Randomly allocated to each galaxy, with a probability P_{trunc} per Gyr that a galaxy will be truncated, and in some cases no truncation will therefore take place.

The model parameters are summarized in Table 7.1.

7.1.2.2 The Influence of Truncation on the Evolution of f_p

Following the model prescription, we obtain best fit values for P_{trunc} as a function of local luminosity and environment to fit the observed evolution in f_p . Figures 7.3 and 7.4 shows P_{trunc} as a function of luminosity in groups and in the field with $\xi_{gr} = 100\%$ (local group members were all group members at z_{CNOC2}) and $\xi_{gr} = 50\%$ (local group members were 50% group members and 50% field galaxies at z_{CNOC2}) respectively. We note that adopting a Salpeter IMF does not significantly alter these results.

Figures 7.3 and 7.4 show the following:

1. P_{trunc} is significantly greater than zero implying that galaxy transformations are

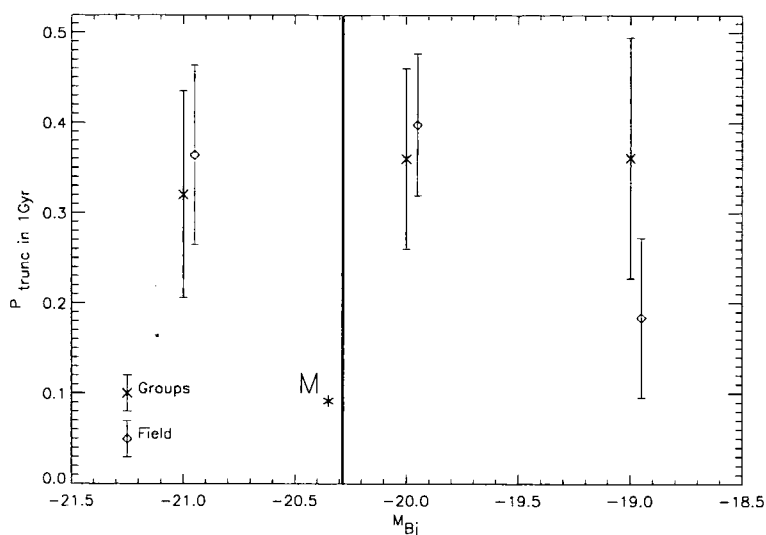


Figure 7.3: The probability (per Gyr) that star formation has been truncated (P_{trunc}) as a function of M_{Bj} as determined by modelling the evolution of f_p between the CNOC2 ($0.3 \leq z_{\text{CNOC2}} \leq 0.55$) and 2dF ($0.05 \leq z_{2dF} \leq 0.1$) samples. The crosses represent the group galaxies and the diamonds represent the field population which has been artificially offset by 0.05mag for clarity. Here, there is assumed to be no density evolution, i.e. all group galaxies were already in groups by z_{CNOC2} ($\xi_{\text{gr}} = 100\%$). The vertical line represents the location of a M_* galaxy in 2dF as determined from the luminosity function of Norberg et al. (2002).

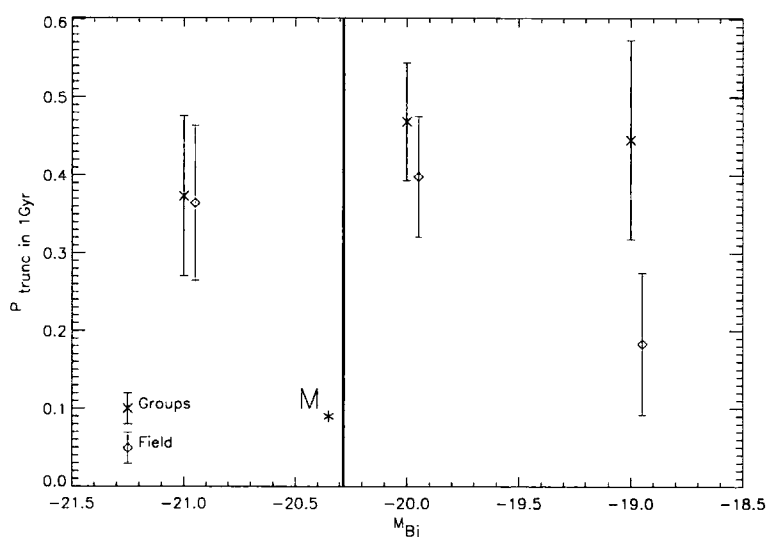


Figure 7.4: As Figure 7.3, but assuming local 2dF groups comprise 50% CNOC2 group galaxies and 50% CNOC2 field galaxies ($\xi_{\text{gr}} = 50\%$).

required over our redshift range, both in groups and the field. This is independent of the assumed evolution of clustering power and agrees with our conclusions in Section 7.1.1.

2. Assuming no density evolution since $z \sim 0.45$, $\xi_{\text{gr}} = 100\%$, (Figure 7.3), we see no evidence that P_{trunc} is larger in groups than in the field. This means that there must be some *global* mechanism in which star formation can be effectively reduced to zero over a short period of time rather than simply declining in a quiescent manner as assumed in Section 7.1.1. However the existence of a more evolved population (higher f_p) in groups suggests that the star formation history prior to $z \sim 0.45$ must depend upon environment in some way. This could be either a nurturing environmental process at $z > 0.45$, or an earlier formation time for galaxies in groups (nature). We emphasize that our model is designed to simply match the observed evolution of f_p . It is not intended to simultaneously match evolution of the luminosity function, which requires a better understanding of the volume-averaged galaxy density. We are also constrained by our definition of “field” which spans the full range of environment.
3. If we assume a strong density evolution with only 50% of local group galaxies in groups at $z \sim 0.45$, $\xi_{\text{gr}} = 50\%$, (Figure 7.4), then a marginally larger P_{trunc} is invoked in groups than in the no density evolution ($\xi_{\text{gr}} = 100\%$) case, although not significantly so. Even at faint luminosities the differences between P_{trunc} in groups and in the field is still of low significance ($< 2\sigma$ in the $-19.5 \leq M_{b_j} \leq -18.5$ bin). Physically, an enhanced P_{trunc} with greater density evolution is consistent with a second transformation process occurring during clustering as a galaxy is infalling into a larger dark matter halo. A strong density evolution with a P_{trunc} which remains constant with redshift could theoretically explain the larger value of f_p in groups than in the field. However, realisations of dark matter halo merger trees suggest that the actual fraction of 2dF group galaxies in groups by $z = 0.45$ was $\sim 80\%$ ($\xi_{\text{gr}} = 80\%$) (Lacey & Cole, 1993).
4. There are no clear trends of P_{trunc} with galaxy luminosity in groups. In the field there is a suggestion ($\sim 2\sigma$ significance) that P_{trunc} decreases in the faintest bin ($-19.5 \leq M_{b_j} \leq -18.5$).

We acknowledge that our model is simple, and neglects the mass and luminosity en-

hancing effects of galaxy-galaxy mergers. These are necessary to build up the population of bright galaxies in the local luminosity function which otherwise simply fade as they cease forming stars. In Chapter 3 we have shown that the CNOC2 groups have a relative excess of bright galaxies compared with the field, a trend which appears to hold in local groups (Figure 5.1). Whilst our model is not designed to match the luminosity function, we note that this population of bright galaxies in local groups can only be matched in the model by incorporating galaxy mergers. Incorporating mergers into our model can only serve to increase the requirement for transformations in the formation of locally bright galaxies from a fainter, more highly star forming population. We also note that in our model transforming galaxies tend to fade into fainter bins of luminosity, a process which affects the computation of P_{trunc} . In Section 7.2 we make comparisons of the data with results from more physically realistic models (e.g. Cole et al., 2000).

7.2 Semi-Analytic Models of Galaxy Formation

7.2.1 Introduction

In this section we compare the emission line properties of group and field galaxies at $z \sim 0$ and $z \sim 0.4$ in catalogues of observed and simulated galaxies. By making a blind comparison of the simulated galaxy population in a mock galaxy catalogue with the 2dF and CNOC2 galaxy populations, we can determine which of the trends identified in Chapters 3 and 5 are reproduced by the model. We can also identify areas in which the model must be improved to better emulate the real Universe.

Our mock catalogue is generated using the semi-analytic model of galaxy formation, GALFORM (Cole et al., 2000, see that paper for details) with a number of recent additions. The basic model of Cole et al. (2000) regulates star formation in galaxy disks through a combination of hot gas cooling onto the disk and reheating of gas by young stars and SNe. Critically, the hot gas is associated only with the most massive progenitor galaxy of a halo (the “central” galaxy) and so the halo’s hot gas cools onto this galaxy only. This leads to a process of strangulation in satellite galaxies which soon exhaust their fuel supplies. Star formation also takes place in starbursts which occur during galaxy mergers. Recent additions to the model are described in Baugh et al. (2004). These include the addition of superwinds which ejects cold gas out of the hot gas halo, and a top-heavy IMF in starbursts (see Baugh et al., 2004, for motivation).

Emission line equivalent widths are computed using exactly the same method as that

used in Section 7.1. Both continuum and emission light is extinguished using the diffuse dust extinction model of Granato et al. (2000). We also wish to test the extent to which additional dust in HII regions can influence the measured emission line equivalent widths. Therefore we introduce a second dust extinction term which only applies to line emission:

$$A_V = A_{V0} \times \frac{Z_{gas}}{Z_{\odot}} \quad (7.1)$$

This additional dust extinction scales linearly with the metallicity of cold gas in the galaxy, Z_{gas} (Lacey et al., in preparation). It introduces 1 new parameter to our model, the dust scaling parameter A_{V0} .

Henceforth we shall call the galaxy population generated using GALFORM the *model population*. The galaxy populations as derived from observations (2dFGRS at $z \sim 0$ and CNOC2 at $z \sim 0.4$) will be known as the *observed populations*.

In Section 7.2.2 we compare the distributions of EW[H α] and EW[OII] in the model population with those in the observed population, testing the effects of varying A_{V0} in the model. We also show how the equivalent width distributions in populations of star forming galaxies alone compare. In Section 7.2.3 we then extend this analysis to investigate whether the fraction of passive galaxies f_p computed for the model population shows the same dependence upon b_J -band luminosity, environment (halo mass) and redshift as seen in the observed populations. Finally in Section 7.2.4 we summarize our findings and discuss the ways in which the model fails to match the observed galaxy population and how we might improve this test in the future in light of this comparison.

7.2.2 H α and [OII] Equivalent Width Distributions

Figure 7.5 shows the distribution of EW[H α] in the 2dFGRS field population (solid black line) and in the full $z = 0$ model population (coloured lines). Distributions are normalised so that the y-axis represents the fraction of galaxies per \AA . Populations are divided into bright galaxies ($M_{b_J} \leq -20.0$, upper panels) and fainter galaxies ($-20.0 \leq M_{b_J} \leq -18.5$, lower panels). EW[H α] distributions are distinctly bimodal in 2dFGRS, with the peak at 0\AA representing the population of passive galaxies (left panels). Therefore to examine the distribution of EW[H α] amongst star forming galaxies only, we renormalise the distributions so that the y-axis represents the fraction of star forming galaxies per \AA where a star forming galaxy is defined to have $\text{EW}[\text{H}\alpha] \geq 4 \text{\AA}$ (Balogh et al., 2004a) (right panels). The 3 model distributions represent different values for the dust scaling parameter A_{V0} . The red line represents the emission line model with extinction due to diffuse dust only

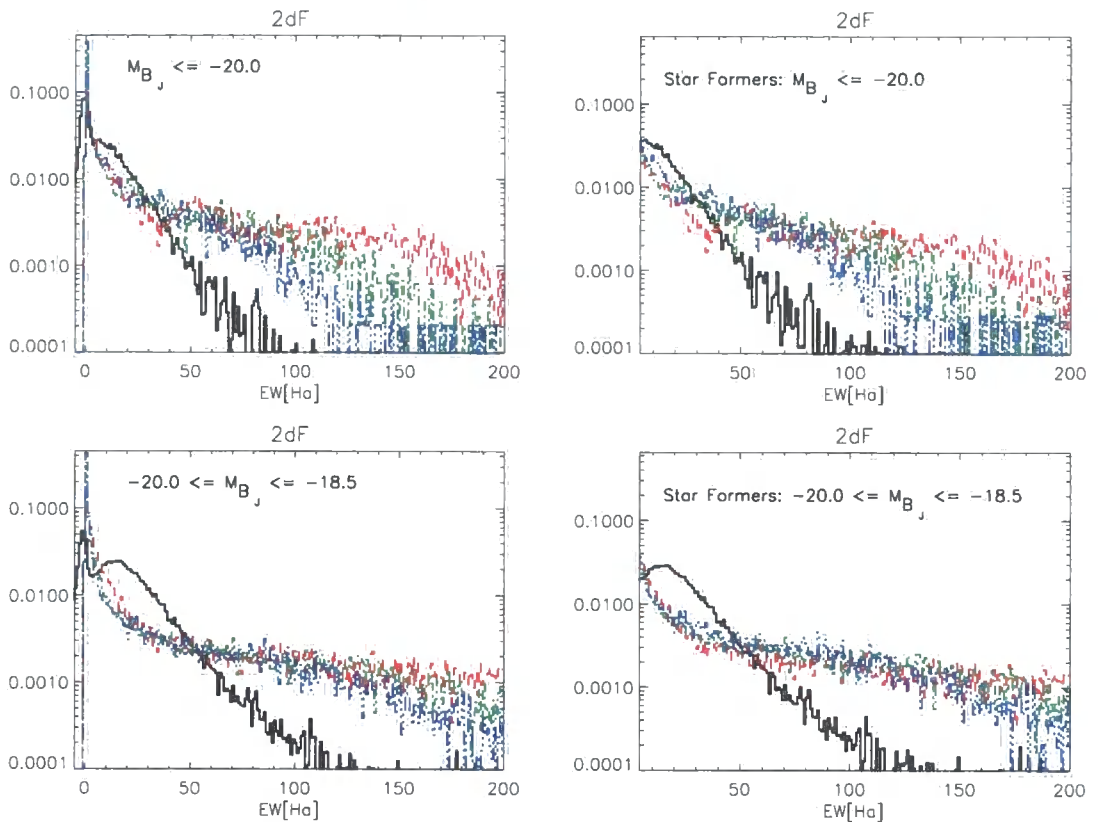


Figure 7.5: A comparison of the distribution of $\text{EW}[\text{H}\alpha]$ in 2dF galaxies (solid black line) with the model galaxy population at $z = 0$ in bright galaxies ($M_{b_j} \leq -20.0$, Top 2 panels) and fainter galaxies ($-20.0 \leq M_{b_j} \leq -18.5$, Bottom 2 panels). The red line represents the emission line model with extinction due to diffuse dust only ($A_{V0} = 0$). The green and blue lines represent emission line models with an additional metallicity-dependent dust extinction in HII regions, with $A_{V0} = 1.0$ and $A_{V0} = 2.0$ respectively. As the galaxy population is bimodal (Chapter 2) we show both the complete distribution and the distribution of star forming galaxies only. **Left:** Distributions are normalised to the fraction of the total population per \AA . **Right:** Distributions are normalised to the fraction of the Star Forming population only (selected to have $\text{EW}[\text{H}\alpha] \geq 4\text{\AA}$).

($A_{V0} = 0$). The green and blue lines represent models which also contain the additional metallicity dependent dust extinction with $A_{V0} = 1.0$ (green line) and $A_{V0} = 2.0$ (blue line), respectively.

From Figure 7.5 we can see that the distribution of $\text{EW}[\text{H}\alpha]$ at $z \sim 0$ is not well matched by the model, even when passive galaxies are excluded. There are too many highly star forming galaxies ($\text{EW}[\text{H}\alpha] \geq 50\text{\AA}$) and too few star forming galaxies with low equivalent widths. This results in the non-existence of the bimodality of $\text{EW}[\text{H}\alpha]$ in the

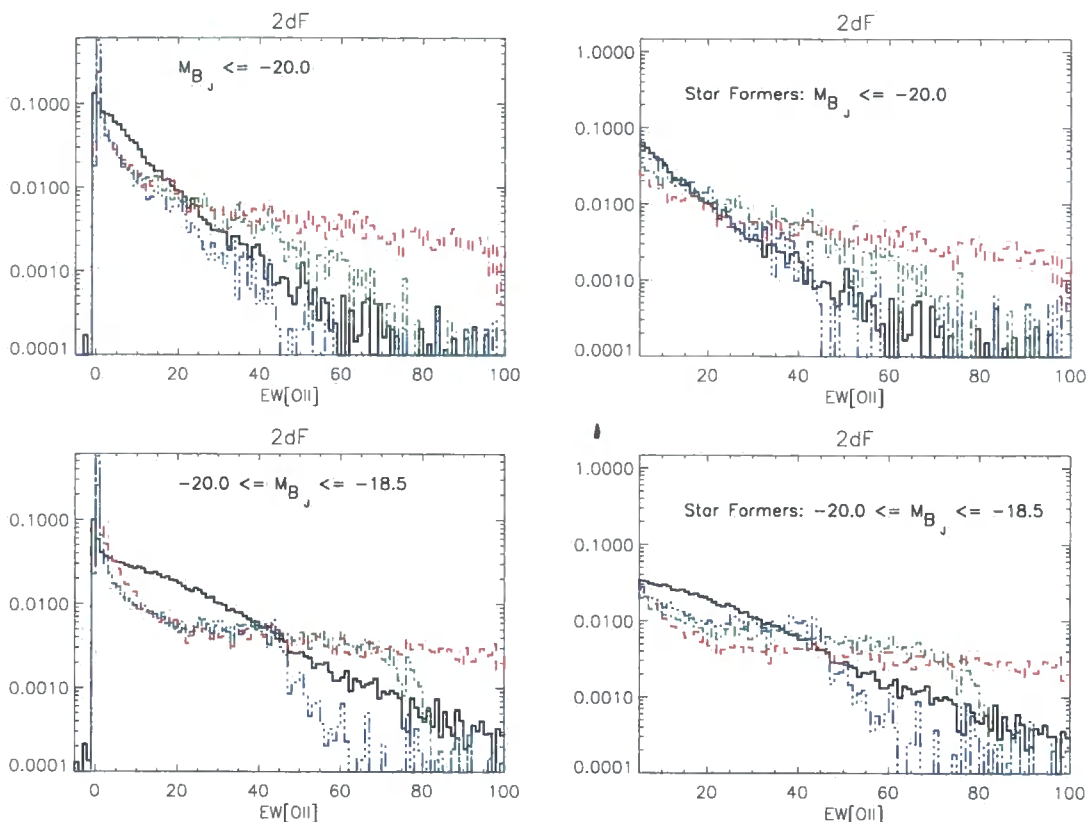


Figure 7.6: As Figure 7.5 but showing a comparison of the $\text{EW}[\text{OII}]$ distribution in 2dF galaxies with the model galaxy population at $z = 0$. The Star Forming population is defined to have $\text{EW}[\text{OII}] \geq 5\text{\AA}$.

model population at these magnitudes. The extra dust extinction in HII regions does little to improve the situation as $\text{EW}[\text{H}\alpha]$ is relatively insensitive to this extinction apart from in very highly star forming galaxies ($\text{EW}[\text{H}\alpha] \gtrsim 100\text{\AA}$).

Figure 7.6 shows the distribution of $\text{EW}[\text{OII}]$ in the 2dFGRS population (solid black line) and $z = 0$ model populations (coloured lines). The populations are again split into bright ($M_{b_j} \leq -20.0$, upper panels) and fainter galaxies ($-20.0 \leq M_{b_j} \leq -18.5$, lower panels). For $\text{EW}[\text{OII}]$, the division between passive and star forming galaxies is made at $\text{EW}[\text{OII}] = 5\text{\AA}$ as discussed in Chapter 3. We apply the same dust models as in Figure 7.5. Whilst the full distributions are not well matched (left panels), the star forming population (right panels) seems to be quite well matched to the observed population, especially with dust models which have additional extinction in HII regions (i.e. $A_{V0} = 2.0$, blue line) and in the brighter galaxies ($M_{b_j} \leq -20.0$). This additional extinction has a much stronger effect on $\text{EW}[\text{OII}]$ than on $\text{EW}[\text{H}\alpha]$ as the $[\text{OII}]$ line strength is much more strongly dependent upon metallicity than $\text{H}\alpha$.

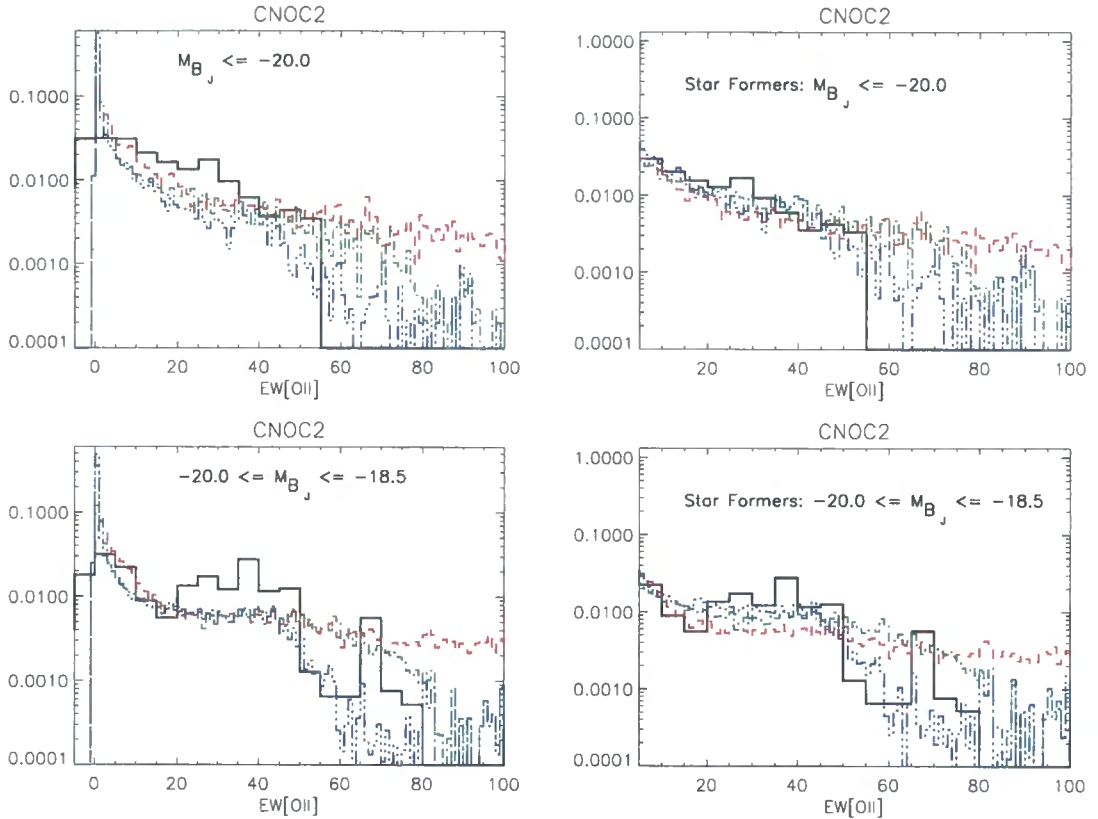


Figure 7.7: As Figure 7.6 but showing a comparison of the EW[OII] distribution in CNOC2 galaxies with the model galaxy population at $z = 0.4$.

Figure 7.7 shows the distribution of EW[OII] in the CNOC2 population (solid black line) and $z = 0.4$ model populations (coloured lines). The panels represent a $z \sim 0.4$ analogue of those in Figure 7.6. The high extinction model again produces a good match to the EW[OII] distribution of star forming CNOC2 galaxies.

7.2.3 The Behaviour of the fraction of passive galaxies, f_p

In this section we investigate the behaviour of the fraction of passive galaxies f_p which is defined using the [OII] division at $\text{EW}[\text{OII}] = 5\text{\AA}$ as in previous chapters. The 4 panels of Figure 7.8 show the behaviour of f_p with varying b_J -band luminosity in the model population, divided into 4 bins of parent halo mass, M_{halo} . The 3 lines in each panel represent 3 different stages of evolution ($z = 0$, solid black; $z = 0.4$, dashed red; $z = 1$, dash-dotted green). In all cases, we use the basic diffuse dust model ($A_{V0} = 0$) to compute EW[OII].

Figure 7.8 shows the clear dependence of f_p on environment and redshift. Galaxies located inside more massive haloes are more likely to be passive. Also galaxy evolution

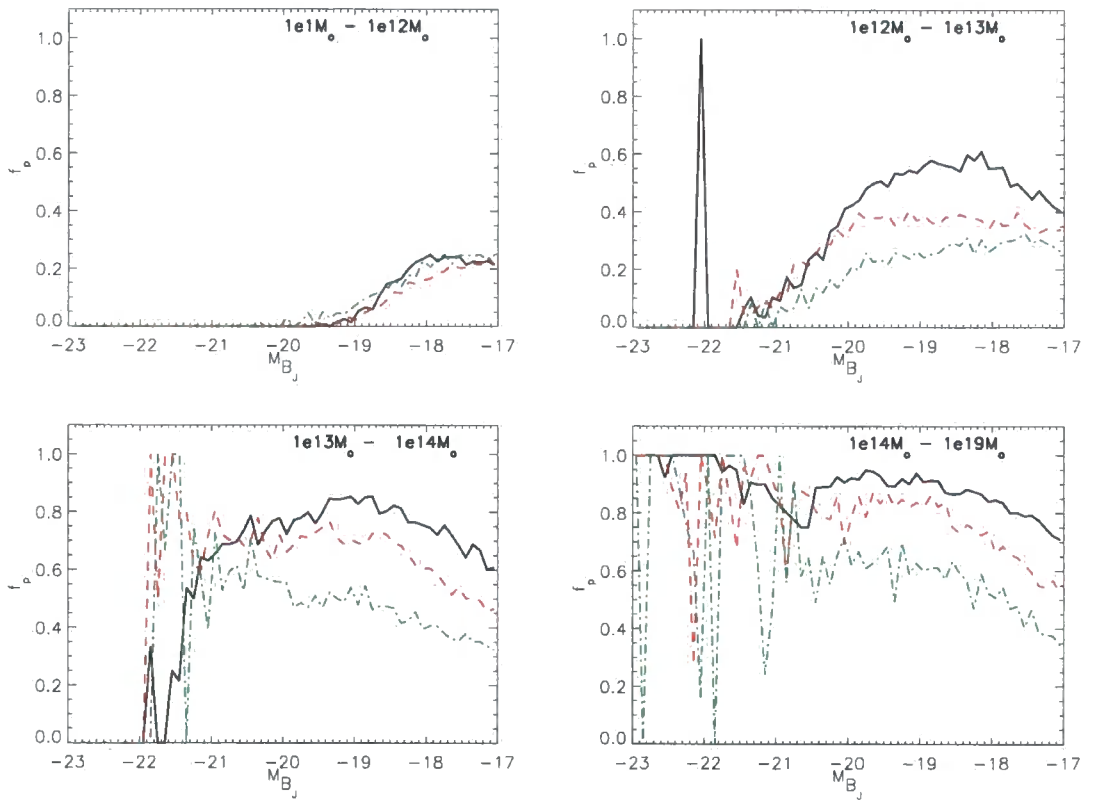


Figure 7.8: The fraction of passive galaxies f_p as a function of luminosity (M_{B_j}) in 4 bins of halo mass, M_{halo} (4 labelled panels). The 3 lines on each panel represent the model galaxy population at $z = 0$ (solid black), $z = 0.4$ (dashed red) and $z = 1$ (dot-dashed green) in each bin of halo mass.

leads to more passive galaxies at low redshift, with strong evolution apparent in all galaxies located in haloes with $M_{halo} \gtrsim 10^{12} M_{\odot}$, equivalent to the halo mass of a massive galaxy. In smaller haloes we see no evolution in f_p . Galaxies do exist brighter than $M_{B_j} \sim -19.0$ in the smallest haloes, even though none of them are passive. They are simply all still forming stars, indicating that in the model star formation is curtailed in processes related to the environment but including haloes down to $M_{halo} \sim 10^{12} M_{\odot}$. This is smaller than the mass of our 2dF or CNOC2 groups. The strong evolution in f_p even since $z = 0.4$ is in agreement with the observational trends (Chapter 5) as is the environmental dependence of f_p . In general however we see no clear trend of decreasing f_p with decreasing luminosity for a given bin of halo mass in the model population, as might be required to match the observations of galaxy groups.

In the top panel of Figure 7.9 we compare the behaviour of f_p in the 2dF field population (solid black line) with the model population at $z = 0$ (coloured lines). The different

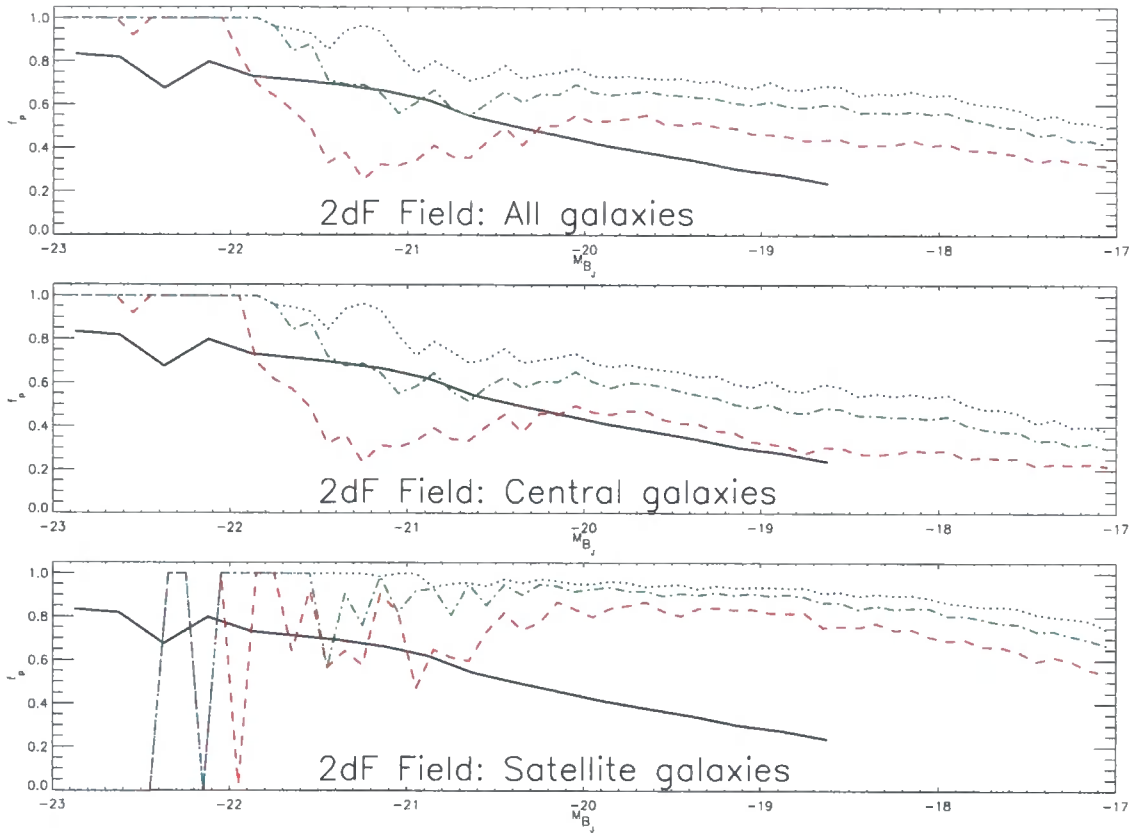


Figure 7.9: The fraction of passive galaxies f_p as a function of luminosity (M_{bj}) in the field population of 2dF (solid black line). This is compared with the model population at $z = 0$, considering [OII] emission with extinction due to diffuse dust only ($A_{V0} = 0$, dashed red line) and with an additional metallicity-dependent dust extinction in HII regions (dot-dashed green and dotted blue lines). We apply $A_{V0} = 1.0$ (green line) and $A_{V0} = 2.0$ (blue line). The 3 panels show the behaviour of f_p for all model galaxies (**Top**), central galaxies only (**Middle**) and satellite galaxies only (**Bottom**). In all cases we compare with the full 2dF population. Whilst the model succeeds in reproducing the shallow luminosity dependence of f_p faintwards of $M_{bj} \sim M_*$ (-20.28), we find f_p to be overestimated in the model at fainter luminosities.

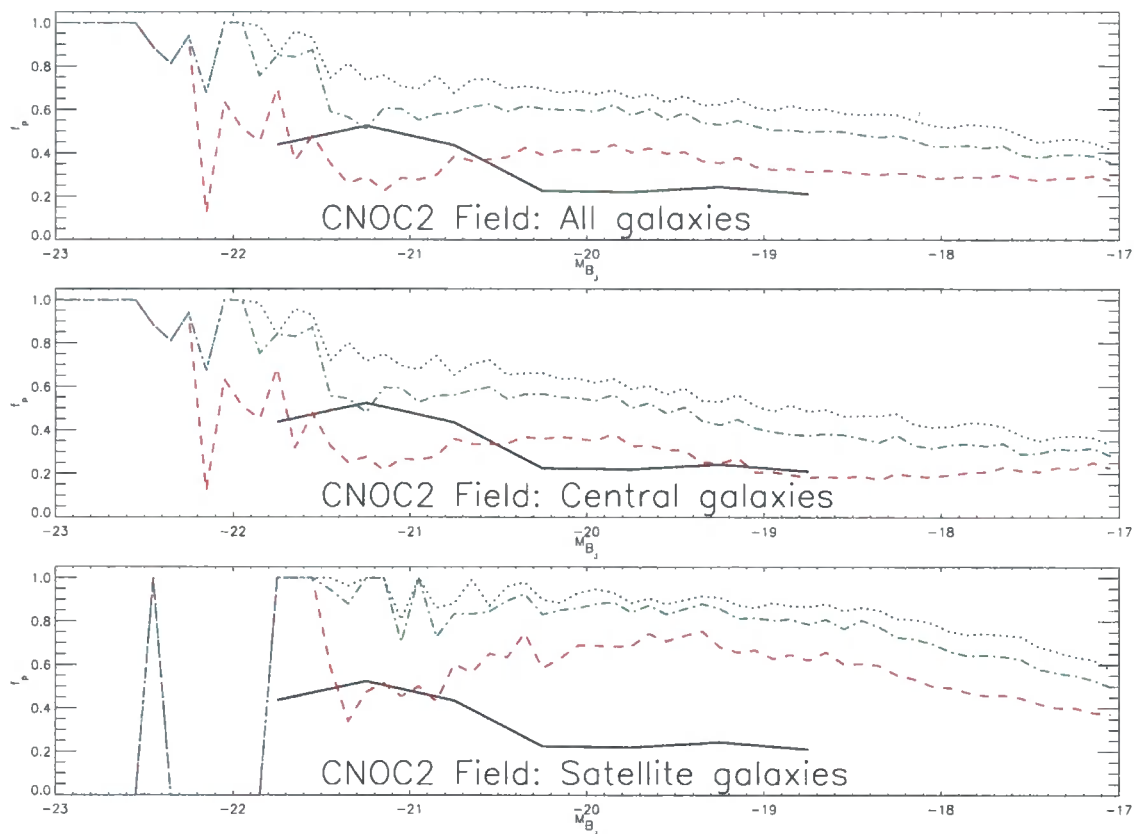


Figure 7.10: As Figure 7.9 but for the CNOC2 field population compared with the model galaxy population at $z = 0.4$.

coloured lines represent different values of the dust scaling parameter A_{V0} . The red line represents $A_{V0} = 0$ and the green and blue lines represent $A_{V0} = 1.0$ and $A_{V0} = 2.0$ respectively. Unsurprisingly when we apply a greater level of extinction the fraction of galaxies deemed “passive” increases. The model succeeds in reproducing the shallow luminosity dependence of f_p faintwards of $M_{b_j} \sim M_*$ (-20.28) where the combination of galaxies in different mass haloes conspires to make f_p lower at fainter luminosities. However, f_p is overestimated in the model with too many passive galaxies, especially where the additional dust extinction term is included. Also at brighter magnitudes the model galaxy population with $A_{V0} = 0$ shows a significant trough in f_p at $M_{b_j} \sim -21.75$ not seen in the observed population. We divide the model population into central galaxies (the most massive progenitor galaxy, middle panel) and satellite galaxies (lower panel). The agreement between model and observed populations is much better for central galaxies than for satellite galaxies. This suggests that the physics invoked in the model to suppress star formation in satellite galaxies is creating too many passive galaxies.

Figure 7.10 makes the same comparison between the CNOC2 field population (solid

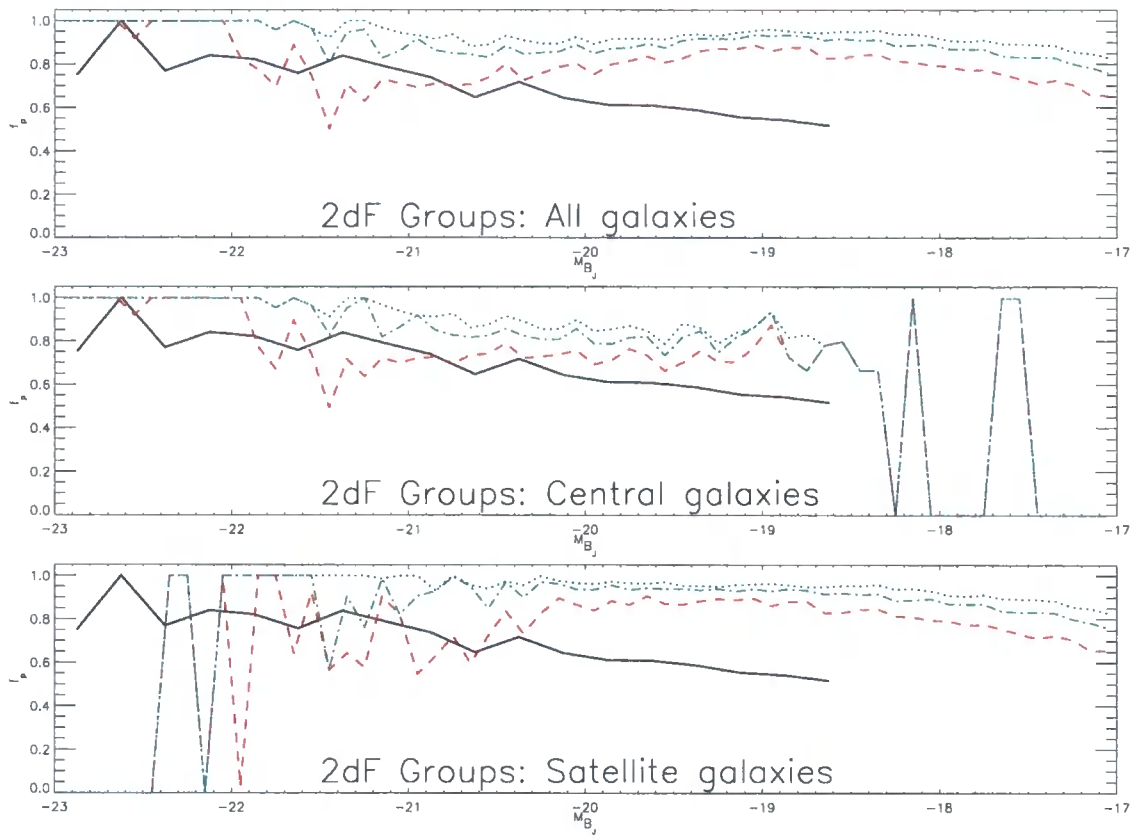


Figure 7.11: As Figure 7.9 but for the 2dFGRS group population compared with the model galaxy population in haloes of $M_{halo} \geq 10^{13} M_{\odot}$ at $z = 0$.

line) and the model population at $z = 0.4$ (coloured lines). The conclusions at $z = 0$ also apply at $z = 0.4$; the $A_{V0} = 0$ model again produces the best agreement with the CNOC2 field.

To isolate galaxy groups in the model we refer back to Figure 2.1 in which we determined that a typical 2dF group is contained within a halo of mass $\gtrsim 10^{12} M_{\odot}$. In fact $\sim 40\%$ of all 2dF galaxies are located in a group with halo mass $\geq 10^{13} M_{\odot}$ (see Chapter 2). This corresponds to $\sim 70\%$ of galaxies identified as group members. To make a comparison between group galaxies in the model and observed populations we select the model galaxy population in haloes $\geq 10^{13} M_{\odot}$ to be the model group population. Most less massive groups are likely to be excluded from our 2dF group catalogue by our requirement that each group contain at least 10 confirmed members. Figure 7.11 compares the behaviour of f_p in the 2dF group population (solid black line) with that in the $z = 0$ model group population (coloured lines). Disagreement between model and observed populations is more significant in the groups than it was in the field because the faint model population is dominated by satellite galaxies. There are clearly too many

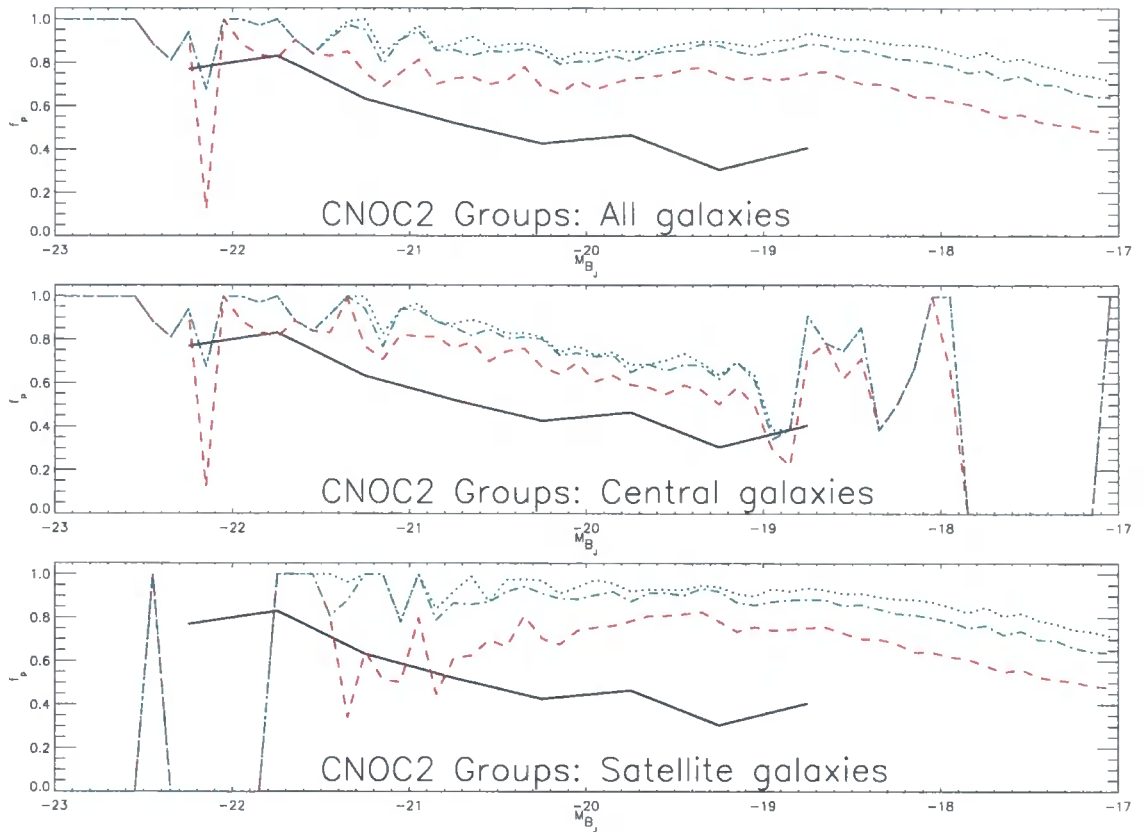


Figure 7.12: As Figure 7.9 but for the CNOC2 group population compared with the model galaxy population in haloes of $M_{halo} \geq 10^{13} M_{\odot}$ at $z = 0.4$.

passive satellite galaxies below $\sim M_*$ in galaxy group sized haloes in the model. This is likely to be related to the process of strangulation in which the hot gas haloes of satellite galaxies becomes associated with the central galaxy's halo. When this happens the hot gas cannot cool onto the satellite galaxies and the star forming cold gas is not replenished (Cole et al., 2000).

Figure 7.12 makes the comparison between the CNOC2 group population and the $z = 0.4$ model group population selected in the same way. Again we see that the model population contains too many passive galaxies in group sized haloes, especially at fainter magnitudes where satellite galaxies dominate the model population.

7.2.4 Summary

We have made simple comparisons between the star forming properties of galaxy populations in 2dF and CNOC2 samples and model populations at $z = 0$, $z = 0.4$ and $z = 1$ generated using the GALFORM semi-analytic galaxy formation code. These comparisons yield some successes and some failures for the model:

- The distribution of $EW[H\alpha]$ in the full 2dF population and in the star forming population are not well matched by the model. There are too many highly star forming galaxies in the model ($EW[H\alpha] \gtrsim 50\text{\AA}$). This situation is not much improved with an additional metallicity dependent dust extinction in HII regions as $H\alpha$ line strength is not a strong function of metallicity.
- The distribution of $EW[OII]$ in the 2dF and CNOC2 star forming populations can both be closely matched by the model by invoking a metallicity dependent dust extinction in HII regions with a dust scaling parameter $A_{V0} \sim 2.0$ (Equation 7.1).
- The fraction of passive galaxies f_p evolves strongly in the model population in haloes of mass $M_{halo} \gtrsim 10^{12} M_{\odot}$. f_p also increases with M_{halo} but shows no strong dependence upon luminosity for each bin of M_{halo} . The trends with redshift and environment are in qualitative agreement with that seen in the observed populations (Chapter 5).
- In the field populations at $z = 0$ and $z = 0.4$ the behaviour of f_p as a function of b_J -band luminosity is reasonably successful at matching that in the observed populations, when using a simple diffuse dust model to compute line strengths. However, f_p is much too high when any additional dust extinction term is invoked ($A_{V0} > 0$).
- In the group populations at $z = 0$ and $z = 0.4$ we find that f_p is much too high in the model population below $\sim M_*$ (-20.28). This occurs because in more massive haloes this faint model population is dominated by satellite galaxies which are much too frequently passive.

There are a number of improvements to this comparison that we might hope to make by utilising mock catalogues generated using the Millennium Run which is a massive N-body simulation, generated by the Virgo Consortium. These should be available in the near future. With detailed information on galaxy positions in redshift space, we will be able to apply exactly the same group-finding algorithms to the mock catalogues as were applied to the observational data. This will ensure that our model group galaxy population should be well matched to the observed populations. This will have the additional advantage that we can directly probe the environmental evolution of galaxies selected to be in 2dF and CNOC2 groups.

We have also been awarded GALEX time to observe the CNO2 group and field galaxies in the ultraviolet (UV). This will allow a more direct comparison of the star formation rate in the CNO2 population and the $z = 0.4$ model population.

7.3 Conclusions

Using the stellar population models of Bruzual & Charlot (2003), we have shown that the rate of evolution in f_p since $z \sim 0.45$ cannot be explained in a quiescent evolution scenario, i.e. by modelling galaxies with a simple e-folding decline in their SFR. Even choosing model parameters geared to maximise this evolution cannot reproduce the observed difference between 2dF and CNO2 galaxies in f_p , especially fainter than $M_* - 0.5$. This conclusion holds both in groups and the field.

We are therefore driven to conclude that transforming events take place in which star formation is abruptly truncated, and have constrained the probability of truncation per Gyr (P_{trunc}) in groups and in the field across the luminosity range $-21.5 \leq M_{b_j} \leq -18.5$. Although we have not constrained the timescale of these events (simply assuming them to be instantaneous), we show that their existence is strongly required by the data ($P_{\text{trunc}} \gg 0$). Surprisingly, we find no strong evidence that P_{trunc} in the group environment exceeds that in the field. The environmental dependence of f_p requires that the star formation history prior to $z \sim 0.45$ must depend upon environment in some way. One possibility is that as the clustering of galaxies progresses, an additional suppression mechanism acts upon star forming galaxies as they fall into groups (nurture). However, it is also possible to imagine a nature scenario in which more strongly clustered galaxies form first and all galaxies undergo transforming events, independently of their environment. A better understanding of the environmental influence on galaxy properties will be made possible by comparisons with semi-analytic models, galaxies in other environments (e.g. Nakata et al., 2004) and higher redshift galaxy systems.

Finally in the simulated Universe, as represented using a semi-analytic model of galaxy formation, we find that the model population shows the same qualitative trends with redshift and environment as has been observed. Therefore we suspect that at least some of the physical processes acting to truncate star formation in model galaxies (driving evolution in f_p only in haloes with mass $M_{\text{halo}} \gtrsim 10^{12} M_{\odot}$) are also taking place in the real Universe. However the model overpredicts the number of passive galaxies, especially in groups, suggesting that the truncation of star formation in infalling satellite galaxies

is too efficient. Finally the model fails to match the distribution of $EW[H\alpha]$ in the 2dF population even when invoking a metallicity dependent dust extinction in HII regions in addition to the diffuse dust extinction. More work is needed to match the emission line properties of galaxies in the model to make it easier to isolate the fundamental physics influencing galaxy evolution.

Chapter 8

Mapping the Infall Regions of Galaxy Clusters with a Wide Field Imaging Camera

8.1 Introduction

It is well known that the galaxy population in cluster cores is dominated by passive early type galaxies which form a tight relation of red galaxies in colour-magnitude space (e.g. Bower et al., 1992). In previous chapters we have shown that this population of passive, early type galaxies is already partly in place in isolated groups at $z \sim 0.45$ when compared with the field population. We now turn to the outskirts of clusters to examine how galaxy properties are influenced by their environment in regions characterised by filamentary structures and infalling groups (Peacock et al., 2001). By investigating how galaxy properties change from cluster cores, into the filaments and infalling groups and out into the field, it is possible to probe galaxy evolution over several decades of local density, in which the passive galaxy population is embedded. For a good review of this topic see Bower & Balogh (2004).

At low redshift it is now possible to probe the outer-cluster environment using spectroscopic data from SDSS and 2dFGRS (Lewis et al., 2002a; Gómez et al., 2003). These papers show that the transition for bright galaxies ($\lesssim M_* + 1$) from a field like star-forming population to a cluster like passive population occurs at local densities of $\Sigma \sim 1 Mpc^{-2}$ regardless of the cluster-centric distance. This corresponds to the average local density at the virial radius of a cluster or in a small galaxy group. At low redshift the relation between galaxy properties and local density seems to be strongly embedded in the galaxy population (e.g. Dressler, 1980; Balogh et al., 2004a,b). To get a glimpse of how, where

and when galaxies are transformed it is important to extend these studies to much higher redshift with a lower fraction of passive galaxies (Chapter 5) and where the morphological mix of galaxy types is in the process of evolving towards the current level (Dressler et al., 1997, Chapter 4).

The advent of the wide field camera means that it is now possible to provide deep imaging of wide fields ($\gtrsim 20' \times 20'$), large enough to encompass a massive cluster at $z \sim 0.45$ and the large scale structure in which it is embedded. Kodama et al. (2001) use Suprime-Cam on the Subaru Telescope to provide deep BVRI imaging of a $27' \times 27'$ field around the $z = 0.41$ cluster A851. At the cluster redshift, this field of view corresponds to $7.3h_{75}^{-1} Mpc \times 7.3h_{75}^{-1} Mpc$ which extends to $\sim 2\times$ the virial radius of the cluster ($R_V \sim 1.7h_{75}^{-1} Mpc$). Using BVRI photometry they obtain photometric redshifts down to $\sim M_* + 4$. They extract a wide photometric redshift slice and perform statistical subtraction of the remaining field contamination to isolate the large scale structure around A851. A filamentary structure is identified with clumpy group sized structures located $\sim 3h_{75}^{-1} Mpc$ from the cluster centre. In this way they can examine the dependence of galaxy colour on the local galaxy density. A transition from the red cluster population to the blue field population is identified in $\lesssim M_* + 1$ galaxies at $\Sigma \sim 20h_{75}^{-2} Mpc^{-2}$, which is a similar density to that identified in low redshift clusters once the different magnitude limits of galaxies used to define local density is taken into account. Most galaxies in regimes typical of this density are in the clumpy structures which are likely to represent infalling groups. This re-emphasises that bright passive galaxies seen in today's galaxy clusters are likely to have ceased forming stars when they were located in infalling groups at higher redshift.

Our aim is to use a similar technique to that of Kodama et al. (2001) to identify the large-scale structure in the outskirts of two clusters at similar redshifts to A851. The clusters selected are RXJ1347-1145 (or LCDCS 0829, hereafter known as RXJ1347) and V199 ([VMF98] 199 or RXJ2059.9-4245). RXJ1347 at $z \sim 0.451$ is the most X-ray luminous cluster of galaxies known with X-ray gas temperatures rising from $kT \approx 6keV$ in the central $17h_{75}^{-1} kpc$ to a mean value of $kT \approx 16keV$ between 0.07 and $0.35h_{75}^{-1} Mpc$ (Allen et al. (2002)). It therefore possibly represents one of the most massive clusters of galaxies in the Universe. Currently the only redshifts of galaxies obtained have been in the cluster core (Cohen & Kneib, 2002; Ravindranath & Ho, 2002). V199 at $z = 0.47$ is selected from the ROSAT cluster survey of Vikhlinin et al. (1998), revised by Mullis et al. (2003). It is selected because it is X-ray faint ($L_x \sim 3.23 \times 10^{43}$ ergs s^{-1}). Our choice of one highly luminous X-ray detected cluster and one X-ray faint cluster is designed to

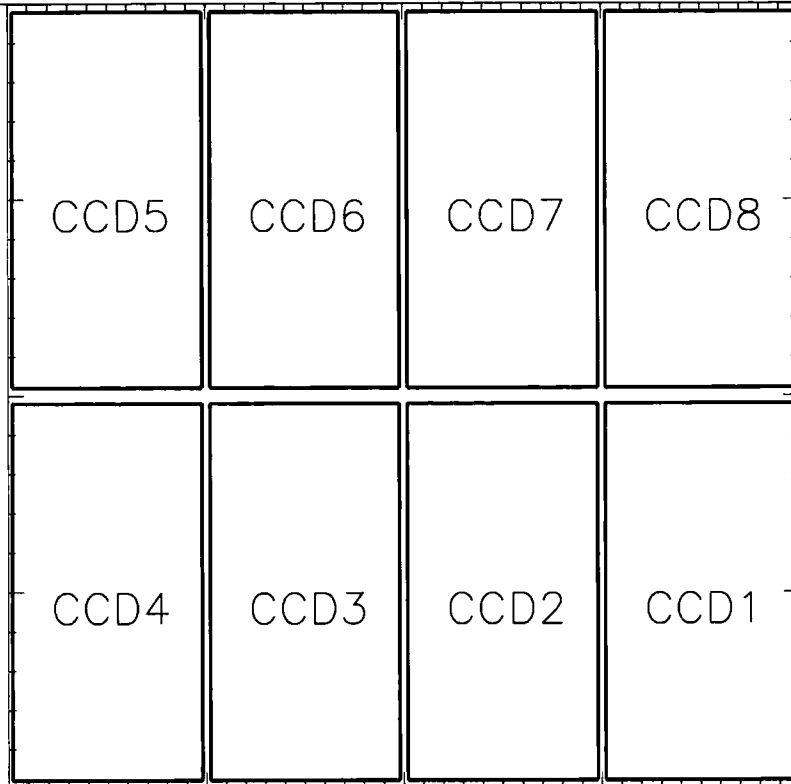


Figure 8.1: The array of CCDs at the focal plane of the WFI instrument on the AAT.

simultaneously investigate the influence of the global cluster potential on galaxies in the outer regions. This data, together with that of Kodama et al. (2001) should allow a direct comparison between the colour-density relations in galaxies under the influence of clusters with vastly different properties.

Our instrument of choice is the Wide Field Imager (WFI) on the Anglo-Australian Telescope (AAT). WFI has a field of view of $\sim 33' \times 33'$ which corresponds to $\sim 8.5h_{75}^{-1} Mpc \times 8.5h_{75}^{-1} Mpc$ at $z = 0.45$. Coverage of this large area is possible because WFI utilises an array of 2×4 CCDs in the focal plane (see Figure 8.1). By making 9 pointings arranged in a 3×3 grid with a small overlap between pointings, we cover a total region of nearly $25h_{75}^{-1} Mpc \times 25h_{75}^{-1} Mpc$. This compares with a virial radius for a typical cluster of $\sim 1.7h_{75}^{-1} Mpc$. This allows us to investigate the embedding large scale structure around each cluster out to $\gtrsim 7R_V$ in which the infalling groups and filamentary structure will be very important. This compares with the “backsplash radius” of $\lesssim 2R_V$ (Balogh et al., 2000; Treu et al., 2003; Mamon et al., 2004, for galaxies which have passed through the cluster core and come out the other side) and the “turnaround radius” of $\lesssim 5R_V$ (Rines et al., 2003, where field galaxies begin their infall). Therefore our field of view allows us to survey the galaxy population across all regimes from the core of the cluster to beyond

the cluster sphere of influence.

To isolate the large scale structure at the redshift of the clusters, we need to obtain photometric redshifts for galaxies in the field of view. We obtained WFI imaging of the clusters in Schott B, Schott V, SDSS R and SDSS I bands down to $R \sim 23$ ($\sim M_* + 2.5$). With photometry of $\sim 0.05\text{mag}$ accuracy we should be able to obtain photometric redshifts accurate to within ~ 0.1 at $z \sim 0.4$ using the photometric redshift code of Kodama et al. (1999). This is sufficient to extract a photometric slice which will reveal the large scale structure around the clusters. With photometry accurate to $\sim 0.1\text{mag}$ the accuracy of photometric redshifts will be reduced to $\gtrsim 0.15$. A statistical field subtraction will also be required to study the colour - local density relation as in Kodama et al. (2001).

8.2 Calibrating Wide Field Imaging Data

Wide field imaging with high precision CCD photometry is a recent development, made possible by the improvements in size, resolution and cost-effectiveness of CCD technology (e.g. Cuillandre et al., 1995; Metzger et al., 1995; Cuillandre et al., 1996; Luppino et al., 1998). However, like any new technology it brings with it a wealth of calibration issues which were of low significance with smaller detectors (e.g. Chromey & Hasselbacher, 1996; Koch et al., 2004). These problems were not well recognised at first and so the number of scientific papers resulting from WFI observations has so far been remarkably low. Indeed the AAO does not possess any detailed calibration (illumination correction, CCD to CCD ZP estimates etc), suggestive that other users have not required such accurate photometry, and there is little support available in terms of recognising these issues or solving them.

Recent work has led to a more detailed understanding of the steps required to accurately calibrate wide field imaging data. In particular there has been extensive planning for the forthcoming wide field OmegaCAM instrument on ESO's survey telescope (VST). The detailed calibration plan has been set up in light of experience on the WFI instrument on the ESO 2.2m telescope at La Silla and from this we can achieve a working knowledge of the ideal calibration procedure for this kind of data (Valentijn et al., 2004). There follows a summary of the most important steps outlined by Valentijn et al. (2004). We note that to minimise sources of error, each CCD should be independently calibrated and each raw frame should be fully calibrated before co-addition.

- Basic Calibration steps:
 - Correct for the overscan regions of each CCD.
 - Subtract Bias.
 - Subtract Dark Current.
 - Correct for non-linearity of CCD gain.
 - Make a map of hot and cold pixels.
 - It is advisable to be aware of any problems with hysteresis (“ghosts” of saturated stars from earlier images).

- Flat Fielding: Any combination of optical components plus detectors will have a non-uniform spatial transmission function across the focal plane. A flat-field frame should map these variations such that when an image is divided by the flat-field, the spatial variations in gain across the CCDs are effectively removed. This is complicated when there is an additional component of scattered light, not only in the science frames, but also in the flat-field frames themselves. Sources of scattered light are discussed below. Here, we outline the basic requirements for flat field calibration. The ideal flat-field combines a bright, uniform illumination with a constant colour well matched to the night sky. There are 3 types of flat-field each with their advantages and disadvantages:
 - Dome flat: This is taken by illuminating the dome using a lamp. Whilst dome flats provide a good measure of small-scale (pixel to pixel) variation, the detector is not uniformly illuminated and so the large scale gain variations cannot be measured in this way.
 - Twilight flat: The twilight sky is a bright and uniform source of illumination and so can measure large scale variations. However twilight is not of constant brightness or colour and the “twilight gradient” (along the ecliptic axis) precludes measuring the largest scale variation.
 - Night sky flats: By combining a large number of photometric science frames one can most closely mimic the illumination properties of the individual science frames. In this way the largest scale variations can be measured. However to create a night sky flat requires effective removal of individual sources from the science frames. Also the illumination can be non-uniform due to scattered light

from inside the instrument (see below). It is better to create night sky flats from raw frames which have been initially flat-fielded using a combination of the dome and twilight flats to remove most of the variation.

Valentijn et al. (2004) conclude that the master flat-field should be created in the following way (ignoring at the moment the effects of scattered light):

- Apply the large scale variations from the twilight flats to the dome flats to create a preliminary master flat-field.
 - Apply the preliminary master flat-field to the raw science frames and remove all sources from these frames. Then combine these to create a night sky flat. Apply this to the preliminary master flat-field to create the master flat-field.
- Corrections for scattered light:

The flat-field is designed to erase the variations in gain across the detector and the efficiency variations in the light path through the optics. However, it will not do so correctly if scattered light contributes significantly to the variations across the flat-field and science frames. A WFI instrument in particular can suffer from the effects of stray light. This takes 2 forms:

- Illumination Correction: The large scale variation of stray light in the focal plane can be characterised by many dithered pointings of a standard star field. Over a wide field it becomes necessary to use secondary standard stars to map the “illumination correction” across each CCD with a high enough resolution. Secondary standard stars can be bootstrapped from the primary standard stars in the same frame. This illumination correction can then be applied to the master flat-field to create a new master flat. Application of this new master flat to science frames will make them photometrically accurate.
- Fringing: Interference effects in the filters and CCDs can introduce wavelength-dependent gain variations on small angular scales. This is important in the night sky lines which are most apparent at red wavelengths. As it is a night sky problem, it is necessary to identify the fringing pattern and subtract from the science frames in the red bands (i.e. I band). Whilst fringe patterns may not affect the local photometric calibration of an object directly, if the fringe patterns are not removed from the master flat then problems are introduced during flat-fielding. It is feasible to decompose the night sky flat into high and

low frequency spatial frequency variations, of which the high frequency components are likely to be due to fringing. Thus a fringe frame can be constructed and subtracted from the science frames. Unfortunately the fringing pattern may vary with time, and so it may be necessary to create a fringe frame for each night of observations.

We also note that ideally, zeropoints should be recalculated on a nightly basis for each CCD (see Photometric Calibration below).

- **Astrometric Calibration:** Images can be astrometrically calibrated by fixing priors (pointing direction, position of rotator axis, plate scale, CCD offsets etc) and then solving to fit the catalogued positions of stars such as from the USNO2 (United States Navy Observatory) catalogue. Over a set of WFI CCDs the astrometric solution is likely to be radially distorted, leading to a non-uniformity of pixel illumination which will can be corrected as part of the illumination correction.
- **Photometric Calibration:**

The zeropoint (ZP) of a detector represents the scaling of calibrated flux per second of exposure to the magnitude of a galaxy. Effectively a gain, the ZP is additive in magnitude-space and varies from CCD to CCD (variations in sensitivity), across each CCD (the illumination correction) and with time (the airmass term). Ideally, after application of the illumination correction, a single ZP should apply to each CCD before correction for atmospheric extinction and spectral response. Then an airmass term, which might vary from night to night as atmospheric conditions change, must be applied to the ZP to account for this extinction. A colour term should also be applied to the ZP, accounting for the different spectral response of each CCD.

The ZP can be calibrated from standard star field observations on any given night. A series of observations of a single standard field at different airmass during the same night can help to constrain the airmass term which should be consistent from CCD to CCD. This might vary from night to night due to changes in atmospheric conditions, but this can be easily implemented as a nightly change in the normalisation of the airmass term. To obtain ZP variations from CCD to CCD and across each CCD (the illumination correction), it is necessary to have dithered images of the same standard field on the same night. To account for the different spectral response of

the detector from that used to measure the magnitudes of standard stars, a colour term (the dependence of ZP on star colour) can be obtained at this stage. By positioning the primary standard stars on every CCD and at different positions on each CCD it is possible to obtain a larger sample of secondary standard stars in this field. By then examining the change in magnitude of each secondary standard star as a function of position on each CCD an illumination correction surface can be constructed.

We emphasise that information on any detailed calibration procedure was lacking at the time of our observation and reduction (2001-2002) and in particular there is still no such information available from the AAO regarding the WFI instrument on the AAT.

8.3 Our Wide Field Imaging Data

WFI observations were obtained over 4 nights from June 22-25 2001 by Michael Balogh. Observations were taken at all 9 positions in both cluster fields. However the conditions were often cloudy and non-photometric and there were additional problems with the shutter, dewar and instrument software which led to time being lost. In apparently photometric conditions the seeing varied between 1" and 2". Only 5 of the RXJ1347 positions were observed in reasonable conditions and of these 2 were at airmass > 2 . Most V199 positions were observed in reasonable conditions (for the site). Most positions were observed with a single set of useful exposures of $2 - 3 \times 300$ s in V,R and I and $5 - 6 \times 600$ s in B. The depth of V, R and I band observations was therefore limited to a brighter magnitude than had been hoped (by up to 1 magnitude in the worst affected positions).

Each night we were able to obtain useful Landolt (1992, hereafter known as L92) standard star fields for night-to-night calibration. On nights 1,3 and 4 the same field was observed at different airmass from which to compute the airmass term. The number of L92 standard stars is low on each WFI chip, especially on CCDs 1, 4, 5 and 8 at the edges of the 2×4 detector array (no standard stars in some standard field observations and ≤ 4 in all observations). A straightforward dithering procedure was implemented on the standard fields, with a maximum of 3 slightly offset positions in the N-S direction per field per night. The aim of this dithering was simply to avoid bad pixels and to bootstrap the ZP from one CCD to another. In perfectly photometric conditions it would be possible to achieve reasonable calibration with this calibration data. However the

observations were frequently not photometric and scattered light appears to be more important than expected in this instrument. Therefore more calibration data would be desirable, in particular more dithered standard fields to estimate the illumination correction by comparing the same stars at different places on the focal plane, at the same airmass. By better constraining the spatial dependence of the ZP, it would be straightforward to bootstrap the airmass term from one night to another, to account for the variable atmospheric conditions (at least where conditions were partially photometric).

For basic calibration we have many bias and dark frames and both dome and twilight flats. Dome flats were taken on afternoons 2 and 3 and twilight flats on nights 1, 2 and 4.

8.3.1 Data Reduction

Data was reduced in the years 2001-2002 when the author was in the first year of the PhD studies presented here. Work was ultimately ended due to difficulties in calibrating non-photometric WFI data and to give precedence to the CNOC2 groups project. In this section, we present the preliminary level of calibration which was achieved. This resulted in a photometric accuracy deemed too low to compute photometric redshifts. In Section 8.3.2 we then present some preliminary results to this level of photometric accuracy. Then in Section 8.3.3 we apply our new working knowledge of WFI data calibration to suggest what would be the optimal calibration possible given the data available (as a “working manual” for future attempts at taking similar data).

For the initial calibration procedures, the *iraf* tool *ccdproc* in the *noao.imred* package was applied to each CCD individually. This involved correction for overscan, bias and dark frame subtraction and a correction for non-linearity of CCD gain. The WFI webpage http://www.aao.gov.au/wfi/wfi_perform.html suggests that hysteresis only exist at the $\leq 1\%$ level and so no steps were taken to examine its importance in our data.

At this stage the raw frames were combined. The combined frames were flat-fielded using a median-combined dome flat. Residual patterns were visible in the background both on small and large scales across at least some of the CCDs. An example of the residual small-scale variations can be seen in Figure 8.2. These are worst in the B and I bands and can be present at up to the $\sim 20\%$ level in intensity for science frames in the B-band (as determined from the variation in background intensity across the frame shown in Figure 8.2). However the twilight flats are even worse at removing this small-scale signal. Therefore, we chose to concentrate on the R and V band calibration.

Large scale variations of ZP across the CCDs are also present at the $\sim 5\%$ level

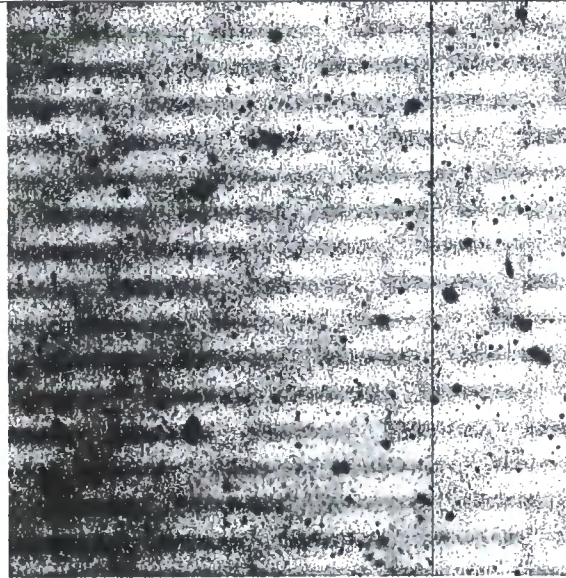


Figure 8.2: Example of the small-scale residual patterns visible in some CCDs even after dome-flattening (This is CCD4 in a B-band frame).

even in the somewhat better R and V bands Experimentation showed that this large scale variation was reduced, by combining the dome flat with the low frequency spatial components from the twilight flats to create a master flat. It could also be further reduced, but not eliminated, by applying a night sky flat (created in this case by combining the already median-combined science frames).

Zeropoints were calibrated using primary standard stars in the L92 fields. Aperture magnitudes are measured using a $7''$ diameter aperture and a background estimate from an annulus of width $3.5''$. Tests have shown aperture magnitudes to be insensitive to further aperture growth. On some CCDs there were as few as 1 unsaturated standard stars (e.g. CCD1). This is insufficient to calibrate the CCD colour term or illumination correction. To resolve this we bootstrapped between standard fields, observed in dithered positions, to see the variation of magnitude in secondary stars with position. Figure 8.3 gives a flavour of the large scale variation, CCD-to-CCD offsets and the remaining scatter of aperture magnitudes measured in the R-band for secondary stars in the dithered L92 standard field SA113. Comparison of measured aperture magnitudes for a given star in two different observations yields a difference in magnitude ($d(mag)$) which often correlates with position on the CCD. In Figure 8.3 we plot $d(mag)$ as a function of the y-axis CCD position of the star at the second pointing. These images were flattened using dome-flats and we only include data from standard fields imaged during conditions which are logged

as “photometric”. In the top two panels we compare the magnitudes of stars which lie on the same CCD in both observations but the second pointing is offset from the first. This leads to a measurement scatter of $\sim 0.05mags$. In the remaining 6 panels we compare the magnitude of stars which appear on one CCD in the first pointing and on a different CCD at the second pointing. The change in magnitude shows that there is a residual difference in ZP between CCDs, and some dependence on the CCD position of the star. From the scatter in the top two panels, we can conclude that it is possible to achieve R-band photometrical accuracy of better than $< 0.05mags$, good enough for our purposes. However, the other panels show us that there is still a residual variation in ZP which relates to differences between CCDs, spatial variations (probably related to scattered light) and possibly differences in the atmospheric conditions and the airmass between the observations (as we could not constrain the airmass term). Similar calibration is achieved in the V band, but better calibration is certainly required in B and I bands where spatial variations and fringing problems dominate the errors.

The webpage for WFI on the AAT¹ suggests that scattered light is not a serious problem. The ZP gradients across most CCDs suggest otherwise. Private correspondence from AAT staff suggests that large scale variations may be due to astrometric distortion over the large field and a doughnut shaped scattered light feature largest in B and I bands. The quoted $< 1\%$ level in V-band is much lower than the $\sim 5\%$ large scale ZP variations we detect in that band. Also the variations of ZP with position are not consistent with a simple astrometric distortion. It also fails to explain the small scale variations, particularly in the B-band where fringing is not expected to be an issue. There may be something wrong with the detector read-out in this case.

The mosaic of science observations provide one more opportunity to cross-calibrate each CCD. The dithered observations overlap by $\sim 80''$ on which a significant number of stars have been detected on both frames. A subarray of four RXJ1347 R-band pointings are all logged as “photometric”. We examine the magnitude of the same stars in the overlap regions, assuming a constant ZP offset for each pointing (difference in airmass and conditions) and a constant ZP offset for each CCD. By bootstrapping from one CCD to another by various routes, we discovered that no consistent solution exists (with variations of $\sim 0.1mags$ depending upon the route). As this is true even in R-band, where we considered our calibration to be good to $\sim 0.05mags$, we believe that other sources of error must be present. With overlaps which are small compared to the CCDs, this is

¹http://www.aao.gov.au/wfi/wfi_perform.html

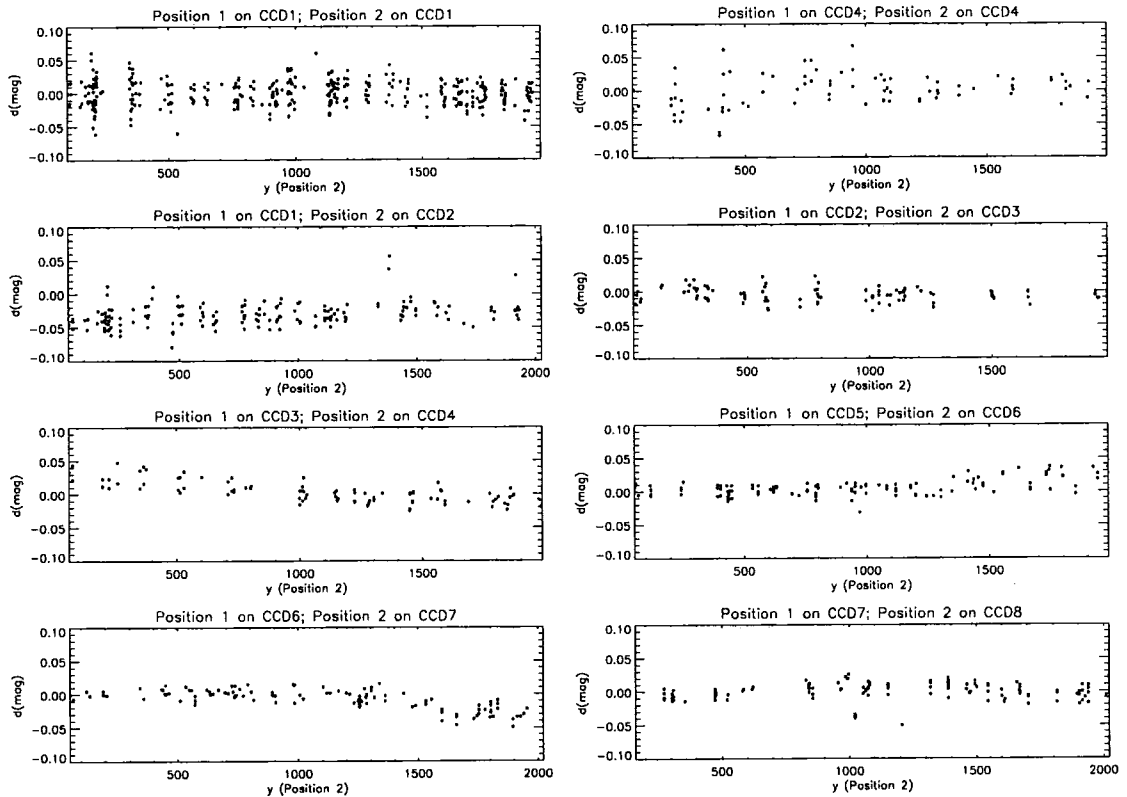


Figure 8.3: Comparison of measured aperture magnitudes for each star located in two different observations, with the second observation offset from the first. Each panel represents the difference in magnitude ($d(mag)$) as a function of the y-axis CCD position of the star in the second observation. In the top 2 panels we compare the magnitudes of stars which lie on the same CCD in both observations. The lower 6 panels compare the magnitude of stars which appear on one CCD in the first pointing and on a different CCD at the second pointing. These images were flattened using dome-flats and we only include data from standard fields imaged during conditions which are logged as “photometric”. Preliminary calibration has already been performed using the L92 standard stars to obtain ZP for each CCD separately (and a global R-band colour term). However, significant large scale variations, CCD to CCD offsets and scatter remain.

likely to be related to the large scale variations across each CCD. Possible origins include scattered light and spatial variations in cloud cover (possible over the 0.5° WFI field of view in five minute exposures).

Finally we note that all of our frames were astrometrically calibrated using a purpose-written automated perlscript. The source detection software, *SExtractor* (Bertin, 1999) was used to catalogue the significant detections in each frame. We also extract objects in the region of interest from the accurate World Coordinate System (WCS) positions available in the United States Naval Observatory 2 (USNO2) catalogue. The brightest objects are selected from both the *SExtractor* catalogue and the USNO2 catalogue and an unsaturated but bright and central *SExtractor* source is chosen. This is fixed to each USNO star in turn. In each configuration, the positions of the bright stars in the two catalogues are correlated based upon initial estimates of pixel scale and roll angle and the best-match configuration is selected. In this configuration, the pixel scale is iteratively improved until a good correlation between the two sets of bright objects is obtained. In the minority of cases, it is necessary to tweak a number of parameters manually to obtain a correct solution. Once a good initial solution has been found, the full USNO catalogue is converted into (x,y) pixel coordinates and matched to the full *SExtractor* catalogue using the matching task *tmatch* in the *iraf* package *ttools*. These matches are fed into the *starlink* package (Wallace, 1998) which determines 4, 6 and 9 coefficient fits to the astrometry depending upon the number of matches. The best available fit is selected in each case.

The experience I have gained since performing this astrometry has led me to recognise that astrometry can be performed more easily and more accurately than by writing a complex script as outlined above. It would also be very useful to imprint the astrometric solution into each image file header.

8.3.2 Preliminary Results

We believe the calibration of our WFI data must be improved before the photometric accuracy is sufficient for our purpose of obtaining photometric redshifts. However at the current level of accuracy it is possible to examine the distribution of galaxies in colour-magnitude space using the better calibrated R and V band data. We use the V and R band images which have been flat-fielded using the dome-flats only and ZP calibrated using primary L92 standard stars for each CCD (accurate to $\sim 0.05mag$ in photometric observations, see Figure 8.3).

At $z = 0.451$ V-R colour corresponds roughly to rest-frame B-V colour and R-band magnitude corresponds roughly to the rest-frame V-band. Passive red galaxies are known to follow a tight relation in colour-magnitude space (e.g. Bower et al., 1992) and so we can attempt to isolate this red-sequence in V-R colour by examining the colour magnitude distribution of galaxies (e.g. Figure 8.4). We make no pre-selection of extended sources as this might lead to the rejection of red sequence elliptical galaxies as well as stars. Simulations indicate that at the redshift of the cluster, $z = 0.451$, the red sequence should be found at $V-R \sim 1.24$ for M_* galaxies ($R \sim 20.6$). Even though the object sample in Figure 8.4 includes the cluster centre, the red-sequence is not well defined and certainly not tight at $V-R \sim 1.24$. However there does appear to be a concentration of bright ($R \leq 21$) galaxies at $V-R \sim 1.2$ with a scatter of $\sim 0.05\text{mag}$.

In Figure 8.5 we isolate the objects in the central pointing image of RXJ1347 with colours in the range $V-R = 1.24 \pm 0.1$ and brighter than $R = 22.5 \sim M_* + 2$ (filled circles). If this truly represents the red-sequence of galaxies in RXJ1347 then these objects should trace the large scale structure in the region of the cluster. We overplot several contour levels which show the relative local density of these objects. The high concentration of objects on the red sequence at the centre of the image correctly identifies the cluster core. We also see a filamentary structure in the NE to SW direction with possible subclumps of galaxies located at a greater distance ($\sim 3h_{75}^{-1} Mpc$ from the cluster centre) along this axis. The idea that infalling groups lie primarily along the filamentary axis is in agreement with Kodama et al. (2001), suggesting that these clumps might in fact be real. However we await better photometric accuracy and photometric redshifts to be certain of this and to extend the scientific analysis.

8.3.3 Optimal Calibration Method

With our new working knowledge of WFI calibration we can outline the optimal calibration method for our data taking into account its limitations. We note that each science and L92 frame must first be astrometrically calibrated (complete for our data). The procedure outlined below should be applied to each CCD separately:

- We would not change our basic calibration steps (overscan, bias, dark, linearity correction) except to obtain a weighting mask from the master flat to deal with hot and cold pixels.

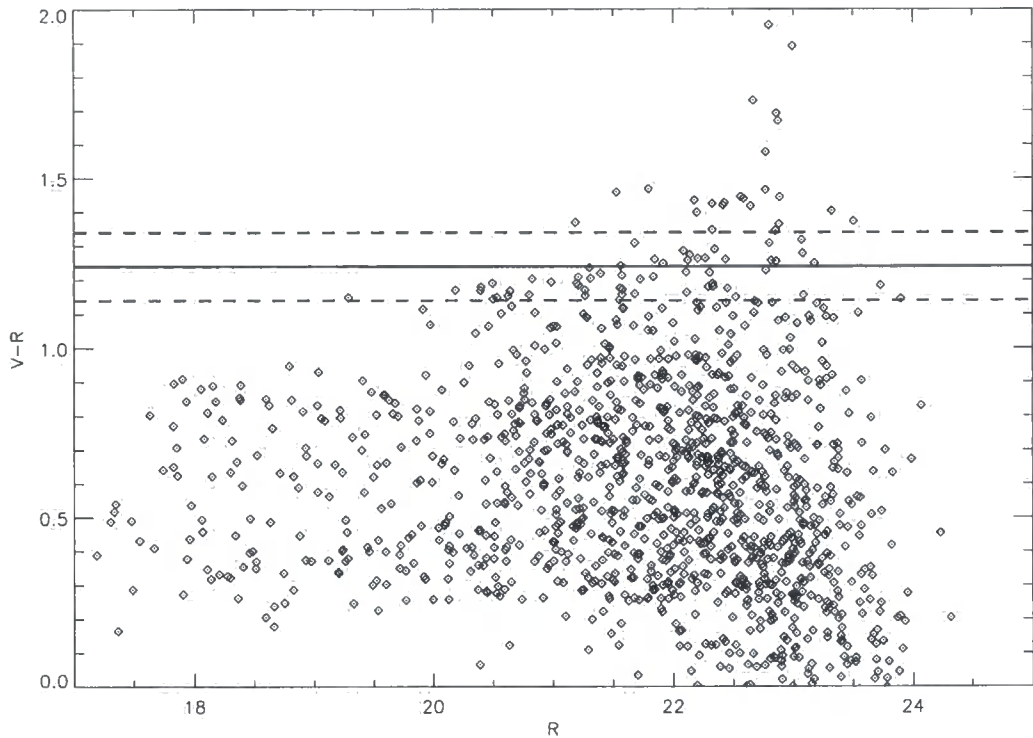


Figure 8.4: An example colour-magnitude plot in the region of RXJ1347. The points represent objects located on CCD2 at position E in the field of RXJ1347 which contains the cluster centre. V-R colour (y-axis) is measured using aperture magnitudes and R magnitude (x-axis) is measured using the estimated total magnitude (SExtractor's MAGBEST parameter). Simulations indicate that at the redshift of the cluster, $z = 0.451$, the red sequence should be found at $V-R \sim 1.24$ for M_* galaxies ($R \sim 20.6$). The solid line indicates this isochrone and dashed lines indicate the boundary for galaxies within 0.1 magnitude of this colour. A concentration of objects can be seen at $V-R \sim 1.2$ which might represent this red sequence.

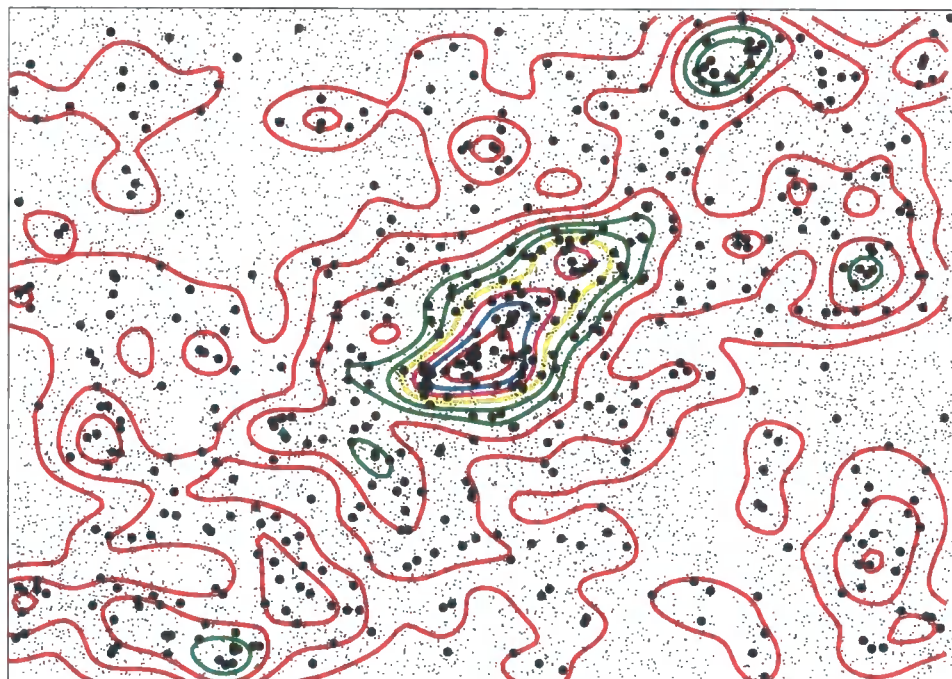


Figure 8.5: A contour plot of objects in the central mosaic position of RXJ1347 (position E). Objects located within the colour range $V-R = 1.24 \pm 0.1$ and brighter than $R = 22.5 \sim M_* + 2$ are represented by filled circles. The contour levels show the relative local density levels of these objects. We see a filamentary structure in the NE to SW direction with possible subclumps of galaxies located at a greater distance ($\sim 3h_{75}^{-1} Mpc$ from the cluster centre) along this axis.

- The preliminary master flat would then be created from a combination of twilight and dome flats (as described in Section 8.2). This is applied to all photometric *raw* science frames.
- Sources must then be removed from each raw science frame and these frames are then median combined to create night sky flats for the whole run and for each night. A fringe map should be generated by examining the small scale variation of the night sky flat of each night as fringing might vary with time.
- A master flat would then be generated by combining the preliminary master flat with the night sky flat from the whole run and subtracting the fringe frame. At this point it is also possible to create a weighting mask to identify hot and cold pixels.
- The master flat must now be applied to the photometric standard star (L92) frames. The source catalogue can then be generated and saturated stars eliminated. At this stage we can generate a catalogue of L92 primary standard stars. This includes the night of observation, CCD number and (x,y) position of the star, star colour and extinction of the observation.
- By comparing the change in magnitude of L92 primary standards in the same position at different airmass and on the same night, an airmass term can be computed. The change from night to night can be estimated by comparing observations of the same field and at the same position on different nights. We can do this using photometric observations from nights 1, 3 and 4. After removing the airmass term, the ZP and colour term of each CCD can be determined by plotting the measured magnitude minus the Landolt magnitude for each primary standard star, as a function of colour, for each CCD. We note that for some CCDs there are insufficient primary standards to fix the colour term and so we will have to assume that these are the same as for other CCDs with similar characteristics.
- Next a much larger catalogue of standard stars (secondary standards) can be generated in the L92 standard fields. Magnitudes for these stars can be estimated using the ZP computed in the previous stage (as a function of night, airmass, CCD and colour). We possess dithered observations of L92 fields on nights 3 and 4. In these frames we must then determine the magnitude of the same stars in dithered frames as a function of their position. As all dithered observations were offset in declination (the CCD x-axis) we can thus determine the x-dependence of the illumination

correction. The y -dependence can be estimated on some CCDs by plotting the ZP residual of primary standards as a function of y position.

- The form of the illumination correction should be contrasted with the expected astrometric distortion across the focal plane. Where the illumination correction closely mimics the predicted distortion then this can be used to model the full illumination correction in both x and y directions. However this appears not to be the case in our preliminary analysis. The illumination correction (normalised to 1) must be applied to the master flat to form a new master flat. Application of this new master flat to the photometric science frames should make them photometrically flat. The scaled fringe-frame must also be subtracted from the science frames.
- At this stage it might be possible to improve the illumination correction (especially the y -dependence) from science frames by performing photometry in the overlap regions using the existing ZP calibrations, assuming that the science frames are photometric (which does not seem to be the case). By contrasting the measured magnitudes of each star in the two positions (and on different CCDs) we can hope to improve the offsets of ZP from CCD to CCD and the illumination correction (in particular the y -dependence). The only guaranteed method of characterising the illumination correction, however, is via a detailed AAO study using this instrument with sufficient dithering of standard fields in photometric conditions. This is not currently available with our choice of filters.

Once the master flats, fringe frames and ZP calibration are well understood, a final source catalogue can be created from the median-combined science frames. Given the conditions during the observing run we would expect V199 data and some RXJ1347 data to be reasonably well calibrated, assuming that both small and large scale variation across WFI CCDs has been effectively removed. However it is impossible to calibrate non-photometric data such as that in at least 4 of the 9 RXJ1347 mosaic positions. In truth there has been insufficient support in outlining the details of WFI calibration. This makes the calibration of WFI data very difficult indeed, and we look forwards to a new generation of better understood WFI instruments.

8.4 How we will proceed

We require photometric data in the region of RXJ1347 and V199 in order to obtain photometric redshifts. If this cannot be achieved by applying a maximal calibration plan, such as described in Section 8.3.3, then we will need to reobserve these targets, perhaps with the ESO WFI camera at La Silla where conditions are more frequently photometric than at the AAO.

We were also able to use guaranteed time on both Magellan 6.5m telescopes with LDSS2 to obtain multi-object spectroscopy of galaxies in the region of RXJ1347. This took place during two observing runs in April 2002 and March 2003. As the photometric data were not well calibrated we made our target selection based upon the large scale structure evident in Figure 8.5. We targeted primarily the filamentary structure and subclumps visible in that figure but to avoid biasing our spectroscopy towards passive galaxies we made no colour selection. Selection was made using the same automated procedure used to allocate galaxies to masks in the CNOC2 group fields. Priority of allocation was based upon the galaxy magnitude and mask position only, in a way which changed from run 1 to run 2.

In run 1 (April 2002) we observed a total of 400 targets on 15 masks positioned in 11 different locations (all within the central WFI position). Priority was given to objects brighter than $R = 22$ with fainter objects allocated where mask space was available. In run 2 (March 2003) we decided that objects brighter than $R \sim 20$ are likely to be mostly in the foreground. Therefore priority was given to objects in the range $20 \leq R \leq 22$ with fainter and brighter objects allocated to the remaining space. On this occasion a total of 219 objects on 8 masks in 6 different positions were targeted. Exposures were also increased by a factor ~ 2 to ensure that redshifts can be obtained down to $R \sim 22$, without strong bias towards emission redshifts, as in the CNOC2 groups study (see Chapter 3). Tables 8.1 and 8.2 show the mask number, position and position angle as well as the number of targets and exposure time for each mask observed in runs 1 and 2 respectively.

These data will be utilised in conjunction with photometric data to examine the properties of galaxies in RXJ1347. This will include the comparison of spectroscopic with photometric redshifts, confirmation of structure with spectroscopic redshifts and the investigation of EW[OII] as a function of environment in the outer regions of RXJ1347 to complement the colour-local density relation and the EW[OII] properties of CNOC2 group galaxies also at $z \sim 0.45$.

Table 8.1: LDSS2 Observations made in the region of the massive cluster of galaxies RXJ1347 in April 2002.

Mask	RA	Dec	PA ^o	Number of Targets	Exposure (s)
1A	13 48 17.02	-11 38 03.8	270	29	4800
2A	13 48 04.31	-11 39 26.5	270	23	4800
3A	13 47 49.14	-11 41 57.1	270	30	3600
4A	13 47 14.72	-11 48 09.0	270	26	3600
5A	13 46 51.81	-11 50 03.4	270	28	3600
6A	13 46 45.32	-11 53 15.0	270	29	3600
7A	13 47 15.81	-11 58 40.7	270	26	3600
7B	13 47 15.81	-11 58 40.7	270	26	3600
8A	13 48 13.91	-11 57 23.9	270	28	3600
8B	13 48 13.91	-11 57 23.9	270	27	3600
9A	13 47 49.06	-11 33 15.7	270	25	7200
9B	13 47 49.06	-11 33 15.7	270	27	3600
10A	13 46 52.99	-11 32 50.1	270	24	5400
10B	13 46 52.99	-11 32 50.1	270	25	1200
12A	13 47 33.37	-11 45 10.9	270	27	3600

Table 8.2: LDSS2 Observations made in the region of the massive cluster of galaxies RXJ1347 in March 2003.

Mask	RA	Dec	PA ^o	Number of Targets	Exposure (s)
1A	13 47 17.82	-11 43 10.9	270	26	6300
1B	13 47 17.82	-11 43 10.9	270	28	7004
2A	13 47 19.17	-11 48 09.0	270	31	6300
3A	13 46 43.76	-11 51 12.9	270	25	6300
4A	13 47 47.77	-11 43 15.8	270	25	7200
5A	13 48 15.40	-11 40 11.0	270	30	4200
6A	13 47 47.76	-11 48 07.1	270	27	8400
6B	13 47 47.76	-11 48 07.1	270	27	7200

Chapter 9

Conclusions and Future Prospects

We began this thesis by asking the question: “When, where and how are blue star-forming galaxies transformed into red passive galaxies?”. Galaxy groups were identified as the typical environment at which the galaxy population begins to differ significantly from the field (Lewis et al., 2002a; Gómez et al., 2003; Balogh et al., 2004a). Therefore we have focused on the group environment to investigate the influence of clustering on galaxy evolution. By supplementing the kinematically selected CNOC2 group catalogue of Carlberg et al. (2001b) with our own spectroscopy using the Magellan BAADE 6.5m telescope at Las Compañas Observatory (LCO) in Chile, we possess a unique catalogue of intermediate redshift ($0.3 \leq z \leq 0.55$) groups, highly complete down to $\sim M_* + 1.75$. Combined with the CNOC2 5 colour photometry and deep HST ACS imaging, we have been able to investigate the properties of galaxy morphology, star formation and luminosity in these groups and contrast with a population of field galaxies, serendipitously observed in the Magellan and HST fields of view.

We have complemented our CNOC2 group sample with a local group sample selected from 2dFGRS (Eke et al., 2004) to track the evolution of galaxy properties in the group environment. Combining these data with simple models has allowed us to constrain the rate of transformations in the group environment and this is contrasted with the evolution predicted in semi-analytic models (Cole et al., 2000).

Finally we have examined the use of Wide Field Imaging (WFI) to isolate the large scale structure around galaxy clusters. Using photometric redshifts to detect large numbers of galaxies in the infalling groups and filamentary structure surrounding large clusters has significant potential, eliminating the enormous overheads associated with large spectroscopic surveys, especially at high redshift. However we have demonstrated that the accurate calibration of these data, required for photometric redshift software, is extremely difficult, involving calibration issues not previously encountered as a significant issue (e.g. scattered light). These instruments will have enormous benefit to studies of galaxy evo-

lution, but only once meticulous software pipelines are available to match the ingenuity of the hardware.

In Section 9.1 we summarize the conclusions from each chapter, emphasizing the most important results. We then draw on our major findings and on the scientific literature to discuss our current picture of galaxy evolution and the role of clustering in Section 9.2. Finally we explore the future of this topic in Section 9.3, highlighting the areas we believe would benefit most from further investigation and how we may tackle the fundamental questions of galaxy evolution using data from current and future projects.

9.1 Summary

9.1.1 Stellar Populations in Group and Field Galaxies

In Chapter 2 we saw that whilst the fraction of star-forming galaxies at $z \sim 0$ depends critically upon local galaxy density (environment), the distribution of EW[H α] for star-forming galaxies is approximately independent of environment (Balogh et al., 2004a). Therefore the process which truncates the star formation must act on short timescales ($\lesssim 1$ Gyr) such that the distribution of EW[H α] amongst star-forming galaxies is not significantly altered in dense environments. This motivates us to divide the galaxy population in our CNOC2 sample into passive (EW[OII] $< 5\text{\AA}$) and star-forming (EW[OII] $\geq 5\text{\AA}$) galaxies. In Chapters 3 and 5 this data has revealed the following:

- The fraction of passive galaxies, f_p , is significantly greater overall in CNOC2 groups than in the field. Despite no clear correlation with velocity dispersion ($\sigma(v)_{intr}$) or group concentration, there is a suggestion that f_p is most strongly enhanced in the higher velocity dispersion, concentrated systems ($\sigma(v)_{intr} \gtrsim 400 \text{ km s}^{-1}$).
- f_p is strongly correlated with luminosity both locally (in the 2dF sample) and at $z \sim 0.45$ such that fainter galaxies are more likely to be forming stars in groups or the field any time since $z \sim 0.45$. This is in accordance with the idea of downsizing (Cowie et al., 1999; Kauffmann et al., 2003), such that the more massive galaxies cease to form stars at earlier times.
- There is strong evolution of f_p since $z \sim 0.45$, both in groups and in the global population (field).

- We find a weak trend of f_p with group-centric radius in 2dF groups which is not statistically significant in CNOC2 groups. However this trend becomes stronger when we measure f_p as a function of local density based on the distance to the nearest group member.
- The luminosity function of CNOC2 group galaxies shows a significant excess of bright galaxies ($M_{b_J} \lesssim -21.0$) analogous to the low redshift results of Blanton et al. (2003). However, only in more massive groups $\sigma(v)_{intr} \gtrsim 400 \text{ km s}^{-1}$ are these galaxies prevalently more passive than in the field. In the most massive groups $\sigma(v)_{intr} \gtrsim 600 \text{ km s}^{-1}$ we also see an excess of faint passive galaxies ($M_{b_J} \gtrsim -20.0$).

9.1.2 Morphological Properties of Group and Field Galaxies

In Chapter 4 we introduced our targeted HST ACS imaging of CNOC2 groups, with group and field galaxies visually classified by morphological type. These data reveal an interesting picture in which the prevalence in groups of each morphological type depends critically on the group velocity dispersion and galaxy luminosity:

- The composition of CNOC2 groups is approximately 40% elliptical, 40% spiral and 20% S0, ignoring a small contribution from irregular and merger types which become more important at fainter magnitudes. This compares with $\sim 30\%$ E+S0 and $\sim 70\%$ spiral in the field. Perhaps surprisingly, the group composition matches that of the MORPHS sample of irregular clusters at $z \sim 0.5$ (Dressler et al., 1997) and that of X-ray faint clusters at $z \sim 0.25$ (Balogh et al., 2002), even though the groups lie in a much lower density regime ($\Sigma \sim 1.6 \text{ Mpc}^{-2}$) suggesting that the morphologies of these cluster galaxies were embedded in the infalling groups. Low redshift groups (Zabludoff & Mulchaey, 1998; Tran et al., 2001; Helsdon & Ponman, 2003) yield similar or smaller fractions of bulge-dominated galaxies, despite the apparent local excess of S0s over ellipticals in groups (Postman & Geller, 1984).
- There is a significant excess of bright ($M_{b_J} \leq -20.5$) S0 galaxies over the field, most strikingly in groups 37 and 39 (both with velocity dispersions $400 - 500 \text{ km s}^{-1}$). In these groups the bright S0 galaxies are spatially in close proximity, suggesting a common history.
- Below M_* ($M_{b_J} \sim -20.3$ at $z \sim 0$ (Norberg et al., 2002)) the elliptical population becomes especially prevalent in groups, driving the excess of faint passive galax-

ies especially in the more massive groups. This is analogous to studies linking the abundance of faint, passive, early-type galaxies to environment at low redshift (Christlein, 2000; Zabludoff & Mulchaey, 2000; Christlein & Zabludoff, 2003; De Propris et al., 2003a; Croton et al., 2004; Coziol et al., 2004) and a nurturing mechanism such as harassment (Moore et al., 1996) or strong tidal encounters might be required to build this population.

- Less massive groups ($\sigma(v)_{intr} \lesssim 600 \text{ km s}^{-1}$) also contain a significant excess of bright passive spiral galaxies ($M_{b_j} \leq -20.0$). These are often located towards the centre of these groups and in close proximity to one another and to S0 galaxies, suggesting a formation mechanism common in this regime and at the outskirts of clusters (Goto et al., 2003). Interactions with the intragroup medium or with other galaxies are likely to result in the exhaustion of cold gas in the disk and the truncation of star formation, without necessarily causing any dramatic transformation of a galaxy's morphology. We favour interactions with other galaxies, since these passive group spirals are preferentially bright, contrary to expectations of interactions with the IGM.
- The CNOC2 group galaxies appear less frequently disturbed than field galaxies and we find no evidence that galaxy mergers are any more common in groups than in the field. However there is an indication that the frequency of galaxy-galaxy interactions is higher in groups.

9.1.3 Modelling the Evolution of Group and Field Galaxies

Interpretation of the evolution of galaxy properties is no straightforward task: Evolution of an individual galaxy cannot be directly observed as significant changes occur over periods of many millions if not billions of years. In Chapter 7 we combined simple empirical modelling with a more physically oriented semi-analytic technique to deduce how group and field galaxy evolution since $z \sim 0.4$ relies upon galaxy transformations. This comparison uncovers a set of requirements to which any model of galaxy formation and evolution must conform:

- The evolution required to explain the data is inconsistent with a quiescent model of galaxy evolution; instead, discrete events in which galaxies cease forming stars (truncation events) are required. In a simple “closed box” model in which galaxies

evolve independently, we have constrained the probability of truncation per Gyr to be $P_{\text{trunc}} \sim 0.3 \text{ Gyr}^{-1}$, required to match the evolution of the fraction of passive galaxies (f_p) since $z \sim 0.4$. Surprisingly, there is no strong evidence that P_{trunc} in the group environment exceeds that in the field, nor that there is any dependence on galaxy luminosity. The dependence of f_p on environment and luminosity appears to be embedded in the galaxy population prior to $z \sim 0.4$.

- We find that the observed evolution and environmental dependence of f_p is also qualitatively displayed by a model population of galaxies, generated in a simulated Universe represented using a semi-analytic model of galaxy formation (GALFORM Cole et al., 2000; Baugh et al., 2004). However the model produces too many passive galaxies in group-sized halos, suggesting an overefficient truncation of star formation in satellite galaxies. The model also fails to match the distribution of $\text{EW}[\text{H}\alpha]$ in the 2dF star-forming population despite some success in matching the distribution of $\text{EW}[\text{OII}]$.

9.2 Discussion

In this section, we tie together our results and ask how our picture of galaxy evolution is molded by these findings.

Figure 9.1 shows a modified “Madau plot” in which we show the fraction of passive galaxies f_p as a function of redshift in different environmental regimes. The cluster core data are taken from Nakata et al. (2004), originating in the 2dFGRS, CNOC1 and high redshift cluster samples of van Dokkum et al. (2000) and Postman et al. (2001). These data are limited to within $0.75h_{75}^{-1}$ Mpc of the cluster centres and to match the Nakata et al. (2004) sample we apply a luminosity limit of $M_{b_j} = -19.65$ to all data. This figure neatly illustrates the strength of evolution observed for f_p in groups and the field whilst galaxies in dense cluster cores were already largely passive by $z \sim 1$. Indeed, the weak evolution in the cluster core value of f_p is likely to be exaggerated by the increasing errors on $\text{EW}[\text{OII}]$ in higher redshift clusters, leading to an increased scatter of passive galaxies to $\text{EW}[\text{OII}] > 5\text{\AA}$ with redshift.

This figure brings together our picture of galaxy evolution and its dependence on environment. The transformation of galaxies from star-forming blue galaxies to passive red galaxies seems to be more active in the group environment than in dense cluster cores since at least $z \sim 1$. Therefore the group environment appears to be more important in

driving the process of transformation. With a significant contribution to the global galaxy budget ($\sim 50\%$ locally), the evolution of group galaxies makes an important contribution to the global evolution of f_p which proceeds at a similar rate. The decline of global star formation since $z \gtrsim 1$ (e.g. Lilly et al., 1996; Madau et al., 1998; Wilson et al., 2002; Hopkins, 2004) is likely to be driven largely by such transformations although we cannot rule out a contribution from internal processes. We note that despite these clear trends in a large statistical sample, the group to group and cluster to cluster variations in f_p remain large, representing the wide variety of histories experienced by the constituent galaxies. However, the underlying dependence on local environment (on a group scale) can be seen in the strong correlation of f_p with local galaxy density. Indeed it seems likely that the morphological composition of the irregular MORPHS clusters (Dressler et al., 1997) and the X-ray faint clusters of Balogh et al. (2002) is dictated by infalling groups, since it is well matched to our CNOC2 group composition.

In Figure 9.2 we show the equivalent modified “Madau plot” for a simulated galaxy population generated using the GALFORM semi-analytic model (Cole et al., 2000; Baugh et al., 2004). Instead of dividing the model population into group, cluster and field categories, we make a selection based upon the mass of the underlying dark matter halo. The evolution of f_p proceeds at a similar rate since $z \sim 1$ in all environments, excepting the global population (the field) for which there is a mildly stronger evolution, representing the accretion of galaxies onto more massive halos. The evolution of f_p is much too weak since $z = 0.4$ in galaxy groups and in the field and too strong in clusters, although not significantly so. In our GALFORM model the predicted decline in global SFR since $z = 1$ is a factor of ~ 5 . As the fraction of star-forming galaxies declines from $\sim 80\%$ at $z = 1$ to $\sim 50\%$ at $z = 0$ this can only account for a factor of ~ 1.6 , requiring a decline in the SFR of ~ 3 for a typical star-forming galaxy. This is caused by increased feedback into the hot gas halo and superwinds. The model also overpredicts the number of passive, faint satellite galaxies in groups and the field and so is unlikely to match the downsizing of galaxy mass for a typical star-forming galaxy, as observed (Cowie et al., 1996). We find that by extending the luminosity range to a fainter limit, f_p actually increases in the model groups instead of decreasing as seen in observations.

Our observations suggest that the rate of change in f_p is a more important factor in the decline of global star formation than is the SFR of a typical star-forming galaxy, since $z \sim 0.4$ (Chapter 5). We also detect a strong dependence of f_p on galaxy luminosity, even in groups. Therefore we suggest that the model underestimates the importance

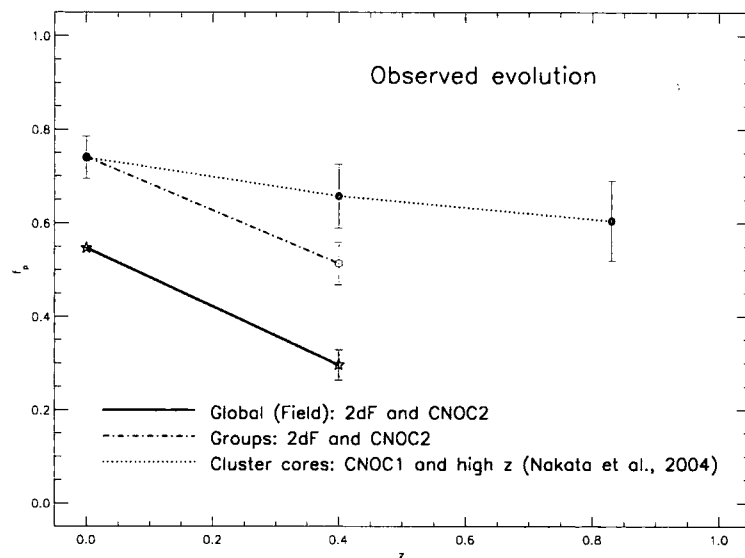


Figure 9.1: The fraction of passive galaxies, f_p , plotted as a function of redshift in different environments. The group and field data are selected from our 2dF and CNOC2 samples. We overplot the equivalent fractions in cluster cores, selected from the samples of Nakata et al. (2004). These data originate in the 2dFGRS, CNOC1 and high redshift cluster samples of van Dokkum et al. (2000) and Postman et al. (2001). Cluster data are selected only within the inner $0.75h_{75}^{-1}$ Mpc of the cluster centre and we match the luminosity limit of Nakata et al. (2004) ($M_{b_j} = -19.65$). This figure shows the strong decline of f_p in the Universe since $z \sim 0.4$ in groups and clusters whilst the passive population in the dense core regions of clusters is consistent with having been mostly in place since $z \sim 1$.

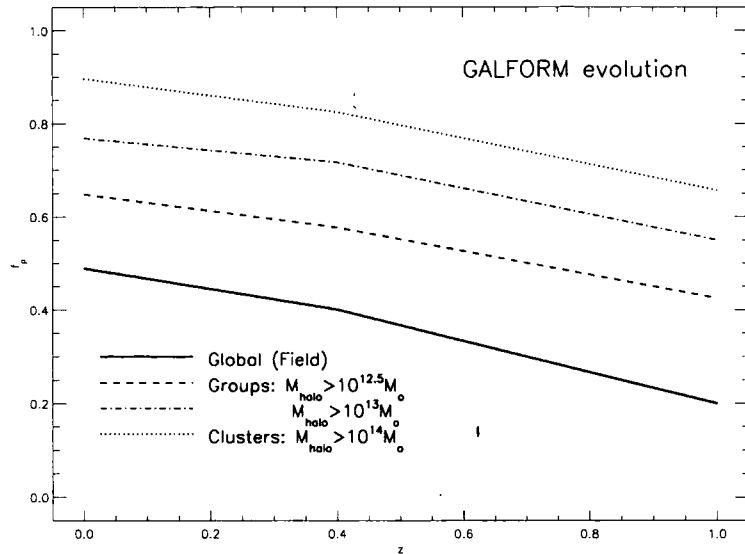


Figure 9.2: The predicted fraction of passive galaxies f_p computed in the GALFORM semi-analytic model (Cole et al., 2000; Baugh et al., 2004), plotted as a function of redshift in a range of environments (halo mass). The galaxy sample is limited to $M_{b_j} = -19.65$ to match Figure 9.1. The model displays a remarkably similar rate of evolution in each environment with perhaps slightly stronger evolution in the global population (the field) as more galaxies are accreted onto more massive halos. Whilst the direction of evolution and the environmental dependence of f_p is in agreement with observations, the rate of evolution is too weak since $z = 0.4$ in groups and the field, and potentially too strong in massive clusters.

of transformation mechanisms common in groups and overestimates the importance of strangulation in faint satellite galaxies.

We also suggest that GALFORM produces too many highly star-forming galaxies (starbursts, triggered by galaxy mergers), required by the model to make up for the overpassive faint population in the global budget of star formation. The 2dF distribution of $\text{EW}[\text{H}\alpha]$ would be better matched by a greater population of quiescently star-forming galaxies.

We can conclude that the group environment plays an important role in galaxy evolution. Transformations in groups generate a galaxy population significantly more passive than in lower density environments, with the morphological composition of a young irregular cluster. These transformations include the formation of a population of passive spiral galaxies and S0s brighter than M_* through interactions with the intragroup medium and other galaxies. The formation of a large S0 type galaxy population represents a relatively recent stage of evolution. They are apparently generated at a great rate since

$z \sim 0.5$ (Dressler et al., 1997) via transformations apparently favouring the group and outercluster environment. Accretion via minor mergers may also play a role in generating a larger population of bright galaxies in groups than is seen in the field. Below M_* , other mechanisms such as harassment might be responsible for an excess of passive elliptical galaxies in groups, potentially steepening the faint-end slope of the galaxy luminosity function in massive groups and clusters (e.g. Christlein, 2000) and driving a relationship in local groups between early-type fraction and velocity dispersion or X-ray luminosity (e.g. Zabludoff & Mulchaey, 1998). Whilst detailed semi-analytic models such as GALFORM exhibit general trends in agreement with observations, such as the decline of global star formation (Baugh et al., 2004) and a predominantly passive group and cluster population, it may yet do so by invoking an oversimplified or even false physical model of star formation. Only by matching the more detailed evolutionary trends such as the downsizing of the characteristic mass of a star-forming galaxy, and the evolution of f_p as a function of environment will the fundamental physical processes responsible for galaxy evolution be truly laid bare.

9.3 Future Prospects

Recent developments in astronomical technology spanning the electromagnetic spectrum and utilising high resolution, multiplexing and wide-field instrumentation promise a rich future for studies of galaxy evolution. In this final section we identify some key areas which will utilise these technologies to unravel the history of galaxy evolution.

9.3.1 Understanding Individual Groups

Whilst the importance of galaxy evolution in groups has been emphasized in the current work, we have also seen large group to group variations in galaxy populations. Understanding the reason why some groups are more evolved than others is the key to determining how transformations proceed in groups. Deeper, more complete spectroscopy will provide a better estimate of the group velocity dispersion and dynamical structure, a vital key to understand the gravitational interplay of group members. By probing the fainter galaxy population of intermediate and high redshift groups, we can also confirm whether the faint end slope of the luminosity function is a strong function of environment as suggested at low redshift (Christlein, 2000; Zabludoff & Mulchaey, 2000), relating the formation of the faint elliptical population of galaxies to a group and cluster origin. K-

band imaging provides a more direct estimate of stellar mass in galaxies, removing the degeneracy between blue luminosity and star formation. Deep X-ray observations will link the star formation and morphology of group galaxies to the intragroup medium, with clues to the mechanisms responsible for galaxy transformations such as the formation of passive spirals and S0 type galaxies in groups.

9.3.2 Multi-Wavelength Studies of Star Formation

Whilst the presence of an emission line is sufficient to reveal trends in f_p , to reveal the precise SFR for an individual galaxy a multi-wavelength approach is required. One can survey the total UV emission (for example with the GALEX satellite), mid to far infra-red emission (with the Spitzer satellite, good for identifying dusty star formation typical of starbursts) and optical emission lines (with optical MOS and future infra-red MOS instruments to identify $H\alpha$ at high redshifts). In this way the distribution of galaxy SFR can be understood in more detail and with more accurate calibration via models. We have GALEX time to observe the CNOC2 groups and expect that these data will isolate important internal (e.g. morphological) and external (e.g. environmental) influences on the star formation of a galaxy and also allow easier comparisons with semi-analytic models.

9.3.3 Direct Observations of a Transforming Galaxy

Integral Field Units (IFUs) provide highly resolved spectroscopy of an individual galaxy. By observing group galaxies which are candidates for transforming galaxies (high current or recent star formation / disturbed morphology) we can obtain a clearer picture of how that transformation proceeds via resolved star formation and gas and stellar dynamics.

9.3.4 The Millennium Run

The Virgo Consortium's Millennium Run is the largest supercomputer simulation of the Universe to date. Combining semi-analytic techniques with the high resolution of the Millennium Run will provide a catalogue of galaxies with fully predicted positions and velocities. By selecting groups and clusters of galaxies from this catalogue using observational techniques we can match the selection criteria of observational samples with unprecedented accuracy. Not only will this allow us to examine our selection criteria in detail, it will also provide a model framework for implementing a wide range of physical

processes which might drive galaxy transformations, and permit easy comparisons with observations.

9.3.5 Higher Redshift Groups and Clusters

To understand the contribution of group and cluster galaxies to the global budget of star formation it is important that higher redshift systems be identified. Critically, by placing a point on the modified Madau plot for groups and the global population at $z \sim 1$, we will be able to understand in much more detail the role of groups in driving the transformations of galaxies during the period of global SFR decline. We would like to know if f_p in $z \sim 1$ groups is even more different to clusters than at $z \sim 0.4$ and whether it is more closely matched to the global (field) value. Using ultraviolet and infra-red measurements of SFR we can also better understand whether a typical star-forming galaxy was forming stars at a much greater rate at $z \sim 1$ and the importance of starbursts to the global budget. This will be a critical test of semi-analytic models. Deep spectroscopy of high redshift systems will also be of vital importance to how we understand the downsizing of galaxy mass for a typical star-forming galaxy, and whether this is linked to the formation of red elliptical galaxies in overdense regions of the Universe (the formation time of which is apparently related to galaxy luminosity in clusters (Kodama et al., 2004b; De Lucia et al., 2004)). This may in turn be linked to the relation between the abundance of faint passive ellipticals and group mass in local groups (Christlein, 2000; Zabludoff & Mulchaey, 2000).

The existence of new deep spectroscopic redshift surveys such as GOODS (Cowie et al., 2004; Vanzella et al., 2004) and DEEP2 (Madgwick et al., 2003) makes the detection of groups at $z \sim 1$ substantially easier (e.g. Gerke & DEEP2 Team, 2003). Kinematically selected groups from these surveys will provide high redshift counterparts to the CNOC2 and local group catalogues. The multiwavelength approach to these surveys will allow us to develop a thorough picture of galaxy properties at $z \sim 1$, and the relationship with environment. In addition the EDisCS survey provide spectroscopic data for a variety of systems ranging from groups to clusters over the redshift range $0.5 \leq z \leq 0.8$ (Halliday et al., 2003).

We also feel that once the calibration issues are well understood, wide field imaging techniques will provide a tool, via photometric redshifts, to isolate the infalling groups surrounding galaxy clusters. This might be applied to clusters at high redshift such as the sample of Rosati et al. (1998) for which deep multicolour imaging already exists in some fields (Demarco et al., 2004). Finally, it might also be possible to detect some

more massive isolated groups using photometric redshifts (Botzler et al., 2004) although spectroscopic follow up is essential.

9.3.6 Isolated Galaxies

Finally we emphasise the importance of obtaining large samples of isolated galaxies. In the age of cluster studies it was usually considered sufficient to compare cluster with the “field” environment. However, the local abundance of groups ($\sim 50\%$) is such that the field is largely composed of groups. Therefore comparisons between group and field (such as the one presented in this thesis) are severely limited by the “field” definition. By selecting a large sample of isolated galaxies we can separate the internal evolution of a galaxy from the nurturing effects of environment, placing an evolutionary path for isolated galaxies on the modified Madau plot. Fossil group galaxies may also make an important contribution to the isolated galaxy population, resulting from the complete merger of all members of a group (Mulchaey & Zabludoff, 1999; Jones et al., 2000). By tracking this evolution to higher redshift, when some or most fossil galaxies may not yet have formed, we can understand the dynamical process behind the creation of this end product and discriminate between these galaxies and those which have been isolated since formation.

Galaxies with no near neighbours represent the most difficult galaxies to select. Only with 100% complete spectroscopy down to a sufficiently faint magnitude limit that minimises external influences from other galaxies, can the isolation be absolutely confirmed. However, photometric redshifts and galaxy colours can also be used to reject the proximity of galaxies along the line of sight. Using a combination of these techniques it is possible to build a catalogue of isolated galaxies in regions of sky with high coverage by spectroscopic redshift surveys. The extent of evolution seen in isolated galaxies will be a critical test of the role of groups and clusters in driving global galaxy evolution.

Bibliography

- Abadi, M. G., Navarro, J. F., Steinmetz, M., & Eke, V. R. 2003, *ApJ*, 597, 21
- Abell, G. O. 1958, *ApJS*, 3, 211
- . 1965, *ARA&A*, 3, 1
- Abraham, R. G., Valdes, F., Yee, H. K. C., & van den Bergh, S. 1994, *ApJ*, 432, 75
- Allen, S. W., Schmidt, R. W., & Fabian, A. C. 2002, *MNRAS*, 335, 256
- Allington-Smith, J. R., Ellis, R., Zirbel, E. L., & Oemler, A. J. 1993, *ApJ*, 404, 521
- Andreon, S. & Ettore, S. 1999, *ApJ*, 516, 647
- Andreon, S., Willis, J., Quintana, H., Valtchanov, I., Pierre, M., & Pcaud, F. 2004, *MNRAS*, 263
- Babcock, H. W. 1939, *Lick Observatory Bulletin*, 19, 41
- Bahcall, N. A. 1977, *ApJL*, 218, L93
- Baldry, I. K., Glazebrook, K., Baugh, C. M., Bland-Hawthorn, J., Bridges, T., Cannon, R., Cole, S., Colless, M., Collins, C., Couch, W., Dalton, G., De Propriis, R., Driver, S. P., Efstathiou, G., Ellis, R. S., Frenk, C. S., Hawkins, E., Jackson, C., Lahav, O., Lewis, I., Lumsden, S., Maddox, S., Madgwick, D. S., Norberg, P., Peacock, J. A., Peterson, B. A., Sutherland, W., & Taylor, K. 2002, *ApJ*, 569, 582
- Baldry, I. K., Glazebrook, K., Brinkmann, J., Ivezić, Ž., Lupton, R. H., Nichol, R. C., & Szalay, A. S. 2004, *ApJ*, 600, 681
- Balogh, M., Eke, V., Miller, C., Lewis, I., Bower, R., Couch, W., Nichol, R., Bland-Hawthorn, J., Baldry, I. K., Baugh, C., Bridges, T., Cannon, R., Cole, S., Colless, M., Collins, C., Cross, N., Dalton, G., de Propriis, R., Driver, S. P., Efstathiou, G.,

- Ellis, R. S., Frenk, C. S., Glazebrook, K., Gomez, P., Gray, A., Hawkins, E., Jackson, C., Lahav, O., Lumsden, S., Maddox, S., Madgwick, D., Norberg, P., Peacock, J. A., Percival, W., Peterson, B. A., Sutherland, W., & Taylor, K. 2004a, *MNRAS*, 348, 1355
- Balogh, M. L., Baldry, I. K., Nichol, R., Miller, C., Bower, R. G., & Glazebrook, K. 2004b, *ApJL*, submitted
- Balogh, M. L., Morris, S. L., Yee, H. K. C., Carlberg, R. G., & Ellingson, E. 1999, *ApJ*, 527, 54
- Balogh, M. L., Navarro, J. F., & Morris, S. L. 2000, *ApJ*, 540, 113
- Balogh, M. L., Schade, D., Morris, S. L., Yee, H. K. C., Carlberg, R. G., & Ellingson, E. 1998, *ApJL*, 504, L75+
- Balogh, M. L., Smail, I., Bower, R. G., Ziegler, B. L., Smith, G. P., Davies, R. L., Gaztelu, A., Kneib, J.-P., & Ebeling, H. 2002, *ApJ*, 566, 123
- Barnes, J. 1985, *MNRAS*, 215, 517
- Baugh, C. M., Lacey, C. G., Frenk, C. S., Granato, G. L., Silva, L., Bressan, A., Benson, A. J., & Cole, S. 2004, *astro-ph/0406069*
- Baum, W. A. 1955, *AJ*, 60, 153
- Beers, T. C., Flynn, K., & Gebhardt, K. 1990, *AJ*, 100, 32
- Bell, E. F., Wolf, C., McIntosh, D. H., COMBO-17 Team, & GEMS Collaboration. 2003, American Astronomical Society Meeting, 203
- Bertin, E. 1999, *SExtractor V2.1.3 User's Guide*
- Bertschik, M. & Burkert, A. 2002, *Astrophysics and Space Science*, 281, 405
- Blanton, M. R., Hogg, D. W., Bahcall, N. A., Baldry, I. K., Brinkmann, J., Csabai, I., Eisenstein, D., Fukugita, M., Gunn, J. E., Ivezić, Ž., Lamb, D. Q., Lupton, R. H., Loveday, J., Munn, J. A., Nichol, R. C., Okamura, S., Schlegel, D. J., Shimasaku, K., Strauss, M. A., Vogeley, M. S., & Weinberg, D. H. 2003, *ApJ*, 594, 186
- Borne, K. D., Bushouse, H., Lucas, R. A., & Colina, L. 2000, *ApJL*, 529, L77
- Botzler, C. S., Snigula, J., Bender, R., & Hopp, U. 2004, *MNRAS*, 349, 425

- Bower, R. G. & Balogh, M. L. 2004, in *Clusters of Galaxies: Probes of Cosmological Structure and Galaxy Evolution*, 326
- Bower, R. G., Lucey, J. R., & Ellis, R. S. 1992, *MNRAS*, 254, 601
- Brinchmann, J., Charlot, S., White, S. D. M., Tremonti, C., Kauffmann, G., Heckman, T., & Brinkmann, J. 2004, *MNRAS*, 351, 1151
- Bruzual, G. & Charlot, S. 2003, *MNRAS*, 344, 1000
- Butcher, H. & Oemler, A. 1984, *ApJ*, 285, 426
- Byrd, G. & Valtonen, M. 1990, *ApJ*, 350, 89
- Carlberg, R. G., Yee, H. K. C., Morris, S. L., Lin, H., Hall, P. B., Patton, D. R., Sawicki, M., & Shepherd, C. W. 2001a, *ApJ*, 563, 736
- . 2001b, *ApJ*, 552, 427
- Christlein, D. 2000, *ApJ*, 545, 145
- Christlein, D. & Zabludoff, A. I. 2003, *ApJ*, 591, 764
- Chromey, F. R. & Hasselbacher, D. A. 1996, *PASP*, 108, 944
- Cohen, J. G., Hogg, D. W., Blandford, R., Cowie, L. L., Hu, E., Songaila, A., Shopbell, P., & Richberg, K. 2000, *ApJ*, 538, 29
- Cohen, J. G. & Kneib, J. 2002, *ApJ*, 573, 524
- Cole, S., Lacey, C. G., Baugh, C. M., & Frenk, C. S. 2000, *MNRAS*, 319, 168
- Colless, M., Dalton, G., Maddox, S., Sutherland, W., Norberg, P., Cole, S., Bland-Hawthorn, J., Bridges, T., Cannon, R., Collins, C., Couch, W., Cross, N., Deeley, K., de Propris, R., Driver, S. P., Efstathiou, G., Ellis, R. S., Frenk, C. S., Glazebrook, K., Jackson, C., Lahav, O., Lewis, I., Lumsden, S., Madgwick, D., Peacock, J. A., Peterson, B. A., Price, I., Seaborne, M., & Taylor, K. 2003, *astro-ph/0306581*
- Conselice, C. J. 2003, *ApJS*, 147, 1
- Conselice, C. J., Grogin, N. A., Jogee, S., Lucas, R. A., Dahlen, T., de Mello, D., Gardner, J. P., Mobasher, B., & Ravindranath, S. 2004, *ApJL*, 600, L139
- Couch, W. J., Barger, A. J., Smail, I., Ellis, R. S., & Sharples, R. M. 1998, *ApJ*, 497, 188

- Couch, W. J. & Sharples, R. M. 1987, *MNRAS*, 229, 423
- Cowie, L. L., Barger, A. J., Hu, E. M., Capak, P., & Songaila, A. 2004, *AJ*, 127, 3137
- Cowie, L. L., Songaila, A., & Barger, A. J. 1999, *AJ*, 118, 603
- Cowie, L. L., Songaila, A., Hu, E. M., & Cohen, J. G. 1996, *AJ*, 112, 839
- Coziol, R., Brinks, E., & Bravo-Alfaro, H. 2004, *AJ*, 128, 68
- Croton, D. J., Farrar, G. R., Norberg, P., Colless, M., Peacock, J. A., Baldry, I. K., Baugh, C. M., Bland-Hawthorn, J., Bridges, T., Cannon, R., Cole, S., Collins, C., Couch, W., Dalton, G., De Propris, R., Driver, S. P., Efstathiou, G., Ellis, R. S., Frenk, C. S., Glazebrook, K., Jackson, C., Lahav, O., Lewis, I., Lumsden, S., Maddox, S., Madgwick, D., Peterson, B. A., Sutherland, W., & Taylor, K. 2004, astro-ph/0407537, in press:
- Cuillandre, J.-C., Mellier, Y., Dupin, J.-P., Tilloles, P., Murowinski, R., Crampton, D., Wooff, R., & Luppino, G. A. 1996, *PASP*, 108, 1120
- Cuillandre, J. C., Melliers, Y., Murowinski, R., Crampton, D., Luppino, G., & Arsenault, R. 1995, in *IAU Symp. 167: New Developments in Array Technology and Applications*, 213
- Dalcanton, J. J. 1996, *ApJ*, 466, 92
- Davis, M., Efstathiou, G., Frenk, C. S., & White, S. D. M. 1985, *ApJ*, 292, 371
- de Lapparent, V., Geller, M. J., & Huchra, J. P. 1986, *ApJL*, 302, L1
- De Lucia, G., Poggianti, B. M., Aragón-Salamanca, A., Clowe, D., Halliday, C., Jablonka, P., Milvang-Jensen, B., Pelló, R., Poirier, S., Rudnick, G., Saglia, R., Simard, L., & White, S. D. M. 2004, *ApJL*, 610, L77
- De Propris, R., Colless, M., Driver, S. P., Couch, W., Peacock, J. A., Baldry, I. K., Baugh, C. M., Bland-Hawthorn, J., Bridges, T., Cannon, R., Cole, S., Collins, C., Cross, N., Dalton, G. B., Efstathiou, G., Ellis, R. S., Frenk, C. S., Glazebrook, K., Hawkins, E., Jackson, C., Lahav, O., Lewis, I., Lumsden, S., Maddox, S., Madgwick, D. S., Norberg, P., Percival, W., Peterson, B., Sutherland, W., & Taylor, K. 2003a, *MNRAS*, 342, 725
- De Propris, R., Stanford, S. A., Eisenhardt, P., & Dickinson, M. 2003b, *Astrophysics and Space Science*, 285, 43

- de Vaucouleurs, G. 1959, *Handbuch der Physik*, 53, 311
- Demarco, R., Rosati, P., Lidman, C., Nonino, M., Mainieri, V., Stanford, A., Holden, B., & Eisenhardt, P. 2004, in *Clusters of Galaxies: Probes of Cosmological Structure and Galaxy Evolution*
- Diaferio, A., Kauffmann, G., Balogh, M. L., White, S. D. M., Schade, D., & Ellingson, E. 2001, *MNRAS*, 323, 999
- Domínguez, M., Muriel, H., & Lambas, D. G. 2001, *AJ*, 121, 1266
- Dressler, A. 1980, *ApJ*, 236, 351
- Dressler, A., Oemler, A., Jr., Poggianti, B. M., Smail, I., Trager, S., Shectman, S. A., Couch, W., & Ellis, R. 2004, *astro-ph/0408490*
- Dressler, A., Oemler, A. J., Butcher, H. R., & Gunn, J. E. 1994, *ApJ*, 430, 107
- Dressler, A., Oemler, A. J., Couch, W. J., Smail, I., Ellis, R. S., Barger, A., Butcher, H., Poggianti, B. M., & Sharples, R. M. 1997, *ApJ*, 490, 577
- Dressler, A. & Shectman, S. A. 1987, *AJ*, 94, 899
- Dressler, A., Smail, I., Poggianti, B. M., Butcher, H., Couch, W. J., Ellis, R. S., & Oemler, A. J. 1999, *ApJS*, 122, 51
- Driver, S. & De Propriis, R. 2003, *Astrophysics and Space Science*, 285, 175
- Efron, B. 1982, *The Jackknife, the Bootstrap and other resampling plans* (CBMS-NSF Regional Conference Series in Applied Mathematics, Philadelphia: Society for Industrial and Applied Mathematics (SIAM), 1982)
- Eke, V. R., Baugh, C. M., Cole, S., Frenk, C. S., Norberg, P., Peacock, J. A., Baldry, I. K., Bland-Hawthorn, J., Bridges, T., Cannon, R., Colless, M., Collins, C., Couch, W., Dalton, G., de Propriis, R., Driver, S. P., Efsthathiou, G., Ellis, R. S., Glazebrook, K., Jackson, C., Lahav, O., Lewis, I., Lumsden, S., Maddox, S., Madgwick, D., Peterson, B. A., Sutherland, W., & Taylor, K. 2004, *MNRAS*, 348, 866
- Ellingson, E., Lin, H., Yee, H. K. C., & Carlberg, R. G. 2001, *ApJ*, 547, 609
- Emsellem, E., Cappellari, M., Peletier, R. F., McDermid, R. M., Bacon, R., Bureau, M., Copin, Y., Davies, R. L., Krajnović, D., Kuntschner, H., Miller, B. W., & de Zeeuw, P. 2004, *MNRAS*, 352, 721

- Fairley, B. W., Jones, L. R., Wake, D. A., Collins, C. A., Burke, D. J., Nichol, R. C., & Romer, A. K. 2002, *MNRAS*, 330, 755
- Flores, H., Hammer, F., Elbaz, D., Cesarsky, C. J., Liang, Y. C., Fadda, D., & Gruel, N. 2004, *A&A*, 415, 885
- Gómez, P. L., Nichol, R. C., Miller, C. J., Balogh, M. L., Goto, T., Zabludoff, A. I., Romer, A. K., Bernardi, M., Sheth, R., Hopkins, A. M., Castander, F. J., Connolly, A. J., Schneider, D. P., Brinkmann, J., Lamb, D. Q., SubbaRao, M., & York, D. G. 2003, *ApJ*, 584, 210
- Georgakakis, A., Hopkins, A. M., Sullivan, M., Afonso, J., Georgantopoulos, I., Mobasher, B., & Cram, L. E. 2003, *MNRAS*, 345, 939
- Gerke, B. F. & DEEP2 Team. 2003, American Astronomical Society Meeting, 203
- Gioia, I. M. & Luppino, G. A. 1994, *ApJS*, 94, 583
- Girardi, M., Rigoni, E., Mardirossian, F., & Mezzetti, M. 2003, *A&A*, 406, 403
- Gladders, M. D. & Yee, H. K. C. 2000, *AJ*, 120, 2148
- Gnedin, O. Y. 2003, *ApJ*, 582, 141
- Goderya, S. N. & Lolling, S. M. 2002, *Astrophysics and Space Science*, 279, 377
- Goto, T., Okamura, S., Sekiguchi, M., Bernardi, M., Brinkmann, J., Gómez, P. L., Harvanek, M., Kleinman, S. J., Krzesinski, J., Long, D., Loveday, J., Miller, C. J., Neilsen, E. H., Newman, P. R., Nitta, A., Sheth, R. K., Snedden, S. A., & Yamauchi, C. 2003, *Publications of the Astronomical Society of Japan*, 55, 757
- Granato, G. L., Lacey, C. G., Silva, L., Bressan, A., Baugh, C. M., Cole, S., & Frenk, C. S. 2000, *ApJ*, 542, 710
- Gunn, J. E. & Gott, J. R. I. 1972, *ApJ*, 176, 1
- Halliday, C., Poggianti, B. M., Milvang-Jensen, B., Poirier, S., Aragon-Salamanca, A., Jablonka, P., Pello, R., Saglia, R. P., White, S., & The Ediscs Collaboration. 2003, *The Cosmic Cauldron*, 25th meeting of the IAU, Joint Discussion 10, 18 July 2003, Sydney, Australia, 10

- Hammer, F., Flores, H., Lilly, S. J., Crampton, D., Le Fevre, O., Rola, C., Mallen-Ornelas, G., Schade, D., & Tresse, L. 1997, *ApJ*, 481, 49
- Hashimoto, Y. & Oemler, A. J. 2000, *ApJ*, 530, 652
- Hashimoto, Y., Oemler, A. J., Lin, H., & Tucker, D. L. 1998, *ApJ*, 499, 589
- Helsdon, S. F. & Ponman, T. J. 2003, *MNRAS*, 339, L29
- Hickson, P. 1982, *ApJ*, 255, 382
- Hickson, P., Kindl, E., & Auman, J. R. 1989, *ApJS*, 70, 687
- Hinkley, S. & Im, M. 2001, *ApJL*, 560, L41
- Hopkins, A. M. 2004, *astro-ph/0407170*
- Hopkins, A. M., Miller, C. J., Nichol, R. C., Connolly, A. J., Bernardi, M., Gómez, P. L., Goto, T., Tremonti, C. A., Brinkmann, J., Ivezić, Ž., & Lamb, D. Q. 2003, *ApJ*, 599, 971
- Hubble, E. 1929, *Proceedings of the National Academy of Science*, 15, 168
- Huchra, J. P. & Geller, M. J. 1982, *ApJ*, 257, 423
- Humason, M. L. 1936, *ApJ*, 83, 10
- Jansen, R. A., Franx, M., & Fabricant, D. 2001, *ApJ*, 551, 825
- Jones, L. R., McHardy, I., Newsam, A., & Mason, K. 2002, *MNRAS*, 334, 219
- Jones, L. R., Ponman, T. J., & Forbes, D. A. 2000, *MNRAS*, 312, 139
- Joseph, R. D. & Wright, G. S. 1985, *MNRAS*, 214, 87
- Kauffmann, G., Heckman, T. M., White, S. D. M., Charlot, S., Tremonti, C., Peng, E. W., Seibert, M., Brinkmann, J., Nichol, R. C., SubbaRao, M., & York, D. 2003, *MNRAS*, 341, 54
- Kauffmann, G., White, S. D. M., Heckman, T. M., Ménard, B., Brinchmann, J., Charlot, S., Tremonti, C., & Brinkmann, J. 2004, *MNRAS*, 314
- Kelson, D. D. 2003, *PASP*, 115, 688
- Kenney, J. D. P., van Gorkom, J. H., & Vollmer, B. 2004, *AJ*, 127, 3361

- Kennicutt, Robert C., J. 1998, *ARA&A*, 36, 189
- Kennicutt, R. C. 1983, *ApJ*, 272, 54
- . 1992, *ApJS*, 79, 255
- Kennicutt, R. C., Tamblyn, P., & Congdon, C. W. 1994, *ApJ*, 435, 22
- Kent, S. M. 1994, *Astrophysics and Space Science*, 217, 27
- Kewley, L. J., Geller, M. J., & Jansen, R. A. 2004, *AJ*, 127, 2002
- King, C. R. & Ellis, R. S. 1985, *ApJ*, 288, 456
- Kneib, J., Ellis, R. S., Santos, M. R., & Richard, J. 2004, *ApJ*, 607, 697
- Koch, A., Odenkirchen, M., Grebel, E. K., & Caldwell, J. A. R. 2004, *Astronomische Nachrichten*, 325, 299
- Kodama, T., Balogh, M. L., Smail, I., Bower, R. G., & Nakata, F. 2004a, *MNRAS*, 388
- Kodama, T., Bell, E. F., & Bower, R. G. 1999, *MNRAS*, 302, 152
- Kodama, T., Smail, I., Nakata, F., Okamura, S., & Bower, R. G. 2001, *ApJL*, 562, L9
- Kodama, T., Yamada, T., Akiyama, M., Aoki, K., Doi, M., Furusawa, H., Fuse, T., Imanishi, M., Ishida, C., Iye, M., Kajisawa, M., Karoji, H., Kobayashi, N., Komiyama, Y., Kosugi, G., Maeda, Y., Miyazaki, S., Mizumoto, Y., Morokuma, T., Nakata, F., Noumaru, J., Ogasawara, R., Ouchi, M., Sasaki, T., Sekiguchi, K., Shimasaku, K., Simpson, C., Takata, T., Tanaka, I., Ueda, Y., Yasuda, N., & Yoshida, M. 2004b, *MNRAS*, 350, 1005
- Koopmann, R. A. & Kenney, J. D. P. 2004, *astro-ph/0406243*
- Kurtz, M. J. & Mink, D. J. 1998, *PASP*, 110, 934
- Lacey, C. & Cole, S. 1993, *MNRAS*, 262, 627
- Landolt, A. 1992, *AJ*, 104, 340
- Larson, R. B., Tinsley, B. M., & Caldwell, C. N. 1980, *ApJ*, 237, 692
-
- Lewis, I., Balogh, M., De Propris, R., Couch, W., Bower, R., Offer, A., Bland-Hawthorn, J., Baldry, I. K., Baugh, C., Bridges, T., Cannon, R., Cole, S., Colless, M., Collins, C.,

- Cross, N., Dalton, G., Driver, S. P., Efstathiou, G., Ellis, R. S., Frenk, C. S., Glazebrook, K., Hawkins, E., Jackson, C., Lahav, O., Lumsden, S., Maddox, S., Madgwick, D., Norberg, P., Peacock, J. A., Percival, W., Peterson, B. A., Sutherland, W., & Taylor, K. 2002a, *MNRAS*, 334, 673
- Lewis, I. J., Cannon, R. D., Taylor, K., Glazebrook, K., Bailey, J. A., Baldry, I. K., Barton, J. R., Bridges, T. J., Dalton, G. B., Farrell, T. J., Gray, P. M., Lankshear, A., McCowage, C., Parry, I. R., Sharples, R. M., Shortridge, K., Smith, G. A., Stevenson, J., Straede, J. O., Waller, L. G., Whittard, J. D., Wilcox, J. K., & Willis, K. C. 2002b, *MNRAS*, 333, 279
- Lilly, S. J., Le Fevre, O., Hammer, F., & Crampton, D. 1996, *ApJL*, 460, L1+
- Lin, H., Yee, H. K. C., Carlberg, R. G., Morris, S. L., Sawicki, M., Patton, D. R., Wirth, G., & Shepherd, C. W. 1999, *ApJ*, 518, 533
- Luppino, G. A., Tonry, J. L., & Stubbs, C. W. 1998, in *Proc. SPIE Vol. 3355*, p. 469-476, *Optical Astronomical Instrumentation*, Sandro D'Odorico; Ed., 469-476
- Madau, P., Pozzetti, L., & Dickinson, M. 1998, *ApJ*, 498, 106
- Madgwick, D. S., Coil, A. L., Conselice, C. J., Cooper, M. C., Davis, M., Ellis, R. S., Faber, S. M., Finkbeiner, D. P., Gerke, B., Guhathakurta, P., Kaiser, N., Koo, D. C., Newman, J. A., Phillips, A. C., Steidel, C. C., Weiner, B. J., Willmer, C. N. A., & Yan, R. 2003, *ApJ*, 599, 997
- Mamon, G. A., Sanchis, T., Salvador-Solé, E., & Solanes, J. M. 2004, *A&A*, 414, 445
- Margoniner, V. E., de Carvalho, R. R., Gal, R. R., & Djorgovski, S. G. 2001, *ApJL*, 548, L143
- Martínez, H. J., Zandivarez, A., Domínguez, M., Merchán, M. E., & Lambas, D. G. 2002, *MNRAS*, 333, L31
- Mehlert, D., Thomas, D., Saglia, R. P., Bender, R., & Wegner, G. 2003, *A&A*, 407, 423
- Metzger, M. R., Luppino, G. A., & Miyazaki, S. 1995, *Bulletin of the American Astronomical Society*, 27, 1389
- Mobasher, B., Colless, M., Carter, D., Poggianti, B. M., Bridges, T. J., Kranz, K., Komiyama, Y., Kashikawa, N., Yagi, M., & Okamura, S. 2003, *ApJ*, 587, 605

- Moore, B., Katz, N., Lake, G., Dressler, A., & Oemler, A. 1996, *Nature*, 379, 613
- Mulchaey, J. S., Davis, D. S., Mushotzky, R. F., & Burstein, D. 2003, *ApJS*, 145, 39
- Mulchaey, J. S. & Zabludoff, A. I. 1998, *ApJ*, 496, 73
- . 1999, *ApJ*, 514, 133
- Mullis, C. R., McNamara, B. R., Quintana, H., Vikhlinin, A., Henry, J. P., Gioia, I. M., Hornstrup, A., Forman, W., & Jones, C. 2003, *ApJ*, 594, 154
- Nakata, F., G. B. R., Balogh, M. L., & J., W. D. 2004, *MNRAS*, submitted
- Norberg, P., Cole, S., Baugh, C. M., Frenk, C. S., Baldry, I., Bland-Hawthorn, J., Bridges, T., Cannon, R., Colless, M., Collins, C., Couch, W., Cross, N. J. G., Dalton, G., De Propris, R., Driver, S. P., Efstathiou, G., Ellis, R. S., Glazebrook, K., Jackson, C., Lahav, O., Lewis, I., Lumsden, S., Maddox, S., Madgwick, D., Peacock, J. A., Peterson, B. A., Sutherland, W., & Taylor, K. 2002, *MNRAS*, 336, 907
- Oemler, A. J. 1974, *ApJ*, 194, 1
- Oemler, A. J., Dressler, A., & Butcher, H. R. 1997, *ApJ*, 474, 561
- Osmond, J. P. F. & Ponman, T. J. 2004, *MNRAS*, 350, 1511
- Pavlovsky, C., Riess, A., Mack, J., & Gilliland, R. 2004, *ACS Data Handbook*, Version 3.0 (Baltimore: STScI)
- Peacock, J. A., Cole, S., Norberg, P., Baugh, C. M., Bland-Hawthorn, J., Bridges, T., Cannon, R. D., Colless, M., Collins, C., Couch, W., Dalton, G., Deeley, K., De Propris, R., Driver, S. P., Efstathiou, G., Ellis, R. S., Frenk, C. S., Glazebrook, K., Jackson, C., Lahav, O., Lewis, I., Lumsden, S., Maddox, S., Percival, W. J., Peterson, B. A., Price, I., Sutherland, W., & Taylor, K. 2001, *Nature*, 410, 169
- Perlmutter, S., G.Aldering, G.Goldhaber, R.A.Knop, P.Nugent, P.G.Castro, S.Deustua, S.Fabbro, A.Goobar, D.E.Groom, I.M.Hook, A.G.Kim, M.Y.Kim, J.C.Lee, N.J.Nunes, R.Pain, C.R.Pennypacker, R.Quimby, C.Lidman, R.S.Ellis, M.Irwin, R.G.McMahon, P.Ruiz-Lapuente, N.Walton, B.Schaefer, B.J.Boyle, A.V.Filippenko, T.Matheson, A.S.Fruchter, N.Panagia, H.J.M.Newberg, & W.J.Couch. 1999, *ApJ*, 517, 565
- Pierini, D. & Möller, C. S. 2003, *MNRAS*, 346, 818

- Pimblet, K. A., Smail, I., Kodama, T., Couch, W. J., Edge, A. C., Zabludoff, A. I., & O'Hely, E. 2002, *MNRAS*, 331, 333
- Poggianti, B. M. & Barbaro, G. 1996, *A&A*, 314, 379
- Poggianti, B. M., Bridges, T. J., Komiyama, Y., Yagi, M., Carter, D., Mobasher, B., Okamura, S., & Kashikawa, N. 2004, *ApJ*, 601, 197
- Poggianti, B. M., Smail, I., Dressler, A., Couch, W. J., Barger, A. J., Butcher, H., Ellis, R. S., & Oemler, A. J. 1999, *ApJ*, 518, 576
- Postman, M. & Geller, M. J. 1984, *ApJ*, 281, 95
- Postman, M., Lubin, L. M., & Oke, J. B. 2001, *AJ*, 122, 1125
- Quilis, V., Moore, B., & Bower, R. 2000, *Science*, 288, 1617
- Ramella, M., Geller, M. J., & Huchra, J. P. 1989, *ApJ*, 344, 57
- Ravindranath, S. & Ho, L. C. 2002, *ApJ*, 577, 133
- Reddy, N. A. & Steidel, C. C. 2004, *ApJL*, 603, L13
- Rines, K., Geller, M. J., Kurtz, M. J., & Diaferio, A. 2003, *AJ*, 126, 2152
- Rosati, P., della Ceca, R., Norman, C., & Giacconi, R. 1998, *ApJL*, 492, L21+
- Sandage, A. 1961, *The Hubble Atlas of Galaxies* (Washington: Carnegie Institution, 1961)
- Sandage, A. & Bedke, J. 1994, *The Carnegie Atlas of Galaxies* (Washington, DC: Carnegie Institution of Washington with The Flintridge Foundation, —c1994)
- Schade, D., Lilly, S. J., Le Fevre, O., Hammer, F., & Crampton, D. 1996, *ApJ*, 464, 79
- Schlegel, D. J., Finkbeiner, D. P., & Davis, M. 1998, *apj*, 500, 525
- Sekiguchi, K. 1987, *ApJ*, 316, 145
- Severgnini, P. & Saracco, P. 2001, *Astrophysics and Space Science*, 276, 749
- Shepherd, C. W., Carlberg, R. G., Yee, H. K. C., Morris, S. L., Lin, H., Sawicki, M., Hall, P. B., & Patton, D. R. 2001, *ApJ*, 560, 72
- Shier, L. M. & Fischer, J. 1998, *ApJ*, 497, 163

- Simard, L., Willmer, C. N. A., Vogt, N. P., Sarajedini, V. L., Phillips, A. C., Weiner, B. J., Koo, D. C., Im, M., Illingworth, G. D., & Faber, S. M. 2002, *ApJS*, 142, 1
- Smail, I., Dressler, A., Couch, W. J., Ellis, R. S., Oemler, A. J., Butcher, H., & Sharples, R. M. 1997, *ApJS*, 110, 213
- Smith, G. P., Treu, T., Ellis, R. S., Moran, S. M., & Dressler, A. 2004, *astro-ph/0403455*
- Sofue, Y. & Habe, A. 1992, *Publications of the Astronomical Society of Japan*, 44, 325
- Stasinska, G. 1990, *A&ASS*, 83, 501
- Stocke, J. T., Keeney, B. A., Lewis, A. D., Epps, H. W., & Schild, R. E. 2004, *AJ*, 127, 1336
- Stoughton, C., Lupton, R. H., Bernardi, M., Blanton, M. R., & the SDSS team. 2002, *AJ*, 123, 485
- Strateva, I., Ivezić, Ž., Knapp, G. R., Narayanan, V. K., Strauss, M. A., Gunn, J. E., Lupton, R. H., Schlegel, D., Bahcall, N. A., Brinkmann, J., Brunner, R. J., Budavári, T., Csabai, I., Castander, F. J., Doi, M., Fukugita, M., Gyóry, Z., Hamabe, M., Hennessy, G., Ichikawa, T., Kunszt, P. Z., Lamb, D. Q., McKay, T. A., Okamura, S., Racusin, J., Sekiguchi, M., Schneider, D. P., Shimasaku, K., & York, D. 2001, *AJ*, 122, 1861
- Tamura, N. & Ohta, K. 2003, *AJ*, 126, 596
- Tonry, J. & Davis, M. 1979, *AJ*, 84, 1511
- Tran, K. H., Simard, L., Zabludoff, A. I., & Mulchaey, J. S. 2001, *ApJ*, 549, 172
- Treu, T., Ellis, R. S., Kneib, J., Dressler, A., Smail, I., Czoske, O., Oemler, A., & Natarajan, P. 2003, *ApJ*, 591, 53
- Tucker, D. L., Oemler, A. J., Hashimoto, Y., Sheckman, S. A., Kirshner, R. P., Lin, H., Landy, S. D., Schechter, P. L., & Allam, S. S. 2000, *ApJS*, 130, 237
- Valentijn, E., Begeman, Boxhoorn, Deul, Rengelink, & Vermeij. 2004, *OmegaCAM Data Flow System - CALIBRATION PLAN Version 2.11*
- van-den Bergh, S. 2002, *PASP*, 114, 797
- van Dokkum, P. G., Franx, M., Fabricant, D., Illingworth, G. D., & Kelson, D. D. 2000, *ApJ*, 541, 95

- Vanzella, E., Cristiani, S., Dickinson, M., Kuntschner, H., Moustakas, L. A., Nonino, M., Rosati, P., Stern, D., Cesarsky, C., Ettori, S., Ferguson, H. C., Fosbury, R. A. E., Giavalisco, M., Haase, J., Renzini, A., Rettura, A., & Serra, P. 2004, astro-ph/0406591
- Varela, J., Moles, M., Márquez, I., Galletta, G., Masegosa, J., & Bettoni, D. 2004, *A&A*, 420, 873
- Vikhlinin, A., McNamara, B. R., Forman, W., Jones, C., Quintana, H., & Hornstrup, A. 1998, *ApJ*, 502, 558
- Vogt, N. P., Haynes, M. P., Giovanelli, R., & Herter, T. 2004a, *AJ*, 127, 3300
- . 2004b, *AJ*, 127, 3325
- Vollmer, B., Beck, R., Kenney, J. D. P., & van Gorkom, J. H. 2004, *AJ*, 127, 3375
- Wallace, P. 1998, *Astrom Basic Astrometry Program V3.6 User's Guide*
- Weedman, D. W., Feldman, F. R., Balzano, V. A., Ramsey, L. W., Sramek, R. A., & Wu, C.-C. 1981, *ApJ*, 248, 105
- Whitaker, R. J., Morris, S. L., & The CNOC2 Team. 2004, *MNRAS*, in preparation
- Whitmore, B. C. & Gilmore, D. M. 1991, *ApJ*, 367, 64
- Whitmore, B. C., Gilmore, D. M., & Jones, C. 1993, *ApJ*, 407, 489
- Wilson, G., Cowie, L. L., Barger, A. J., & Burke, D. J. 2002, *AJ*, 124, 1258
- Wu, H., Shao, Z., Mo, H. J., Xia, X., & Deng, Z. 2004, astro-ph/0404226, in press
- Yamauchi, C. & Goto, T. 2004, *MNRAS*, 352, 815
- Yee, H. K. C., Ellingson, E., & Carlberg, R. G. 1996, *ApJS*, 102, 269
- Yee, H. K. C., Morris, S. L., Lin, H., Carlberg, R. G., Hall, P. B., Sawicki, M., Patton, D. R., Wirth, G. D., Ellingson, E., & Shepherd, C. W. 2000, *ApJS*, 129, 475
- Young, P., Lynds, C. R., Sargent, W. L. W., Boksenberg, A., & Hartwick, F. D. A. 1978, *ApJ*, 222, 450
- Zabludoff, A. I. & Mulchaey, J. S. 1998, *ApJ*, 496, 39
- . 2000, *ApJ*, 539, 136
- Zwicky, F. 1937, *ApJ*, 86, 217

